**Transactions of the ASME, Journal of Heat Transfer** (ISSN 0022-1481) is published monthly by The American Society of Mechanical Engineers, Three Park Avenue, New York, NY 10016. Periodicals postage paid at New York, NY and additional mailing offices. POSTMASTER: Send address changes to Transactions of the ASME, Journal of Heat Transfer, c/o THE AMERICAN SOCIETY OF MECHANICAL ENGINEERS, 22 Law Drive, Box 2300, Fairfield, NJ 07007-2300. **CHANGES OF ADDRESS** must be received at Society headquarters seven weeks before they are to be effective. Please send old label and new address. **STATEMENT from By-Laws.** The Society shall not be responsible for statements or opinions advanced in papers or ... printed in its publications (B7.1, Para. 3).


# Journal of Heat Transfer

**Published Monthly by ASME**

**VOLUME 128 • NUMBER 2 • FEBRUARY 2006**

## RESEARCH PAPERS



## TECHNICAL BRIEFS



**(Contents continued on inside back cover)**

This journal is printed on acid-free paper, which exceeds the ANSI Z39.48-1992 specification for permanence of paper and library materials. ♾™
♻ 85% recycled content, including 10% post-consumer fibers.

**Journal of Heat Transfer** **Volume 128, Number 2** **FEBRUARY 2006**



## CALL FOR PAPERS



The ASME Journal of Heat Transfer is abstracted and indexed in the following:

*Applied Science and Technology Index, Chemical Abstracts, Chemical Engineering and Biotechnology Abstracts (Electronic equivalent of Process and Chemical Engineering), Civil Engineering Abstracts, Compendex (The electronic equivalent of Engineering Index), Corrosion Abstracts, Current Contents, E & P Health, Safety, and Environment, Ei EncompassLit, Engineered Materials Abstracts, Engineering Index, Enviroline (The electronic equivalent of Environment Abstracts), Environment Abstracts, Environmental Engineering Abstracts, Environmental Science and Pollution Management, Fluidex, Fuel and Energy Abstracts, Index to Scientific Reviews, INSPEC, International Building Services Abstracts, Mechanical & Transportation Engineering Abstracts, Mechanical Engineering Abstracts, METADEX (The electronic equivalent of Metals Abstracts and Alloys Index), Petroleum Abstracts, Process and Chemical Engineering, Referativnyi Zhurnal, Science Citation Index, SciSearch (The electronic equivalent of Science Citation Index), Theoretical Chemical Engineering*

# Thermal Characterization of Cu/CoFe Multilayer for Giant Magnetoresistive Head Applications

**Y. Yang**
Mechanical Engineering Department
Carnegie Mellon University,
Pittsburgh, PA 15213

**R. M. White**
Electrical and Computer Engineering Department
Carnegie Mellon University,
Pittsburgh, PA 15213

**M. Asheghi**[1]
Mechanical Engineering Department
and Electrical and Computer Engineering
Department,
Carnegie Mellon University,
Pittsburgh, PA 15213

*Giant magnetoresistance (GMR) head technology is one of the latest advancements in the hard disk drive (HDD) storage industry. The GMR head multilayer structure consists of alternating layers of extremely thin metallic ferromagnetic and nonmagnetic films. A large decrease in the electrical resistivity from antiparallel to parallel alignment of the film magnetizations is observed, known as the GMR effect. The present work characterizes the in-plane electrical and thermal conductivities of* Cu/CoFe *GMR multilayer structures in the temperature range of* 50 K *to* 340 K *using Joule-heating and electrical resistance thermometry on suspended bridges. The thermal conductivity of the GMR layer monotonically increases from* 25 $W m^{-1} K^{-1}$ *(at* 55 K*) to nearly* 50 $W m^{-1} K^{-1}$ *(at room temperature). We also report a GMR ratio of 17% and a large magnetothermal resistance effect (GMTR) of 25% in the* Cu/CoFe *multilayer structure.* [DOI: 10.1115/1.2136916]

*Keywords: GMR, heat transfer, measurement techniques, nanoscale, ultra-thin films*

## 1 Introduction

Magnetic hard disk drives continue to be the primary, high performance technology for data storage in computers and data processing systems. High areal densities have been achieved by introducing new technology and by proportionally reducing the dimensions of the sensor parts inside the hard disk drives. The most significant advancements have been the giant magnetoresistive (GMR) head technology that greatly enhances the sensitivity of the reading sensor to the magnetic field from the disk. This increased sensitivity makes it possible to detect smaller recorded bits and read them at higher data rates. Larger signals from GMR sensors also lead to a larger signal-to-noise ratio. GMR heads are expected to support areal densities beyond 100 Gbits/in.$^2$ by 2005 [1].

The magnetic data storage industry has developed a growing concern and interest toward the electrostatic discharge (ESD) phenomenon in the GMR head sensors [2]. The ESD failure has become the primary reliability issue for the production of GMR heads. ESD occurs when the GMR leads are brought in contact with charged objects during the manufacturing and packaging processes, causing large current transients to flow through the small GMR sensor. The induced Joule heating could either melt the sensor (physical damage), or alter the internal magnetic structure (magnetic damage) [2]. The performance and reliability of the GMR heads are adversely affected by the ESD failure due to the aggressive scaling of its dimensions to increase areal density [2]. The GMR sensor is embedded in a dielectric gap of thickness of the order of tens of nanometers. Due to the much lower thermal resistance of the gap dielectric layers, relative to the metallic GMR layer, the heat generated during the ESD event is conducted in the lateral direction toward the large area lead contacts. The shape of the temperature distribution in the GMR layer and the extent of lateral diffusion into the GMR and/or lead layers strongly depend on the thermal conductivities of the GMR and gap layers, $k_{GMR}$ and $k_{gap}$, as well as their corresponding thicknesses $d_{GMR}$ and $d_{gap}$ [3]. Investigation of the mechanism responsible for ESD damages in a GMR head has been primarily carried out experimentally [4,5]. However, more advanced GMR head design involves complete numerical modeling to find the temperature distribution and to predict the probable ESD failure voltage. Such modeling, on the other hand, requires accurate values for the thermal properties, such as thermal conductivity, of the GMR element and gap layers which is partially addressed in this paper.

**1.1 Physics of the GMR Effect.** The GMR sensor is a multilayer structure consisted of alternating layers of magnetic and nonmagnetic materials (10–20 Å each layer), as shown in Fig. 1. The multilayer structure can display relatively large changes (roughly 20%–50%) in its electrical resistivity in the presence of a magnetic field, known as the giant magnetoresistance (GMR) effect [6,7]. The GMR effect is generally due to the spin dependent electron bulk and interfacial scattering in the GMR multilayer structures. The bulk scattering is generally assumed to be spin-dependent, while the spin-dependence of the interfacial scattering is due to the differences in reflection and transmission coefficients of spin-up and spin-down electrons at the nonmagnetic-magnetic layer interfaces. The qualitative features of the GMR effect can be understood from a layered structure, consisting of two identical ferromagnetic CoFe layers separated from each other by a nonmagnetic Cu space layer, as shown schematically in Fig. 2. In this three layer system, the distance between the layers is relatively small compared to the mean free paths of electrons. In the absence of a magnetic field, the adjacent magnetic layers are magnetized at opposite directions. Assuming that the nonmagnetic interlayer has a good atomic lattice match to the magnetic layers, electrons will pass through this spacer layer without scattering. However, once the spin-up electrons from the top CoFe layer reach the bottom nonmagnetic-magnetic interface, they will be strongly scattered because their spin-polarizations are in the opposite direction to the magnetization of bottom CoFe layer. Similarly, the spin-down electrons coming from the bottom CoFe layer will also be scattered when they enter in the top CoFe layer. This will create a high electrical resistivity state for the GMR structure. If an external field is applied with sufficient

[1]Corresponding author.

Contributed by the Heat Transfer Division of ASME for publication in the JOURNAL OF HEAT TRANSFER. Manuscript received June 10, 2004; final manuscript received June 21, 2005. Review conducted by C. P. Grigoropoulos.

  

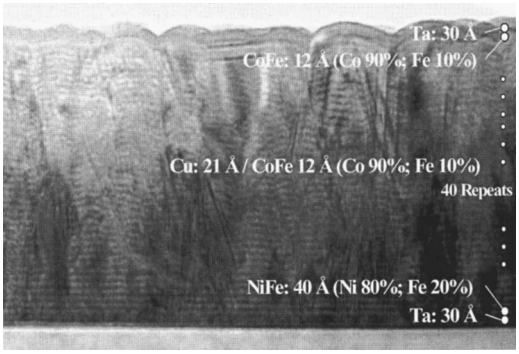


**Fig. 1 Tunneling electron micrograph (TEM) of the GMR structure. The GMR layer consists of (from top to bottom) Ta: 30 Å; CoFe: 12 Å (Co 90%; Fe 10%); 40 repeats: Cu: 21 Å CoFe 12 Å (Co 90%; Fe 10%); NiFe: 40 Å (Ni 80%; Fe 20%) and Ta: 30 Å.**

strength, the magnetization direction in the magnetic layers will be aligned in the same direction. The spin-down electrons will be scattered strongly at both nonmagnetic-magnetic interfaces. The spin-up electron, however, will be more likely to pass through the nonmagnetic-magnetic interface with less scattering, and the overall resistivity of the parallel GMR structure will be reduced. The variation of the GMR effect with the thickness of the ferromagnetic layers also contains information about the ratio of bulk and interfacial spin dependent scattering. It is clear that the GMR phenomenon is inherently a nanoscale effect in terms of charge and, therefore, heat transport in ultra-thin multilayer structures.

Electron transport in metallic thin films for giant magnetoresistance has been studied extensively in the past for obvious scientific and technological reasons [8]. Wang et al. [9] recently described an experimental four-point probe setup for in situ electrical and magneto transport measurements of Co/Cu GMR layers during the film growth, in order to study the effect of boundary scattering and surface specularity for both spin-independent and spin-dependent electrons. However, in order to understand the nature of the spin-dependent electron scattering mechanism, responsible for the GMR effect, both electrical and thermal transport properties of such multilayer structures must be measured and understood [10–12]. It is suggested that the thermal transport property measurements in GMR can be used to judge whether the scattering processes responsible for the GMR have elastic and/or inelastic components [11]. In comparison with the studies of electron transport, research involving the thermal transport of GMR layers has been very limited, in part due to experimental difficulties [10–12]. While the electrical resistivity measurement of deposited layers on an insulating substrate is rather trivial, these samples are unsuitable for thermal characterization due to the large contribution of the substrate to the thermal conduction. Films with several tens of microns thickness must also be grown to yield sufficiently accurate results [12]. As a result, the majority of the previous works have focused on the measurement of the field-dependent, rather than the absolute values of thermal transport properties [11,13,14]. The exceptions are the reported thermal conductivity measurements of the free standing Co-Ag granular [12] and Co/Cu multilayer [10] with thickness of 100 and 1 $\mu$m, respectively. In these measurements, the thermal conductivity of the films were measured using the traditional heat-sink four-probe method, in which the temperature gradient was established by a resistive heater mounted one end of the film, with the other side attached to a copper block at a known temperature. Although the measurement method is straightforward, the heat loss due to the radiation and air conduction must be carefully accounted for; otherwise significant error in the measurements may occur. In order to achieve a high level of accuracy in the measurements, film thickness from several to one hundred microns is required to obtain substantial thermal conductance [12]. This is nearly two orders of magnitude thicker than the nanometer size structures incorporated in the existing GMR devices. In many cases, electron-boundary scattering at the top and bottom of the layer may also become significant in addition to the spin-dependent electron scattering at the interfaces of the multilayers. It appears that many of the arguments used to describe the underlying observed physical phenomena in GMR technology are contradictory and resolving them will not be possible without reliable electro-thermal transport property measurements. For example, it is argued that the "large-angle elastic scattering processes are responsible for the electrical transport effects in MBE-grown (111) Co/Cu multilayers" [10] while others suggested that "the scattering mechanisms in multilayer samples have a significant inelastic, spin-flip component" [11]. The arguments about the relative contribution of electrons and phonons to heat transport have been even more controversial [10,11].

In this paper, we report the experimental results for temperature-dependent in-plane electrical resistivity and thermal conductivity measurements of the CoFe/Cu GMR multilayers. The thermal conductivity of the GMR layer is also measured in the presence of an external magnetic field. The steady-state Joule heating and electrical resistance thermometry is used for the thermal conductivity measurements.

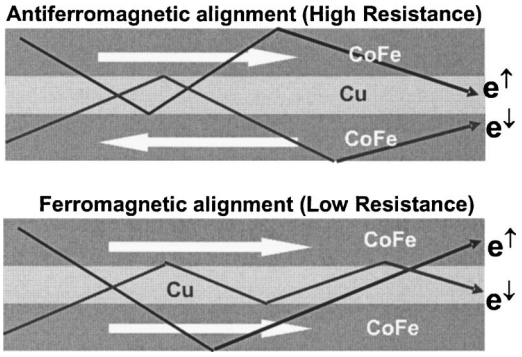


**Fig. 2 Schematic representation of electron transport in a GMR multilayer structure, consisting of top and bottom CoFe magnetic layers and Cu nonmagnetic space layer. The distance between the layers is relatively small compared to the mean free paths of electrons. Large decreases in the electrical and thermal resistivities are expected due to the spin-dependent scattering at the interfaces of the CoFe and Cu multilayer structure.**

## 2 Experimental Details

**2.1 Test Structure.** Figure 3 shows a schematic and an optical microscope image of the experimental structure. The steady state technique adopted here, which uses a nearly uniformly heated suspended bridge, is based on the method used by Tai et al. [15] to measure the lateral thermal conductivity of heavily doped LPCVD polycrystalline silicon films. Lu et al. [16] performed thermal conductivity measurements on platinum thin wires using the same method. The GMR layer was deposited (on top of the 20 nm thermally grown silicon dioxide/385 $\mu$m silicon wafer) using a Connexion Sputtering System. A 1-$\mu$m-thick photoresist layer (Dupont 2556) is spun onto the wafers and developed, followed by an ion milling process to pattern the GMR structure. The photoresist is then removed by a combination of oxygen plasma and standard acetone cleansing processes. Subsequently, another layer of photoresist layer (Dupont 2556) is spun onto the wafer and developed to define the regions on the silicon substrate that would be exposed for the isotropic reactive ion etching process. The STS machine is then used to undercut and release the GMR structures followed by an ion milling process using an oxygen ion coupled plasma etcher to remove the photoresist from the sus-

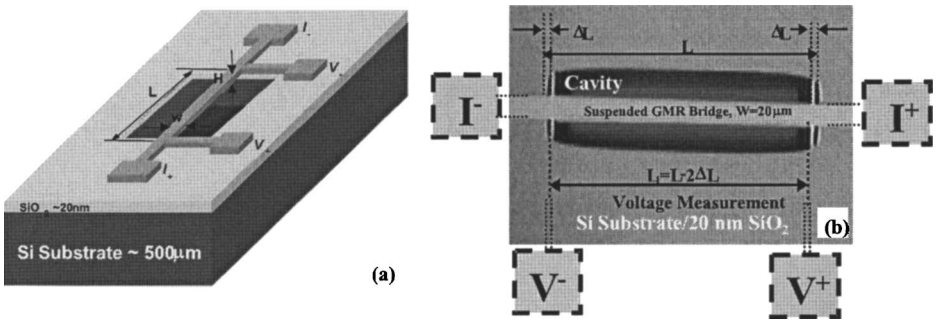


**Fig. 3 The fabricated suspended microbridge structure: (*a*) schematic, and (*b*) top view image taken using an optical microscope. The dimension $\Delta L$ is the length of the over-etched area near the bases of the suspended structure. Voltage pads are connected to the suspended structure by nearly 2-$\mu$m-wide interconnects.**

pended structures. The targeted dimensions of the suspended structures were: widths, $w=16$, 18 and 20 $\mu$m, lengths, $L_1=200$, 250, 300 and 500 $\mu$m, and thickness, $d=144$ nm. The electrical resistance of the suspended beam is measured using the four-probe measurement technique through the current and voltage access pads depicted in Fig. 3. There is a slight over-etch at the bases of the suspended beam, $\Delta L \sim 5$ $\mu$m, which must be carefully accounted for in the analyses and extraction of the thermal conductivity data. The GMR layer consists of (from top to bottom) Ta: 30 Å; CoFe: 12 Å (Co 90%; Fe 10%); 40 repeats: Cu: 21 Å CoFe 12 Å (Co 90%; Fe 10%); NiFe: 40 Å (Ni 80%; Fe 20%) and Ta: 30 Å. The TEM of the GMR structure (Fig. 1) clearly shows the repeated bi-layers Cu/CoFe as well as the grains boundaries formed across the layer. In addition, as we move from the bottom to the top of the multilayer structure, a certain level of waviness in the bi-layer structures is observable.

**2.2 Thermal Conduction Analysis.** Steady-state Joule heating and electrical resistance thermometry are used to measure the lateral thermal conductivity of the GMR structure. The average temperature rise of the bridge is calculated from the measured electrical resistance by solving the heat diffusion equation in the structure. The model is based on the one-dimensional heat conduction with the following approximations: (1) the end-supports of the bridge are kept at the ambient temperature $T_0$, the same as that of the silicon wafer; (2) heat loss from the surfaces, due to the thermal radiation and free-molecule air conduction, are negligible, and (3) the temperature of the planar cross sections perpendicular to the bridge is uniform. Under these assumptions, with a dc electrical current $I$ passing through the bridge, the one-dimensional heat diffusion equation with volumetric heat generation in the bridge is described by the following equations and boundary conditions

$$k_{\mathrm{GMR}}\frac{d^2T}{dx^2}+\frac{I^2R_0[1+\alpha_{\mathrm{GMR}}(T-T_0)]}{wd_{\mathrm{GMR}}L}=0 \tag{1a}$$

$$T(x=\pm L/2)=T_0 \tag{1b}$$

where $k_{\mathrm{GMR}}$ and $\alpha_{\mathrm{GMR}}$ are the lateral thermal conductivity and the temperature coefficient of the electrical resistance (TCR) of the GMR structure. $R_0$ is the electrical resistance of the bridge at temperature, $T_0$. The length, width, and thickness of the bridge are $L$, $w$, and $d_{\mathrm{GMR}}$, respectively. Introducing the new variable, $\theta=1+\alpha_{\mathrm{GMR}}(T-T_0)$ into Eq. (1*a*) and the corresponding boundary conditions (1*b*)

$$\frac{d^2\theta}{dx^2}+m^2\theta=0 \tag{2a}$$

$$\theta(x=\pm L/2)=1 \tag{2b}$$

where $m^2=I^2R_0\alpha_{\mathrm{GMR}}/(wd_{\mathrm{GMR}}Lk_{\mathrm{GMR}})$. This equation can be solved to yield

$$\theta(x)=\cos mx/\cos(mL/2) \tag{3}$$

Integrating the above equation from $-L/2$ to $+L/2$, the average temperature of the bridge is given by

$$\overline{T}=T_0-\frac{1}{\alpha_{\mathrm{GMR}}}[1-(2/mL)\tan(mL/2)] \tag{4}$$

The average electrical resistance of the bridge is given by

$$R=R_0[(2/mL)\tan(mL/2)] \tag{5}$$

The lateral thermal conductivity along the bridge can be obtained by fitting Eq. (5) to the experimental data for electrical resistance, as shown in Fig. 4. Careful heat conduction analyses are performed to verify the approximations (1) through (3). An analytical solution for heat conduction in the suspended bridge with nearly uniform heat generation and surface heat losses due to radiation and molecular conduction are developed to quantitatively examine the effect of unwanted heat loss mechanisms from the bridge. The results indicate that the heat losses from the surface by both radiation and molecular gas conduction are negligible. These findings are consistent with the existing analysis of the structures with

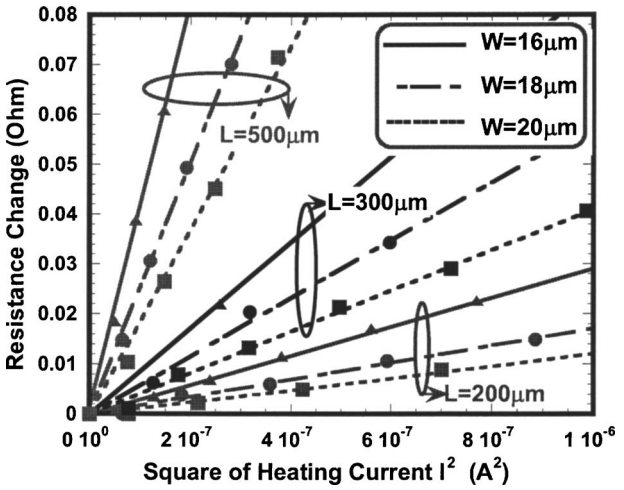


**Fig. 4 Changes in the electrical resistances of the suspended bridge as a function of square of current, $I^2$. Curve fits for bridges of the same width and different lengths yield $k_{\mathrm{GMR}}=51$ W m$^{-1}$ K$^{-1}$, for the GMR layer.**

comparable dimensions [15]. More specifically, assuming the emissivity of one, $\epsilon=1$, and for average temperature rise in the bridge up to $\sim 25°C$ above the room temperature, the heat loss due to radiation can be neglected. In the present measurements, the average temperature rise in the bridge was kept well below 5°C. This fact is further verified experimentally by realizing that the thermal conductivity data for different bridge lengths and widths showed very little variations. An analysis of the spreading effect into the substrate was made and concluded that the base temperature can be assumed at $T_0$ for all practical purposes. We also performed the necessary heat conduction analysis and confirmed that the portion of the beams that rest on the substrate can be assumed to have temperatures near $T_0$. This can be done by comparing the thermal resistance along the bridge, $R_{\text{th,bridge}} \sim (L/2)/(k_{\text{GMR}} \times w \times d_{\text{GMR}})$ with that of the thin silicon dioxide layer at the base $R_{\text{th,base}} \sim d_o/(k_o \times A_{\text{eff}})$ where $d_o$ and $k_o$ are the thickness and thermal conductivity, respectively, and $A_{\text{eff}}=w \times L_h$ is the effective area for conduction to the substrate. Here $L_h$ is the healing length defined as $L_h=(k_{\text{GMR}} \times d_{\text{GMR}} \times d_o/k_o)^{1/2}$. The ratio of $R_{\text{th,bridge}}/R_{\text{th,base}}$ yields a simple expression of $\sim L/L_h$, which is on the order of 100 for the given geometry and dimensions of the present experimental structure. Furthermore, the complete heat conduction equation for both the suspended and the on-substrate portions is solved assuming that the heat loss to the silicon substrate occurs through the 20-nm-thick silicon dioxide layer. The above-noted calculations indicate that the slight temperature rise on the order of 0.05°C, at the end of the base, can be neglected compared to the average temperature rise in the beam, which is kept between 3 and 5°C. The high resolution IR thermometry was also performed, which essentially verified the above analysis.

**2.3 Test Procedures.** The measurements are performed in a special model Janis ST-100 continuous flow cryostat that is capable of reaching vacuum levels on the order of $5 \times 10^{-4}$ Torr and temperatures below 10 K by using liquid helium. The sample dies are placed in a 68-pin LCC chip carrier and wire-bonded to provide electrical access to the suspended beams. The electrical resistances of the GMR beam elements are measured using the four-probe measurement technique. The LCC chip carrier is packaged in a socket that is attached to the copper sample holder. Electrical connections to the socket are made via feedthroughs on the cryostat. A diode temperature sensor with accuracy of ±50 mK is attached to the sample die, to monitor the substrate temperature. The substrate temperature can be precisely controlled through a resistor heater on the sample holder whose current is adjusted by the Lakeshore-331S temperature controller.

In the present study, the measurements are performed in a relatively high vacuum ($\sim$1 mTorr) environment to eliminate the heat loss by gas conduction. For eliminating the radiation heat loss, the sample was surrounded by a polished aluminum radiation shield kept at substrate temperature $T_0$. This radiation shield, with high surface reflectivity, helped greatly to minimize the radiation from the sample to the environment, especially for the measurements performed above the room temperature. Detailed calculations indicate that heat losses by air conduction and thermal radiation are at least two orders of magnitude lower than heat conduction along the bridge to the substrate. As was discussed previously, due to the slight over-etch of the silicon substrate near the bases, the ideal boundary condition described by Eq. (1*b*) may not accurately describe the situation. In other words, these equations are only applicable if the voltage access interconnects meet the suspended bridge exactly at its base. We attempted to account for this by calculating the average temperature of the bridge by integrating Eq. (3) from $(-L/2 \pm \Delta L)$ to $(+L/2 - \Delta L)$, where $\Delta L$ is the distance from the bridge ends to the voltage interconnects/probes that contact the GMR suspended bridge (Fig. 3).

The experimental data collection process is completely automated using a computer to control the temperature controller, power supply, and multimeters. The temperature controller is used to set the substrate or base temperature, $T_0$. Once the temperature reading becomes stable, the current dependent resistance of the bridge is recorded by measuring the current through and voltage drop along the bridge. This procedure is repeated for the desired temperature range with temperature interval of 10 K. The current passing through the bridge is limited to ensure the temperature rise (usually 3–5 K) is less than the set temperature interval. The temperature coefficient of the electrical resistance $\alpha_{\text{GMR}}$ is obtained by extrapolating $R_0$ from *R-I* curve at small currents to avoid self-heating, at a given base temperature. The temperature-dependent thermal conductivity of the GMR bridge is determined from Eq. (5).

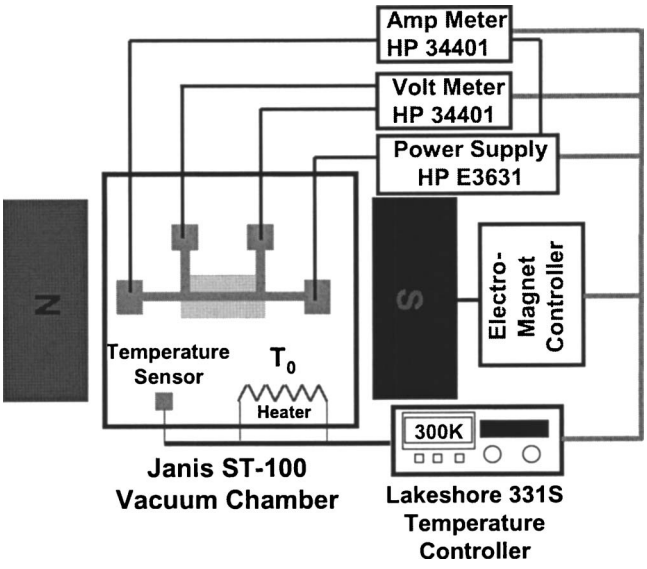


**Fig. 5 Experimental apparatus for field-dependent measurement**

The electrical resistivity of a GMR multilayer structure changes significantly when an external magnetic field is applied. Therefore, it is also expected that the electronic thermal conductivity will undergo similar changes. To verify this effect, we performed the magnetic-field-dependent thermal conductivity measurement using the present GMR multilayer structure. The field-dependent measurements of resistivity and thermal conductivity of the GMR multilayer structure were achieved by placing the entire cryostat into the gap of the electromagnet, which has a uniform magnetic field distribution (Fig. 5). The magnetic field is applied along the GMR bridge and its strength can be varied from −3000 Oe (antiparallel to the current direction) to 3000 Oe (parallel to the current direction).

For the field-dependent measurement, the previously described procedure should be repeated at different field strengths. The straightforward way to accomplish this is to keep the magnetic field constant and then to measure the *R* versus *I* variations at different base temperatures. Then the same procedure should be repeated at different field strengths. However, several practical problems and issues prevented us from adopting this procedure. The long-term stability of the magnetic field, especially at large field strength, is problematic since a large electrical current $\sim$30 A is required. On the other hand, the base temperature can be maintained constant within ±0.02 K by using the PID temperature controller. In addition, varying the base temperature is a slow process due to the large thermal mass of the sample holder while the magnetic field can be switched rapidly. In order to overcome these shortcomings, we adopted an alternative experimental procedure, which is schematically depicted in Fig. 6. In this procedure, *R* versus *I* curves are measured at different field strength

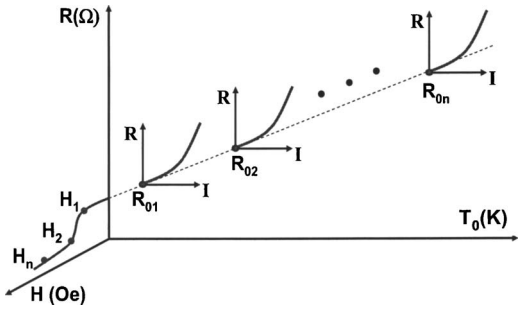


**Fig. 6 Schematic of the calibration procedure. The *R* versus *I* curves for the GMR bridge were measured at different field strength while keeping the base temperature constant. The same process was repeated at different base temperatures.**

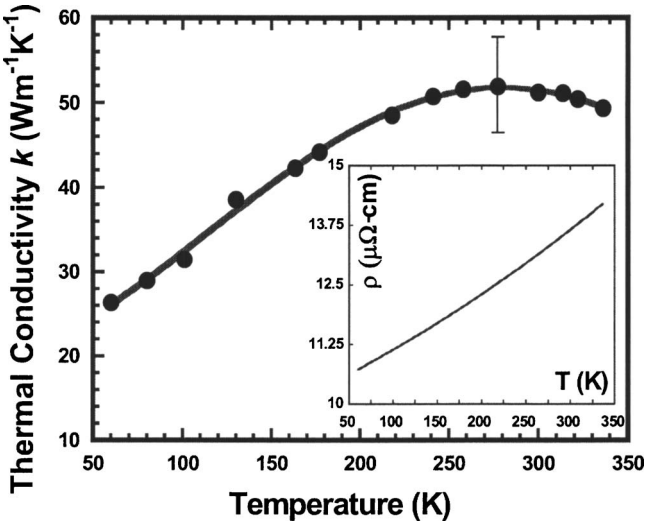


**Fig. 7 Temperature dependence of thermal conductivity for Cu/CoFe GMR multilayer structure. The electrical resistivity is shown in the right inset.**

while keeping the base temperature constant. Then the same process was repeated at other base temperatures. During the required time period to reach a new thermal equilibrium, the electromagnet can be switched off to avoid overheating. The outcome of this procedure would simply yield the electrical resistivity as a function of current, temperature, and strength of the magnetic field, $R=R(I,T,H)$. The temperature coefficient of the electrical resistance $\alpha_{\mathrm{GMR}}$, for a given field strength, can be obtained by extrapolating the $R$ versus $I$ curves at small currents while keeping $H$ constant. The temperature-dependent thermal conductivity of GMR structure at different field strengths can be extracted using Eq. (5).

**2.4 Uncertainty Analysis.** The measurement of $k_{\mathrm{GMR}}$ involves fitting the solution of Eq. (5) to the measured electrical resistance change as function of applied current. Based on the uncertainty analysis developed by Holman [17], the uncertainty in thermal conductivity, $\Delta k_{\mathrm{GMR}}$, can be expressed as

$$\Delta k_{\mathrm{GMR}}^2 = \Delta_{\mathrm{fit}}^2 + \Delta_{\mathrm{exp}}^2 \tag{6}$$

where $\Delta_{\mathrm{fit}}$ is uncertainty from the fitting procedure and $\Delta_{\mathrm{exp}}$ is associated with uncertainty of the measured parameters used in Eq. (5) such as: current, voltage, TCR, and dimensions of the bridge (width, length and thickness). The term, $\Delta_{\mathrm{fit}} \sim 3\%$, was estimated by calculating the standard deviation of the fitted $k_{\mathrm{GMR}}$ from bridges with different lengths and widths. The measurement sensitivity is defined as

$$\Omega_r = r\frac{\partial R}{\partial r} \tag{7}$$

where $R$ is the function given by Eq. (5) and $r$ can be any of the independent variables (e.g., current, voltage, etc.) necessary to evaluate Eq. (5). The $\Delta_{\mathrm{exp}}$ can be expressed as

$$\Delta_{\mathrm{exp}} = \frac{1}{\Omega_{k_{\mathrm{GMR}}}}\left(\sum_r (\Omega_r \Delta r)^2\right)^{1/2} \tag{8}$$

where $\Delta r$ is the uncertainty of the independent variables, and $\Omega_{k_{\mathrm{GMR}}}$ is the measurement sensitivity with respect to $k_{\mathrm{GMR}}$. For the present suspended GMR bridges, the $\Delta_{\mathrm{width}}$ and $\Delta_{\mathrm{length}}$, from different dies, were measured using SEM and profilometer, which proved to be accurate within ±2% and ±0.1%, respectively. The TCR of the GMR bridge, $\alpha_{\mathrm{GMR}}$, is measured to be around $1.01 \times 10^{-3}\ \mathrm{K}^{-1}$ at 300 K with the uncertainty $\Delta\alpha_{\mathrm{GMR}}$ around ±3%. The relatively large uncertainty in this value is due to the fact that the temperature sensor was slightly further away from the LCC chip carrier. The measured current and voltages are accurate to $\Delta_I = \pm 0.01\%$ and $\Delta_V = \pm 0.1\%$, respectively. Using Eqs. (6) and (8), the total relative uncertainty for the reported values of the thermal conductivity, $k_{\mathrm{GMR}}$, is estimated to be smaller than ±10%.

**2.5 Experimental Results and Discussions.** Complete experiments and analysis were carried out for the bridges with different lengths and widths, yielding nearly identical thermal $k_{\mathrm{GMR}}$ values. For brevity, the results reported here were taken from the average values of different bridges. Figure 7 depicts the measured thermal conductivity and electrical resistivity (inset) of 144 nm CoFe/Cu GMR layer in the temperature range of 50–340 K. The thermal conductivity of the GMR layer monotonously increased from $k_{\mathrm{GMR}} = 25\ \mathrm{W\,m^{-1}\,K^{-1}}$ at 55 K to nearly $50\ \mathrm{W\,m^{-1}\,K^{-1}}$ at room temperature. It appears that the thermal conductivity reaches a maximum, near 280 K, and then slightly reduces. The trend of the experimental data indicates strong electron-boundary scattering at the interfaces that is consistent with the size effect experimental data for thermal conductivity of thin metallic [18,19] layers as well as the giant magnetoresistive theory [20]. The origin of the change in the GMR due to bulk and surface scattering can be understood in terms of lateral confinement changing the effective mean free paths within the Cu/CoFe multilayer system [13]. The length scale at which this occurs is of the order of the film thickness and the corresponding mean free paths.

Previously reported thermal conductivity data for 200 bilayers of (111) Co (25 Å) and Cu (~25 Å) of total thickness 1 $\mu$m are comparable with those of the bulk Cu near the room temperature [10]. These results contradict the electron-surface [18] and grain-boundary [19] scattering theories as well as our experimental data over the entire temperature range. In order to resolve this issue we also measured the thermal conductivity of the 144 nm Cu layer, $k_{\mathrm{Cu}}$, over the temperature range of 50–450 K. The room temperature thermal conductivity value is nearly $250\ \mathrm{W\,m^{-1}\,K^{-1}}$, which is significantly lower than the bulk value of $\sim 400\ \mathrm{W\,m^{-1}\,K^{-1}}$. The predictions for thermal conductivity of the 144 nm Cu layer using the electron-grain boundary scattering theory [18] agrees with the experimental data assuming that the electron reflection coefficient at grain boundaries, $R$, to be 0.23 and 0.13 at room temperature and 50 K, respectively [18,21]. It is also assumed that the average grain size dimension, $d_g$, is about 8 nm [18]. It would be too speculative to extend this theory to 10–20 Å Cu layers. However, one would expect that the thermal conductivity of the GMR layer to be ***certainly*** greater than the thermal conductivity of a 21 Å Cu layer yet ***significantly*** smaller than that of a 144 nm Cu film. It is worthwhile to mention that the thermal conductivity of 144 CoFe layers, $k_{\mathrm{CoFe}}$, is also measured to be around $30\ \mathrm{W\,m^{-1}\,K^{-1}}$ at room temperature. However, it would be difficult to estimate the thermal conductivity of the 12 Å CoFe by extrapolating these data

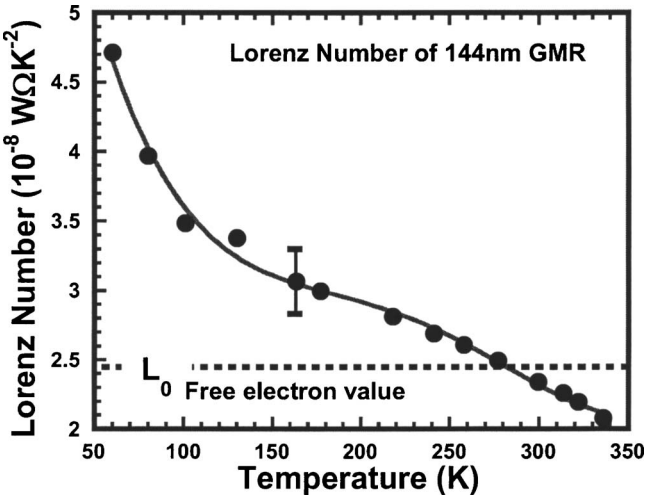


**Fig. 8 Lorenz number values for 144 nm GMR layer of the present study as a function of temperature. The Lorenz number value for free electron is nearly $L_0 = 2.45 \times 10^{-8}$ W Ω K$^{-2}$.**

due to the possible variations in the grain size and distribution. There is an indication that the mean free paths of the electrons that would traverse through the repeated Cu/CoFe multilayers are greater than the thickness of the individual layers, which is consistent with the giant magnetoresistive theory [20]. Full understanding of electron transport in laterally confined ***giant magnetoresistance*** multilayers would be extremely challenging and requires systematic measurements and rigorous atomistic simulations. Therefore, any additional comments on the nature of the heat and charge transport in these structures would be too speculative at the present time.

Experimental data for electron thermal conductivity, $k_e$, and electrical resistivity, $\rho$, of the Cu/CoFe multilayer (Fig. 7) are used to generate the Lorenz number (Fig. 8),

$$L_z = \frac{k_e \rho}{T} \tag{9}$$

where $T$ is the absolute temperature. This expression assumes that lattice contribution is negligible compared to electronic contribution to the thermal conductivity. The $L_z$ in Eq. (9) compares the mean free path or relaxation times (scattering rate) of the conduction electrons for thermal and electrical transport. The value $L_0 = 2.45 \times 10^{-8}$ W Ω K$^{-2}$ indicates that the mean free paths for heat and charge transports are nearly identical, $\Lambda_T = \Lambda_e$. The value of $L_z/L_0 > 1$ implies that the heat transport is less impeded compare to the charge transport, $\Lambda_T > \Lambda_e$. Contrarily, the thermal transport is more inhibited than the charge transport if $L_z/L_0$ is less then unity. For the typical metal, the deviation of the measured Lorenz number from the limiting value $L_0$ is rather small above the Debye temperature $\Theta_D$, where elastic electron-phonon scattering is dominated for both charge and thermal transport. In the intermediate temperature range, where the small wave vector phonon dominates, the electron-phonon scattering is small angle and inelastic in nature. This inelastic electron scattering usually suppresses the thermal conductivity more than the electrical conductivity, resulting in the Lorenz number being smaller than $L_0$. As shown in Fig. 8, the Lorenz number of the present GMR multilayer structures is nearly equal to $L_0$ at room temperature and decreases rapidly as the temperature is increased to 380 K. In contrast, at low temperatures, the Lorenz number is between a factor of two to three larger than the $L_0$. It is stated that the contribution of phonons to the heat transport is negligible for pure and metal alloys if the resistivity is less than 100 $\mu\Omega$ cm [22]. The electrical resistivity of the GMR layer is about 12 $\mu\Omega$ cm at room temperature indicating that contribution of phonons to the heat transport is insignificant compared to the electrons. From Fig. 8, it is concluded that Wiedemann-Franz law does not hold for the GMR multilayer structures, but no direct comparison with previous studies (e.g., Refs. [10,11]) can be made since none of these studies succeeded in accurately measuring the absolute thermal conductivity of the GMR structure. The Lorenz numbers for 144 nm Cu and CoFe are also measured to be $\sim 1.8 \pm 0.2 \times 10^{-8}$ W Ω K$^{-2}$ and $\sim 1.65 \pm 0.2 \times 10^{-8}$ W Ω K$^{-2}$, respectively, compared to the value of $2.25 \pm 0.2 \times 10^{-8}$ W Ω K$^{-2}$ for the GMR layer. It is noted that the Lorenz number for the CoFe is smaller than those of the GMR and Cu at room temperature.

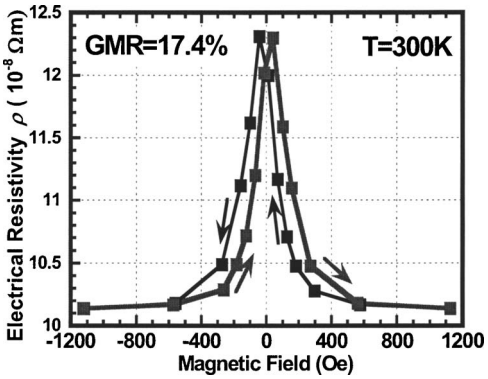


**Fig. 9 Resistivity change of the 144 nm Cu/CoFe GMR multilayer structure as a function of applied field**

Figures 9 and 10 show the measured electrical resistivity and thermal conductivity change as a function of external magnetic field strength at 300 K, where the field is applied along the bridge, parallel to the direction of electrical current passing through the bridge. The GMR multilayer exhibits the largest resistivity at zero field strength and decreases as the field strength is increased. The GMR ratio, defined as $(\rho_0 - \rho_s)/\rho_0$, for the present 144 nm thickness GMR layer, at 300 K, is measured to be ~17%. The $\rho_s$ and $\rho_0$ are the electrical resistivity at saturation and zero fields, respectively. The thermal conductivity increases as the field strength increases and finally saturates when the field is large enough to align the magnetization of the CoFe layers parallel with each other. There are two peaks in the thermal conductivity appearing at $\sim \pm 250$ Oe. We have not been able to find a convincing explanation for this effect. Interestingly enough, the peaks disappear at temperatures above 350 K. The field-dependent thermal conductivity, referred to as the giant magnetothermal resistance (GMTR) effect, has the same order of magnitude as the GMR effect,

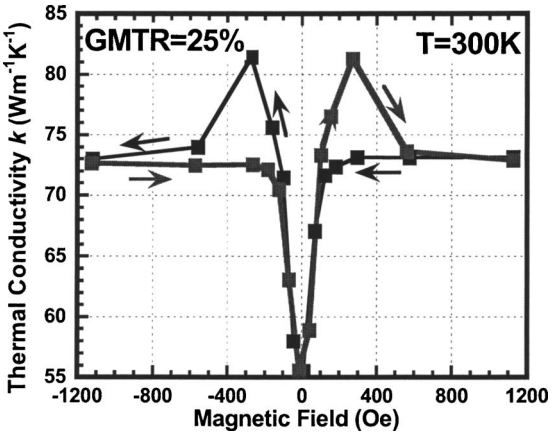


**Fig. 10 Thermal conductivity change of the 144 nm Cu/CoFe GMR multilayer structure as a function of applied field**

~25%, at room temperature. Here the GMTR effect is defined as $(k_s - k_0)/k_s$, where $k_s$ and $k_0$ are the thermal conductivity at saturation and zero field, respectively. This further suggests that the GMR and GMTR effects both originate from the scattering of the conduction electrons, since the phonon thermal conductivity and thermal leakages should be independent of magnetic field. The larger percentage change in thermal resistance, 25%, compared to the 17% change in electrical resistance can be explained as follows: In the antiferromagnetic (high resistivity) state the electron scattering rate for thermal transport is larger than that for charge transport as the scattering events occur when the electrons enter into the neighboring CoFe layers. This is consistent with the fact that the Lorenz number for the CoFe, $1.65 \pm 0.2 \times 10^{-8}$ W Ω K$^{-2}$, is significantly smaller than $L_0$ at room temperature. In the ferromagnetic states the spin-up electrons move through multiple CoFe and Cu layers with relatively less scattering compared to the antiferromagnetic state. One can imagine that in this state the effective scattering media (CoFe) for thermal transport is somewhat removed and therefore the electron scattering rates for thermal and charge transport is dictated by a combination of Cu and CoFe medium. As a result, one should expect a larger percentage change in electron scattering rate for thermal transport compared with the charge transport as the latter was less affected by the presence of the CoFe in the antiferromagnetic state.

The results presented here are very interesting and potentially very valuable in the fundamental study of the charge and heat transport. However, additional work is required to verify these results using other thin film thermal characterization techniques that do not require interpretation of the average temperature rise in the suspended structure [23] or those that use an additional metallic bridge, insensitive to the variation in external magnetic field such as Cu, as heater and thermometer [24]. As part of the verification process, the GMTR effect for 144-nm-thick copper and CoFe are also measured at room temperature. As expected, no GMR or GMTR effects were observed for the copper layer, while a very small anisotropic magnetoresistive (AMR) effect ~1.7% was observed for CoFe layer.

## 3 Conclusion

In this work, the temperature-dependent electrical and thermal conductivity of a 144 nm Cu/CoFe GMR multilayer was measured using Joule heating and electrical resistance thermometry in a suspended microbridge structure. It is concluded that the Wiedemann-Franz law is not valid for the GMR multilayer structures at very low and high temperatures. In addition, a large magnetothermal resistance (GMTR) effect ~25% is observed, which is larger than the GMR effect ~17%, indicating that the mechanisms responsible for the charge and heat transport may not be identical. A systematic study of thermal transport in multilayer structures of different film/period thicknesses is needed to provide a clearer picture of the heat transport in metallic multilayer structures.


## Acknowledgment

The authors would like to acknowledge support from the Data Storage Systems Center (DSSC) at Carnegie Mellon University and Dr. Peng in DSSC for doing the TEM of GMR samples. This work is also partially supported by a grant from National Science Foundation (NSF-0103082) for Nanotechnology Interdisciplinary Research Team (NIRT).


## Nomenclature

$A_{\text{eff}}$ = effective area for heat conduction to the substrate at the base of the bridge, m$^2$
$d_{\text{GMR}}$ = thickness of the GMR element in GMR head, m
$d_g$ = average gain size in Cu film, nm
$d_{\text{gap}}$ = thickness of gap layer in GMR head, m
$d_o$ = thickness of the silicon dioxide layer, m
$H$ = magnetic field, Oe
$I$ = electrical current in the suspended bridge, A
$k_{\text{CoFe}}$ = thermal conductivity of CoFe layer, W m$^{-1}$ K$^{-1}$
$k_{\text{Cu}}$ = thermal conductivity of Cu layer, W m$^{-1}$ K$^{-1}$
$k_{\text{GMR}}$ = thermal conductivity of GMR layer, W m$^{-1}$ K$^{-1}$
$k_o$ = thermal conductivity of silicon dioxide layer, W m$^{-1}$ K$^{-1}$
$k_0$ = thermal conductivity of GMR layer at zero magnetic field, W m$^{-1}$ K$^{-1}$
$k_s$ = thermal conductivity of GMR layer at saturation magnetic field, W m$^{-1}$ K$^{-1}$
$m$ = parameter in Eq. (2), m$^{-1}$
$\rho$ = electrical resistivity of GMR layer, Ω m
$\rho_0$ = electrical resistivity of GMR layer at zero magnetic field, Ω m
$\rho_s$ = electrical resistivity of GMR layer at saturation magnetic field, Ω m
$L$ = length of the suspended GMR bridge, μm
$L_0$ = Lorenz number for the free electron system, $2.45 \times 10^{-8}$ W Ω K$^{-2}$
$L_1$ = length of the suspended GMR bridge between voltage pads, μm
$L_z$ = parameter in Eq. (9), W Ω K$^{-2}$
$R$ = electrical resistance of the suspended GMR bridge, Ω
$R_0$ = electrical resistance of the suspended GMR bridge without self-heating, Ω
$R_{\text{th,base}}$ = normal thermal resistance from bridge to the base, m$^2$ K W$^{-1}$
$R_{\text{th,bridge}}$ = lateral thermal resistance along the suspended bridge, m$^2$ K W$^{-1}$
$T$ = temperature of the suspended GMR bridge, K
$T_0$ = temperature of the base, K
$V$ = voltage across the suspended bridge, V
$w$ = width of the suspended GMR bridge, μm
$\alpha_{\text{GMR}}$ = temperature coefficient of electrical resistance in GMR multilayer, K$^{-1}$
$\epsilon$ = emmissivity
$\theta$ = parameter in Eq. (3)
$\Theta_D$ = Debye temperature, K
$\Omega_r$ = sensitivity of the resistance change to the GMR bridge properties
$\Delta_{\text{exp}}$ = uncertainty in measurement of GMR properties, %
$\Delta_{\text{fit}}$ = uncertainty in fitting procedure, %
$\Delta_I$ = uncertainty in current measurement, %
$\Delta k_{\text{GMR}}$ = uncertainty in measured $k_{\text{GMR}}$, %
$\Delta L$ = distance from ride ends to the voltage probes that contact the GMR suspended bridge, μm
$\Delta_V$ = uncertainty in voltage measurement, %

## References


[1] Thompson, D. A., and Best, J. S., 2000, "The Future of Magnetic Data Storage Technology," IBM J. Res. Dev., **44**(3), pp. 311–322.
[2] Wallash, A., 2003, "Electrostatic Discharge (ESD) Challenges in Magnetic Recording: Past, Present and Future," *Proc. IEEE International Reliability Physics Symposium*, Dallas, TX, March 30–April 4, pp. 222–228.
[3] Yang, Y., Sadeghipour, S. M., and Asheghi, M., 2003, "Modeling of Temperature Rise in Giant Magnetoresistive (GMR) Sensor during an Electrostatic Discharge (ESD) Event," *ASME Summer Heat Transfer Conference*, HT2003-47266, Las Vegas, Nevada, July 21–23.
[4] Wallash, A., and Kim, Y. K., 1997, "Electrostatic Discharge Sensitivity of Giant Magnetoresistive Recording Heads," J. Appl. Phys., **81**, pp. 4921–4923.
[5] Wallash, A., and Kim, Y. K., 1998, "Magnetic Changes in GMR Heads caused by Electrostatic Discharge," IEEE Trans. Magn., **34**, pp. 1519–1521.
[6] Baibich, M. N., Broto, J. M., Fert, A., Nguyen Van Dau, F., Petroff, F., Eitenne, P., Creuzet, G., Friederich, A., and Chazelas, J., 1988, "Giant Magnetoresistance of (001)Fe/(001)Cr Magnetic Superlattices," Phys. Rev. Lett., **61**, pp. 2472–2475.

[7] Binasch, G., Grünberg, P., Saurenbach, F., and Zinn, W., 1989, "Enhanced Magnetoresistance in Layered Magnetic Structures with Antiferromagnetic Interlayer Exchange," Phys. Rev. B, **39**, pp. 4828–4830.
[8] Persat, N., Van den Berg, H. A. M., and Dinia, A., 1999, "Electrical Transport in Metallic Thin Films for Giant Magnetoresistance Modeling Purposes," J. Magn. Magn. Mater., **198–199**, pp. 89–91.
[9] Wang, S. X., Yamada, K., and Bailey, W. E., 2000, "Specularity in GMR Spin Valves and In Situ Electrical and Magnetotransport Measurements," IEEE Trans. Magn., **36**(5), pp. 2841–2846.
[10] Tsui, F., Chen, B., Wellman, J., Uher, C., and Clarke, R., 1997, "Heat Conduction of (111) Co/Cu Superlattices," J. Appl. Phys., **81**(8), pp. 4586–4588.
[11] Shi, J., Pettit, K., Kita, E., Parkin, S. S. P., Nakatani, R., and Salamon, M. B., 1996, "Field-dependent Thermoelectric Power and Thermal Conductivity in Multilayered and Granular Giant Magnetoresistive Systems," Phys. Rev. B, **54**(21), pp. 15273–15283.
[12] Piraux, L., Cassart, M., Iiang, I., Xiao, I., and Chien, C. L., 1993, "Magnetothermal Transport Properties of Granular Co-Ag Solids," Phys. Rev. B, **48**(1), pp. 638–641.
[13] Sato, H., Aoki, Y., Kobayashi, Y., Yamamoto, H., and Shinjo, T., 1993, "Giant Magnetic Field Effect on Thermal Conductivity of Magnetic Multilayers, Cu/Co/Cu/Ni(Fe)," J. Phys. Soc. Jpn., **62**(2), pp. 431–434.
[14] Sato, H., Henmi, H., Kobayashi, Y., and Aoki, Y., 1994, "Giant Magnetoresistance Related Transport Properties in Multilayers and Bulk Materials," J. Appl. Phys., **76**(10), pp. 6919–6924.
[15] Tai, Y. C., Mastrangelo, C. H., and Muller, R. S., 1988, "Thermal Conductivity of Heavily Doped Low-pressure Chemical Vapor Deposited Polycrystalline Silicon Films," J. Appl. Phys., **63**(5), pp. 1442–1447.
[16] Lu, L., Yi, W., and Zhang, D. L., 2001, "3$\omega$ Method for Specific Heat and Thermal Conductivity Measurements," Rev. Sci. Instrum., **72**(3), pp. 2996–3003.
[17] Holman, J. P., 1984, *Experimental Methods for Engineers*, McGraw-Hill, New York, pp. 50–57.
[18] Sondheimer, E. H., 1952, "The Mean Free Path of Electrons in Metals," Adv. Phys., **1**, pp. 1–42.
[19] Qiu, T. Q., and Tien, C. L., 1993, "Size Effects on Nonequilibrium Laser Heating of Metal Films," ASME J. Heat Transfer, **115**(4), pp. 842–847.
[20] Majumdar, K., Chen, J., and Hershfield, S., 1998, "Calculation of Giant Magnetoresistance in Laterally Confined Multilayers in the Current-In-Plane Geometry," Phys. Rev. B, **57**(5), pp. 2950–2954.
[21] Mayadas, A. F., and Shatzkes, M., 1970, "Electrical-Resistivity Model for Polycrystalline Films: The Case of Arbitrary Reflection at External Surfaces," Phys. Rev. B, **1**(4), pp. 1382–1389.
[22] Zhang, Y., Ong, N. P., Xu, Z. A., Krishana, K., Gagnon, R., and Taillefer, L., 2000, "Determining the Wiedemann-Franz Ratio from the Thermal Hall Conductivity: Application to Cu and $YBa_2Cu_3O_{6.95}$," Phys. Rev. Lett., **84**(10), pp. 2219–2222.
[23] Asheghi, M., Kurabayashi, K., Kasnavi, R., and Goodson, K. E., 2002, "Thermal Conduction in Doped Single-Crystal Silicon Films," J. Appl. Phys., **91**(8), pp. 5079–5088.
[24] Zhang, S., Yang, Y., Barmak, K., and Asheghi, M., 2004, "High Resolution Nanocalorimetry," *ASME International Mechanical Engineering Congress & Exposition*, IMECE-62332, November 13–29, Anaheim, CA.

# Thermal-Hydraulic Performance of MEMS-based Pin Fin Heat Sink

**Ali Koşar**

**Yoav Peles**[1]
e-mail: pelesy@rpi.edu

Department of Mechanical, Aerospace and Nuclear Engineering, Rensselaer Polytechnic Institute, Troy, NY 12180

*An experimental study on heat transfer and pressure drop of de-ionized water over a bank of shrouded staggered micro pin fins* 243 $\mu$m *long with hydraulic diameter of* 99.5 $\mu$m *has been performed. Average heat transfer coefficients have been obtained for effective heat fluxes ranging from 3.8 to* 167 $W/cm^2$ *and Reynolds numbers from 14 to 112. The results were used to derive the Nusselt numbers, total thermal resistances, and friction factors. It has been found that for Reynolds numbers below* ~50 *long tube correlations overpredicted the experimental Nusselt number, while at higher Reynolds numbers existing correlations predicted the results moderately well. Endwall effects, which diminish at high Reynolds numbers, and a delay in flow separation for compact pin fins were attributed to the obtained trend.* [DOI: 10.1115/1.2137760]

*Keywords: MEMS, heat sink, pin fin, cross flow, friction factor, microchannel*

## 1 Introduction

In pursuit of cooling solutions for the ever-increasing demand for integrated circuit (IC) power density, micro scale heat sinks carved from silicon utilizing microelectromechanical systems (MEMS) technology have been aggressively studied over the past half decade. The vast majority of studies have investigated the physical phenomena occurring in single phase [1–4] and boiling flow [5–16] in microchannels. Recently, other MEMS-based heat sink configurations have surfaced as alternative cooling methods to microchannels. Kandlikar and Grande [17] have discussed microscale research opportunities in meeting the cooling demand of future IC chips, and Peles et al. [18] and Koşar et al. [19] addressed the potential advantages of utilizing microscale pin fin heat sinks as the cooling method of choice for many ultra-high heat flux cooling systems.

Heat transfer and pressure drop of flow across tube bundles/pin fins have been a subject of extensive research over the last century [20]. The Nusselt number and friction factor correlations obtained primarily through experimental studies have been developed for circular [21–25], rectangular [26,27], oval [28], elliptical [29], diamond [30], hexagonal [31], and lenticular [32] configurations, among others. Dimensional analysis suggests that the convective heat transfer across long cylinders in cross flows varies with the Reynolds and Prandtl numbers.

Flows over intermediate size pin fin banks have been commonly used in turbine cooling systems to increase the internal heat transfer characteristics. The pin height-to-diameter, $H/d$, ratios of typical heat sinks used for such applications were between $1/2$ and 4 [33]. A concise review of staggered array arrangements for intermediate pin sizes was provided by Armstrong and Winstanley [33]. The vast majority of studies on intermediate size pin fins were performed with air at turbulent flow conditions. It was found that the average heat transfer coefficient for relatively short pin fins was lower than for long cylinders. The reduction was attributed to a decrease in the near-wall cylinder heat transfer relative to the heat transfer away from the wall where the cylinder was unaffected by the endwalls [33]. Sparrow et al. [34] have observed that cylinder-endwall interactions penetrate deeper into the freestream flow with a decreasing Reynolds number. Thus, at low Reynolds number the effect of endwalls is expected to be prevalent over a significantly broader range of $H/d$ values compared to high Reynolds numbers. However, the extent of this effect can currently not be fully determined since very little data are available on laminar Reynolds numbers (especially for $Re < 100$). Friction factors, on the other hand, displayed no such deviation for turbulent flow [33,35,36], but for laminar flow it was found [19,37] that the pin fin height-to-diameter ratio plays a vital role in determining the friction factor.

Data concerning heat transfer and pressure drop over tube/pin fin bundles at conventional scale provides a wealth of knowledge to evaluate such systems at the microscale. However, it is unclear whether the correlations and prediction tools developed for conventional scale systems are applicable to microdevices. Furthermore, a literature survey reveals the absence of any such scaling studies pertinent to cross flow configuration, and the data on heat transfer and friction factor for intermediate size cylinders (and non-cylindrical pin fins) at conventional scales is limited and primarily available for transitional and turbulent flows ($Re > 1000$). In addition, considerable deviations of heat transfer coefficients between short and long pin fins were registered for intermediate size pin fins at turbulent flow conditions and friction factor for laminar flows. Moreover, the vast majority of studies on large scale systems were performed with air as the primary working fluid, but a large range of applications (e.g., electronic cooling, ultra-compact heat exchangers, etc.) may greatly benefit from employing other fluids (e.g., water, various coolants) with significantly superior thermal properties and most often higher Prandtl numbers. In diverse physical configurations, the Nusselt number occasionally exhibits significant differences in the parametric trends and magnitudes between various fluids of different thermophysical properties (e.g., Li and Garimella [38], Garimella [39]). Since the effect of wall-pin interaction on heat transfer is noticeably marked at lower than at higher Prandtl numbers, it is predicted that experiments performed on water will deviate considerably from results obtained for air in a manner not fully predicted. Thus, before resorting to correlations and extracting knowledge obtained using a large scale apparatus, a comprehensive study of heat transfer over intermediate size pin fins at low Reynolds number is imperative for the successful realization of microscale pin fin heat sinks.

In a previous study Peles et al. [18] developed a model to elucidate the total thermal resistance over a pin fin heat sink. In the lack of data/correlations of heat transfer and pressure drop pertained to microscale systems (i.e., low Reynolds numbers flows over intermediate pin fins) existing large scale correlations were used. To unveil the hydrodynamic characteristics Koşar et al. [19] experimentally determined the friction factors at low Rey-

[1]Corresponding author.

Contributed by the Heat Transfer Division of ASME for publication in the JOURNAL OF HEAT TRANSFER. Manuscript received March 3, 2005; final manuscript received August 8, 2005. Review conducted by Suresh V. Garimella.

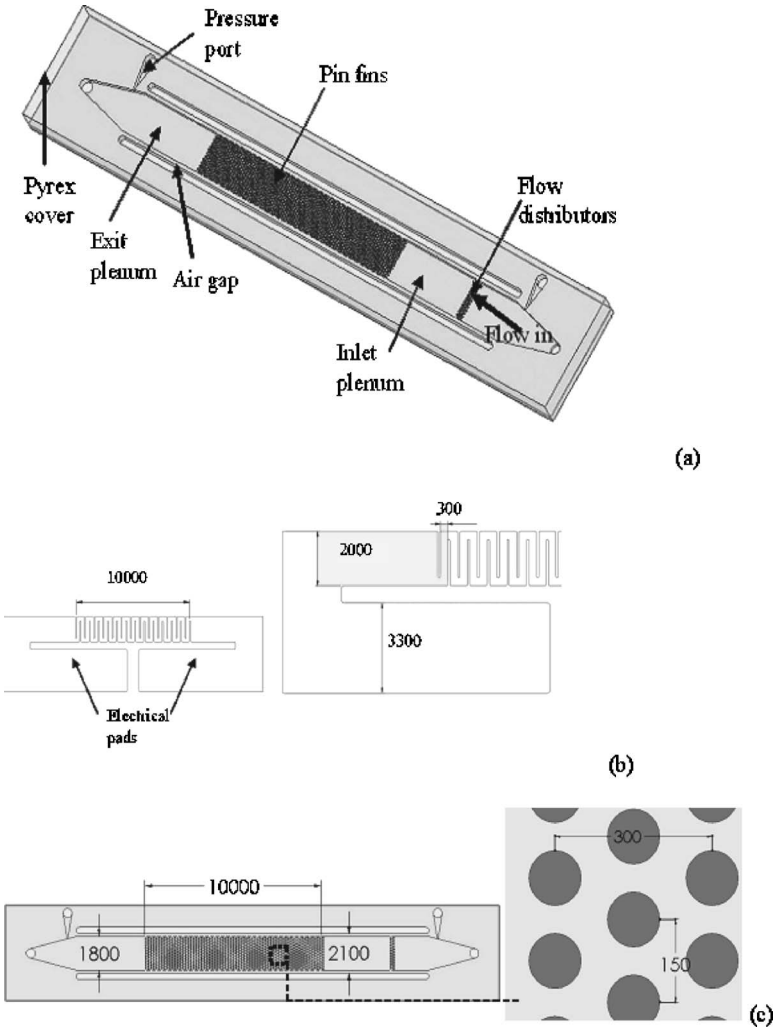


**Fig. 1** (*a*) **CAD model of the micro pin fin heat sink.** (*b*) **Heater dimensions (dimensions in mm).** (*c*) **Top view of the device (dimensions in $\mu$m).**

nolds number over short pin fin bundles. The objectives of this work are to evaluate the heat transfer characteristics of de-ionized water flow over an intermediate size, staggered, shrouded micro pin fin heat sink, and to extend pressure drop data relevant to micro domains. Heat transfer coefficients, Nusselt numbers, total thermal resistances, and friction factors under a range of thermal and hydrodynamic conditions are presented and discussed. Existing large scale correlations are utilized and evaluated based on their ability to predict experimental results and to investigate wall-pin interactions on heat transfer and friction factor.

The micro pin fin heat sink device overview is presented in Sec. 2. The design, fabrication, experimental setup description, and the experimental procedure are provided in Sec. 3. Section 4 presents data reduction and uncertainty analysis, and Sec. 5 is devoted to the discussion of the experimental results. Finally, Sec. 6 presents the conclusions of this investigation.

## 2 Device Overview

A Computer Aided Design (CAD) model of the device consisting of an 1800-$\mu$m-wide and a 1-cm-long microchannel of depth 243 $\mu$m is shown in Fig. 1. The microchannel contains an array of 12 and 13 (in tandem) staggered 99.5-$\mu$m-diam circular pin fins with pitch-to-diameter ratio of 1.5 (longitudinal and transverse spacing are equal). De-ionized water is propelled through the inlet plenum into the pin fin matrix, absorbs the heat dissipated by the heater residing on the opposite side (Fig. 1(*b*)), and leaves the heat sink through the exit plenum. The heater also serves as a thermistor for temperature measurements. In order to minimize ambient heat losses an air gap is formed on the two ends of the side walls, and an inlet and exit plenum, 4 mm long each, are etched on the thin silicon substrate ($\sim$147 $\mu$m). A Pyrex™ cover seals the device from the top and allows flow visualization. Pressure taps are created at the inlet and exit of the device.

## 3 Device Fabrication, Experimental Apparatus, and Procedures

**3.1 Microchannel Fabrication Method.** A double side polished, *n*-type $\langle 100 \rangle$ single crystal silicon wafer was processed on both sides to create a MEMS device, which consisted of a microchannel enclosing an array of fins. In the fabrication process (Fig. 2) first, the top side and bottom side masks were designed and fabricated. A 1-$\mu$m-thick thermal oxide was grown on both sides of the silicon wafer to protect the bare wafer surface. The heater and the vias were formed on the back side of the wafer using cryopumped CVC 601 sputter deposition system. A 70-Å-thick layer of titanium was initially deposited to enhance adhesion characteristics and was followed by sputtering a 1-$\mu$m-thick layer of aluminum containing 1% silicon and 4% copper. Subsequent photolithography and concomitant wet bench processing created the heater on the back side of the wafer. Next, the microchannel with micro pin fins was formed on the top side of the wafer. For this,

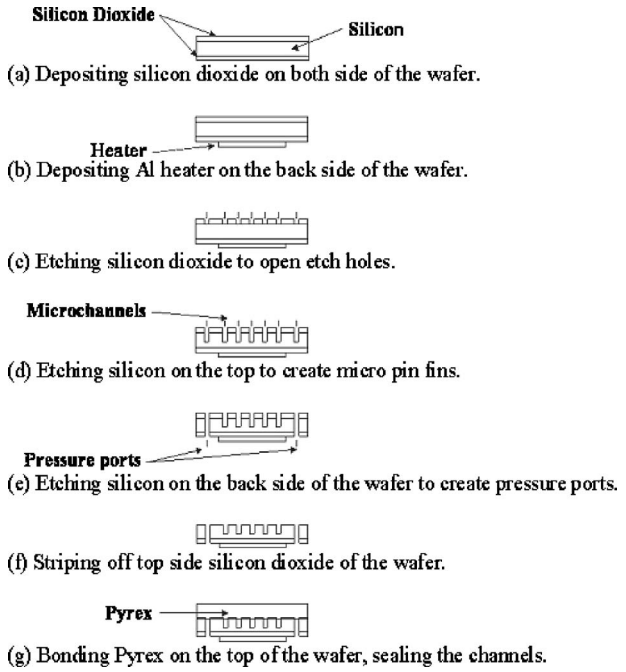


**Fig. 2 Micro pin fin heat sink fabrication process (not to scale)**

the wafer was taken through a photolithography step and a reactive ion etching (RIE) oxide removal process to mask certain areas on the wafer, which were not to be etched during the DRIE (deep reactive ion etching) process. The wafer was consequently etched in a DRIE process, and silicon was removed from places not protected by the photoresist/oxide mask. The DRIE process formed deep vertical trenches on the silicon wafer with a characteristic scalloped sidewall possessing a peak-to-peak roughness of $\sim 0.3\ \mu$m. A profilometer and an SEM were employed to measure and record various dimensions of the device. The wafer was flipped and the back side was then processed, so that an inlet, exit, side air gap, and pressure port taps for the transducers were formed. Photolithography followed by a buffered oxide etch (BOE) (6:1) oxide removal process was carried out to create a pattern mask. The wafer was then etched-through in a DRIE process to create the fluidic ports. Thereafter, electrical contacts/pads were opened on the back side of the wafer by performing another round of photolithography and RIE processing. Finally, the processed wafer was stripped of any remaining resist or oxide layers and anodically bonded to a 1-mm-thick polished Pyrex™ (glass) wafer to form a sealed device. After successful completion of the bonding process, the processed stack was die-sawed to separate the devices from the parent wafer.

**3.2 Experimental Apparatus.** In Fig. 3, a schematic of the experimental setup is shown. Major components are the pump, filter, flowmeters (rotameters), packaging module, and micro pin fin device. The micro pin fin device was packaged by sandwiching it between two plates, as shown in Fig. 4. The fluidic seals were forged using miniature "o-rings." The external electrical connections to the heater were installed from beneath through spring-loaded pins, which connected the heater to electrical pads residing away from the main micro pin fin device body. Resistance, pressure, and flow measurements were taken at a fixed flow rate in the loop. The electrical power was supplied to the device with an INSTEK programmable power supply, while electrical current and voltage were measured using a HP3457A digital multimeter. An HNP Mikrosysteme microannular gear pump capable of generating flow rates from 0.3 to 18 ml/min was used to propel the liquid from a reservoir through the MEMS device at various flow rates. The inlet temperature was measured by an Omegaette HH308

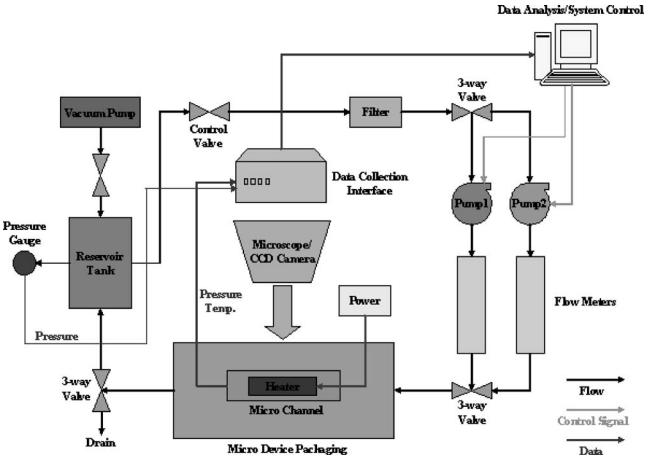


**Fig. 3 Experimental setup**

Type K Thermometer. Inlet and exit pressures were measured via pressure transducers. An Omega F-111 flow meter was used for flow rate measurements. Pressure and flow rate data were acquired together with the voltage and current data to the spreadsheet file for data reduction. The flow was visualized with a microscope and flow images were taken via a Vision Research Phantom V-4 series high-speed camera capable of capturing frames with a rate up to 90,000 frames/s, a maximum resolution of $512 \times 512$ pixels, and a minimum exposure time of 2 $\mu$s. Flow visualization was performed to check for the functionality of the device during experimentation and particle contamination free operation.

**3.3 Experimental Procedure.** The flow rate was fixed at the desired value, and data were taken after a steady flow rate was reached, while exit pressure was kept at atmospheric pressure. Water was utilized as the working fluid. Before taking any data the device was calibrated in a well insulated and temperature controlled oven, and the heater electrical resistance-temperature linear calibration curve with a slope of $47.77^{\circ}\mathrm{C}/\Omega$ was generated (Fig. 5). A standard deviation of $0.16^{\circ}$C was obtained between the individual data points and the best fit for the calibration data. The curve was then used during data reduction process to extract the average surface temperature of the device.

Prior to acquiring experimental data the electrical resistance of the heater was measured at room temperature. The flow meter reading was adjusted to the desired flow rate, and the pressure difference between the inlet and exit pressure ports was recorded through a LabView® interface to a spreadsheet file. This procedure was followed until all the pressure differences corresponding to desired flow rates were recorded. To obtain heat transfer data,

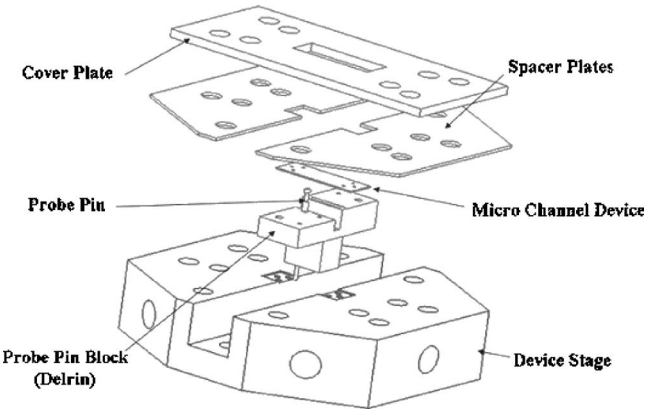


**Fig. 4 Device package**

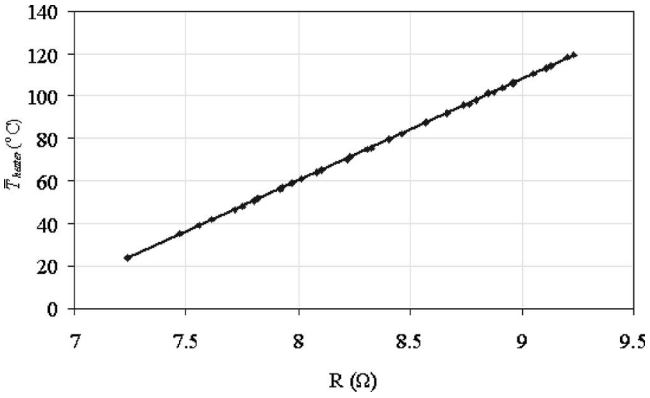


**Fig. 5 Average temperature as a function of electrical resistance**

voltage was applied in 0.5 V increments across the heater, and the current/voltage data were recorded while ensuring the constancy of the flow rate. The same procedure was repeated for other flow rates.

## 4 Data Reduction and Uncertainty Analysis

The data obtained from the voltage, current, flow rate, and pressure measurements were reduced to the average wall temperatures, heat transfer coefficients, and single-phase friction factors. The electrical input power and resistance were calculated using the measured voltage and current values. The average heater temperature was calculated using the electrical resistance (Fig. 5). Under the 1D steady state heat conduction assumption, the surface temperature at the base of the microchannels was expressed as

$$\overline{T} = \overline{T}_{\text{heater}} - \frac{(P - \dot{Q}_{\text{loss}})t}{k_s A_p} \tag{1}$$

**4.1 Heat Transfer.** The heat transfer coefficient was obtained using Newton's law of cooling jointly with 1D steady-state adiabatic tip fin equation as follows

$$(P - \dot{Q}_{\text{loss}}) = h_{\text{av}}\left(\eta_f N_t \pi d H + wL - N_t \frac{\pi d^2}{4}\right)\left[\overline{T} - \left(\frac{T_i + T_e}{2}\right)\right] \tag{2}$$

where

$$\eta_f = \frac{\tanh(m_f H)}{m_f H}, \quad T_e = T_i + \frac{P - \dot{Q}_{\text{loss}}}{\dot{m}c_p} \quad \text{and} \quad m_f = 2\sqrt{\frac{h_{\text{av}}}{k_{\text{fin}} d}}$$

Equation (2) was solved iteratively to obtain $h_{\text{av}}$. The Nusselt number corresponding to each net input power at a fixed flow rate was calculated using the average heat transfer coefficient obtained from Eq. (2) as

$$(\text{Nu})_{\text{av}} = \frac{h_{\text{av}} d}{k_{\text{fluid}}} \tag{3}$$

Average values of the heat transfer coefficient and Nusselt number for a fixed Reynolds number were then calculated according to

$$\overline{h} = \frac{1}{M}\sum_{j=1}^{M} (h)_{\text{av},j} \tag{4}$$

$$\overline{\text{Nu}} = \frac{1}{M}\sum_{j=1}^{M} (\text{Nu})_{\text{av},j} \tag{5}$$

Finally, the total thermal resistance ($R_{\text{tot}}$) was expressed as the sum of three components that accounted for conduction through the silicon substrate excluding the fin region ($R_{\text{cond}}$), convection to the flow ($R_{\text{conv}}$), and thermal resistance due to an increase in the flow temperature as it flows through the fins and absorbs heat ($R_{\text{heat}}$). Since the substrate thickness is small (147 $\mu$m) and the thermal conductivity of silicon is large ($\sim$150 W/m°C), $R_{\text{cond}}$ is small and was neglected, so that the thermal resistance became

$$R_{\text{tot}} = R_{\text{heat}} + R_{\text{conv}} = \frac{1}{\dot{m}c_p} + \frac{1}{\overline{h}(A_b + \eta_f A_{\text{fin}})} = \frac{1}{\dot{m}c_p} + \frac{d}{\overline{\text{Nu}} k_{\text{fluid}}(A_b + \eta_f A_{\text{fin}})} \tag{6}$$

**4.2 Pressure Drop.** Once the inlet and exit pressures were obtained, friction factor, $f$, was found using

$$f = \frac{(P_i - P_e)2\rho}{N_{\text{row}} G^2} \tag{7}$$

where the mass velocity ($G$) was calculated based on the minimum cross-sectional flow area using

$$G = \frac{Q\rho}{A_{\min}} \tag{8}$$

The Reynolds number based on the pin fin diameter and $A_{\min}$ for staggered fin configuration were expressed as

$$\text{Re} = \frac{Gd}{\mu} \tag{9}$$

$$A_{\min} = \frac{S_T - d}{S_T} wH \tag{10}$$

**4.3 Heat Losses.** One-dimensional fin analysis on the inlet and exit plenum was performed to estimate heat losses from the micro pin fin sink. Heat loss from the bottom surface is estimated by assuming one-dimensional conduction through a 2 mm air gap (gap between the chip bottom and the top electrical probe pin block), while thermal losses comprising the conduction through the Pyrex substrate and natural convection were used to estimate heat losses from the top surface. Maximum heat losses from the top and bottom surfaces yielded $\sim$0.02 W and $\sim$0.01 W, respectively, which were considerably smaller than the applied heater power (0.8–22 W). Thus, heat losses from the top and bottom surfaces were neglected. On the other hand, heat losses to the inlet and exit plenum through conduction could not be completely neglected. In order to verify the estimated heat loss, electrical power was applied to the test section after evacuating the water from the test loop. Once the temperature of the test section reached steady-state conditions, the temperature difference between the ambient and test section was recorded at the corresponding power. The temperature difference versus power curve was plotted (Fig. 6(*a*)) and used to compare the heat loss associated with each experimental data point to the fin analysis. The results from this comparison showed very good agreement. Thus, the measured heat loss was subtracted from the total heat supplied to the heat sink under forced flow conditions, and the corresponding values were used in subsequent analysis of the data reduction. Heat loss curve for Re=112 is shown in Fig. 6(*b*).

**4.4 Uncertainty Analysis.** The uncertainties of the measured values, given in Table 1, were obtained from the manufacturer's specification sheets, while the uncertainties of the derived parameters were calculated using the method developed by Kline and McClintock [40], and the comparison of the experimental data with existing correlations was accomplished through the mean absolute error (MAE).

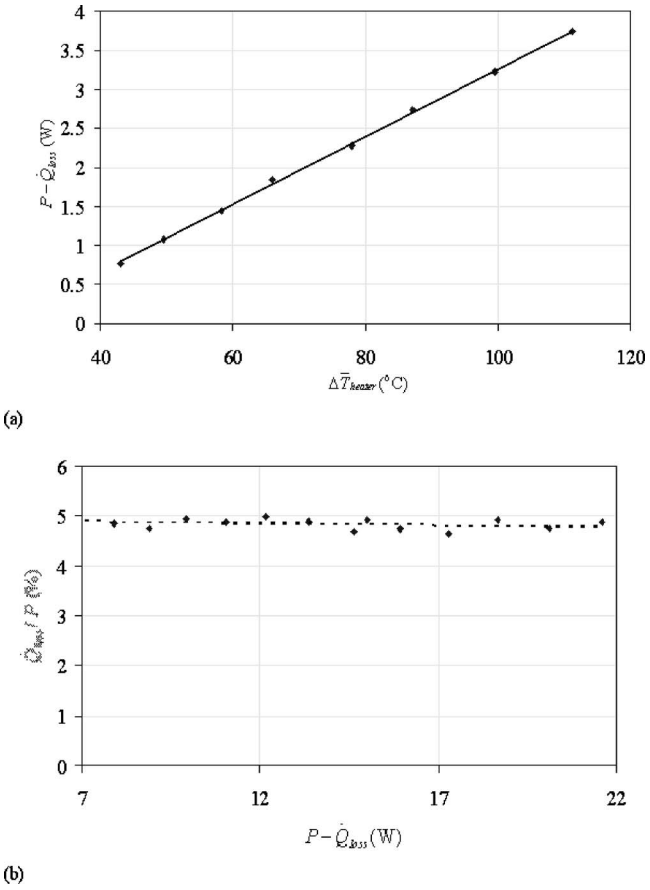


**Fig. 6 (*a*) Heat loss calibration curve. (*b*) Heat loss curve for Re=112.**

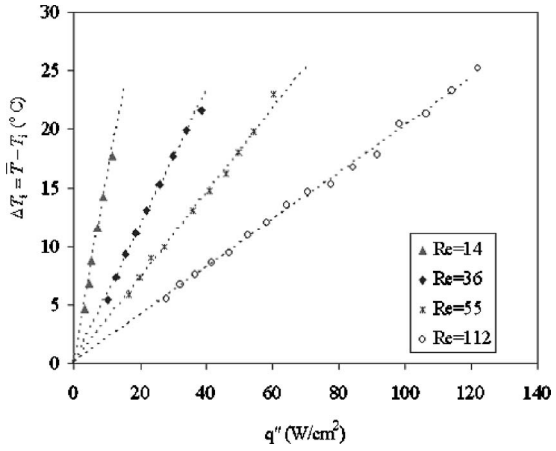


**Fig. 7 $\bar{T}-T_i$(°C) versus $q''$ profile**

## 5 Results and Discussion

**5.1 General Observations.** Figure 7 shows the dependence of the wall average temperature on the effective heat flux for four different Reynolds numbers. The average wall temperature exhibits a linear slope with heat flux, which is a common characteristic of single-phase heat transfer at constant heat flux [41]. As expected, lower Reynolds numbers result in a steeper slope. This is a result of two underlying factors: the dependence of the liquid temperature and heat transfer coefficient on the Reynolds number. In the thermal performance analysis of heat sinks, it is common to express the total thermal resistance as the sum of two components [18] in a manner similar to Eq. (6). One accounts for convection, $R_{\text{conv}}$, and the other term for the thermal resistance due to an increase in the fluid temperature as it flows through the fins and absorbs heat, $R_{\text{heat}}$. Since higher Reynolds numbers correspond to higher mass flow rates, the $1/\dot{m}c_P$ term diminishes. Furthermore, the Nusselt number for flow across pin fins and tube bundles has been found to correlate well according to

$$\overline{\text{Nu}} = C\,\text{Re}^m\text{Pr}^n \tag{11}$$

(where $m>0$). Thus, heat transfer coefficient increases with Reynolds number ($1/\bar{h}A_t$ term in Eq. (6)), further reducing the total thermal resistance and reducing the temperature for a fixed heat flux.

The data shown in Fig. 7 have been used to deduce the heat transfer coefficients at various heat fluxes as shown in Fig. 8. Average heat transfer coefficient varies from $5,365\ \text{W/m}^2\,\text{K}$ for Re=14 to $44,090\ \text{W/m}^2\,\text{K}$ at Re=112. The large heat transfer coefficient values are in complete agreement (trend-wise) with large scale knowledge, which links increasing heat transfer coefficient with diminishing length scale. This is a result of boundary layer (hydrodynamic and thermal) thinning. The large heat transfer coefficient values result in very low surface-liquid temperature difference, which in turn increases experimental measurement uncertainties. This is reflected by a relatively large scatter (up to ±20%) in the heat transfer coefficient, which is also shown in Fig. 9. In order to obtain superior accuracy in heat transfer coefficient (Nusselt number) measurements, it is necessary to either perform experiments at very high heat fluxes (increasing wall-fluid temperature difference) or employ fluids having low thermal conductivity (reducing heat transfer coefficient while maintaining the same Reynolds and Prandtl numbers), so that a significant difference between the average surface temperature and bulk temperature will be apparent.

**Table 1 Experimental uncertainties**

| Uncertainty | Error |
|---|---|
| Flow rate, $Q$ (for each reading) | ±1.0% |
| Voltage supplied by power source, $V$ | ±0.1% |
| Current supplied by power source, $I$ | ±0.1% |
| Ambient temperature, $T_{amb}$ | ±0.1°C |
| Electrical power, $P$ | ±0.15% |
| Electrical resistance, $R$ | ±0.15% |
| Average temperature, $\bar{T}$ | ±0.5°C |
| Friction factor, $f$ | ±7.2% |
| Thermal resistance, $R_{tot}$ | ±2.2% |
| Average heat transfer coefficient, $\bar{h}$ | ±12.9% |
| Average Nusselt number, $\overline{Nu}$ | ±13.0% |

**5.2 Comparison with Other Correlations.** In order to present the experimental results in a more general manner and to perform comparison with large scale correlations, the Nusselt number is derived from the heat transfer coefficient data. The average Nusselt numbers are shown in Fig. 10 as a function of the Reynolds number along with several correlations obtained on large scale systems. Prandtl number varies from 4 to 6 depending on the liquid temperature.

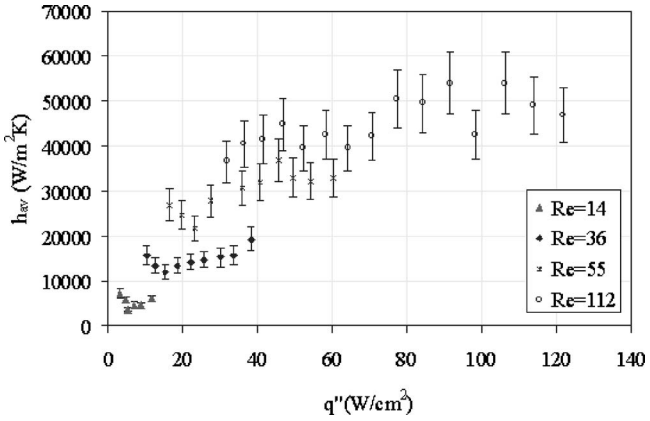


**Fig. 8 Average heat transfer coefficient as a function of heat flux**

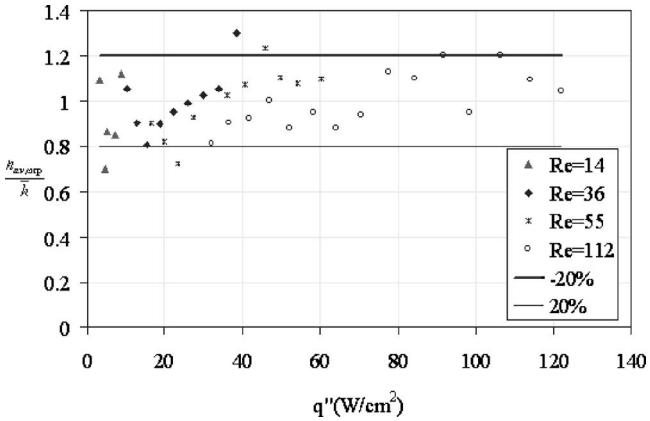


**Fig. 9 $h_{av,exp}/\bar{h}$ versus $q''$ profile**

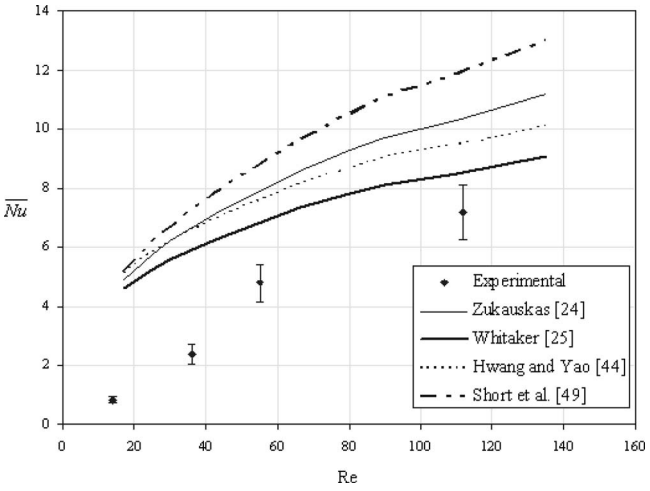


**Fig. 10 Average Nusselt number as a function of Reynolds number**

While attempting to compare the experimental Nusselt number obtained in the current study to available correlations reported in archival literature it was apparent that very few correlations provide a proper base for comparison, namely, for flow over shrouded intermediate size pin fins at Reynolds numbers ranging from ~10 to ~100. Correlations developed for pin fins between $1<H/d<4$ are mostly available for turbulent Reynolds numbers [35,36,42,43] and were obtained based on experimental results using air.

A number of correlations developed for laminar flow across long and short tubes/pin fins were used to evaluate the Nusselt number. In the present study, three long tube correlations (correlations 1, 2, 3) and one intermediate size pin fin correlation (correlation 4) are included, which are summarized in Table 2. In the absence of any adequate correlation, which can fully account for the present conditions, these correlations are included to provide

**Table 2 Single-phase heat transfer coefficient correlations**

| Correlation number | Reference | Shape and geometry of pin fins, working fluid | Working fluid | Correlation | MAE (%) All data and Re>50 |
|---|---|---|---|---|---|
| 1 | Zukauskas [24] | Circular, $0.5<\mathrm{Pr}<500$ $10<\mathrm{Re}<100$ | All fluids | $\overline{\mathrm{Nu}}=0.9\,\mathrm{Re}^{0.4}\mathrm{Pr}^{0.36}\left(\frac{\mathrm{Pr}}{\mathrm{Pr}_s}\right)^{0.25}$ | 192.4 (for all the data) 70.6 (for Re>50) |
| 2 | Whitaker [25] | Circular, Laminar $\varepsilon\leq 0.65$ | Air | $\overline{\mathrm{Nu}}=1.526\,\mathrm{Re}^{1/3}(\beta^2-1)^{-2/3}\mathrm{Pr}^{1/3}\left(\frac{\mu}{\mu_s}\right)^{0.14}$ $\beta=\left(\frac{1}{1-\varepsilon}\right)^{0.5}$ | 170.7 (for all the data) 39.8 (for Re>50) |
| 3 | Hwang and Yao [44] | Circular, $\mathrm{Re}<200$ $S_T/d<2$ | Air | $\overline{\mathrm{Nu}}=0.83\,\mathrm{Re}^{1/3}\gamma^{1/3}\mathrm{Pr}^{1/3}\left(\frac{\mu}{\mu_s}\right)^{0.14}$ $\gamma=\frac{\beta^4-1}{(1+\beta^4)\ln\beta^2+(1-\beta^4)}\quad\beta=\left(\frac{1}{1-\varepsilon}\right)^{0.5}$ | 175.1 (for all the data) 54.7 (for Re>50) |
| 4 | Short et al. [49] | Circular, $100<\mathrm{Re}<1000$ $2<S_T/d<6.41$ $1.83<S_L/d<3.21$ $1.9<H/d<7.5$ | Air | $\overline{\mathrm{Nu}}=0.419\,\mathrm{Re}^{0.45}\mathrm{Pr}^{1/3}\left(\frac{S_T}{d}\right)^{0.2}\left(\frac{S_L}{d}\right)^{0.077}\left(\frac{H}{d}\right)^{-0.3}$ | 143.4 (for all the data) 25.7 (for Re>50) |

some (although limited) comparison. The experimental Nusselt numbers, together with the calculated ones obtained from these correlations, are presented in Table 2 including the resulting MAEs.

As can be seen at low Reynolds numbers the experimental Nusselt numbers are considerably lower than all other correlations by a factor of more than 2. Zukauskas [24], Whitaker [25], and Hwang and Yao [44] correlations are recommended for long tubes and do not account for endwall effects (endwall effects account for the interaction between the pin fins and the base on which they reside (top and bottom walls)). The low Nusselt number values (compared to large scale correlations' prediction) can be linked to endwall effects, which result in lower heat transfer coefficients for the intermediate pins compared to long pin fins at reduced Reynolds numbers. A similar trend has been reported for turbulent air flow in conventional scale systems by Armstrong and Winstanley [33]. This is also in accordance with Sparrow et al. [34] (again for turbulent flow), who observed that at $\mathrm{Re}=3500$ the boundary layer thickness ($U/U_\infty=0.98$) was 1.3 of the pin fin diameter, $d$, and reduced to $0.8d$ at $\mathrm{Re}=23,000$. It can be inferred that the reduction in the heat transfer coefficient is established by effectively generating a boundary layer in the vicinity of the wall-pin intersection. Lower Reynolds number flows tend to support thicker boundary layers, and therefore, diminishing heat transfer coefficients of short fins compared to their long fins counterparts ensues with the reduction in the Reynolds number. Thus, higher Reynolds power-law is expected in the Nusselt number correlation than for long tubes (higher $m$ values in Eq. (11)), as observed in the current study.

An additional factor that might adversely contribute to the lower heat transfer coefficients at low Reynolds numbers arises from a delay in flow separation. For long cylinders, flow separation commences at $\mathrm{Re}\sim 4$ leading to a formation of two attached steady standing eddies [45], which increases the heat transfer coefficient for fins in the following row [46] (and the average heat transfer coefficient). Flow over a cylinder confined by two endwalls with a finite (and relatively small) aspect ratio is modified by the presence of the walls in a manner which tends to delay separation to higher Reynolds number [47,48]. Furthermore, the more compact the tube bank is, the larger the Re number range is in which nonseparating flow is preserved [24]. Thus, heat transfer enhancement is delayed to higher Reynolds number as $H/d$ and the pitch-to-diameter ratio diminish. Since the Reynolds number in the present study spans from 14 to 112, a suppression of the heat transfer coefficient might be instigated at low Reynolds numbers (prior to flow separation), while at higher values (proceeding flow separation) a trend similar to long tubes is developed.

The poor prediction of large scale correlations at low Reynolds numbers might also be partly attributed to the limited accuracy of the correlations. Discrepancies between various conventional scale correlations were registered for staggered tube arrangement at $\mathrm{Re}<100$ (especially for $\mathrm{Re}<40$), which was attributed [24] to varying accuracy in determining the thermophysical properties of the thermal carrier used in various experiments.

Short et al. [49] correlation is the only laminar correlation developed for intermediate size pin fins. However, it is recommended for $\mathrm{Re}>100$, a range mainly not pertinent to the experimental data, which might explain its poor prediction at low Reynolds numbers and modest predictability at higher Reynolds numbers. For $\mathrm{Re}>50$, all correlations predicted the experimental data moderately well. The improved prediction of Whitaker [25], and Hwang and Yao [44] correlations over Zukauskas [24] correlation primarily stems from the inclusion of longitudinal and transverse pitch ratio effects.

The choice of the working fluid (e.g., water, air) can strongly affect the Nusselt number in ways previously not fully considered. Conducting an experimental study with water and air on identical devices might result in significantly different Nusselt number correlations even if the conventional $\mathrm{Pr}^n$ term is factored in. Such anomalies in the dependence of the Nusselt number on the fluid thermophysical properties have been previously observed in confined and submerged jet impingement systems [38]. Perhaps a similar approach used by Li and Garimella [38] to correlate the Nusselt number might be appropriate for the current heat sink configuration. However, a comprehensive parametric study on a wide range of pin fins $H/d$, Reynolds numbers values, and employing various types of fluids (water, air, refrigerants, etc.) should be conducted before generating generalized Nusselt number correlations pertinent to microscale pin fin heat sinks.

**5.3 Thermal Resistance.** Thermal resistance is a useful engineering parameter, which is often used to evaluate the thermal performance of heat sinks. Total thermal resistance of a pin fin heat sink is given as

$$R_{\mathrm{tot}}=\frac{\overline{R}_{\mathrm{tot}}}{\dot{m}c_p} \tag{12}$$

As discussed by Peles et al. [18] the dimensionless thermal resistance ($\overline{R}_{\mathrm{tot}}$) is expressed as the sum of convective resistance, $\pi_1$, and the thermal resistance due to the heat absorbed by the liquid, as follows

$$\overline{R}_{\mathrm{tot}}=1+\pi_1 \tag{13}$$

The dimensionless convective resistance is a function of geometrical and thermal-hydraulic parameters given by Ref. [18] as

$$\pi_1=\frac{\mathrm{Re}^{1-m}\mathrm{Pr}^{0.64}}{C_3C_2\left(\frac{L}{H}\right)\left(\frac{\mathrm{Pr}}{\mathrm{Pr}_s}\right)^{0.25}\left\{1+2\left(\frac{1-\epsilon}{\epsilon}\right)\frac{\tanh[2(H/d)\sqrt{C_3\mathrm{Re}^m\mathrm{Pr}^{0.36}(\mathrm{Pr}/\mathrm{Pr}_s)^{0.25}k_{\mathrm{fluid}}/k_{\mathrm{fin}}}]}{\sqrt{C_3\mathrm{Re}^m\mathrm{Pr}^{0.36}(\mathrm{Pr}/\mathrm{Pr}_s)^{0.25}k_{\mathrm{fluid}}/k_{\mathrm{fin}}}}\right\}} \tag{14}$$

Figure 11 presents the experimental $R_{\mathrm{tot}}$ as a function of Reynolds number jointly with Eq. (13). Although, the heat transfer coefficient used to derive Eq. (14) is correlation 1 (Table 2), which resulted in relatively large deviations from the current heat transfer coefficient, the agreement is good (MAE=15.4%), mainly because the convective thermal resistance is considerably smaller than the total thermal resistance ($0.24<\pi_1<0.352$ in Eq. (13)). This is a general characteristic of flow over microscale pin fins. The very effective convective heat transfer gives primary importance to elucidating means to augment mass flow rates at minimum cost. However, an increase in flow rates necessitates higher pressure drops and pumping powers. Thus, acquiring knowledge of pressure drop/friction factor is vital, and is therefore subsequently discussed.

**5.4 Pressure Drop and Friction Factor.** Pressure drop data shown in Fig. 12 have been reduced to friction factors. Friction factor as a function of Reynolds number is displayed in Fig. 13 along with five correlations available in the literature. Three of the

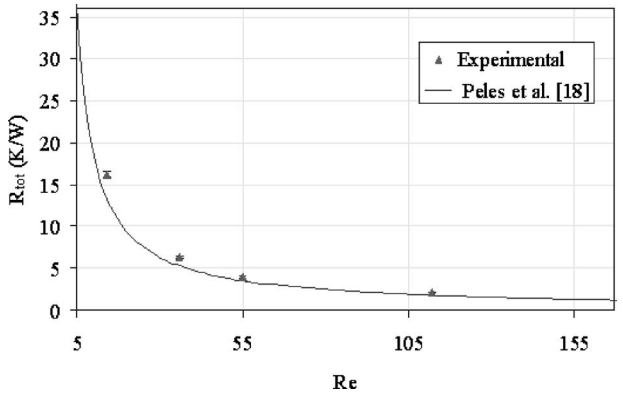


**Fig. 11 Total thermal resistance as a function of Reynolds number**

correlations were developed based on experimental results on long tubes (Gunther and Shaw [50], HEDH [51], Gaddis and Gnielski [52]) while the remaining two were developed based on results for $1<H/d<6$ pin fins (Short et al. [49], Koşar et al. [19]). The resulting MAEs of the correlations are listed in Table 3. In general, the long tube correlations provide a good prediction of the experimental data. However, a moderate shift in the trend is discernible when comparing long tube correlations to the experimental data. At low Reynolds numbers a lower friction factor is observed, while at high Reynolds numbers long tube correlations predict the results quite well. The discrepancy between the correlation of Koşar et al. [19] and the current results at low Reynolds numbers might suggest that for $H/d=1$ the thickening of the boundary layer (on the endwalls) predominates over "flow separation delay" effects, which in turn significantly increases the friction factor. For $H/d=2.43$, "flow separation delay" prevails over boundary layer effects, resulting in a low friction factor. The low friction factor values (in comparison to long tube correlations) at $Re=14$ and $Re=36$ might be indicative of "such flow separation delay." Furthermore, once separation is instigated for $H/d=2.43$ friction factor exhibits similar values to long tube correlations, indicating marginal boundary layer effects as observed for $Re=55$ and $Re=112$.

Although friction factor does not seem to be notably affected by endwalls, Koşar et al. [19] have shown that end walls significantly increase the friction factor for $H/d=1$ at low Reynolds numbers, which overshadows the reducing effect of "flow separation delay" at short cylinders. However, this effect diminishes at some value of $H/d$ between 1 and 2 (depending on Reynolds number).

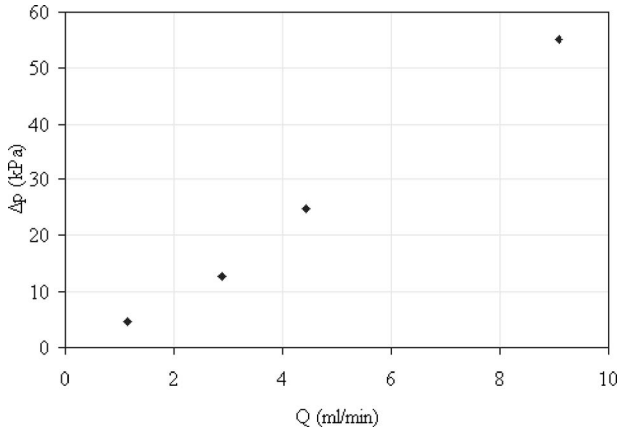


**Fig. 12 Pressure drop as a function of volumetric flow rate**

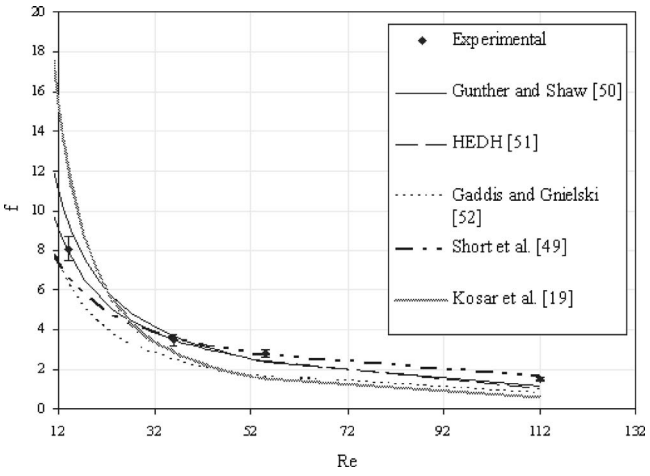


**Fig. 13 Friction factor predictions of existing correlations**

## 6 Conclusions

Thermal-hydraulic analysis over a bank of micro pin fins has been conducted experimentally and the concomitant results have been compared to available correlations in the literature. The main conclusions drawn from this investigation are as follows:

- Heat transfer coefficients comparable to boiling flow were registered. These values were in complete agreement with large scale knowledge linking increasing heat transfer coefficient with diminishing length scale.
- Similar to large scale systems, the average Nusselt number increased with the Reynolds number. However, the dependence of the Nusselt number on the Reynolds number was considerably more notable than for long tube correlations as a result of endwall effects.
- From the large number of conventional scale correlations, only a few provided the correct ground for comparison, since endwall effects were significant at a low Reynolds number flow over intermediate pin fins ($1/2<H/d<6$). While relatively large numbers of correlations are available for low Reynolds number flow over long tubes, literature concerning heat transfer on pin fins shorter than $H/d\sim 6$ was obtained primarily for turbulent flow of air and therefore not applicable to microscale systems. Existing correlations overpredicted experimental Nu data by more than a factor of 2 for low Reynolds numbers, and resulted in moderate agreement at high Reynolds numbers.
- Two intrinsically coupled physical factors adversely affected the heat transfer coefficient at $10<Re<100$ for flow over intermediate size pin fins: the thermal and hydrodynamic boundary layer established at the endwall and a delay in flow separation to higher Reynolds numbers. The suppression of the heat transfer coefficient was amplified with the reduction of $H/d$ ratio and is more evident at low Reynolds numbers. To fully account and quantify this phenomenon, comprehensive analytical, numerical, and experimental studies over a range of fin height-to-diameter ratios, type of flows, Reynolds numbers, and pin fin configurations (pitch-to-diameter ratios, staggered/in-line arrangement, etc.) are needed.
- The very effective convective heat transfer gives primary importance to elucidating means to augment mass flow rates at minimum cost. However, an increase in flow rates necessitates higher pressure drops and pumping powers. Thus, acquiring knowledge of the pressure drop/friction factor is vital, and should be of primary concern during the design process of microscale pin fin heat sinks. Furthermore, a comprehensive design and development effort should be undertaken to design and develop novel approaches which exploit the inherit advantages offered by microfabrication technology. Heat sinks containing pin fin geometrical con-

**Table 3 Single-phase friction factor correlations**

| Correlation number | Reference | Shape and geometry of pin fins | Wprking fluid | Correlation | MAE (%) |
|---|---|---|---|---|---|
| 5 | Gunther and Shaw [50] | Circular, laminar, long tubes | Air | $f=\frac{180}{\mathrm{Re}}\left(\frac{4}{\pi d^2}\frac{S_T S_L}{}-1\right)^{0.4}\left(\frac{d\,b_G}{S_T}\right)^{0.6}$ <br> $b_G=\frac{S_L}{d}$ for in line tube configuration <br> $b_G=\frac{S_d}{d}$ for staggered tube configuration | 17.5 |
| 6 | HEDH [51] | Circular, laminar, long tubes | All fluids | $f=4b_1\left(\frac{1.33}{S_T/d}\right)^{b_2}(\mathrm{Re})^{b_3}$ <br> $b=\frac{b_4}{1+0.14(\mathrm{Re})^{b_3}}$ | 22.3 |
| 7 | Gaddis and Gnielski [52] | Circular, laminar, long tubes | All fluids | $f=\frac{280\pi\left(\left(\left(\frac{S_L}{d}\right)^{0.5}-0.6\right)^2+0.75\right)}{\mathrm{Re}\left(4\frac{S_L S_T}{d^2}-\pi\right)c^{1.6}}$ <br> where <br> $c=\frac{S_T}{d}$ for in line arrangement and a staggered arrangement with $\frac{S_L}{d}\geq\frac{1}{2}\sqrt{2\frac{S_T}{d}+1}$ <br> $c=\frac{S_d}{d}$ for in line arrangement and a staggered arrangement with $\frac{S_L}{d}<\frac{1}{2}\sqrt{2\frac{S_T}{d}+1}$ | 44.2 |
| 8 | Short et al. [49] | Circular <br> $100<\mathrm{Re}<1000$ <br> $2<S_T/d<6.41$ <br> $1.83<S_l/d<3.21$ <br> $1<H/d<6$ | Air | $f=140.4\left(\frac{S_L}{d}\right)^{-1.3}\left(\frac{S_T}{d}\right)^{-0.78}\left(\frac{H}{d}\right)^{-0.55}\mathrm{Re}^{-0.65}$ | 9.5 |
| 9 | Koşar et al. [19] | Circular <br> $17<\mathrm{Re}<135$ <br> $S_T/d=S_l/d=1.5$ <br> $H/d=2.43$ | Water | $f=\frac{1739}{\mathrm{Re}^{1.7}}\left(\frac{H/d}{H/d+1}\right)^{1.1}\left(\frac{S_T S_L}{A_c}\right)^{-0.3}+\frac{345}{\mathrm{Re}_d}\left(\frac{1}{1+H/d}\right)^{2.0}\left(\frac{S_T S_L}{A_c}\right)^{-0.3}$ <br> where <br> $\mathrm{Re}_d=4\frac{G A_{\min} L}{A\mu}$ $\quad A=\pi dH N_t+2\left(wL-\frac{\pi d^2}{4}N_t\right)$ $\quad A_{\min}=\left(\left(\frac{w}{S_T}-1\right)c+(S_T-d)\right)H$ <br> $c=\begin{cases}S_T-d & \text{if } S_T-d<S_d-d\\ S_d-d & \text{if } S_d-d<S_T-d\end{cases}$ | 43.3 |

figurations which significantly reduce the pressure drop while maintaining superior heat transfer characteristics will greatly benefit the rapid advancement of numerous novel ultra-high-power systems.

## Acknowledgment

The microfabrication was performed at the Cornell NanoScale Facility (a member of the National Nanotechnology Infrastructure Network) which is supported by the National Science Foundation under Grant No. ECS-0335765, its users, Cornell University, and industrial affiliates. The authors are also thankful to the staff of RPI's machine shop for their support and perspicacious advice.

## Nomenclature

$A_b$ = base area (surface area without pin fins) ($m^2$)
$A_{\mathrm{fin}}$ = total fin surface area ($m^2$)
$A_{\min}$ = minimum cross-sectional area ($m^2$)
$A_p$ = planform area (surface area of silicon block) ($m^2$)
$A_t$ = total heat transfer area ($A_b+\eta_f A_{\mathrm{fin}}$) ($m^2$)
$b$, $b_1$, $b_2$, $b_3$, $b_4$ = parameters in correlation 6
$b_G$ = parameter in correlation 5
$c$ = parameter in correlations 7 and 9
$C$, $C_2$, $C_3$ = constants
$c_p$ = specific heat at constant pressure ($\mathrm{kJ\,kg^{-1}{}^{\circ}C^{-1}}$)
$d$ = pin fin diameter (m)
$f$ = friction factor
$G$ = mass velocity ($\mathrm{kg\,m^{-2}\,s^{-1}}$)
$\overline{h}$ = average heat transfer coefficient at a definite flow rate ($\mathrm{W\,m^{-2}{}^{\circ}C^{-1}}$)
$H$ = channel height, fin height (m)
$h_{\mathrm{av}}$ = average heat transfer coefficient at a definite heat flux ($\mathrm{W\,m^{-2}{}^{\circ}C^{-1}}$)
$k_{\mathrm{fin}}$ = thermal conductivity of the fin (silicon) ($\mathrm{W\,m^{-1}{}^{\circ}C^{-1}}$)
$k_{\mathrm{fluid}}$ = thermal conductivity of the fluid ($\mathrm{W\,m^{-1}{}^{\circ}C^{-1}}$)
$k_s$ = thermal conductivity of the silicon block ($\mathrm{W\,m^{-1}{}^{\circ}C^{-1}}$)
$L$ = channel length (m)
$m$ = constant
$M$ = number of data points
$\dot{m}$ = mass flow rate ($\mathrm{kg\,s^{-1}}$)
$m_f$ = fin parameter in Eq. (2)
MAE = mean absolute error
$n$ = constant
$N$ = number of pin fins in a single column
$N_{\mathrm{row}}$ = number of pin fins in a single row
$N_t$ = total number of pin fins
$\underline{\mathrm{Nu}}$ = Nusselt number
$\overline{\mathrm{Nu}}$ = average Nusselt number at a definite Reynolds number
$\mathrm{Nu}_{\mathrm{av}}$ = average Nusselt number at a definite heat flux
$P$ = electrical power (W)
$p_e$ = exit pressure (kPa)
$p_i$ = inlet pressure (kPa)
Pr = Prandtl number
$q''$ = heat flux ($\mathrm{W\,cm^{-2}}$)
$Q$ = volumetric flow rate ($\mathrm{m^3\,s^{-1}}$)
$\dot{Q}_{\mathrm{loss}}$ = heat loss (W)
$R$ = electrical resistance Ω
$R_{\mathrm{conv}}$ = convective part of total thermal resistance ($\mathrm{K\,W^{-1}}$)

$R_{heat}$ = thermal resistance due to heating of fluid ($K\,W^{-1}$)
$R_{tot}$ = total thermal resistance ($K\,W^{-1}$)
$\overline{R}_{tot}$ = dimensionless total thermal resistance
Re = Reynolds number based on the pin fin diameter
$Re_d$ = Reynolds number defined in correlation 9
$S_d$ = diagonal pitch (m)
$S_L$ = longitudinal pitch (m)
$S_T$ = transverse pitch (m)
$t$ = thickness of the silicon block (m)
$T$ = temperature (°C)
$\overline{T}$ = average surface temperature (°C)
$T_e$ = exit temperature (°C)
$\overline{T}_{heater}$ = average heater surface temperature (°C)
$T_i$ = inlet temperature (°C)
$W$ = channel width (m)

**Greek**

$\beta$ = parameters used in correlations 2 and 3
$\Delta p$ = pressure drop (kPa)
$\Delta T_i$ = temperature difference between $\overline{T}$ and $T_i$ (°C)
$\gamma$ = parameter used in correlation 3
$\epsilon$ = porosity
$\eta_f$ = fin efficiency
$\mu$ = viscosity ($kg\,m^{-1}\,s^{-1}$)
$\pi_1$ = second term of the right-hand side in Eq. (13)
$\rho$ = density ($kg\,m^{-3}$)

**Subscript**

amb = ambient
av = average
$e$ = exit
$f$ = fluid
fin = fin
$i$ = inlet
$j$ = index in Eqs. (4) and (5)
$s$ = surface

## References


[1] Kandlikar, S. G., and Grande, W. J., 2004, "Evaluation of Single-Phase Flow in Microchannels for High Heat Flux Chip Cooling—Thermohydraulic Performance Enhancement and Fabrication Technology," Heat Transfer Eng., **25**(8), pp. 5–16.
[2] Mehendale, S. S., Jacobi, A. M., and Shah, R. K., 2000, "Fluid Flow and Heat Transfer at Micro- and Meso-Scales with Application to Heat Exchanger Design," Appl. Mech. Rev., **53**(7), pp. 175–193.
[3] Owhaib, W., and Palm, B., 2004, "Experimental Investigation of Single-Phase Convective Heat Transfer in Circular Microchannels," Exp. Therm. Fluid Sci., **28**(2-3), pp. 105–110.
[4] Celata, G. P., Cumo, M., and Zummo, G., 2004, "Thermal-Hydraulic Characteristics of Single-Phase, Flow in Capillary Pipes," Exp. Therm. Fluid Sci., **28**(2-3), pp. 87–95.
[5] Jiang, L., Wong, M., and Zohar, Y., 2001, "Forced Convection Boiling in Microchannel Heat Sink," J. Microelectromech. Syst., **10**(1), pp. 80–87.
[6] Warrier, G. R., Dhir, V. K., and Momoda, L. A., 2002, "Heat Transfer and Pressure Drop in Narrow Rectangular Channel," Exp. Therm. Fluid Sci., **26**, pp. 53–64.
[7] Qu, W., and Mudawar, I., 2003, "Flow Boiling Heat Transfer in Two-Phase Micro-Channel Heat Sink—I. Experimental Investigation and Assessment of Correlation Methods," Int. J. Heat Mass Transfer, **46**(15), pp. 2755–2771.
[8] Wu, H. Y., and Cheng, P., 2003, "Visualization and Measurements of Periodic Boiling in Silicon Microchannels," Int. J. Heat Mass Transfer, **46**(14), pp. 2603–2614.
[9] Steinke, M. E., and Kandlikar, S. G., 2004, "An Experimental Investigation of Flow Boiling Characteristics of Water in Parallel Microchannels," ASME J. Heat Transfer, **126**(4), pp. 518–526.
[10] Lee, P. C., Tseng, F. G., and Pan, C., 2004, "Bubble Dynamic in Microchannels. I. Single Microchannel," Int. J. Heat Mass Transfer, **47**(25), pp. 5575–5589.
[11] Thome, J. R., 2004, "Boiling in Micro Channels: A Review of Experiment and Theory," Int. J. Heat Fluid Flow, **25**, pp. 128–139.
[12] Koo, J.-M., Im, S., Jiang, L., and Goodson, K. E., 2005, "Integrated Microchannel Cooling for Three-Dimensional Electronic Circuit Architectures," ASME J. Heat Transfer, **127**(1), pp. 49–58.
[13] Zhang, L., Wang, E. N., Goodson, K. E., and Kenny, T. W., 2005, "Phase Change Phenomena in Silicon Microchannels," Int. J. Heat Mass Transfer, **40**(8), pp. 1572–1582.
[14] Owhaib, W., Martín-Callizo, C., and Palm, B., 2004, "Evaporative Heat Transfer in Vertical Circular Microchannels," Appl. Therm. Eng., **24**, pp. 1241–1253.
[15] Koşar, A., Kuo, C. J., and Peles, Y., 2005, "Boiling Heat Transfer in Rectangular Microchannels with Reentrant Cavities," Int. J. Heat Mass Transfer, **48**(23-24), pp. 4867–4886.
[16] Koşar, A., Kuo, C. J., and Peles, Y., 2005, "Reduced Pressure Boiling Heat Transfer in Rectangular Microchannels with Interconnected Reentrant Cavities," ASME J. Heat Transfer, **127**(10), pp. 1106–1114.
[17] Kandlikar, S. G., and Grande, W. J., 2004, "Evaluation of Single Phase Flow in Microchannel for High Flux Chip Cooling—Thermohydraulic Performance Enhancement and Fabrication Technology," Paper No. ICMM2004-2321, Presented at the Second International Conference on Microchannels and Minichannels, ASME, New York, pp. 67–76.
[18] Peles, Y., Kuo, C. J., Koşar, A., Mishra, C., and Schneider, B., 2005, "Forced Convective Heat Transfer Across a Pin Fin Micro Heat Exchanger," Int. J. Heat Mass Transfer , **48**(17), pp. 3615–3627.
[19] Koşar, A., Mishra, C., and Peles, Y., 2005, "Laminar Flow Across a Bank of Low Aspect Ratio Micro Pin Fins," ASME J. Fluids Eng., **127**(3), pp. 419–430.
[20] Sparrow, E. M., Abraham, J. P., and Tong, J. C. K., 2004, "Archival Correlations for Average Heat Transfer Coefficients for Non-Circular and Circular Cylinders and for Spheres in Cross-Flow," Int. J. Heat Mass Transfer, **47**(24), pp. 5285–5296.
[21] El-Sheikh, H. A., and Garimella, S. V., 2000, "Heat Transfer from Pin Fin Heat Sinks under Multiple Impinging Jets," IEEE Trans. Adv. Packag., **23**(1), pp. 113–120.
[22] El-Sheikh, H. A., and Garimella, S. V., 2000, "Enhancement of Air Jet Impingement Heat Transfer Using Pin Fin Heat Sinks," IEEE Trans. Compon. Packag. Technol., **23**(2), pp. 300–308.
[23] Brignoni, L. A., and Garimella, S. V., 2000, "Heat Transfer from a Finned Surface in Ducted Air Jet Suction and Impingement," J. Electron. Packag., **122**, pp. 282–285.
[24] Zukauskas, A. A., 1972, "Heat Transfer from Tubes in Cross Flow," *Advances in Heat Transfer*, Academic, New York, Vol. 8, pp. 93–160.
[25] Whitaker, S., 1972, "Forced Convection Heat-Transfer Correlations for Flow in Pipes, Past Flat Plates, Single Cylinders, Single Spheres, and for Flow in Packed-Beds and Tube Bundles," AIChE J., **18**(2), pp. 361–371.
[26] Igarashi, T., 1987, "Fluid Flow and Heat Transfer Around Rectangular Cylinders (the Case of a Width/Height Ratio of a Section of 0.33-1.5)," Int. J. Heat Mass Transfer, **30**, pp. 893–901.
[27] Chyu, M. K., Hsing, Y. C., and Natarajan, V., 1998, "Convective Heat Transfer of Cubic Fin Arrays in a Narrow Channel," ASME J. Heat Transfer, **120**, pp. 362–367.
[28] Merker, G. P., and Hanke, H., 1986, "Heat Transfer and Pressure Drop on the Shell-Side of Tube-Banks Having Oval-Shaped Tubes," Int. J. Heat Mass Transfer, **29**(12), pp. 1903–1909.
[29] Reiher, H., 1925, "Der Wärmeübergang von Strömender Luft an Rohrbündel in Kreuzstrom," VDI-Forschungsh., **269**, pp. 47.
[30] Sparrow, E. M., and Grannis, V. B., 1991, "Pressure Drop Characteristics of Heat Exchangers Consisting of Arrays of Diamond-Shaped Pin Fins," Int. J. Heat Mass Transfer, **34**(3), pp. 589–600.
[31] Hilpert, R., 1933, "Der Wärmeabgabe von Geheizten Drahten und Rohren im Luftstorm," Forsch. Geb. Ingenieurwes., **4**, pp. 215–224.
[32] Ruth, E. K., 1983, "Experiments on a Cross Flow Heat Exchanger with Tubes of Lenticular Shape," ASME J. Heat Transfer, **105**, pp. 571–575.
[33] Armstrong, J., and Winstanley, D., 1988, "A Review of Staggered Array Pin Fin Heat Transfer for Turbine Cooling Applications," ASME J. Turbomach., **110**, pp. 94–103.
[34] Sparrow, E. M., Stahl, T. J., and Traub, P., 1984, "Heat Transfer Adjacent to the Attached End of a Cylinder in Crossflow," Int. J. Heat Mass Transfer, **27**, pp. 233–242.
[35] Damerow, W. P., Murtaugh, J. C., and Burgraf, F., 1972, "Experimental and Analytical Investigation of the Coolant Flow Characteristics in Cooled Turbine Airfoils," NASA Contract Rep. NASA CR, **CR-120883**.
[36] Metzger, D. E., Fan, Z. N., and Shepard, W. B., 1982, "Pressure Loss and Heat Transfer Through Multiple Rows of Short Pin Fins," *Proceedings of the 7th International Heat Transfer Conference*, Munich, Germany, Vol. **3**, pp. 137–142.
[37] Short, B. E., Jr., Price, D. C., and Raad, P. E., 2004, "Design of Cast Pin Fin Coldwalls for Air-Cooled Electronic Systems," ASME J. Electron. Packag., **126**, pp. 67–73.
[38] Li, C. -Y., and Garimella, S. V., 2001, "Prandtl Number Effects and Generalized Correlations for Confined and Submerged Jet Impingement," Int. J. Heat Mass Transfer, **44**, pp. 3471–3480.
[39] Garimella, S. V., 1999, "Heat Transfer and Flow Fields in Confined Jet Impingement," Annu. Rev. Heat Transfer, **11**, pp. 413–494.
[40] Kline, S., and McClintock, F. A., 1953, "Describing Uncertainties in Single-Sample Experiments," Mech. Eng. (Am. Soc. Mech. Eng.), **75**(1), pp. 3–8.
[41] Incropera, F. P., and DeWitt, D. P., 2002, *Introduction to Heat Transfer*, 4th

ed., Wiley, New York, pp. 396.
[42] Brigham, B. A., and Van Fossen, G. J., 1984, "Length to Diameter Ratio and Row Number Effects in Short Pin Fin Heat Transfer," ASME J. Eng. Gas Turbines Power, **106**(1), pp. 241–245.
[43] Marques, C., and Kelly, K. W., 2004, "Fabrication and Performance of a Pin Fin Micro Heat Exchanger," ASME J. Heat Transfer, **126**(3), pp. 434–444.
[44] Hwang, T. H., and Yao, S. C., 1986, "Crossflow Heat Transfer in Tube Bundles at Low Reynolds Numbers," ASME J. Heat Transfer, **108**(3), pp. 697–700.
[45] Panton, R., 1996, *Incompressible Flow*, 2nd ed., Wiley, New York, pp. 384–400.
[46] Çengel, Y. A., and Turner, R. H., 2001, *Fundamentals of Thermal-Fluids Sciences*, McGraw Hill, Boston, pp. 575–577.
[47] Shair, F. H., Grove, A. S., Petersen, E. E., and Acrivos, A., 1963, "The Effect of Confining Walls on the Stability of the Steady Wake Behind a Circular Cylinder," J. Fluid Mech., **17**, pp. 546–550.
[48] Nishioka, M., and Sato, H., 1973, "Measurements of Velocity Distributions in the Wake of a Circular Cylinder at Low Reynolds Number," J. Fluid Mech., **65**, pp. 97–112.
[49] Short, B. E., Jr., Raad, P. E., and Price, D. C., 2002, "Performance of Pin Fin Cast Aluminum Coldwalls. 2. Colburn j-Factor Correlations," J. Thermophys. Heat Transfer, **16**(3), pp. 397–403.
[50] Gunther, A. Y., and Shaw, W. A., 1945, "A General Correlation of Friction Factors for Various Types of Surfaces in Cross Flow," Trans. ASME, **67**, pp. 643–660.
[51] Taborek, J., 1983, "Shell-and-Tube Heat Exchangers: Single Phase Flow," *Handbook of Heat Exchanger Design*, Hemisphere, New York, Chap. 3.3.
[52] Gaddis, E. S., and Gnielski, V., 1985, "Pressure Drop in Horizontal Cross Flow Across Tube Bundles," Int. Chem. Eng., **25**(1), pp. 1–15.

# Investigation of Lightpipe Volumetric Radiation Effects in RTP Thermometry

**David J. Frankman**
**Brent W. Webb**
**Matthew R. Jones**

Department of Mechanical Engineering,
Brigham Young University,
Provo, UT 84602-4201

*A major obstacle to the widespread implementation of rapid thermal processing (RTP) is the challenge of wafer temperature measurement. Frequently, lightpipe radiation thermometers are used to measure wafer temperatures in RTP reactors. While the lightpipe distorts the wafer temperature profile less than temperature measurement techniques which require physical contact, the presence of the lightpipe influences the wafer temperature profile. This paper presents the results of a theoretical study exploring that influence for an idealized RTP reactor in which the wafer is treated as a nonconducting, opaque, constant-heat-flux surface imaged by the lightpipe. The coupled radiation/conduction transport in the lightpipe measurement enclosure is solved numerically. Radiation transfer in the system is modeled with varying levels of rigor, ranging from a simple volumetrically nonparticipating treatment to a full spectral solution of the radiative transfer equation. The results reveal a rather significant effect of the lightpipe on the wafer temperature, which depends on the separation between the lightpipe tip and the wafer. The study illustrates clearly the need to model the lightpipe as a volumetrically participating, semitransparent medium, and further, the importance of accounting for spectral variation of the lightpipe properties in the prediction of the radiative transfer. Finally, two primary mechanisms are identified by which the lightpipe affects the wafer temperature distribution.* [DOI: 10.1115/1.2136917]

## Introduction

Rapid thermal processing (RTP) is a key technology in the fabrication of integrated circuits. A significant advantage of RTP over conventional batch processing techniques is a shorter processing time, which minimizes diffusion of the dopants and results in smaller feature sizes. Process efficiency and product yield are strongly dependent on the wafer temperature level and uniformity. A limiting factor in the widespread implementation of RTP has been the challenge of accurately measuring the temperature of the wafer. Lightpipe radiation thermometers (LPRT) are commonly used to monitor wafer temperatures in an RTP reactor [1].

Designs for RTP reactors frequently require that the LPRT view the wafer through a small hole in a reflecting shield. In this configuration, the lower portion of the RTP reactor can be modeled as an enclosure consisting of opaque surfaces. Traditional methods such as the net-radiation method have been used to calculate the radiative transfer within the enclosure, and the total irradiation incident on the LPRT can be calculated. For this scenario, the LPRT measurement is corrupted by radiation emitted by surfaces other than the wafer and by radiation reflected from the wafer and the other surfaces comprising the enclosure. This extraneous radiation may be accounted for by defining an effective emissivity for the wafer which is greater than the actual wafer emissivity. However, determining the effective emissivity involves a complex analysis in which the temperatures and radiative surface properties of all the surfaces in the enclosure must be known [2].

An alternative approach is to minimize the stray radiation incident on the LPRT by inserting it through the lower surface of the enclosure and positioning the tip in close proximity to the wafer. In this configuration, however, the LPRT acts as a heat sink, causing a localized depression in the wafer temperature. Recent studies have been conducted in an effort to quantify this effect. Kreider et al. conducted a study in which radiative exchange only between surfaces in the lightpipe enclosure was considered, and the lightpipe was modeled as opaque, diffuse, and gray [3]. In other words, the lightpipe participated radiatively only through surface exchange. Ball et al. have constructed a highly instrumented experimental RTP facility, which is being used to develop an absolute calibration standard for pyrometers [4]. Detailed modeling of the radiation field within the full chamber of this facility has been conducted [5,6], but the important effect of volumetric emission/absorption within the lightpipe on the wafer temperature profile has yet to be characterized.

The objective of this paper is to explore the scenario of the lightpipe as a volumetrically participating (radiatively absorbing/emitting) medium for an idealized scenario wherein the wafer is specified to be an opaque, constant-heat-flux surface. Since the focus of this work is the characterization of volumetric radiation effects in the lightpipe, the radiation/conduction interaction within the wafer is neglected. Accounting for the volumetric nature of the lightpipe represents more rigor than the modeling of the lightpipe's participation in the radiative transfer within the enclosure as purely surface exchange. The effect of the semi-transparent nature of the lightpipe can be identified by comparison with previous approaches which have treated radiative interaction between lightpipe and the RTP tool as purely surface exchange.

## Problem Formulation

Rigorous modeling of the thermal transport in the full RTP chamber and measurement enclosure would require a solution of the coupled radiation, conduction, and convection problems for all components and surfaces within the chamber. The wafer is itself a semi-transparent, thermally conducting medium which would require a fully coupled conduction/radiation analysis of the entire RTP reactor including the spectral nature of the irradiating lamps. The primary purpose of this study is to explore the effect of the semi-transparent nature of the lightpipe on thermal transport within the RTP measurement enclosure. To that end, an idealized lightpipe enclosure is modeled as the axisymmetric system comprised of the wafer, shield, sidewall, and lightpipe, shown sche-

Contributed by the Heat Transfer Division of ASME for publication in the JOURNAL OF HEAT TRANSFER. Manuscript received November 18, 2004; final manuscript received July 28, 2005. Review conducted by Ashley F. Emery.

  

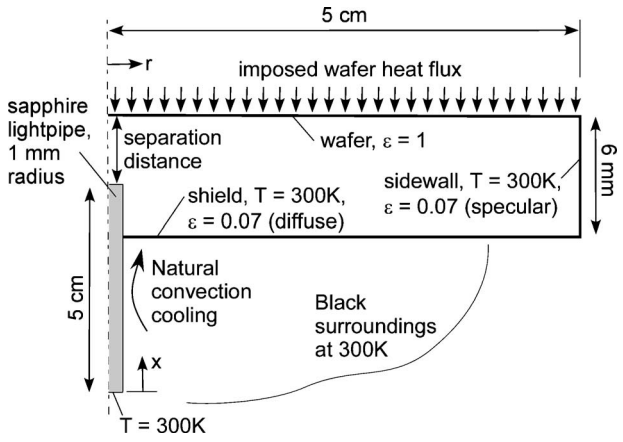


**Fig. 1 Schematic of the computational domain modeled**

matically in Fig. 1. The wafer is modeled here as a radiatively black surface on which a uniform heat flux is imposed. The cylindrical sidewall of the lightpipe enclosure is maintained at a constant temperature of 300 K, and is treated as a specularly reflective surface of emissivity 0.07. This sidewall definition minimizes the dependence of predicted wafer temperatures on the outside radius of the enclosure, which was specified here to be 5 cm. The lower portion of the enclosure consists of a cooled radiation shield, spaced 6 mm from the wafer. The shield is also maintained at a constant temperature of 300 K, with a diffuse emissivity of 0.07. Although in practice the lightpipe enclosure would likely be filled with gas (most often nitrogen), the effects of conduction/convection through the gas layer separating the wafer from the shield in the enclosure are neglected. This may be justified by the fact that the gas in the enclosure is stably stratified thermally, and conduction through the gas layer will serve only to increase the required heating rate to achieve a prescribed wafer processing temperature. A heat flux magnitude of 12.6 $kW/m^2$ was imposed at the simulated wafer surface to achieve a wafer temperature near 1300 K. This is representative of nominal target wafer temperatures in RTP reactors. The enclosure cylindrical sidewall was deliberately specified here to be specularly reflecting in order to maximize wafer temperature uniformity in the absence of the lightpipe by minimizing edge effects. Under these conditions, predictions without the lightpipe present revealed the wafer temperature to be uniform at 1335.7 K to within ±0.1 K.

A sapphire (aluminum oxide) lightpipe of fixed length 5 cm and radius 1 mm is inserted through the shield along the centerline, and positioned a known distance from the wafer. The lightpipe is assumed to be conductively isolated from the cooled shield. (Conductive contact would locally reduce the lightpipe temperature, thereby increasing the wafer temperature depression.) The lightpipe length was chosen based on a simple conducting fin analysis, such that increases in length yielded no appreciable change in the temperature distribution. The bottom boundary of the lightpipe is assumed black and maintained at 300 K, and the environment-exposed side surface (external to the lightpipe enclosure) is cooled convectively with a heat transfer coefficient of $h=25\ W/m^2\,K$ and a convective environment of $T_\infty=300$ K. (The radiative boundary condition at the lightpipe bottom is explored later.) Although conduction/convection heat transfer to the lightpipe surface within the measurement enclosure is neglected as explained previously, convective cooling is accounted for on the lightpipe surface external to the enclosure because of the significantly higher surface area and heat transfer coefficient there. This heat transfer coefficient was determined from an empirical correlation for natural convection heat transfer from slender vertical cylinders, and was found to be relatively insensitive to surface temperature [7,8] in the range encountered here. Additionally, the portion of the lightpipe which protrudes from the lightpipe enclosure is exposed to radiatively black surroundings at $T_{surr}=300$ K.

Available data for the spectral absorption coefficient and index of refraction for sapphire are reproduced in Fig. 2 [9]. The figure also shows the Planck blackbody spectral distribution for the two bounding temperatures in the system, 300 K and 1300 K. Over the spectral range of radiation significance in the RTP problem (approximately 1.5–40 $\mu$m), the spectral absorption coefficient ($\kappa_\lambda$) varies by nearly seven orders of magnitude, while the real part of the complex index of refraction ($n_\lambda$) varies by two orders of magnitude. It is further noted that radical variations in both $\kappa_\lambda$

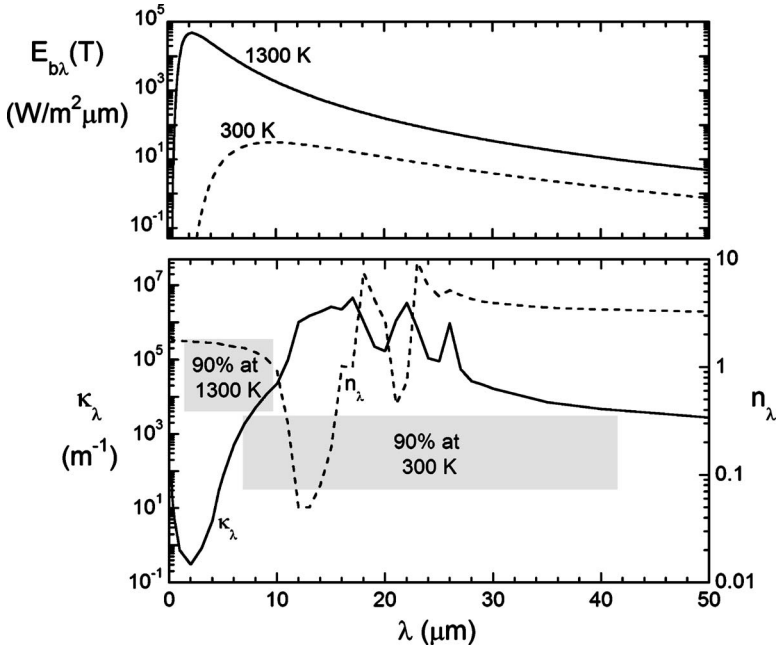


**Fig. 2 Spectral absorption coefficient and index of refraction for sapphire [9]**

and $n_\lambda$ occur in portions of the spectrum where there is significant radiant energy interaction in the system, noted by the shaded areas in the lower panel indicating the spectral range containing 90% of blackbody energy (5% limits above and below the range shown) at 300 K and 1300 K, respectively. Finally, it is observed that the lightpipe is semi-transparent at wavelengths where much of the wafer emission is concentrated, but more opaque at wavelengths characterizing low-temperature emission. Such extreme variations with wavelength render selection of appropriate mean properties for gray calculations quite challenging, and make spectral calculations both necessary and difficult.

Radiation transfer by surface exchange occurs between wafer, sidewall, and shield surfaces within the enclosure. The lightpipe, however, participates thermally through both volumetric radiative and conductive transfer. Radiation transfer from the high-temperature wafer enters the lightpipe through both the semitransparent tip and enclosure-exposed lateral surface. The lightpipe thus acts as a radiative/conductive heat sink, drawing energy from the heated wafer. This results in a localized temperature depression on the wafer.

The steady-state, coupled radiative and conductive heat transfer within the lightpipe is governed by the energy equation

$$\nabla \cdot \boldsymbol{q} = 0 \tag{1}$$

where $\boldsymbol{q}(x,r)$ is the local combined radiation and conduction heat flux vector

$$\boldsymbol{q} = \boldsymbol{q}_{\text{rad}} + \boldsymbol{q}_{\text{cond}} \tag{2}$$

Using Fourier's law and combining Eqs. (1) and (2) results in

$$\nabla \cdot k \nabla T = \nabla \cdot \boldsymbol{q}_{\text{rad}} \tag{3}$$

The divergence of the radiative heat flux vector therefore acts as a source term in the heat diffusion equation applied to the lightpipe. If the divergence of the radiative heat flux vector is known, Eq. (3) may be solved for the temperature profile in the lightpipe. The radiation transport within the lightpipe is governed by the radiative transfer equation (RTE). Assuming the lightpipe to be an absorbing, emitting, and nonscattering medium, the RTE is given as [10]

$$\hat{s} \cdot \nabla I_\lambda = \kappa_\lambda [n_\lambda^2 I_{b\lambda}(T) - I_\lambda] \tag{4}$$

where $I_\lambda$ is the local spectral radiation intensity in the direction $\hat{s}$, and $\kappa_\lambda$ and $n_\lambda$ are the spectral absorption coefficient and index of refraction, respectively, of the lightpipe material. $I_{b\lambda}(T)$ is the spectral blackbody intensity given by the Planck function, evaluated at the local temperature. The radiative heat flux vector is determined from the solution of the RTE by integration of the intensity over all directions and wavelengths

$$\boldsymbol{q}_{\text{rad}} = \int_{4\pi} \hat{s} \int_0^\infty I_\lambda d\lambda d\Omega \tag{5}$$

The divergence of the radiative flux is determined from the intensity field by the relation [10]

$$\nabla \cdot \boldsymbol{q}_{\text{rad}} = 4\pi \int_0^\infty \kappa_\lambda n_\lambda^2 I_{b\lambda}(T) d\lambda - \int_0^\infty \kappa_\lambda \int_{4\pi} I_\lambda d\lambda d\Omega \tag{6}$$

The energy equation, Eq. (3), and the RTE, Eq. (4), are coupled and must be solved simultaneously. The solution of the RTE depends on local lightpipe temperature through the emission term via the Planck blackbody intensity $I_{b\lambda}(T)$, and the local flux divergence $\nabla \cdot \boldsymbol{q}_{\text{rad}}$, which appears as a source term in the energy equation, is determined from the intensity distribution.

Radiative interaction between the lightpipe and the enclosure is modeled here in four ways, listed in increasing level of complexity and rigor:

1. *Volumetrically Nonparticipating*. In this approximation, radiation transfer between the lightpipe and the enclosure occurs by surface exchange only, determined by analysis of radiative transfer in the enclosure formed by the wafer, the shield, the cylindrical sidewall, and the enclosure-exposed lightpipe tip and side surfaces. Energy transfer within the lightpipe occurs by conduction only, and the flux divergence vanishes in Eq. (3). Thermal interaction between the lightpipe and the enclosure thus occurs only at the shared boundary. In this model the surfaces of the lightpipe are assumed opaque and gray with an emissivity of 0.88, consistent with a dielectric material of refractive index of 1.7 [10]. This model reproduces the approach reported by Kreider et al. [3].
2. *Optically Thick*. In this model the spectral absorption coefficient of the lightpipe material is assumed to be very large. Under this assumption volumetric radiation transfer occurs within the lightpipe, but takes place only between immediately adjacent layers in the sapphire. Consequently, the directional nature of the radiative transfer ceases to be important. The radiation transfer thus reduces to a diffusion-like process in which the thermal conductivity $k$ is effectively augmented by a temperature-dependent effective radiative conductivity $k_{\text{rad}}$ which accounts for the volumetric emission/absorption between adjacent layers. This radiative contribution to the local molecular thermal conductivity in the Optically Thick model can be shown to be [10]

$$k_{\text{rad}} = \frac{16 n^2 \sigma T^3}{3 \kappa_R} \tag{7}$$

where $\kappa_R$ is the Rosseland mean absorption coefficient [10]. Thus, only when the local lightpipe temperature is sufficiently high will the radiative conductivity $k_{\text{rad}}$ be significant, and the Optically Thick model predictions depart from the Volumetrically Nonparticipating model.
3. *Gray, Finite Optical Thickness*. In this approximation the lightpipe participates radiatively in the overall energy transport as a semitransparent medium. The spectral absorption coefficient of the lightpipe material is assumed to be finite and gray. Radiative energy is thus able to penetrate the lightpipe some distance before absorption. Further, the lightpipe emits radiation volumetrically. Consequently, the directional character of the radiation intensity must be accounted for [10]. The gray assumption neglects spectral variations in absorption coefficient and index of refraction, and therefore, appropriate mean values for the two properties must be specified. The Optically Thick model outlined earlier is thus a limiting case for the Gray, Finite Optical Thickness model for $\kappa \to \infty$. The simulations carried out as part of this study reveal that increasing the (gray) absorption coefficient above a magnitude $\kappa \approx 10^4\ \text{m}^{-1}$ (yielding an optical thickness based on lightpipe diameter, $2\kappa r_0 = 20$) results in no further change in the predicted wafer temperature profile, and represents the Optically Thick limit. For the Gray, Finite Optical Thickness case the surfaces of the lightpipe are assumed to be radiatively semi-transparent, and the Fresnel relations applicable to radiation interaction with a smooth surface [10] are used to determine the refraction/reflection characteristics of the interface as a function of the specified gray index of refraction. Further, the change in wavelength as radiant energy passes between lightpipe and the enclosure is properly accounted for. (The enclosure medium is assumed to have an index of refraction of unity.)
4. *Spectral*. In this model the RTE is integrated rigorously on a spectral basis, accounting for the variation in absorption coefficient and index of refraction with wavelength. This is accomplished here using the band-energy

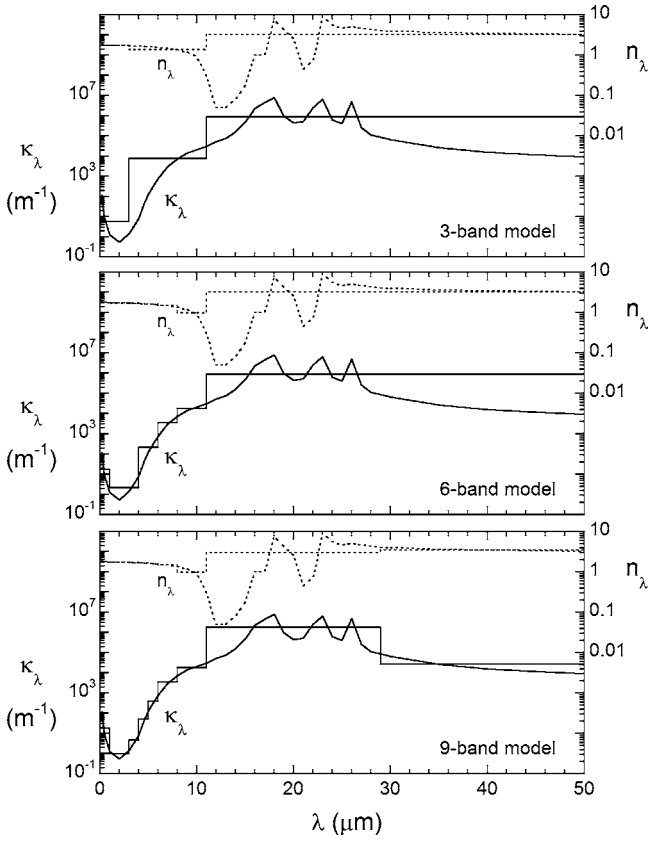


**Fig. 3 Band model approximations to the spectral variation of sapphire absorption coefficient and index of refraction**

approach, dividing the spectrum into finite wavelength intervals, or bands, over which $\kappa_\lambda$ and $n_\lambda$ are assumed constant. The RTE is then solved for each spectral band, accounting for the radiative energy within that band. Spectral approximations for $\kappa_\lambda$ and $n_\lambda$ were formulated using three, six, and nine bands, as illustrated in Fig. 3. The constant properties within each band were calculated as averages of the spectral variation within that band. Care was taken in the refinement of the band model approximations to cluster spectral resolution in the range where (i) the radiative energy is concentrated, and (ii) the highest spectral gradients in absorption coefficient exist. This was principally $\lambda < 10$ $\mu$m where the lightpipe behaves as semi-transparent to the radiant energy incident from the heated wafer. The same spectral band boundaries are required for both absorption coefficient and index of refraction. Total radiative quantities are thus calculated by integrating (summing) the spectral (band) quantities over all wavelengths as, for example, with the radiative intensity

$$I = \int_0^\infty I_\lambda d\lambda \tag{8}$$

The conduction heat transfer in the lightpipe was solved using the control volume approach [11], and the finite volume method was employed for the solution of the RTE [12,13]. The physical domain (enclosure and lightpipe) is discretized into multiple cells and the energy and radiative transfer equations are integrated over each finite (but small) cell. Discretization over angular direction is also required for the solution of the RTE, which is accomplished by dividing all directions ($4\pi$ sr) into discrete angular intervals over which the radiative intensity is assumed constant. The governing equations (energy equation and RTE for each direction) are then integrated over an arbitrary cell (and directionally over a discrete angular interval in the case of the RTE), and appropriate assumptions for the variation of the dependent variables (temperature and intensity) between nodes and among discrete directions are made to evaluate the integrals. The result is a set of nominally linear algebraic equations for the dependent variables at each node.

The solution methodology is iterative in nature. The RTE is solved based on an assumed (or recently updated) temperature distribution in the enclosure and lightpipe. The local divergence of the radiative flux vector is calculated from Eq. (6), and the result is substituted as source term in the overall energy equation. The energy equation is then solved subject to appropriate boundary conditions, and the resulting temperature distribution becomes the next estimate for the solution of the RTE. In this study, iterations were carried out until the maximum residual of thermal and radiative energy (local imbalance in energy conservation over any cell in the domain) ceased to change with further iteration. At convergence the residuals in global and radiative energy were always below $10^{-7}$, and energy was conserved globally to better than 0.5%. Simulations often required several tens of thousands of iterations.

Because the thermal conductivity of aluminum oxide varies by a factor of 4 in the temperature range 300 K to 1300 K [14], its dependence was accounted for in the numerical predictions. There is very little information available on the temperature dependence of the spectral radiative properties of sapphire. Consequently, these spectral properties were assumed to be independent of temperature.

In practice, the solution of the energy equation and the RTE in both the lightpipe and enclosure domains was treated in an integral fashion, solving for the radiative and overall energy transfer in both domains simultaneously. The thermal and radiative conditions at the shared boundaries were appropriately linked through relevant interface conditions (continuity of temperature and heat flux, Fresnel reflection/refraction). Since the enclosure is volumetrically nonparticipating, the absorption coefficient in this spatial region was set artificially low ($\kappa = 10^{-6}$ m$^{-1}$) to simulate surface exchange only. Further, negligible conduction/convection in the enclosure was modeled by specifying a vanishingly small value of the thermal conductivity ($k = 10^{-6}$ W/mK).

A comprehensive study was conducted to determine the spatial and angular resolution required for grid-independent solutions. The grid was successively refined (both spatially, and in the solution of the RTE, directionally) until the predicted wafer temperature profile ceased to change appreciably. The resulting grid consisted of nominally 8000 triangular cells in an unstructured grid, and 16 angular increments of the azimuthal and zenith directions in each octant for the two-dimensional domain (for a total of 1024 directions in solution of the RTE). It was found that this extraordinarily high angular resolution was required to properly resolve the radiation transfer in the system with such small geometric features. Employing this spatial and angular resolution, the predicted wafer temperature distribution changed by less than 1 K relative to a less refined grid. It should also be noted that radiative transfer predictions using the Spectral model are significantly more computationally intensive than the gray calculations, since one RTE solution is required for each spectral band. The nine-band Spectral model typically required of the order of 30 days of computation on an SGI Origin 3900 supercomputer (operated in single-CPU mode).

The Gray, Finite Optical Thickness radiation modeling approach requires the specification of an appropriate mean absorption coefficient and refractive index. The Planck and Rosseland mean absorption coefficients [10] may be used as bounding values for the gray absorption coefficient. The Planck and Rosseland mean absorption coefficients were calculated at a temperature of

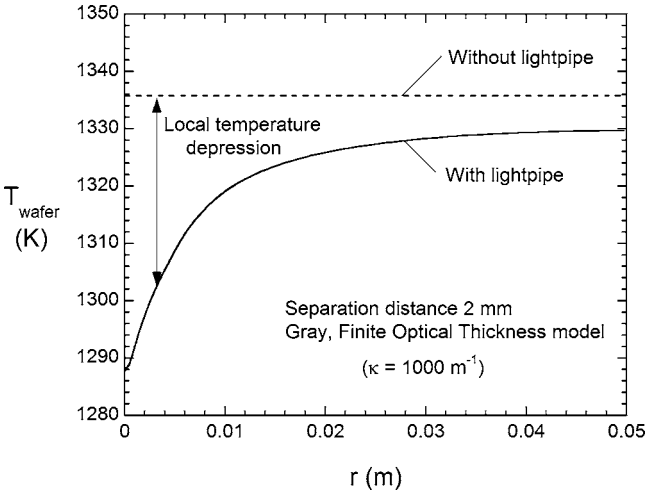


**Fig. 4 Representative predicted wafer temperature profiles with and without the lightpipe for the 2 mm separation distance, Gray, Finite Optical Thickness radiation model, $\kappa = 1000\ m^{-1}$**

1300 K to be $\kappa_P = O(10^5)\ m^{-1}$ and $\kappa_R = O(1)\ m^{-1}$, respectively. In this study, a gray index of refraction of $n = 1.7$ was used, representative of the index of refraction for the spectral range of significance here. The impact of index of refraction will be explored in more detail in a section to follow.

Calculations were performed both with and without the lightpipe present in the enclosure. The influence of the lightpipe's presence on the radial temperature profile on the wafer was then quantified by defining a local wafer temperature depression as

$$\Delta T_{\text{wafer}} = T(r)_{\text{with lightpipe}} - T(r)_{\text{without lightpipe}} \tag{9}$$

The local wafer temperature depression as defined here is always negative, and its magnitude is of primary interest in this study. The maximum wafer temperature depression, $\Delta T_{\text{wafer,max}}$, is the peak depression of all local values (which always occurs at the centerline, $r = 0$). The separation distance is defined as the distance between the exposed tip of the lightpipe inside the enclosure and the wafer. Predictions were made for separation distances between the lightpipe tip and wafer of 2 mm, 4 mm, and 6 mm, which are representative of separation distances proposed for use in RTP reactors.

## Results and Discussion

Figure 4 illustrates the predicted wafer temperature profiles for a representative case with the lightpipe present for a separation distance of 2 mm, and without the lightpipe. For the case with no lightpipe, the small aperture through which the lightpipe is inserted is replaced by reflecting shield. The radiative transfer approximation used with the lightpipe present in Fig. 4 is the Gray, Finite Optical Thickness model with a gray absorption coefficient $\kappa = 1000\ m^{-1}$. As stated previously, for the conditions studied here the wafer temperature is spatially uniform as desired at a temperature of 1335.7 K ± 0.1 K (for the 12.6 $kW/m^2$ imposed flux on the wafer) without the lightpipe present. With the lightpipe, however, the wafer experiences a temperature depression which exhibits a minimum at the enclosure radial extreme, and a maximum directly above the lightpipe. Since the object of this study is to quantify the effect of the lightpipe on the wafer temperature, the results shown hereafter will focus principally on the local wafer temperature depression $\Delta T_{\text{wafer}}$ in degrees Kelvin. The predicted temperature distribution within the lightpipe is also of interest, and it will be explored as well.

Figures 5(*a*)–5(*c*) show, respectively, the predicted wafer temperature depression using the Spectral model with the three-, six-, and nine-band approximations, to the spectral absorption coefficient and spectral index of refraction shown in Fig. 3 for the three lightpipe separation distances investigated. The data reveal that three bands (as constituted in Fig. 3) are insufficient to adequately resolve the strong variation in spectral radiative properties for accurate radiative transfer predictions. Results for a refined spectral band model reveal only slight difference (<1 K) between the six-band and nine-band predicted wafer temperature depression. It is concluded here that the nine-band model provides sufficient resolution for accurate spectral solution of the RTE here. It should again be underlined that spectral calculations are significantly more costly than gray predictions, since the RTE must effectively be solved once for each spectral band. Results presented hereafter for the Spectral model are those for the nine-band model, which serves as the benchmark prediction against which other radiative transfer approximations are compared.

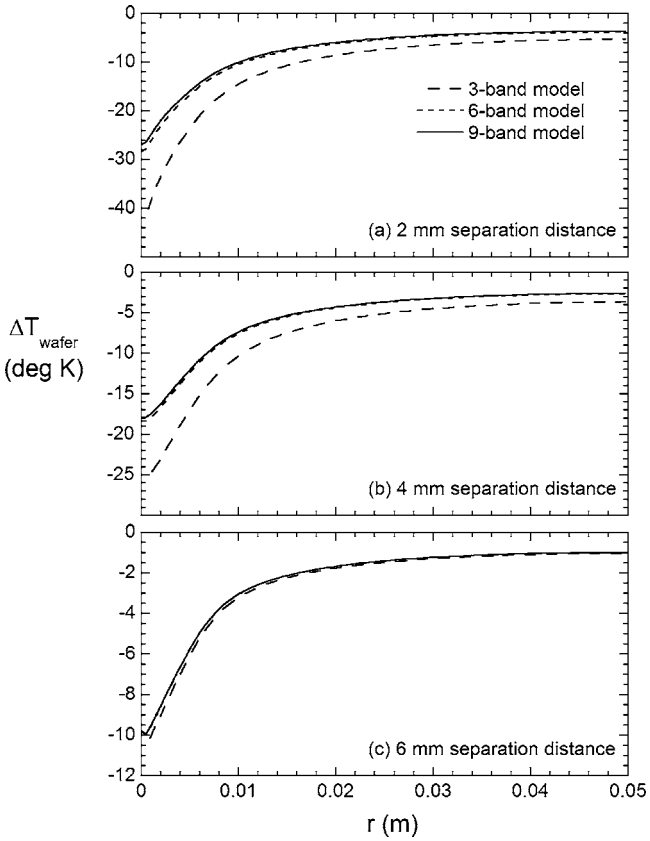


**Fig. 5 Predicted local wafer temperature depression using the three-, six-, and nine-band Spectral model for separation distances of (a) 2 mm, (b) 4 mm, and (c) 6 mm**

Figures 6(*a*)–6(*c*) illustrate the predicted local wafer temperature depression as a function of radial location for the three separation distances studied using the four radiative transfer models of varying rigor outlined previously. Relative differences in predicted wafer temperature depression for the different radiative transfer models employed are similar for all three separation distances investigated, but are most pronounced for the 2 mm distance in Fig. 6(*a*). It is seen that the Volumetrically Nonparticipating lightpipe model predicts the greatest lightpipe influence on the wafer temperature. Indeed, on the lightpipe centerline ($r = 0$) the predicted temperature depression for the case accounting for purely surface radiative exchange has a magnitude of slightly more than 50 K. Predictions are also shown using the Gray, Finite Optical Thickness model with gray absorption coefficients varying between 1 and 1000 $m^{-1}$. At a vanishing absorption coefficient $\kappa \to 0$, the lightpipe is virtually transparent to radiative exchange,

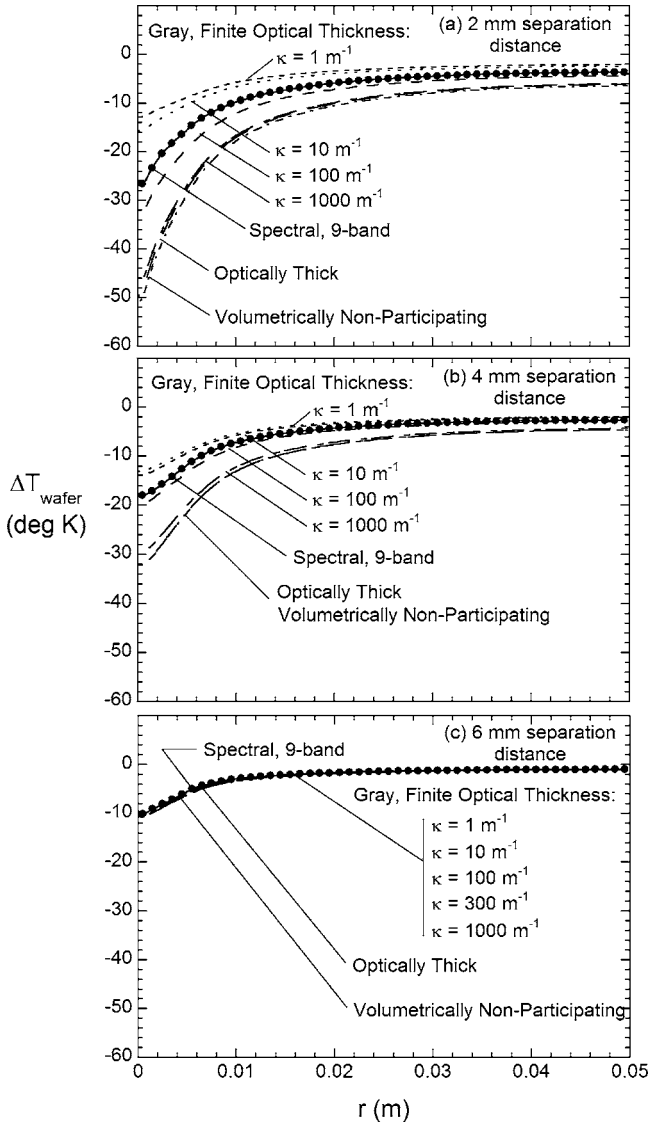


**Fig. 6 Predicted local wafer temperature depression using all radiation transfer models for separation distances of (a) 2 mm, (b) 4 mm, and (c) 6 mm. Spectral model results are shown by closed symbols.**

and the radiative interaction between wafer and lightpipe is by reflection, refraction, and transmission only. Although the wafer temperature depression is finite over the entire wafer surface, it is confined primarily to the region immediately above the lightpipe. As the gray absorption coefficient increases the wafer temperature depression also increases. Higher $\kappa$ results in greater absorption of radiative transfer within the lightpipe, and subsequent higher temperature gradients driving the conduction heat transfer. As $\kappa$ increases, the results approach the Optically Thick model result. As stated previously, increases in gray absorption coefficient beyond $\kappa \approx 10^4$ m$^{-1}$ yield no further changes in predictions.

Spectral model (nine-band) predictions are shown as symbols (every fourth symbol shown) in Fig. 6 for the three lightpipe separation distances studied. By comparison with the benchmark spectral calculations, it is clear that the simplistic Volumetrically Nonparticipating and Optically Thick approximations over-predict the wafer temperature depression. This observation is consistent with experimental measurements [3]. Further, gray radiative transfer predictions using a mean absorption coefficient of magnitude between $\kappa=10$ and 100 m$^{-1}$ most closely match the Spectral model predictions. The comparison between Gray, Finite Optical Thickness and the benchmark Spectral model results illustrate the difficulty in estimating a priori an appropriate mean absorption coefficient for use in the less computationally intensive gray predictions.

As the separation distance between lightpipe and wafer increases (shown by comparing Figs. 6(*a*)–6(*c*)), the influence of the lightpipe on the wafer temperature distribution decreases. Increasing the separation distance from 2 mm (Fig. 6(*a*)) to 4 mm (Fig. 6(*b*)) significantly decreases the wafer temperature depression, with a drop in the predicted maximum magnitude of $\Delta T_{\text{wafer}}$ from 50 K to 34 K for the Volumetrically Nonparticipating model, and 28 K to 18 K for the Spectral model. Further, relative differences between predictions from the various radiation transfer model approximations decrease as well. It should be noted that the lightpipe is positioned flush with the enclosure shield for the highest (6 mm) separation distance. In this case the wafer interacts radiatively with the lightpipe only through the exposed circular tip. Therefore, the effect of different lightpipe radiative properties on wafer temperature is minimized; it may be seen in Fig. 6(*c*) that there is little difference in wafer temperature depression at the 6 mm separation distance between the Gray, Finite Optical Thickness (for all values of $\kappa$), Optically Thick, Volumetrically Nonparticipating, and Spectral radiation model predictions. However, even when the lightpipe does not protrude into the enclosure, the temperature depression is still finite over the entire wafer, reaching a maximum magnitude of approximately 12 K directly above the lightpipe and 0.5 K at the wafer radial extreme boundary ($r=5$ cm) for the enclosure and wafer heat load specified in this study.

As stated previously, Fig. 6 reveals that the radial extent over which the wafer temperature is substantially perturbed is reduced as the tip of the lightpipe is moved further from the wafer. For increasing separation distance there is less of the lateral (cylindrical) lightpipe surface exposed to the enclosure. Consequently, the wafer interacts radiatively with less of the exposed lightpipe, and the temperature depression is confined to smaller radial regions above the lightpipe. Nevertheless, a finite temperature depression prevails over the entire wafer for all three separation distances, indicating that the lightpipe exercises influence on the entire wafer. It should be noted that even for $\kappa \to 0$ (in the Gray, Finite Optical Thickness model), the wafer temperature depression increases slightly as the lightpipe is brought closer to the wafer. Radiant energy entering the lightpipe through the tip and exposed side surface inside the enclosure may either exit the lightpipe within the enclosure, or be internally reflected at the lightpipe interface. Ultimately, after multiple reflections from the interface, a portion of the radiant energy entering the lightpipe exits through the circular aperture flush with the bottom shield through which the lightpipe is inserted. This might appropriately be called a lens effect, since the internal reflections arise due to discontinuity in index of refraction between enclosure and lightpipe. This phenomenon will be further explored in a section to follow. Two distinct mechanisms thus emerge for lightpipe influence on the wafer temperature. They are (i) the absorbing nature of the lightpipe, which results in subsequent conduction of wafer energy to the cool environment, and (ii) the lens effect, in which the lightpipe draws energy from the wafer by reflection/refraction/transmission.

Figure 7 illustrates the predicted maximum wafer temperature depression (which occurs at $r=0$) as a function of absorption coefficient in the Gray, Finite Optical Thickness model for the three separation distances studied. Also included in the figure for comparison is the maximum wafer temperature depression predicted by the Volumetrically Nonparticipating model (shown as open symbols) and Spectral model (shown to the right of the figure). These data summarize the potential error incurred in modeling the lightpipe with the various radiation transfer approximations. The figure reveals asymptotic limits in $\Delta T_{\text{wafer,max}}$ corresponding to an optically thin ($\kappa \to 0$) and optically thick ($\kappa \to \infty$) lightpipe. In both of these limits the wafer temperature is only weakly depen-

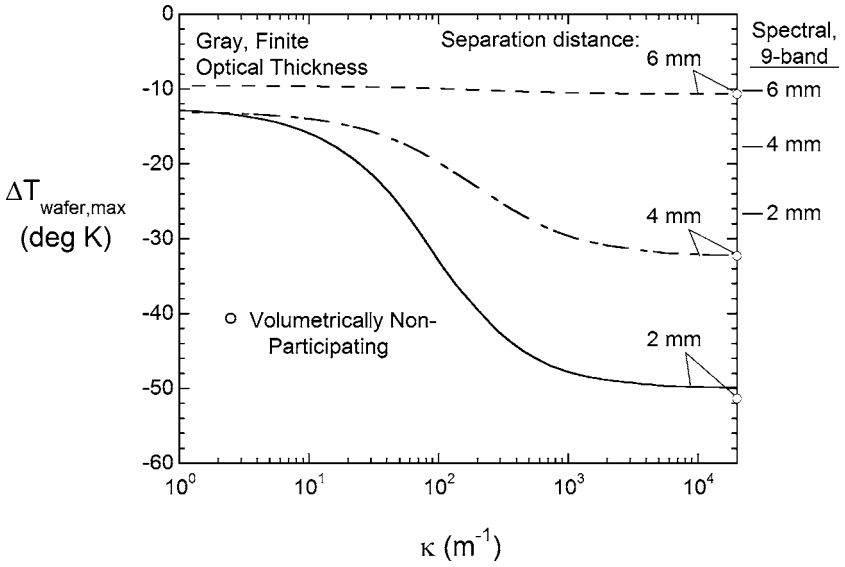


**Fig. 7 Predicted maximum wafer temperature depression as a function of gray absorption coefficient and separation distance. Predicted Spectral (nine-band) and Volumetrically Nonparticipating model results are shown on the right axis.**

dent on absorption coefficient. Between these two limits the predicted temperature depression depends strongly on $\kappa$, except (as has been noted previously) for the 6 mm separation distance. The Volumetrically Nonparticipating model overpredicts the effect of the lightpipe on the wafer temperature, although the magnitude of the maximum wafer temperature depression, $\Delta T_{\text{wafer,max}}$, is very near that determined using the Optically Thick model. As was seen in Fig. 6, significant error can be incurred in the determination of the maximum wafer temperature depression unless rigorous spectral calculations are performed. For the 2 mm separation distance the $\Delta T_{\text{wafer,max}}$ predicted by the Volumetrically Nonparticipating model is nominally 2 K higher than of the Optically Thick model. Slight differences in the Volumetrically Nonparticipating and Optically Thick ($\kappa \rightarrow \infty$) model predictions are due to the enhancement of thermal conduction due to the effective radiative conductivity presented in Eq. (7). In spatial regions where the lightpipe temperature is sufficiently high (as will be shown later to be the case principally for small separation distances), this radiative conductivity $k_{\text{rad}}$ becomes large enough relative to the molecular conductivity $k$ to enhance the molecular conductive transport. The results of Fig. 7 again underline the errors incurred in employing the Volumetrically Nonparticipating and Optically Thick models, and the difficulty in specifying an appropriate mean absorption coefficient $\kappa$ for the Gray, Finite Optical Thickness model relative to the benchmark spectral simulations.

The predicted temperature profiles along the axis of the lightpipe for each of the radiative transfer models employed are presented in Fig. 8 for the three separation distances explored. As shown in Fig. 1, the origin, $x=0$, is at the bottom of the lightpipe. Predictions (not shown here) revealed that the temperature distribution within the lightpipe was nearly one-dimensional; radial gradients were found to be less than 0.4 K from lightpipe axis to boundary. The data of Fig. 8 reveal that for all separation distances, the lightpipe reaches a maximum temperature at the tip exposed to the hot wafer in the enclosure. The temperature decreases along the axis until it reaches the 300 K temperature imposed at the bottom boundary. As the absorption coefficient decreases in the Gray, Finite Optical Thickness model, absorption within the lightpipe vanishes and the temperature becomes nearly uniform at 300 K. With near-zero axial temperature gradients, conduction as a mechanism for lightpipe influence on the wafer temperature is minimized. The highest lightpipe tip temperature occurs for the 2 mm separation distance, reaching 1050 K for the Volumetrically Nonparticipating model. However, the Spectral model predicts a substantially lower lightpipe tip temperature of 493 K for this case. The figure indicates that lightpipe temperatures are lower for greater separation distances. The peak lightpipe temperature predicted by the Spectral model is 493 K, 390 K, and 315 K, respectively, for the 2 mm, 4 mm, and 6 mm separation distance. It is again observed that the Volumetrically Nonparticipating and Optically Thick models yield nearly identical predictions for the 4 and 6 mm separation distances, and differ by only a few degrees Kelvin for the 2 mm separation distance (where local temperatures are high enough near the tip for $k_{\text{rad}}$ to be significant enough relative to $k$ to contribute to the overall conduction). Relative to the benchmark Spectral model, treating the radiation within the lightpipe simplistically (as with the Volumetrically Nonparticipating or Optically Thick approximations) dramatically overpredicts both the peak temperature and the magnitude of the axial temperature gradient in the lightpipe. The more rigorous radiation model treating the lightpipe as a semitransparent medium results in lower predicted lightpipe temperatures. Finally, it is noted that lightpipe temperatures are reduced as the separation distance increases.

Figure 9 demonstrates more clearly the lightpipe's tendency to draw energy from the heated wafer due to the lens effect. The figure compares the local wafer temperature depression for two scenarios: (1) a gray, nonabsorbing ($\kappa \rightarrow 0$) lightpipe of nonunity index of refraction ($n=1.7$) with a separation distance of 2 mm, and (2) the lightpipe removed from the enclosure, but with the vacant aperture open to the black environment at 300 K. The case involving no lightpipe is thus a surface exchange problem with a radiatively black, cold spot of radius 1 mm in place of the lightpipe. The figure reveals that the protruding, nonabsorbing lightpipe results in greater temperature depression over the majority of the wafer area than the black aperture at 300 K. Only directly above the lightpipe ($r \approx 0$) is the predicted temperature depression similar for the two cases. Despite the modest reflection from the lightpipe tip, the black aperture and the nonabsorbing lightpipe scenarios present nearly the same radiative environment to the heated wafer directly above the lightpipe. At off-axis radial wafer locations, however, the protruding, nonabsorbing lightpipe collects more radiant energy due to the combined effects of greater

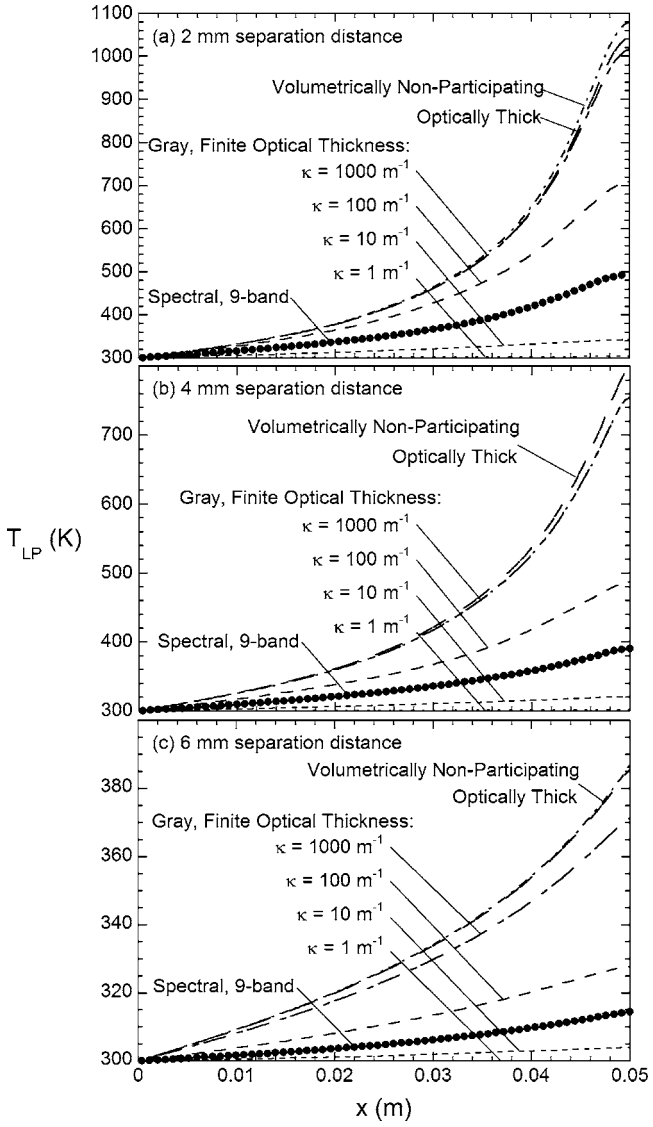


**Fig. 8 Predicted lightpipe centerline temperature profiles for all radiation transfer models for separation distances of (a) 2 mm, (b) 4 mm, and (c) 6 mm. Spectral model results are shown by closed symbols.**

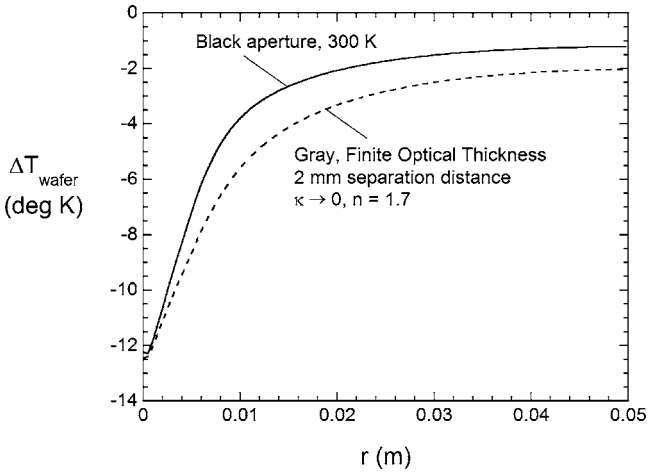


**Fig. 9 Predicted local wafer temperature depression for a gray, non-absorbing ($\kappa \rightarrow 0$) lightpipe of non-unity index of refraction ($n=1.7$) with a separation distance of 2 mm, and lightpipe removed but aperture open to the black environment at 300 K**

enclosure-exposed surface area and internal refraction/reflection. It is emphasized that this phenomenon is independent of absorption in the lightpipe. The results shown in Fig. 9 further demonstrate that the wafer temperature depression is due to both lightpipe absorption and the lens effect.

Figure 10 illustrates the predicted dependence of wafer temperature depression on lightpipe index of refraction for the Gray, Finite Optical Thickness model using $\kappa=60\ \mathrm{m}^{-1}$. This value of the gray absorption coefficient used in these simulations lies in the range identified in Figs. 6 and 8 which yield predictions near those of the benchmark Spectral model, and are thus generally representative of the effective optical thickness of the lightpipe. The range of index of refraction illustrated in Fig. 10, $1.0<n<3.5$, was selected to illustrate the impact of increasing enclosure/lightpipe interface reflection as the relative index of refraction rises. The figure clearly shows that, with the exception of the 6 mm separation distance (for which the lightpipe tip is flush with the shield), increasing lightpipe index of refraction results in a higher maximum wafer temperature depression. As explained previously, this is due to the increasing influence of internal reflection as $n$ is increased (i.e., greater lens effect). The lightpipe's influence is diminished for greater lightpipe separation distances. As the separation distance increases, less lateral lightpipe surface is exposed to the enclosure, thus collecting less radiant energy from the wafer. Unlike the 2 mm and 4 mm separation distance configurations, the maximum wafer temperature depression decreases with increasing $n$ for the 6 mm separation distance. In this case, a higher index of refraction results in increased reflection from the lightpipe tip, the only portion of the lightpipe that is exposed to the hot wafer in the enclosure. The hemispherical reflectivity of a Fresnel (smooth) surface increases from 0 to 0.31 for a corresponding increase in index of refraction from 1.0 to 3.5. For those scenarios where the lightpipe protrudes through the shield (separation distances less than 6 mm), the increased surface reflection as radiation initially interacts with the lightpipe for increasing $n$ is more than offset by subsequent internal reflection within the lightpipe, resulting in greater losses and associated higher wafer temperature depression. Finally, it is noted that for $n=1$, the flush-mounted lightpipe (separation distance of 6 mm) yields a maximum wafer temperature depression of slightly higher magnitude than the 4 mm spacing. For $n=1$ there is no lens effect, and lightpipe absorption (for finite $\kappa$) is the only mechanism perturbing the

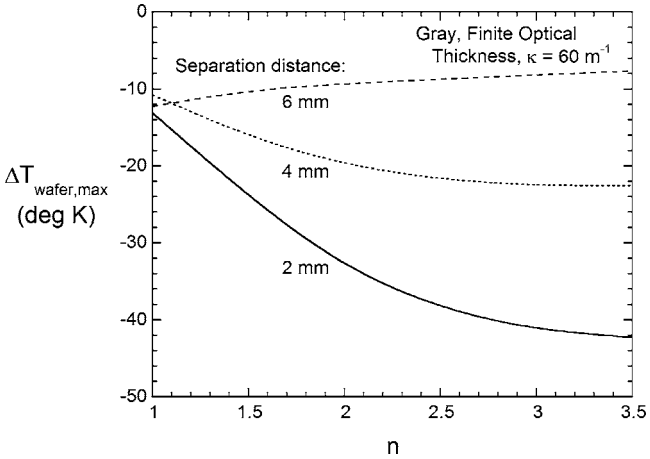


**Fig. 10 Predicted maximum wafer temperature depression as a function of refractive index and separation distance for the Gray, Finite Optical Thickness model, $\kappa=60\ \mathrm{m}^{-1}$**

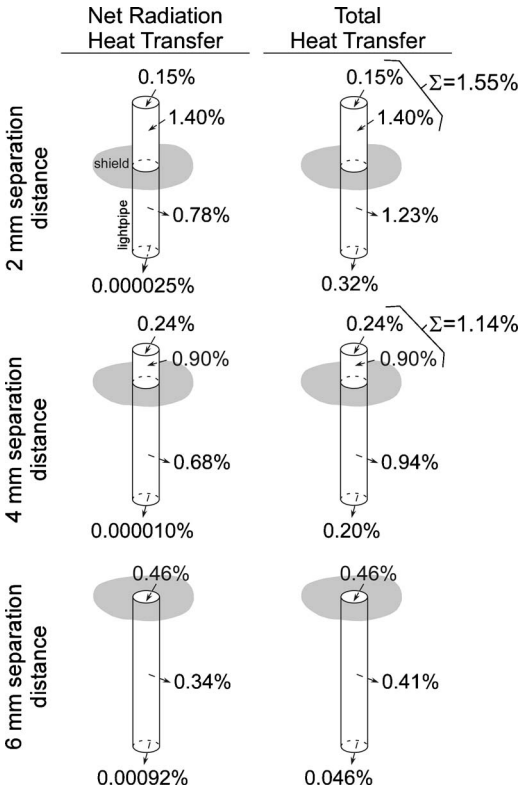


**Fig. 11 Predicted net radiation and total heat transfer through the various lightpipe surfaces (lightpipe tip, enclosure-exposed side, environment-exposed side, and bottom) expressed as a percentage of the total heat input to the wafer for all three separation distances. Arrows indicate the direction of heat transfer on each surface.**

wafer temperature. The figure serves to further illustrate the mechanisms by which the lightpipe draws energy from the heated wafer, and the complex interplay of increased surface area for greater lightpipe protrusion and internal reflection and absorption of radiation within the lightpipe.

Figure 11 depicts schematically the net radiation heat transfer and total heat transfer, respectively, through the various lightpipe surfaces (lightpipe tip, enclosure-exposed side, environment-exposed side external to the enclosure, and bottom) predicted by the model and expressed as a percentage of the total heat input to the wafer (99.7 W), for all three separation distances. Arrows show the direction of heat transfer on each surface. The summation value shown under total heat transfer indicates the total heat transfer (fraction) to the lightpipe through combined tip and (if relevant) enclosure-exposed side surface area (1.55%, 1.14%, and 0.46% of wafer heat input for the 2, 4, and 6 mm separation distances, respectively). Note that while the total heat transfer to the lightpipe is a rather small fraction of the energy input to the wafer (less than 1.55%), it nevertheless exercises a dramatic influence on the wafer temperature nonuniformity. The data reveal that the total energy drawn from the heated wafer increases as the lightpipe is brought into closer proximity to the wafer. Further, it is seen that if the lightpipe protrudes into the enclosure (as is the case for separation distance of 2 mm and 4 mm), the majority of the heat transfer to the lightpipe occurs through the enclosure-exposed side, consistent with the lens effect illustrated previously. Indeed, the radiation transfer through the side surface in the enclosure is between four and ten times that through the small circular tip. It is also observed in Fig. 11 that most of the energy entering the lightpipe exits through the environment-exposed side surface, either as radiative or convective transfer. Conduction heat transfer at the lightpipe bottom surface is modest. Finally, it is noted that very little radiant energy reaches the lightpipe bottom surface. Recall that in RTP thermometry, the radiant energy collected at the lightpipe bottom is used to determine the wafer temperature. Little radiant energy is required for this temperature determination, which is usually performed using dual-wavelength pyrometry. Lightpipes are often configured with interference filters at their bottom surface, which are highly reflective in spectral regions outside the wavelengths of interest for temperature measurement. The lightpipe bottom surface has been assumed to be radiatively black in all results presented in this study. With such small fractions of the radiant energy entering the lightpipe in the enclosure eventually arriving at the bottom (sensor), the radiative boundary condition at the lightpipe bottom thus makes little difference in the thermal transport within the system, and the wafer temperature depression is not materially affected by the radiative boundary condition there. This was confirmed by simulations conducted as part of this study wherein the lightpipe bottom emissivity was changed from highly absorbing (emissivity of unity), to that generally representative of an interference filter condition yielding a highly reflecting boundary (emissivity of 0.05). There was virtually no difference in the predicted wafer or lightpipe axis temperature distributions for these two cases. It may be thus concluded that the energy drawn from the heated wafer by the lightpipe is dissipated, in order of decreasing magnitude, by radiative and convective transfer through the unshielded environment-exposed surface, and conduction through the lightpipe bottom.

## Conclusions

The effect of the presence of a lightpipe on the local wafer temperature in an RTP reactor has been modeled by accounting for both radiation and conduction heat transfer. Radiative transfer in the lightpipe was simulated using Volumetrically Nonparticipating, Gray Finite Optical Thickness, Optically Thick, and Spectral models. The results demonstrate the significant influence of the lightpipe on wafer temperature. This influence is exercised through two mechanisms, absorption and subsequent conduction of energy, and the lens effect. Further, predictions underline the need for treating the lightpipe radiatively as a semitransparent, volumetrically participating medium. Spectral integration of the RTE reveals the significant impact of the variation of the absorption coefficient with wavelength on thermal transport in the system. Because the radiative properties vary so radically with wavelength over the range of radiation significance, relatively fine spectral resolution is required for accuracy in the spectral solutions.

## Nomenclature

$I$ = radiative intensity
$I_b$ = Planck blackbody intensity
$k$ = thermal conductivity
$n$ = index of refraction
$\boldsymbol{q}$ = heat flux vector
$r$ = radial coordinate
$r_0$ = lightpipe radius
$T$ = local temperature
$x$ = axial coordinate
$\kappa$ = absorption coefficient
$\kappa_P$ = Planck mean absorption coefficient
$\kappa_R$ = Rosseland mean absorption coefficient
$\lambda$ = wavelength

**Subscripts**

cond = conduction
rad = radiation
LP = lightpipe quantity
wafer = wafer quantity
max = maximum
$\lambda$ = spectral quantity

## References


[1] Fair, R. B., 1993, "Rapid Thermal Processing—A Justification," in *Rapid Thermal Processing Science and Technology*, R. B. Fair, ed., Academic, New York, pp. 1–11.

[2] Zhang, Z. M., and Zhou, Y. H., 2001, "An Effective Emissivity Model for Rapid Thermal Processing Using the Net-Radiation Method," Int. J. Thermophys., **22**, pp. 1563–1575.

[3] Kreider, K. G., Chen, D. H., DeWitt, D. P., Kimes, W. A., and Tsai, B. K., 2003, "Lightpipe Proximity Effects on Si Wafer Temperature in Rapid Thermal Processing Tools," *Proceedings of the 11th IEEE International Conference on Advanced Thermal Processing of Semiconductors – RTP 2003*, pp. 125–129.

[4] Ball, K. S., Huston, K. S., Noska, B. L., Simonich, M. A., Geyling, F. T., Sing, D., Tichy, R. S., and Baharav, Y., 2001, "The UT/NIST/SA/ISMT Thermometry Test Bed - 2001," *Ninth International Conference on Advanced Thermal Processing of Semiconductors – RTP 2001*, Anchorage AK, pp. 149–162.

[5] Gamba, M., Erturk, H., Ezekoye, O. A., and Howell, J. R., 2002, "Modeling of a Radiative RTP-Type Furnace Through Inverse Design: Mathematical Model and Experimental Results," *Proceedings IMECE2002, ASME International Mechanical Engineering Congress & Exposition*, New Orleans LA, November 2002, IMECE2002-33844.

[6] Ball, K. S., and Howell, J. R., 2004, "Modeling and Experimental Results for an RTP Light-Pipe Radiation Thermometer Calibration Testbed," *12th IEEE International Conference on Advanced Thermal Processing of Semiconductors – RTP 2004*, Portland, OR, pp. 175–180.

[7] Minkowycz, W. J., and Sparrow, E. M., 1974, "Local Nonsimilar Solutions for Natural Convection on a Vertical Cylinder," ASME J. Heat Transfer, **96**, pp. 178–183.

[8] Cebeci, T., 1974, "Laminar Free Convection Heat Transfer from the Outer Surface of a Vertical Slender Circular Cylinder," *Proceedings of the Fifth International Heat Transfer Conference*, ASME/JSME, Tokyo, Vol. 3, pp. 15–19.

[9] Brewster, M. Q., 1992, *Thermal Radiative Transfer & Properties*, John Wiley & Sons, New York.

[10] Modest, M. F., 2004, *Radiative Heat Transfer*, 2nd ed., McGraw-Hill, New York.

[11] Patankar, S. V., 1980, *Numerical Heat Transfer and Fluid Flow*, Hemisphere, New York.

[12] Chui, E. H., and Raithby, G. D., 1993, "Computation of Radiant Heat Transfer on a Non-Orthogonal Mesh Using the Finite-Volume Method," Numer. Heat Transfer, Part B, **23**, pp. 269–288.

[13] Raithby, G. D., and Chui, E. H., 1990, "A Finite-Volume Method for Predicting Radiant Heat Transfer in Enclosures With Participating Media," ASME J. Heat Transfer, **112**, pp. 415–423.

[14] http://www.saphikon.com/semiprop.htm, Saphikon web site, June 1, 2004.

# Magnetohydrodynamic Convective Flow of a Micropolar Fluid Past a Continuously Moving Vertical Porous Plate in the Presence of Heat Generation/Absorption

**M. M. Rahman**[1]
Department of Mathematics,
University of Dhaka,
Dhaka-1000, Bangladesh
Fax: +88 02 8615583
e-mail: mansurdu@yahoo.com

**M. A. Sattar**
Department of Computer Science & Engineering,
North South University,
12 Banani C/A,
Kemal Ataturk Avenue,
Dhaka-1213, Bangladesh

*Magnetohydrodynamic convective flow and heat transfer of a micropolar fluid past a continuously moving vertical porous plate in the presence of heat generation/absorption with constant suction has been analyzed numerically. With appropriate transformations the boundary layer equations are transformed into nonlinear ordinary differential equations. The local similarity solutions of the transformed dimensionless equations for the flow, microrotation, and heat transfer characteristics are evaluated using Nachtsheim-Swigert shooting iteration technique. Numerical results are presented in the form of velocity, microrotation, and temperature profiles within the boundary layer for different parameters entering into the analysis. Also the effects of the pertinent parameters on the local skin friction coefficient and rate of the heat transfer in terms of the local Nusselt number are also discussed.* [DOI: 10.1115/1.2136918]

*Keywords: MHD, convection, micropolar fluid, microrotation, suction, heat generation/absorption*

## 1 Introduction

Micropolar fluids are those which contain micro-constituents that can undergo rotation, the presence of which can affect the hydrodynamics of the flow so that it can be distinctly non-Newtonian. It has many practical applications, for example analyzing the behavior of exotic lubricants, the flow of colloidal suspensions or polymeric fluids, liquid crystals, additive suspensions, animal blood and turbulent shear flows.

Convective flow over a flat plate which is immersed in a micropolar fluid has attracted an increasing amount of attention since the early studies of Eringen [1,2]. Many investigators have studied and reported results for micropolar fluids of whom the names of Jena and Mathur [3], Gorla and Takhar [4], Yucel [5], Gorla [6,7], Gorla et al. [8], Gorla and Nakayama [9] are worth mentioning. The free convection effect in a boundary layer flow of a micropolar fluid along a vertical wavy surface has been studied by Chiu and Chou [10]. Char and Chang [11] have studied the laminar free convection flow of the same fluid past an arbitrary curved surface. Hossain and Chaudhury [12] have studied mixed convection flow of micropolar fluid over an isothermal plate with variable spin gradient viscosity. Wang [13] has studied the coupling condition with mixed convection of micropolar fluids past a vertical plate while Rees and Pop [14] studied the free convection boundary layer flow in the same flow condition. Desseaux and Kelson [15] studied the flow of a micropolar fluid bounded by a stretching sheet. Perdikis and Raptis [16] studied the heat transfer of a micropolar fluid in the presence of radiation. Later Raptis [17] studied the same fluid flow past a continuously moving plate in the presence of radiation. Recently El-Arabawy [18] extended the model of Raptis [17] by taking the effects of suction and injection. Very recently Sattar and Rahman [19] have studied unsteady free convection flow of a micropolar fluid past a continuously moving vertical porous plate in the presence of radiation.

The study of heat generation or absorption in moving fluids is important in problems dealing with chemical reactions and those concerned with dissociating fluids. Possible heat generation effects may alter the temperature distribution; consequently, the particle deposition rate in nuclear reactors, electronic chips, and semiconductor wafers. Vajravelu and Hadjinolaou [20] studied the heat transfer characteristics in the laminar boundary layer of a viscous fluid over a stretching sheet with viscous dissipation or frictional heating and internal heat generation. They considered that the volumetric rate of heat generation, $q'''$ [$\mathrm{W.m^{-3}}$], should be

$$q''' = Q_0(T - T_\infty) \quad \text{for } T \geqslant T_\infty = 0 \quad \text{for } T < T_\infty$$

where $Q_0$ is the heat generation/absorption constant. The above-mentioned relation, explained by Vajravelu and Hadjinolaou [20], is valid as an approximation of the state of some exothermic processes and having $T_\infty$ as the onset temperature. Later Rahman and Sattar [21] studied magnetohydrodynamic (MHD) heat and mass transfer flow with oscillatory plate velocity and constant heat source (the same as Vajravelu and Hadjinolaou [20]) in a rotating system. Recently Molla et al. [22] studied natural convection flow along a heated wavy surface with a distributed heat source as given in Vajravelu and Hadjinolaou [20] for $T > T_\infty$.

In the present study, we have extended the work of El-Arabawy [18] to a MHD flow taking into account the effect of free convection and microrotation inertia term which has been neglected by El-Arabawy [18]. We have also considered the heat generation/absorption effects to a porous plate with constant suction.

[1]Corresponding author.

Contributed by the Heat Transfer Division of ASME for publication in the JOURNAL OF HEAT TRANSFER. Manuscript received November 29, 2004; final manuscript received August 2, 2005. Review conducted by Jacob Chung.

  

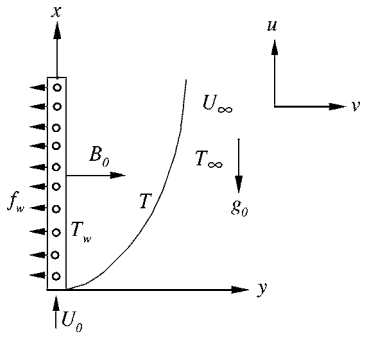


**Fig. 1 Flow configuration**

The organization of the remainder of the paper is as follows. In Sec. 2, we describe the model with its governing equations and boundary conditions. Here we also describe the solution method briefly. In Sec. 3, we present results and discussion. Finally, in Sec. 4, we summarize our results and present our conclusions.

## 2 Mathematical Formulation

We consider a heated vertical flat plate with a constant wall temperature $T_w$ under the influence of a transversely applied magnetic field **B**. The plate is immersed in a micropolar fluid of temperature $T$, where $T_w > T$. The plate is also assumed to be moving with a uniform velocity $U_0$ and there is a suction velocity $v_0$ at the plate. The magnetic Reynolds number of the flow is taken to be small enough so that induced magnetic field is assumed to be negligible in comparison with applied magnetic field so that $\mathbf{B} = (0, B_0, 0)$, where $B_0$ is the uniform magnetic field acting normal to the plate. The flow configuration and the coordinate system are shown in Fig. 1.

Within the framework of the above-noted assumptions the convective flow of a steady incompressible micropolar fluid subject to the Boussinesq approximation can be written in the following form (see Chiu and Chou [10] and Ingham and Pop [23])

$$\frac{\partial u}{\partial x} + \frac{\partial v}{\partial y} = 0 \tag{1}$$

$$u\frac{\partial u}{\partial x} + v\frac{\partial u}{\partial y} = \nu_a \frac{\partial^2 u}{\partial y^2} + g_0\beta(T - T_\infty) + \frac{S}{\rho}\frac{\partial \sigma}{\partial y} - \frac{\sigma' B_0^2 u}{\rho} \tag{2}$$

$$u\frac{\partial \sigma}{\partial x} + v\frac{\partial \sigma}{\partial y} = \frac{\nu_s}{\rho j}\frac{\partial^2 \sigma}{\partial y^2} - \frac{S}{\rho j}\left(2\sigma + \frac{\partial u}{\partial y}\right) \tag{3}$$

$$u\frac{\partial T}{\partial x} + v\frac{\partial T}{\partial y} = \frac{\kappa}{\rho c_p}\frac{\partial^2 T}{\partial y^2} + \frac{Q_0}{\rho c_p}(T - T_\infty) \tag{4}$$

where $u$, $v$ are the velocity components along $x$, $y$ coordinates respectively, $\nu_a = (\mu + S)/\rho$ is the apparent kinematic viscosity, $\mu$ is the coefficient of dynamic viscosity, $S$ is the microrotation coupling coefficient (also known as the coefficient of gyro-viscosity or as the vortex viscosity), $\rho$ is the mass density of the fluid, $\sigma$ is the microrotation component normal to the $xy$ plane, $\sigma'$ is the magnetic permeability, $\nu_s = (\mu + S/2)j$ is the microrotation viscosity (or spin-gradient viscosity), $j$ is the micro-inertia density, $T$ is the temperature of the fluid in the boundary layer, $T_\infty$ is the temperature of the fluid out side the boundary layer, $c_p$ is the specific heat of the fluid at constant pressure, $\kappa$ is the thermal conductivity,

**Table 1 Comparison of $f''(0)$**

| $v_0$ | Pr | El-Arabawy [18] | Present results |
|---|---|---|---|
| −0.7 | 0.73 | −0.2788 | −0.2785 |
| −0.4 | 0.73 | −0.4042 | −0.4037 |
| −0.2 | 0.73 | −0.5041 | −0.5036 |
| 0.0 | 0.73 | −0.6165 | −0.6165 |
| 0.2 | 0.73 | −0.7415 | −0.7414 |
| 0.4 | 0.73 | −0.8775 | −0.8774 |
| 0.7 | 0.73 | −1.0994 | −1.0992 |

**Table 2 Comparison of $g(0)$**

| $v_0$ | Pr | El-Arabawy [18] | Present results |
|---|---|---|---|
| −0.7 | 0.73 | 0.2369 | 0.2366 |
| −0.4 | 0.73 | 0.2870 | 0.2866 |
| −0.2 | 0.73 | 0.3212 | 0.3209 |
| 0.0 | 0.73 | 0.3553 | 0.3553 |
| 0.2 | 0.73 | 0.3893 | 0.3892 |
| 0.4 | 0.73 | 0.4222 | 0.4222 |
| 0.7 | 0.73 | 0.4689 | 0.4688 |

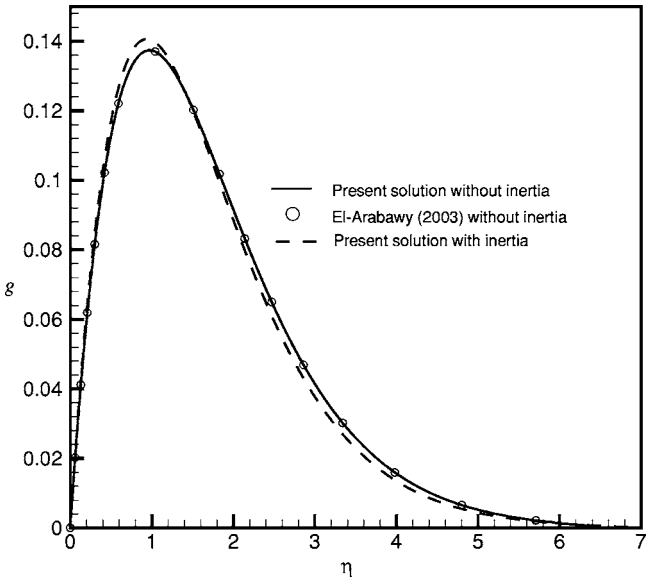


**Fig. 2 Comparison of $g(\eta)$ with El-Arabawy [18]**

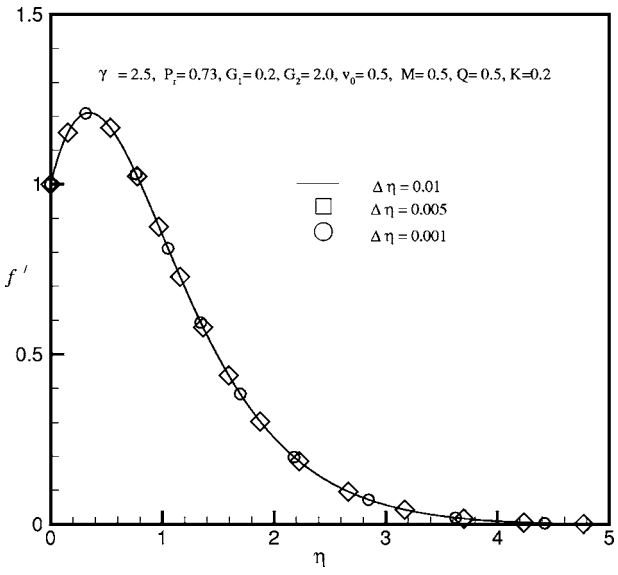


**Fig. 3 Velocity profile for different $\Delta\eta$**

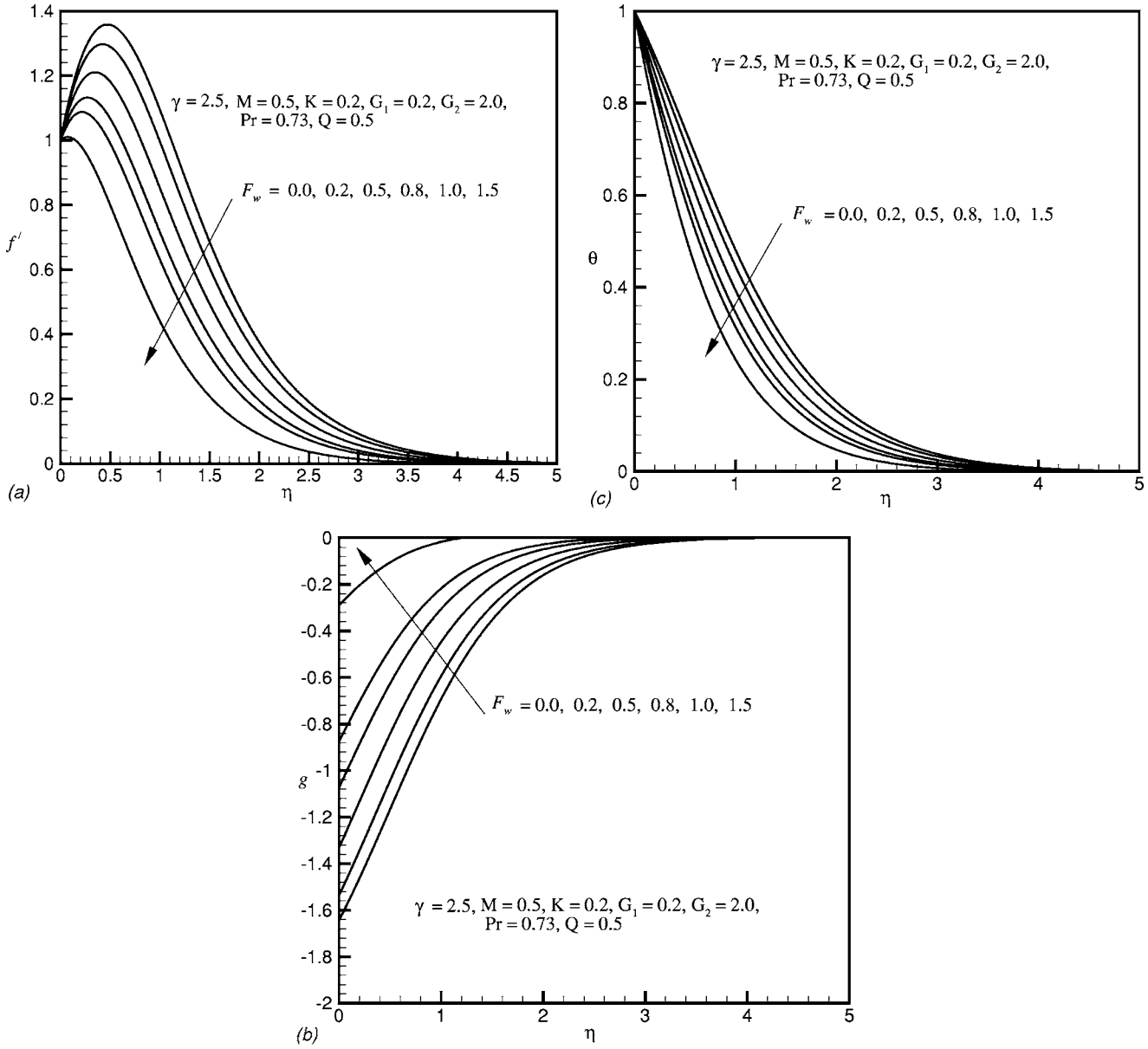


**Fig. 4 (*a*) Velocity, (*b*) microrotation, and (*c*) temperature profiles for different values of $F_w$**

$Q_0$ is the heat generation/absorption constant, $g_0$ is the acceleration due to gravity, $\beta$ is the volumetric coefficient of thermal expansion.

The boundary conditions appropriate to Eqs. (1)–(4) are

$$u = U_0 \quad v = v_0 \quad \sigma = -n\frac{\partial u}{\partial y} \quad T = T_w \text{ at } y = 0$$

$$u = 0 \quad \sigma = 0 \quad T = T_\infty \text{ as } y \to \infty \tag{5}$$

where $n$ is a constant. When $n=0$, we obtain $\sigma=0$ which represents no-spin condition i.e., the microelements in a concentrated particle flow close to the wall are not able to rotate. The case $n=1/2$ represents vanishing of the antisymmetric part of the stress tensor and represents weak concentration. For this case Ahmadi [24] suggested that in a fine particle suspension the particle spin is equal to the fluid velocity at the wall. The case $n=1$ represents turbulent boundary layer flow.

**2.1 Nondimensionalization.** In order to obtain similarity solution of the problem we introduce the following non-dimensional variables

$$\eta = y\sqrt{\frac{U_0}{2\nu_a x}} \quad \psi = \sqrt{2\nu_a x U_0} f(\eta) \quad \sigma = \sqrt{\frac{U_0^3}{2\nu_a x}} g \quad \theta = \frac{T - T_\infty}{T_w - T_\infty} \tag{6}$$

where $\psi$ is the stream function.

Since $u = \partial\psi/\partial y$ and $v = -\partial\psi/\partial x$, we have from Eq. (6)

$$u = U_0 f' \text{ and } v = -\sqrt{\frac{\nu_a U_0}{2x}}(f - \eta f'). \tag{7}$$

Here prime denotes differentiation with respect to $\eta$.

Now substituting Eqs. (6) and (7) in Eqs. (2)–(4) we obtain

$$f''' + ff'' + Kg' + 2\gamma\theta - 2Mf' = 0 \tag{8}$$

$$G_2 g'' - 2G_1(2g + f'') + f'g + g'f = 0 \tag{9}$$

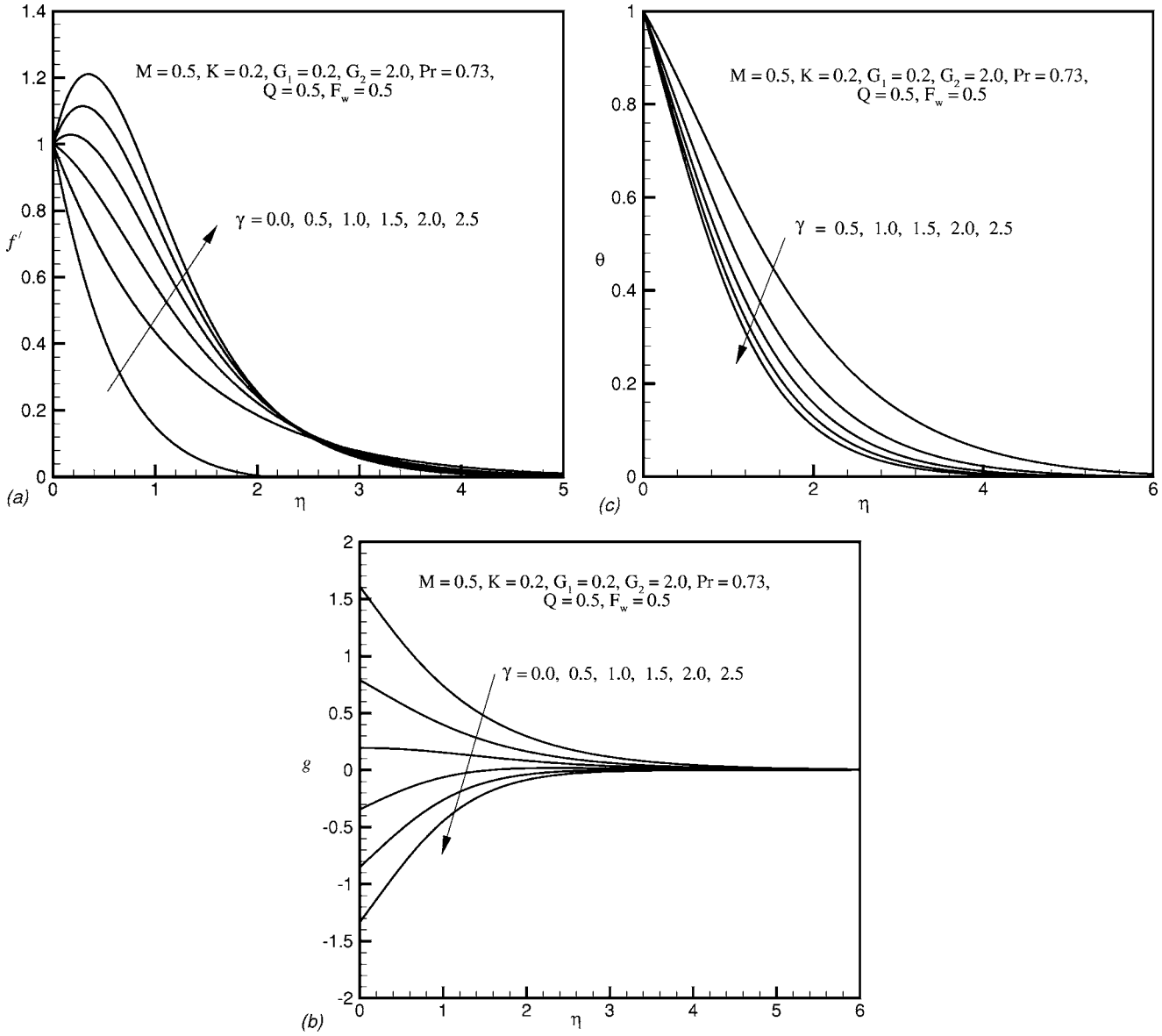


**Fig. 5** (*a*) **Velocity,** (*b*) **microrotation, and** (*c*) **temperature profiles for different values of** $\gamma$

$$\theta'' + \Pr f\theta' + \Pr Q\theta = 0 \tag{10}$$

where $\gamma = \mathrm{Gr}_x/\mathrm{Re}_x^2$ is the Richardson parameter, $\mathrm{Gr}_x = [g_0\beta(T_w - T_\infty)x^3]/\nu_a^2$ is the local Grashof number, $\mathrm{Re}_x = U_0 x/\nu_a$ is the local Reynolds number, $K = S/\rho\nu_a$ is the coupling parameter, $M = \sigma' B_0^2 x/\rho U_0$ is the magnetic field parameter, $G_1 = Sx/\rho j U_0$ is the vortex viscosity parameter, $G_2 = \nu_s/\rho j \nu_a$ is the spin gradient parameter, $\Pr = \mu c_p/\kappa$ is the Prandtl number, $Q = 2Q_0 x/\rho c_p U_0$ is the heat generation/absorption parameter.

The boundary conditions (5) then turn into

$$f = F_w \quad f' = 1 \quad g = -nf'' \quad \theta = 1 \text{ at } \eta = 0$$

$$f' = 0 \quad g = 0 \quad \theta = 0 \text{ as } \eta \to \infty \tag{11}$$

where $F_w = -v_0\sqrt{2x/\nu_a U_0}$ is the suction velocity at the plate for $v_0 > 0$.

The Eqs. (8)–(10) are similar together with the boundary conditions (11). The above-noted systems have been solved numerically for various values of the parameters entering into the problem for different values of $n$.

**2.2 Skin Friction Coefficient and Nusselt Number.** The quantities of chief physical interest are the skin friction coefficient and Nusselt number (rate of heat transfer). The equation defining the wall shear stress is

$$\tau_x = (\mu + S)\left(\frac{\partial u}{\partial y}\right)_{y=0} + S(\sigma)_{y=0} \tag{12}$$

The local skin friction coefficient is defined as

$$C_f = \frac{\tau_x}{\frac{1}{2}\rho U_0^2} = (2\,\mathrm{Re}_x^{-1})^{1/2}[f''(0) + Kg(0)] = (2\,\mathrm{Re}_x^{-1})^{1/2}(1 - nK)f''(0) \tag{13}$$

Thus from Eq. (13) we see that the local values of the skin friction coefficient $C_f$ is proportional to $f''(0)$.

The local heat flux may be written by Fourier's law as

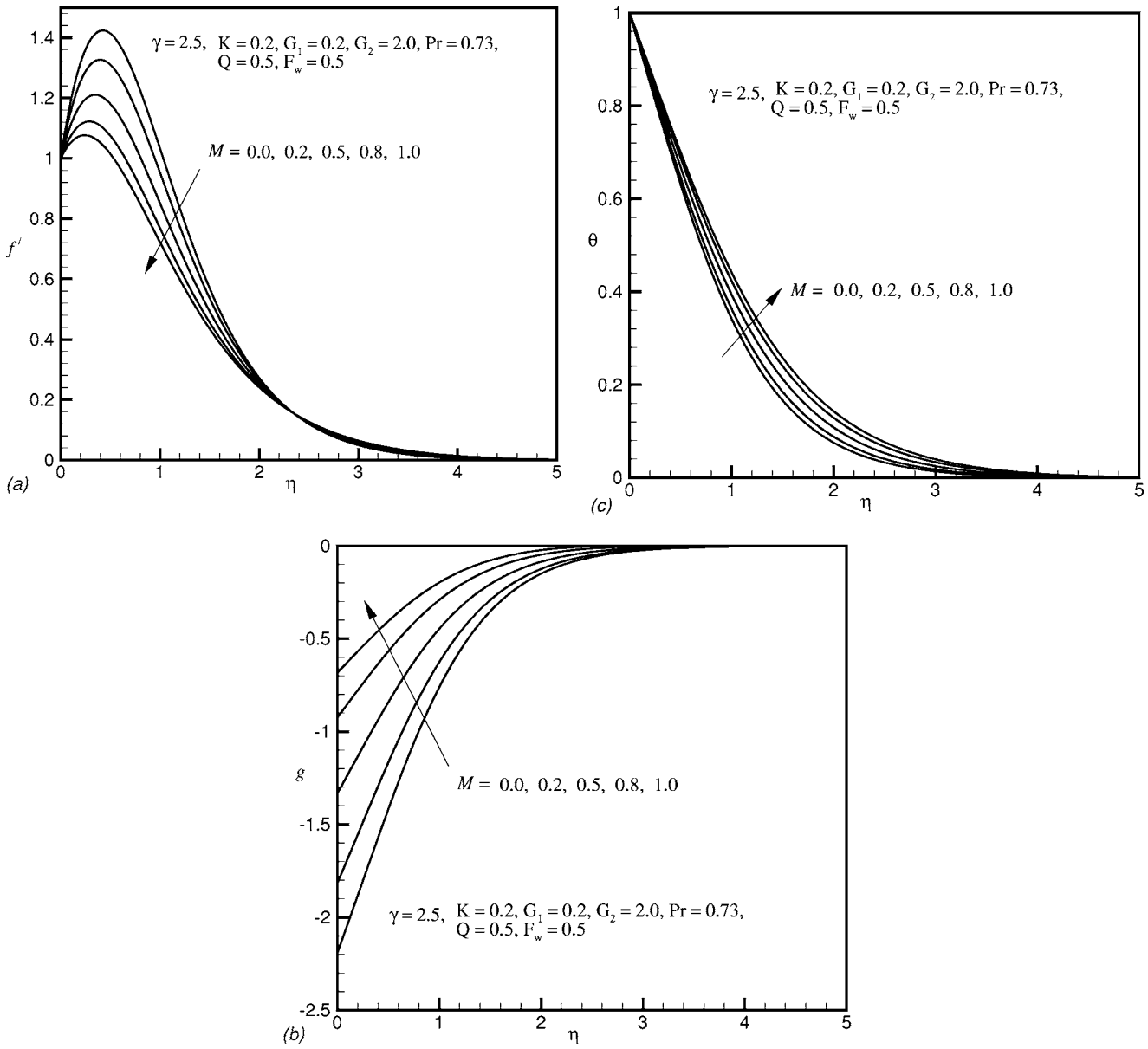


**Fig. 6 (*a*) Velocity, (*b*) microrotation, and (*c*) temperature profiles for different values of *M***

$$q_w(x) = -\kappa\left(\frac{\partial T}{\partial y}\right)_{y=0} = -\kappa(T_w - T_\infty)\left(\frac{\rho U_0}{2\mu x}\right)^{1/2}\theta'(0) \qquad (14)$$

The local heat transfer coefficient is given by $h(x)=q_w(x)/(T_w - T_\infty)$. The local Nusselt number may be written as

$$\mathrm{Nu}_x = \frac{hx}{\kappa} = -(2^{-1}\mathrm{Re}_x)^{1/2}\theta'(0). \qquad (15)$$

Thus from Eq. (15) we see that the local Nusselt number $\mathrm{Nu}_x$ is proportional to $-\theta'(0)$. Hence the numerical values proportional to $C_f$ and $\mathrm{Nu}_x$ are calculated from Eqs. (13) and (15) and are shown graphically in Figs. 11–14.

**2.3 Numerical Solution.** The set of nonlinear ordinary differential Eqs. (8)–(10) with boundary conditions (11) have been solved by using sixth-order Runge-Kutta method along with Nachtsheim-Swigert [25] shooting iteration technique with $\gamma$, $K$, $M$, $G_1$, $G_2$, Pr, $Q$, $F_w$, and $n$ as prescribed parameters. A step size of $\Delta\eta=0.01$ was selected to be satisfactory for a convergence criterion of $10^{-6}$ in all cases. The value of $\eta_\infty$ was found to each iteration loop by the statement $\eta_\infty=\eta_\infty+\Delta\eta$. The maximum value of $\eta_\infty$, to each group of parameters $\gamma$, $K$, $M$, $G_1$, $G_2$, Pr, $Q$, $F_w$, and $n$ is determined when the value of the unknown boundary conditions at $\eta=0$ does not change to successful loop with error less than $10^{-6}$.

To assess the accuracy of our code, we calculated the values of $f''(0)$ and $g'(0)$ which are proportional, respectively, to the local skin friction coefficient and plate couple stress in the boundary layer. Tables 1 and 2 show the comparison of the data produced by the present code and that of El-Arabawy [18]. In fact the results show a close agreement, hence an encouragement for the use of the present code. Figure 2 shows the comparison of the microrotation profile with that of El-Arabawy [18] for $\gamma=0$, $F_w=0$, and $M=0$ applying no-spin condition, $n=0$. Here the solid line represents when the inertia term in the microrotation Eq. (3) has been neglected. The circles represent the solution produced by El-Arabawy [18]. From this figure we see an excellent agreement between them. The dashed line, however, represents the solution when inertia effect has been included.

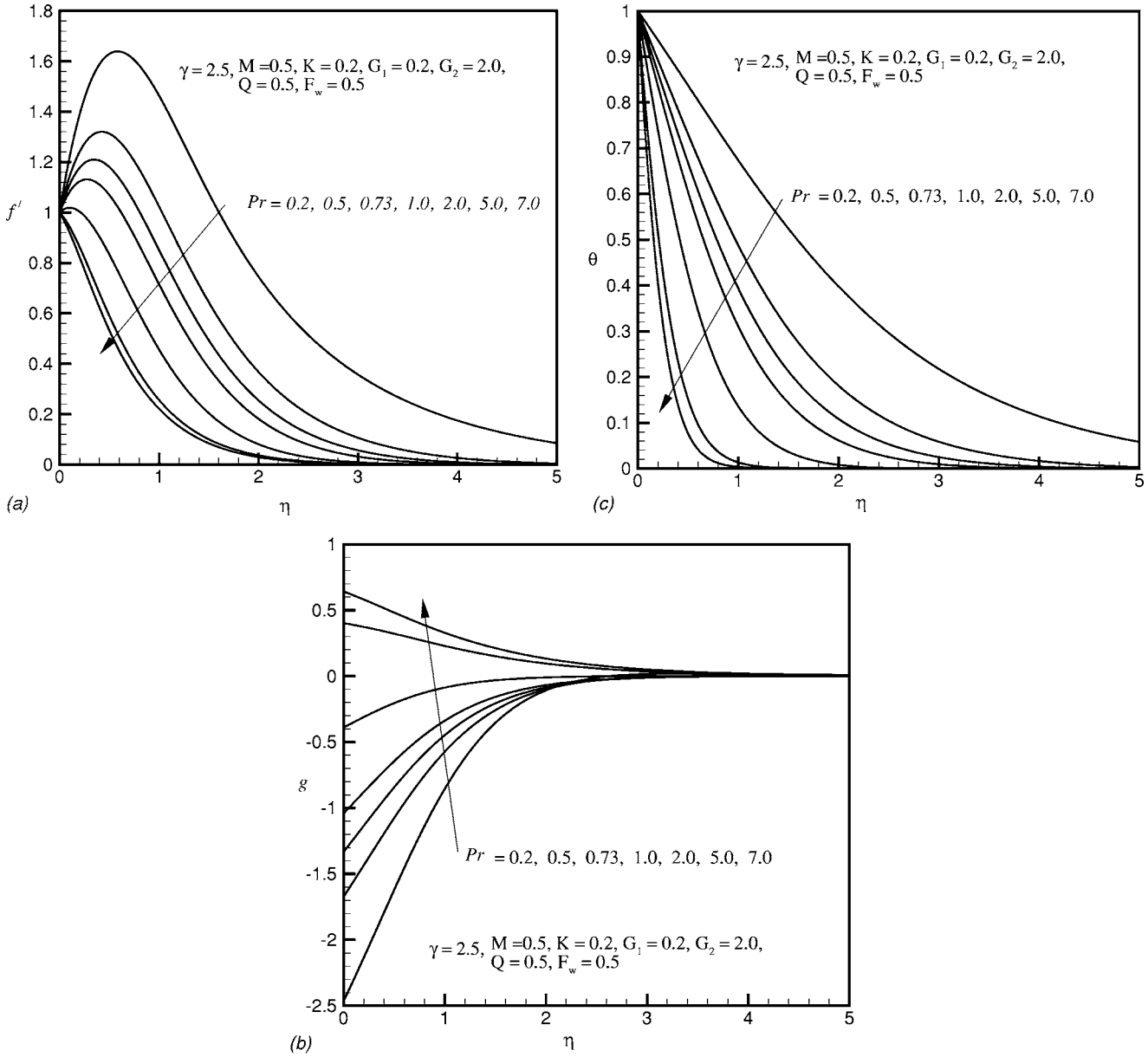


**Fig. 7 (*a*) Velocity, (*b*) microrotation, and (*c*) temperature profiles for different values of Pr**

In order to see the effects of step size ($\Delta\eta$) we ran the code for our model with three different sizes as $\Delta\eta=0.01$, $\Delta\eta=0.005$, $\Delta\eta=0.001$ and in each case we found very good agreement among them. Figure 3 shows velocity profiles for different step sizes.

## 3 Results and Discussion

In this paper, the effect of the internal heat generation/absorption on a steady two-dimensional convective flow of a viscous incompressible micropolar fluid past a vertical porous flat plate has been investigated using Nachtsheim-Swigert shooting iteration technique. Here we discuss the numerical results obtained from Eqs. (8) to (10) using the above-mentioned method. It can be seen that the solutions are affected by the parameters, namely Richardson parameter $\gamma$, coupling parameter $K$, magnetic field parameter $M$, vortex viscosity parameter $G_1$, spin gradient viscosity parameter $G_2$, Prandtl number Pr, heat generation/absorption parameter $Q$, and suction parameter $F_w$. The case $\gamma \gg 1$ corresponds to free convection, $\gamma=1$ corresponds to mixed convection, and $\gamma \ll 1$ corresponds to forced convection. Physically $\gamma<0$ corresponds to an externally heated plate as the free convection currents are considered toward the plate and $\gamma>0$ corresponds to an externally cooled plate while $\gamma=0$ corresponds to the absence of free convection currents. Since we are considering externally cooled plate and the effect of free convection only, positive large values of $\gamma$ are chosen.

Figures 4(*a*)–4(*c*), respectively, show the velocity, microrotation, and temperature profiles for different values of suction parameter $F_w$. It can be seen that the velocity profiles decrease with the increase of suction parameter indicating the usual fact that suction stabilizes the boundary layer growth. The free convection effect is also apparent in this figure. For fixed suction velocity $F_w$, velocity is found to increase and reaches a maximum value in a region close to the leading edge of the plate, then gradually decreases to zero. Figure 4(*b*) shows that microrotation profiles or the angular velocity $g$ remain negative and increase from the value $f''(0)$ to zero as $\eta$ increases from zero to infinity. This figure also indicates that as the suction velocity increases the angular velocity

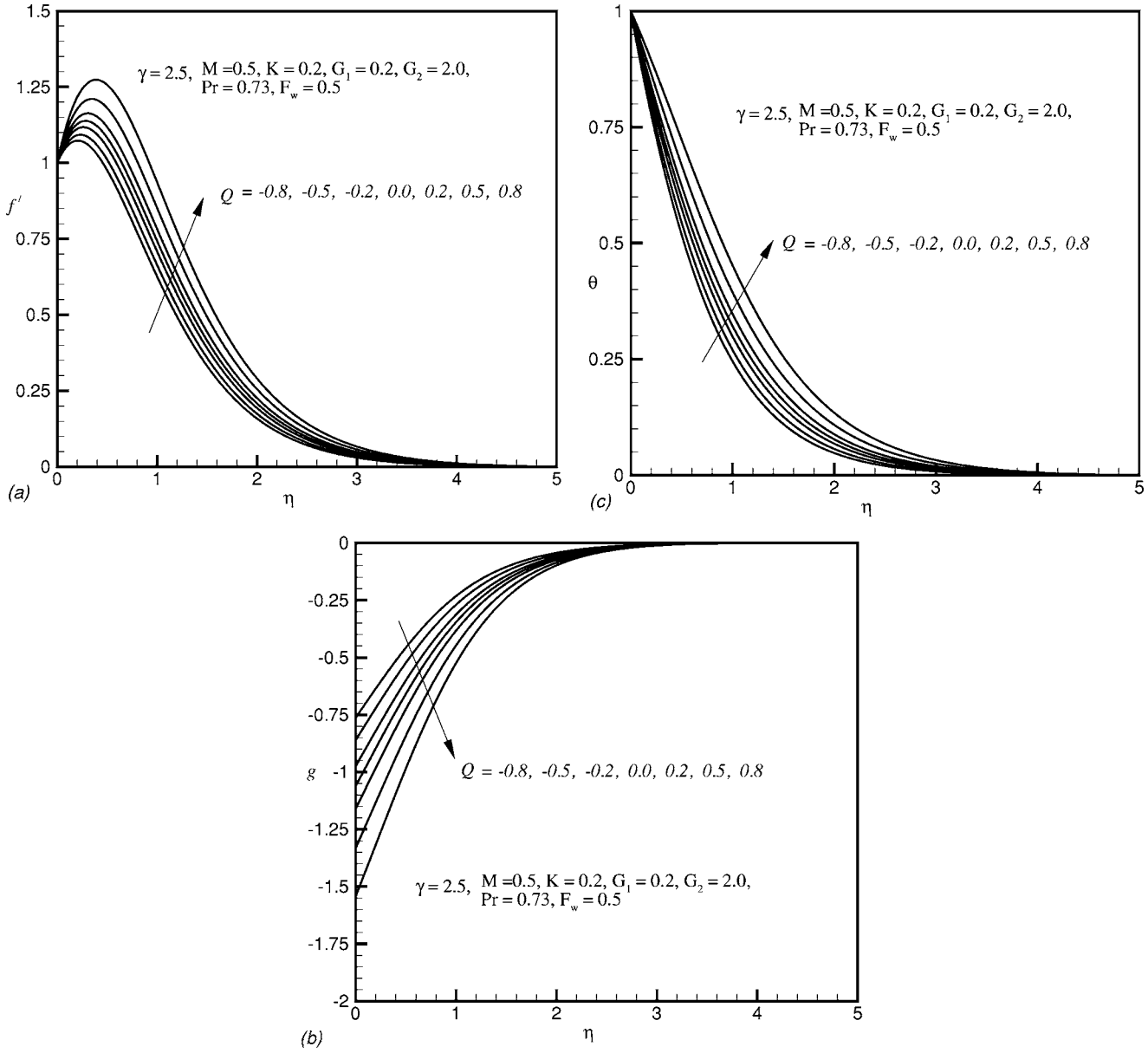


**Fig. 8 (*a*) Velocity, (*b*) microrotation, and (*c*) temperature profiles for different values of *Q***

$g$ has the tendency to become positive. Figure 4($c$), however, shows the usual effects of suction on the temperature profiles.

Figures 5($a$)–5($c$), respectively, show the velocity, microrotation, and temperature profiles for different values of Richardson parameter $\gamma$. Figure 5($a$) shows the free convection as well as the forced convection effects on the velocity profiles. From Fig. 5($b$), it is observed that the angular velocity is positive for purely forced convection as well as for mixed convection ($\gamma \leqslant 1$), whereas for purely free convection ($\gamma > 1$) the angular velocity is negative. Figure 5($c$) shows the decreasing effect on the temperature profiles with the increasing values of $\gamma$.

Figures 6($a$)–6($c$), respectively, show the velocity, microrotation, and temperature profiles for different values of magnetic field parameter $M$. From Fig. 6($a$) we see that velocity profiles decrease with the increase of magnetic effect indicating that magnetic field tends to retard the motion of the fluid. These effects are much stronger near the surface of the plate. From Fig. 6($b$) we see that microrotation profiles remain negative and increase with the increase of magnetic field. Figure 6($c$) shows the effect of $M$ on the temperature profiles. This figure reveals that temperature profiles increase with the increase of $M$. This is due to the fact that the magnetic field tends to retard the velocity filed which in turn induces the temperature field resulting in an increase of the temperature profiles. The magnetic field can therefore be used to control the flow characteristics.

Figure 7($a$) reveals that for small Prandtl number (Pr) values the velocity overshoots the free stream velocity and thus there is a larger growth of the boundary layer. But for larger Pr values (Pr $=5$ or 7) the velocity is found to decrease monotonically and hence there appears a thin boundary layer indicating the decrease of the free convection. From Fig. 7($b$) it is apparent that there are positive spin of the microrotation constituents for larger Pr values in particular for $\mathrm{Pr} > 2$ (not precisely determined) while for $\mathrm{Pr} \leqslant 2$ the spin is negative. The effects of the Prandtl number, seen from Fig. 7($c$), on the thermal boundary layer are similar to those of viscous boundary layer.

Figures 8($a$)–8($c$), respectively, show the velocity, microrotation, and temperature profiles for different values of heat generation/absorption parameter $Q$. From Fig. 8($a$) it is observed that when the heat is generated ($Q > 0$) the buoyancy force in-

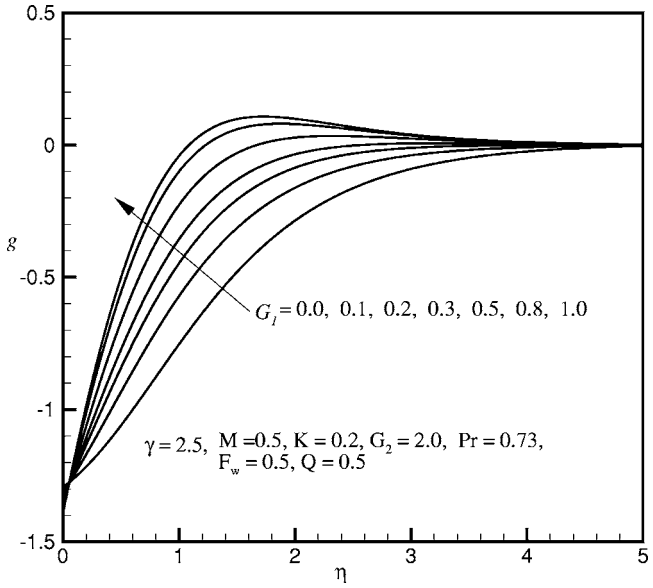


**Fig. 9 Microrotation profile for different $G_1$**

creases which induces the flow rate to increase giving rise to the increase in the velocity profiles. Again when the heat absorption ($Q<0$) intensifies the velocity is found to decrease due to the decrease in the buoyancy force. Figure 8(*b*) shows the effects of heat generation/absorption on the microrotation. The microrotation is found to decrease as we go from strong absorption to strong generation of heat. Owing to the presence of heat generation it is apparent that there is an increase in the thermal state of the fluid. Hence from Fig. 8(*c*) we observe that temperature increases as $Q$ increases for $Q>0$. For heat absorption, opposite phenomenon is revealed.

The above-mentioned calculations have been done for a fixed vortex viscosity parameter. Here we have varied the vortex viscosity parameter $G_1$, keeping all other parameters value fixed. Figure 9 shows the microrotation profiles for different values of $G_1$. From this figure it is understood that as the vortex viscosity increases the rotation of the micropolar constituents gets induced in most of the boundary layer except very close to the wall where kinematic viscosity dominates the flow.

All the above-noted calculations have been carried out for a fixed value of $n=1$. Therefore the effects of $n$ on velocity, microrotation, and temperature are not clear from the earlier discussion. Figure 10 shows the microrotation profiles for different values of $n$. The case $n=0$ corresponds to the boundary condition $g(0)=0$ indicating the no-spin condition. From this figure we see that for $n=0$ the solution remains positive (see El-Arabawy [18]) and increases from zero to zero as $\eta$ increases from zero to infinity. The case $n=\frac{1}{2}$ corresponds to zero antisymmetric part of the stress tensor. For this case $g$ increases from $-\frac{1}{2}f''(0)$ to zero as $\eta$ increases from zero to infinity. From here we further notice three different characteristics of $g$. For $n=0$ all solutions are positive, for $n\geqslant 0.2$ the solutions remain negative and for $0<n\leqslant 0.2$, microrotation $g$increases from $-nf''(0)$ and decreases to zero remaining positive. In general $n$ has a decreasing effect on $g$. No effects of $n$ on velocity and temperature profiles are observed.

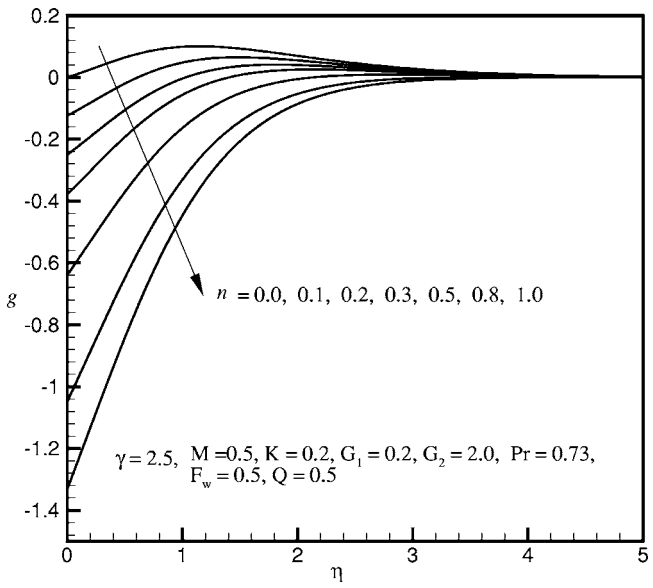


**Fig. 10 Same as Fig. 9 for different $n$**

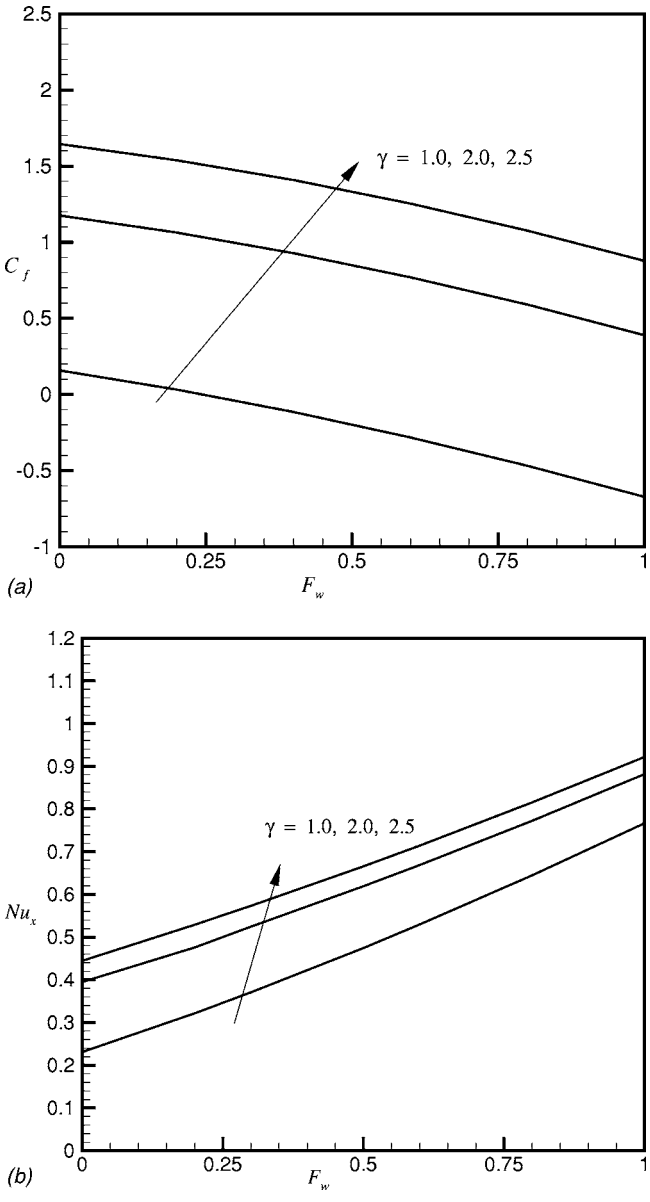


**Fig. 11 (*a*) Local skin friction and (*b*) Nusselt number for different values of $F_w$ and $\gamma$**

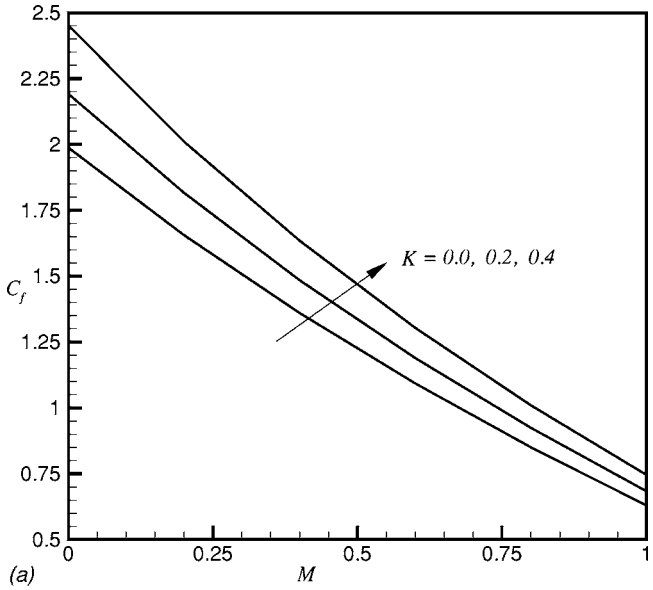


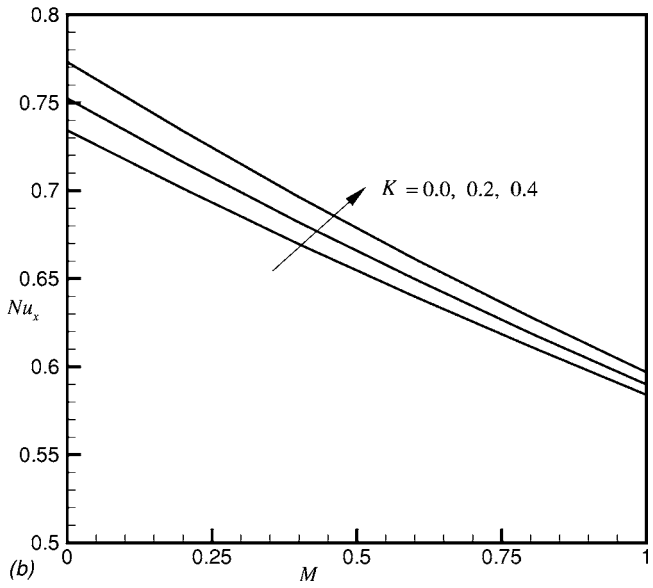


**Fig. 12 (*a*) Local skin friction and (*b*) Nusselt number for different values of *M* and *K***

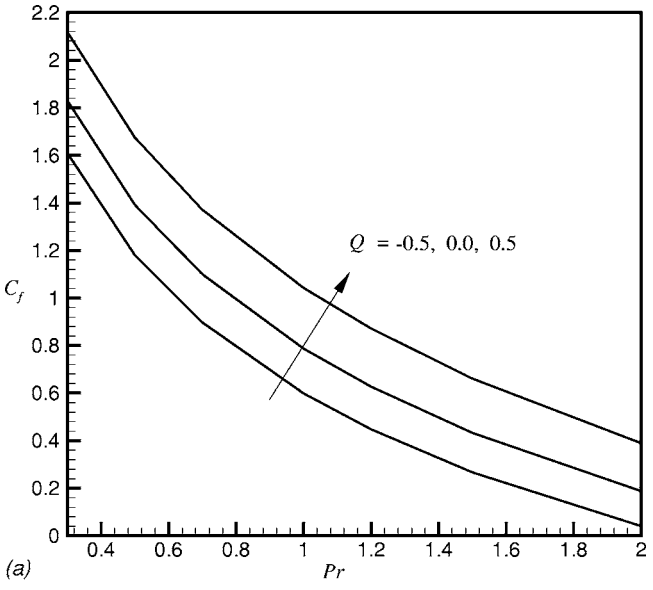


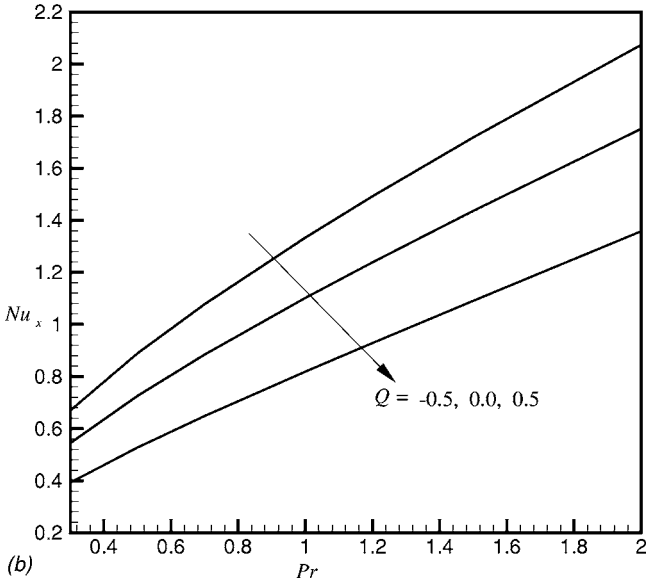


**Fig. 13 (*a*) Local skin friction and (*b*) Nusselt number for different values of Pr and *Q***

We now discuss the effects of various parameters on local skin friction coefficient $C_f$ and rate of the heat transfer $Nu_x$. Figure 11(*a*) shows the local skin friction coefficient for different values of $F_w$ and $\gamma$ keeping all other parameters fixed. From this figure we see that for fixed $\gamma$, $C_f$ decreases as $F_w$ increases. The suction stabilizes the boundary layer and hence reduces the shear stress at the plate. On the other hand for a suction velocity the increase in the buoyancy force leads to the increase in the drag coefficient $C_f$.

Figure 11(*b*) shows the local Nusselt number $Nu_x$ for different values of $F_w$ and $\gamma$. From this figure we see that $Nu_x$ increases as $F_w$ as well as $\gamma$ increase. For increasing $\gamma$, buoyancy forces increase, consequently the rate of the heat transfer increases in the boundary layer.

From Figs. 12(*a*) and 12(*b*) it is observed that as the magnetic field intensifies the shear stress coefficient as well as the heat transfer coefficient reduce considerably for a fixed $K$ value.

The effect of Prandtl number Pr on the skin friction coefficient is shown in Fig. 13(*a*) for different values of $Q$. In the absence of heat generation/absorption ($Q=0$) we see that $C_f$ decreases as Pr increases. In the case of heat generation ($Q>0$) $C_f$ increases and for heat absorption ($Q<0$) $C_f$ decreases.

The effect of internal heat generation/absorption on the rate of heat transfer from the plate for different values of Prandtl number Pr is illustrated in Fig. 13(*b*). From here we see that for fixed Pr the rate of heat transfer from the heated surface decreases with the increases of the heat generation parameter. This is expected, since the heat generation mechanism will increase the fluid temperature near the surface. On the other hand, the presence of heat absorption ($Q<0$) creates a layer of cold fluid adjacent to the heated surface and therefore the heat transfer rate from the surface increases. From this figure it is also clear that rate of heat transfer increases with the increase of Prandtl number.

Figure 14(*a*) deals with the variation of skin friction coefficient for different values of vortex viscosity parameter $G_1$ and $n$. This figure revels that for fixed $G_1$, $C_f$ increases with the increase of $n$. This effect is strong for higher values of $G_1$. For $n=0$, increase in $C_f$ is almost uniform. But for the higher values of $n$ increase in $C_f$ is quite rapid. Figure 14(*b*), however, reveals that the vortex vis-

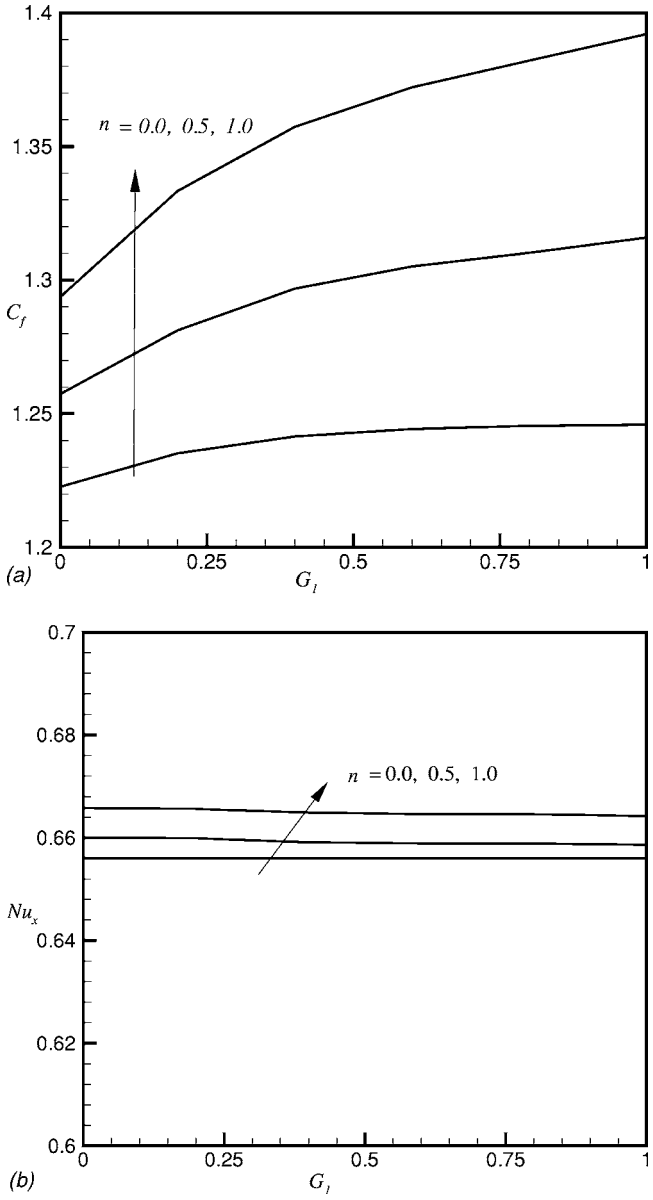


**Fig. 14 (*a*) Local skin friction and (*b*) Nusselt number for different values of $G_1$ and $n$**

cosity parameter $G_1$ has almost no effect on the rate of heat transfer while $n$ has increasing effect on the rate of heat transfer.

## 4 Conclusions

A MHD free convection flow of a micropolar fluid past a continuously moving and uniformly heated vertical porous flat plate has been studied numerically. Using usual similarity transformations the governing equations have been transformed into nonlinear ordinary differential equations and were solved for similar solutions by using the Nachtsheim-Swigert shooting iteration technique. The effects of the various parameters such as suction parameter $F_w$, Richardson parameter $\gamma$, coupling parameter $K$, magnetic field parameter $M$, vortex viscosity parameter $G_1$, spin gradient viscosity parameter $G_2$, Prandtl number Pr, and heat generation/absorption parameter $Q$ on the velocity, microrotation, and temperature profiles are examined. From the present calculations we may conclude that skin friction coefficient decreases monotonically with the increase of suction parameter $F_w$, magnetic field parameter $M$, and the Prandtl number Pr. This coefficient increases with the increase of Richardson parameter $\gamma$, coupling parameter $K$, heat source parameter $Q$, vortex viscosity parameter $G_1$ and $n$.

The heat transfer rate increases monotonically with the increase of suction parameter $F_w$, Richardson parameter $\gamma$, coupling parameter $K$, and the Prandtl number Pr. This rate of heat transfer is forced to decrease with the increase of magnetic field parameter $M$. In case of heat generation, the thermal state of the fluid increases, consequently the heat transfer rate decreases. For this case, the increase of the buoyancy force leads to the increase of the flow rate in the boundary layer. This also leads to the thickening of the velocity boundary layer and the thermal boundary layer. The opposite phenomenon occurs for the heat absorption case.

## Nomenclature

$\mathbf{B}$ = applied magnetic field
$B_0$ = uniform magnetic field
$C_f$ = skin-friction coefficient
$c_p$ = specific heat
$F_w$ = suction parameter
$f$ = dimensionless stream function
$G_1$ = vortex viscosity parameter
$G_2$ = spin gradient viscosity parameter
$\mathrm{Gr}_x$ = local Grashof number
$g$ = dimensionless microrotation
$g_0$ = acceleration due to gravity
$h(x)$ = local heat transfer coefficient
$j$ = micro-inertia density
$K$ = coupling parameter
$M$ = magnetic field parameter
$\mathrm{Nu}_x$ = Nusselt number
$n$ = constant
Pr = Prandtl number
$Q$ = heat source parameter
$Q_0$ = heat generation/absorption constant
$q_w(x)$ = heat flux
$\mathrm{Re}_x$ = local Reynolds number
$S$ = microrotation coupling coefficient
$T$ = temperature within the boundary layer
$T_w$ = temperature at the plate
$T_\infty$ = temperature of the ambient fluid
$u$ = velocity along $x$ axis
$U_0$ = velocity of the moving plate
$v$ = velocity along $y$ axis
$v_0$ = suction velocity
$x$ = coordinate along the plate
$y$ = coordinate normal to the plate

**Greek**

$\beta$ = coefficient of volume expansion
$\gamma$ = Richardson parameter
$\rho$ = density of the fluid
$\mu$ = coefficient of dynamic viscosity
$\nu$ = kinematic viscosity
$\nu_a$ = apparent kinematic viscosity
$\nu_s$ = spin-gradient viscosity
$\sigma$ = microrotation component
$\sigma'$ = magnetic permeability
$\kappa$ = thermal conductivity
$\psi$ = stream function
$\eta$ = similarity parameter
$\tau_x$ = shear stress
$\theta$ = dimensionless temperature
$\Delta\eta$ = step size

## References


[1] Eringen, A. C., 1966, "Theory of Micropolar Fluids," J. Math. Mech., **16**, pp. 1–18.

[2] Eringen, A. C., 1966, "Theory of Thermomicrofluids," J. Math. Anal. Appl., **38**, pp. 480–496.

[3] Jena, S. K., and Mathur, M. N., 1981, "Similarity Solution for Laminar Free Convection Flow of Thermomicropolar Fluid Past a Non-isothermal Vertical Flat Plate," Int. J. Eng. Sci., **19**, pp. 1431–1439.

[4] Gorla, R. S. R., and Takhar, H. S., 1987, "Free Convection Boundary Layer Flow of a Micropolar Fluid Past Slender Bodies," Int. J. Eng. Sci., **25**, pp. 949–962.

[5] Yucel, A., 1989, "Mixed Convection Micropolar Fluid Flow Over Horizontal Plate with Surface Mass Transfer," Int. J. Eng. Sci., **27**, pp. 1593–1608.

[6] Gorla, R. S. R., 1988, "Combined Forced and Free Convection in Micropolar Boundary Layer Flow a Vertical Flat Plate," Int. J. Eng. Sci., **26**, pp. 385–391.

[7] Gorla, R. S. R., 1992, "Mixed Convection in a Micropolar Fluid from a Vertical Surface with Uniform Heat Flux," Int. J. Eng. Sci., **30**, pp. 349–358.

[8] Gorla, R. S. R., Lin, P. P., and Yang, A. J., 1990, "Asymptotic Boundary Layer Solutions for Mixed Convection from a Vertical Surface in a Micropolar Fluid," Int. J. Eng. Sci., **28**, pp. 525–533.

[9] Gorla, R. S. R., and Nakayam, S., 1993, "Combined Convection from a Rotating Cone to Micropolar Fluids," Math. Model. Sci. Compt., **25**, pp. 949–962.

[10] Chiu, C. P., and Chou, H. M., 1993, "Free Convection in Boundary Layer Flow of a Micropolar Fluid along a Vertical Wavy Surface," Acta Mech., **101**, pp. 161–174.

[11] Char, M.-I., and Chang, C.-L., 1995, "Laminar Free Convection Flow of Micropolar Fluids from a Curved Surface," J. Phys. D, **28**, pp. 1324–1331.

[12] Hossain, M. A., and Chaudhury, M. K., 1998, "Mixed Convection Flow of Micropolar Fluid Over an Isothermal Plate with Variable Spin Gradient Viscosity," Acta Mech., **131**, pp. 139–151.

[13] Wang, T.-Y., 1993, "Analysis of Mixed Convection Micropolar Boundary Layer about Two Dimensional or Axisymmetric Bodies," Mingchi Inst. Techn. J., **25**, pp. 25–36.

[14] Rees, D. A. S., and Pop, I., 1998, "Free Convection Boundary Layer Flow of Micropolar Fluid from a Vertical Flat Plate," IMA J. Appl. Math., **61**, pp. 179–197.

[15] Desseaux, A., and Kelson, N. A., 2000, "Flow of a Micropolar Fluid Bounded by a Stretching Sheet," ANZIAM J., **42**(E), pp. C536–C560.

[16] Perdikis, C., and Raptis, A., 1996, "Heat Transfer of a Micropolar Fluid by the Presence of Radiation," Plating, **31**, pp. 381–382.

[17] Raptis, A., 1998, "Flow of a Micropolar Fluid Past a Continuously Moving Plate by the Presence of Radiation," Int. J. Heat Mass Transfer, **41**, pp. 2865–2866.

[18] El-Arabawy, H. A. M., 2003, "Effect of Suction/Injection on the Flow of a Micropolar Fluid Past a Continuously Moving Plate in the Presence of Radiation," Int. J. Heat Mass Transfer, **46**, pp. 1471–1477.

[19] Sattar, M. A., and Rahman, M. M., 2004, "Unsteady Free Convection Flow of a Micropolar Fluid Past a Continuously Moving Porous Plate in the Presence of Radiation," Fluid Dyn. Res. (submitted).

[20] Vajravelu, K., and Hadjinicolaou, A., 1993, "Heat Transfer in Viscous Fluid over a Stretching Sheet with Viscous Dissipation and Internal Heat Generation," Int. Commun. Heat Mass Transfer, **20**, pp. 417–430.

[21] Rahman, M. M., and Sattar, M. A., 1999, "MHD Free Convection and Mass Transfer Flow with Oscillatory Plate Velocity and Constant Heat Source in a Rotating Frame of Reference," Dhaka Uni. J. Sci., **47**(1), pp. 63–73.

[22] Molla, M. M., Hossain, M. A., and Yao, L. S., 2004, "Natural Convection Flow along a Vertical Wavy Surface with Uniform Surface Temperature in Presence of Heat Generation/Absorption," Int. J. Therm. Sci., **43**, pp. 157–163.

[23] Pop, I., and Ingham, D. B., 2001, *Convective Heat Transfer*, Pergamon, New York.

[24] Ahmadi, G., 1976, "Self-Similar Solutions of Incompressible Micropolar Boundary-Layer Flow over a Semi-Infinite Plate," Int. J. Eng. Sci., **14**, pp. 639–646.

[25] Nachtsheim, P. R. and Swigert, P., 1965, "Satisfaction of the Asymptotic Boundary Conditions in Numerical Solution of the System of Nonlinear Equations of the Boundary Layer Type," NASA TND-3004.

# Heat Transfer Around a Cylindrical Protuberance Mounted in a Plane Turbulent Boundary Layer

**Takayuki Tsutsui**

**Masafumi Kawahara**

Department of Mechanical Engineering,
The National Defense Academy,
1-10-20 Hashirimizu, Yokosuka,
Kanagawa 239-8686, Japan
e-mail: tsutsui@nda.ac.jp

*Heat transfer characteristics around a low aspect ratio cylindrical protuberance placed in a turbulent boundary layer were investigated. The diameters of the protuberance, D, were 40 and 80 mm, and the height to diameter aspect ratio H/D ranged from 0.125 to 1.0. The Reynolds numbers based on D ranged from* $1.1\times10^4$ *to* $1.1\times10^5$ *and the thickness of the turbulent boundary layer at the protuberance location, δ, ranged from 26 to 120 mm for these experiments. In this paper we detail the effects of the boundary layer thickness and the protuberance aspect ratio on heat transfer. The results revealed that the overall heat transfer for the cylindrical protuberance reaches a maximum value when* $H/\delta=0.24$. [DOI: 10.1115/1.2136920]

## 1 Introduction

Stacks, piles, cooling towers, and numerous other engineering applications employ cylindrical structures. The fluid flow [1–6] and heat transfer [7–9] characteristics of cylindrical structures have been thoroughly investigated. Specifically, these studies describe the fluid force acting on a cylinder [1,2], the wake structure [2,4], the vortex shedding [3,5], the flow characteristics of the free end [1,6], and the effect of the horseshoe vortex on the heat transfer around a cylinder [8,9]. Most of these studies, though, have concentrated on slender cylinders with aspect ratios $H/D$ (height/diameter) of 1 to 8 [1] or 6 to 17 [4]. However, cylindrical structures with low aspect ratios ($H/D\leqslant1$), such as oil storage tanks and electrical equipment, are also employed in engineering. It is well known that the flow pattern changes dramatically between $H/D=2$ and 4 [3,5], while the shedding vortices change from Kalman type to arch type for low aspect ratio cylindrical structures. When the aspect ratio of a cylinder is decreased, the top face (free end or roof) exercises a greater influence on the overall fluid flow and heat transfer characteristics of the cylindrical structure. Unfortunately, only a few studies have examined fluid flow around low aspect ratio cylinders [5,7] and there has been only limited research into how the heat transfer and flow pattern characteristics change for low aspect ratio cylindrical structures ($H/D\leqslant1$). One study [7] presented the heat transfer characteristics for a short cylinder ($H/D=0.35$), but neglected the effects of the aspect ratio and the boundary layer thickness.

The main objective of this paper is to accumulate fundamental heating and cooling design data for low aspect ratio cylindrical structures ($H/D\leqslant1$), which are referred to as cylindrical protuberances in this study. The local and overall heat transfers for the cylindrical protuberances were measured as functions of diameter, aspect ratio, and turbulent boundary layer thickness. The correlations between these physical quantities and the heat transfer were derived and the optimum heat transfer conditions were established.

## 2 Experimental Apparatus and Method

The experimental setup around the cylindrical protuberance is shown in Fig. 1. The diameters $D$ of the cylindrical protuberance were 40 and 80 mm, and the aspect ratios $H/D$ of these models were varied between 0.125 and 1.0. Experiments were performed in a low-speed wind tunnel with a 400 mm high, 300 mm wide, and 800 mm long working section. The free-stream velocity $U_0$ was varied between 4 and 20 m/s, resulting in Reynolds numbers Re in the range of $1.1\times10^4$–$1.1.\times10^5$. In this range, the turbulent intensity was about 0.4%.

The turbulent boundary layer was induced by attaching a 5, 10, or 12 mm diameter trip wire (T.W.) to the plane 700 mm upstream from the cylindrical protuberance. The boundary layer thickness $\delta$ ranged from 26 to 120 mm at the center position of the model. Figure 2 displays the velocity distribution and fluctuating velocity in the turbulent boundary layer on the plate for $dt=12$ mm. The dash-dotted line in Fig. 2($a$) denotes the experimental universal velocity distribution of the turbulent boundary layer on a flat plate at zero pressure gradient [10] and can be expressed as:

$$u = u_*\{5.85\log(u_*z/\nu) + 5.56\} \tag{1}$$

Figure 2($b$) shows the distribution of the root mean square values of the fluctuating velocity in the turbulent boundary layer. The dash-dotted line in Fig. 2($b$) represents the variation in the longitudinal velocity fluctuation $\sqrt{\overline{u'^2}}/Uo$ [9].

Figure 3 displays a constant heat flux model and a constant temperature model. These two models were used for the local and average heat transfer measurements. The constant heat flux model shown in Fig. 3($a$) was fabricated from acrylic resin disks and pipes, which were then covered with thin 0.02 mm thick stainless steel sheets and attached to the top and side faces of the cylinder. The sheets were connected in series electrically as well as wired independently. Figure 3($b$) shows the arrangement of the subheater. 10 and 15 W light bulbs were employed as subheaters and were placed inside the models to make up for the heat loss from the surface of the 40 and 80 mm diameter cylinders, respectively. The 0.1 mm diameter copper-constantan (C-C) thermocouples were attached to the inside of the stainless steel sheets at 4 mm intervals on the top face, and in 4 mm longitudinal intervals along a spiral arrangement with a ten-degree central angle for the side face, as shown in Fig. 3($c$). During the experiments, the models were heated by applying an alternating current to produce a constant heat flux condition. The temperatures on the top and side faces of the model were measured by rotating the model about its axis. The temperature difference between the heated face and the

Contributed by the Heat Transfer Division of ASME for publication in the JOURNAL OF HEAT TRANSFER. Manuscript received January 31, 2005; final manuscript received July 22, 2005. Review conducted by Sumanta Acharya.

  

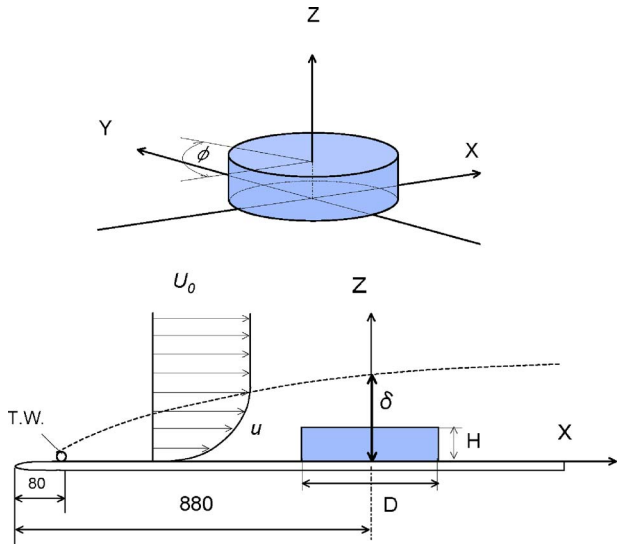


**Fig. 1 Flow geometry and coordinate system**

free stream was maintained at approximately 10°C. The local heat transfer measurements for the constant heat flux condition were verified by comparing the overall heat transfer value with the values measured by the four constant temperature models.

The heat transfer coefficient $h$ was calculated as follows:

$$h = I^2R/\{A(t - t_0)\}, \tag{2}$$

where $I$ is the current, $R$ is the resistance of the stainless steel sheets, $A$ is the active surface area, $t$ is the local temperature on the surface, and $t_0$ is the free-stream temperature. The heat transfer results are then presented in terms of their Nusselt number, a nondimensional parameter, which is defined as

$$\mathrm{Nu} = hD/\lambda. \tag{3}$$

The constant temperature model is shown in Fig. 3(*d*). The diameter of the models was held constant at 40 mm and the heights were 10, 20, 30, and 40 mm. The models were fabricated from copper and a heater was buried in the each model. Eight to twelve C-C thermocouples were attached near the surface. The surface temperature was held constant at approximately 6°C higher than the free-stream temperature, within ±0.05°C. Heat conduction to the base wall was suppressed by laying the subheater at the bottom of a balsa plate, which considerably reduced the uncertainty in the heat condition loss estimation.

The local and mean temperatures on the surface of the cylindrical protuberance were measured with respect to the Re, $H/D$, and $\delta$ parameters. The local and overall heat transfer values were then obtained from the data. Because the effect of the blockage ratio on the heat transfer coefficient is small, the results in this experiment are not corrected for this factor. The surface flow visualization for the plane and cylindrical protuberance were made using an oil-

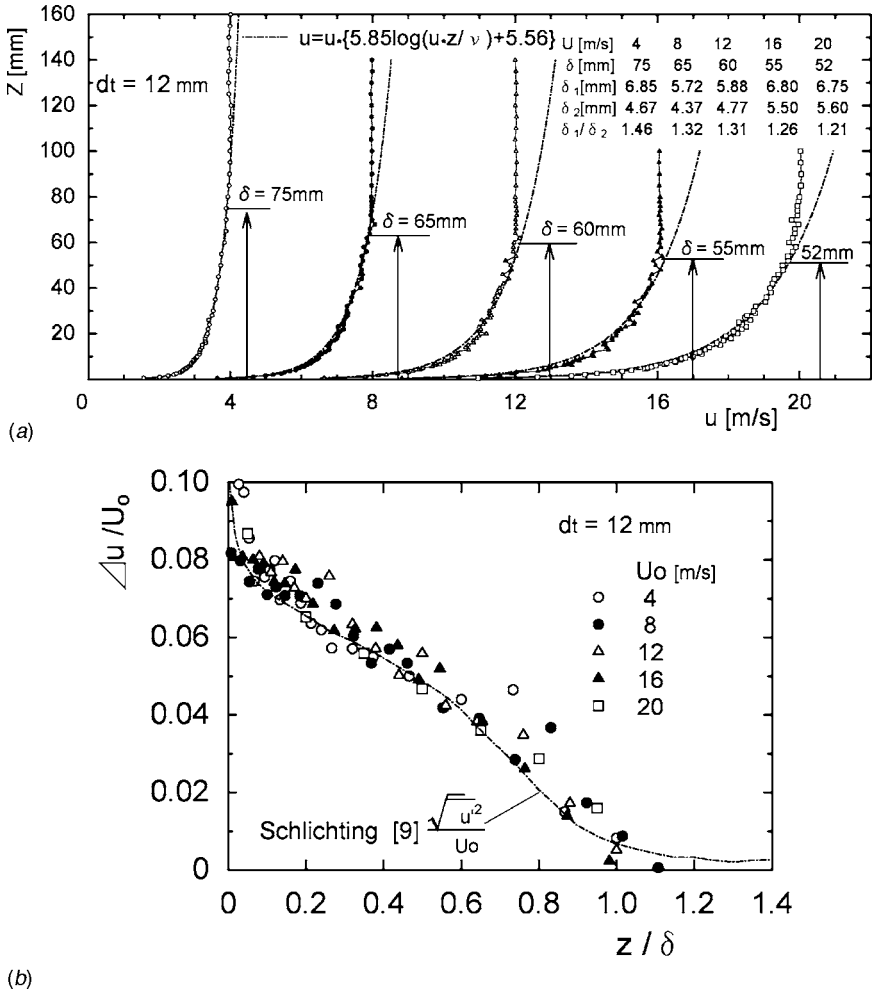


**Fig. 2 Velocity distribution and fluctuating velocity for different free-stream velocities on the plane for *d*t=12 mm: (*a*) velocity distribution and (*b*) fluctuating velocity**

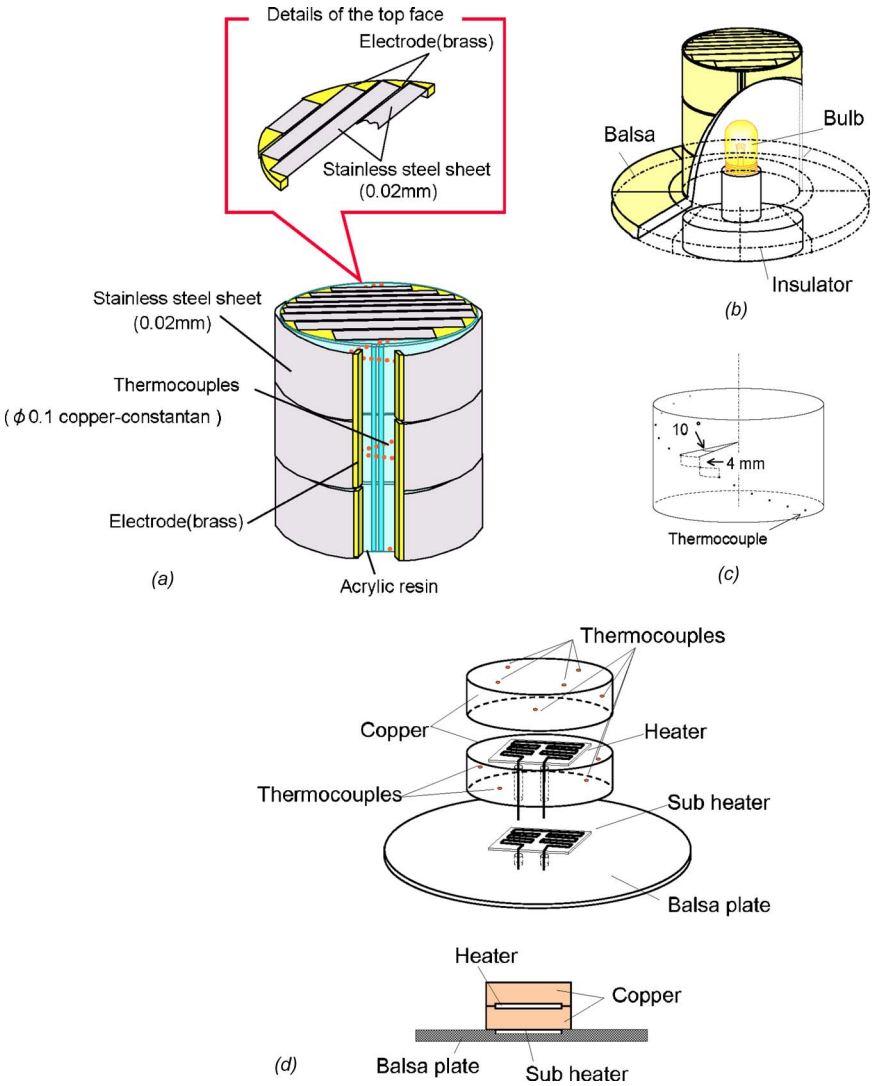


**Fig. 3 Experimental models for the heat transfer measurement: (*a*) constant heat flux model, (*b*) subheater, (*c*) thermocouple arrangement, and (*d*) constant temperature model**

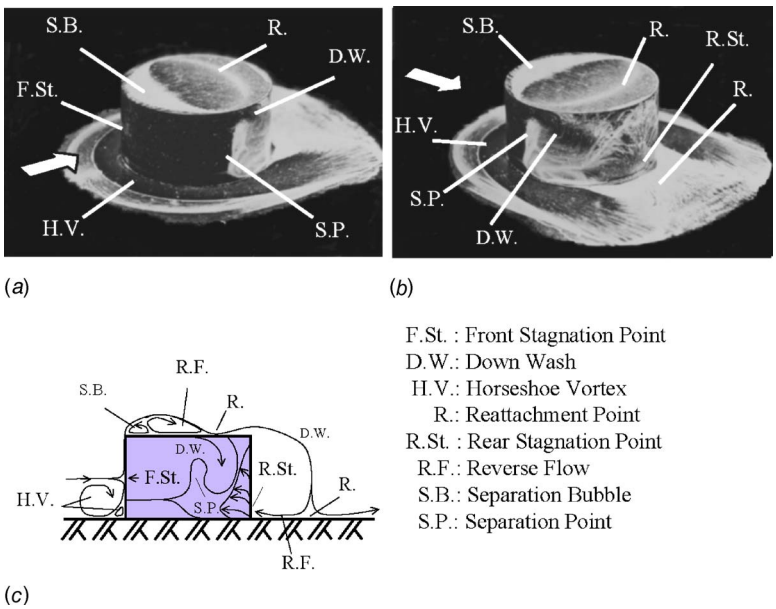


**Fig. 4 Flow around the cylindrical protuberance ($D$=80 mm, $U_o$=20 m/s, Re=1.1×10$^5$, $H/D$=0.5, $\delta$=52 mm): (*a*) front view, (*b*) rear view, and (*c*) flow schematic**

**Table 1 Experimental uncertainty**

| | | $Uo$ [m/s] | $\Delta t/t$ | $\Delta q_{in}/q_{in}$ | $\Delta q_{loss}/q_{loss}$ | $\Delta h/h$ |
|---|---|---|---|---|---|---|
| constant heat flux model (D=40mm) | | 4 | 1.5 | 4.0 | 6.0 | 7.4 |
| | | 20 | 1.5 | 2.5 | 3.2 | 4.3 |
| constant heat flux model (D=80mm) | | 4 | 1.5 | 5.0 | 7.0 | 8.7 |
| | | 20 | 1.5 | 3.0 | 4.0 | 5.2 |
| constant temperature model (D=40mm) | H=10 [mm] | 4 | 1.5 | 2.0 | 3.0 | 3.9 |
| | | 20 | 1.5 | 1.0 | 1.5 | 2.4 |
| | H=20 [mm] | 4 | 1.5 | 2.0 | 3.2 | 4.0 |
| | | 20 | 1.5 | 1.0 | 1.5 | 2.4 |
| | H=30 [mm] | 4 | 1.5 | 2.2 | 3.1 | 4.1 |
| | | 20 | 1.5 | 1.3 | 1.6 | 2.6 |
| | H=40 [mm] | 4 | 1.5 | 2.4 | 3.2 | 4.3 |
| | | 20 | 1.5 | 1.4 | 1.6 | 2.6 |

film method to allow for the observation of the time-averaged flow behavior around the protuberance. The oil film consists of a white oil mixed with oleic acid, titanium oxide, and liquid paraffin. The white oil film was spread on the model surface, and when the air flows around the model, the appearance of the white oil film is altered by the motion of the particles. The changes in their locations yield data about the flow on the model surface.

An uncertainty analysis was then performed on the models. The experimental uncertainties were primarily attributed to the uncertainties in the measured temperature $\Delta t/t$, heat input $\Delta q_{\text{in}}/q_{\text{in}}$, and heat loss $\Delta q_{\text{loss}}/q_{\text{loss}}$. Kline [11] estimated the total uncertainty for the heat transfer coefficient $\Delta h/h$ using the following equation

$$\frac{\Delta h}{h} = \sqrt{\left(\frac{\Delta t}{t}\right)^2 + \left(\frac{\Delta q_{\text{in}}}{q_{\text{in}}}\right)^2 + \left(\frac{\Delta q_{\text{loss}}}{q_{\text{loss}}}\right)^2} \tag{4}$$

where $q_{\text{in}}$ is the input heat confined as $I^2R$ and $q_{\text{loss}}$ is the heat loss through the bottom face, electrodes, and thermocouple. Table 1 presents the uncertainty values for the constant heat flux and constant temperature models for the minimum and maximum velocities, 4 and 20 m/s.

## 3 Results and Discussion

**3.1 Flow Visualization.** Figure 4 presents the typical surface flow around a cylindrical protuberance and floor. Figures 4(*a*) and 4(*b*) are surface oil-flow patterns and Fig. 4(*c*) is a flow schematic. The surface of the cylindrical protuberance was covered with a black color to provide the highest possible contrast to the white oil film. On the top face, a steady separation bubble (S.B.), similar to a lunette, is evident just behind the leading edge and an arc-shaped reattachment line (R.) is present behind the center cord. A reverse flow region (R.F.) forms between the lunette and the arc. A downwash (D.W.) exists from the side edge of the top face to the rear face, a reattachment flow spreads from the rear stagnation point (R.St.), and a horseshoe vortex (H.V.) is evident on the floor. The white oil film remained in two points on the front face, which can be attributed to the interaction of the two horseshoe vortices. The large horseshoe vortex rotates clockwise and induces a downward flow. This phenomenon causes the oil film to remain along the circumference of the protuberance on the floor. The small horseshoe vortex rapidly rotates counterclockwise.

Figure 5 displays the surface oil-flow patterns for cylindrical protuberances with various aspect ratios. The reattachment line on the top face moves forward when the aspect ratio $H/D$ is decreased. In addition, the separation bubble gradually shrinks and the reverse flow region moves forward and is reduced. Very little white oil film remains on the top face when $H/D=0.125$. The front stagnation on the front face and the separation line on the side face exhibit two-dimensional characteristics, except for the upper and lower regions when $H/D=1.0$. Decreasing $H/D$ gradually reduces the amount of two-dimensional flow. In general, the lower the aspect ratio, the less white oil film on the surface.

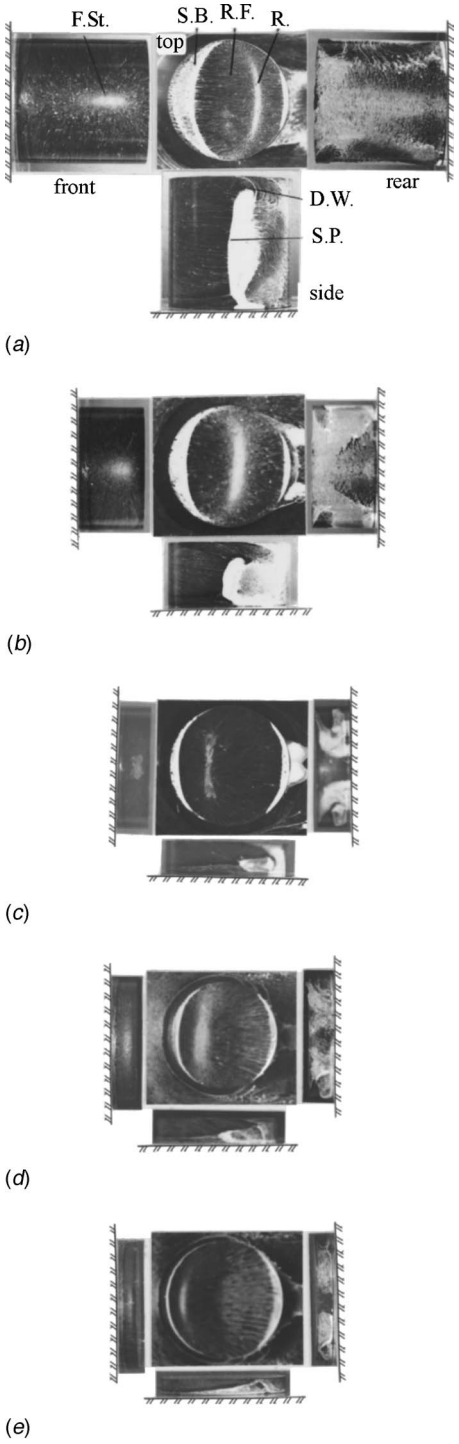


**Fig. 5 Surface oil-flow patterns of the cylindrical protuberance ($D=80$ mm, $U_o=20$ m/s, $\text{Re}=1.1\times10^5$, $\delta=52$ mm): (*a*) $H/D=1.0$, (*b*) $H/D=0.5$, (*c*) $H/D=0.25$, (*d*) $H/D=0.1875$, and (*e*) $H/D=0.125$**

The effects of $H$ are remarkably evident on the top face. Figure 6 shows the correlation between the reattachment point $x_r/\text{D}$ and $H/\delta$, where $x_r$ is the distance between the front edge and reattachment point on the top face. The reattachment points move upstream with decreasing $H/D$ and $H/\delta$.

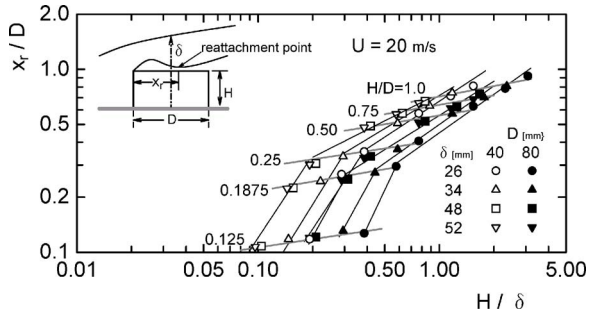


**Fig. 6 Variation in the reattachment point on the top face**

**3.2 Local Heat Transfer.** The local Nusselt number contours on the top and side faces of the cylindrical protuberance are presented in Fig. 7. Five contours on the side face are added in Figs. 7(*b*)–7(*f*). The *z* axes in these figures are magnified to distinguish these contours more easily. Figures 7(*a*)–7(*e*) show the effect of the aspect ratio on the Nusselt number under the same conditions as in Fig. 5. When the aspect ratio is decreased, the high Nusselt number region on the top face moves upstream and the maximum values increase, except for the case of $H/D=0.125$. For example, in Fig. 7(*a*) the highest Nusselt number region is just downstream of the center with a value of over 450. As the aspect ratio is increased, the highest Nusselt number region moves close to the front edge with a value of over 800 in Fig. 7(*d*). When these contours are compared with the oil-film patterns in Fig. 5, the maximum and minimum Nusselt number regions correspond to the reattachment and separation bubble regions, respectively. For the side face, the higher the *z* value, the higher the Nusselt number. The front-upper area of the side face contains the highest Nusselt number, while the downwash and rear-upper areas also exhibit relatively high Nusselt numbers. These values tend to increase with decreasing aspect ratios. The low Nusselt number region appears behind the separation line, which is observable in Fig. 5. Figures 7(*e*) and 7(*f*) show the effect of the boundary layer thickness on the Nusselt number. The position of the high Nusselt

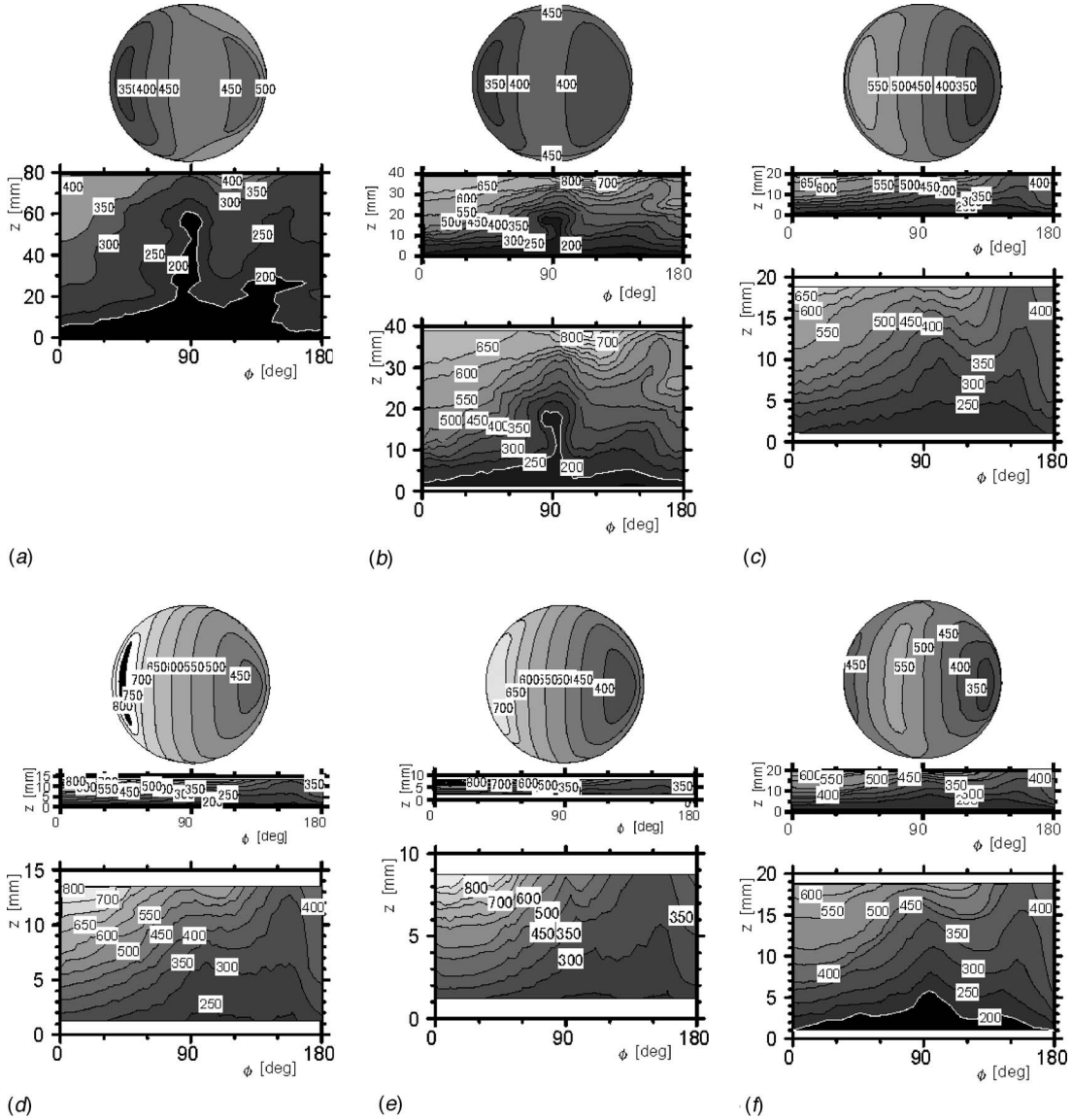


**Fig. 7 Nusselt number contours on the top face and side face ($D=80$ mm, $U_o=20$ m/s, $Re=1.1\times10^5$): (*a*) $H/D=1.0$, $\delta=52$ mm, (*b*) $H/D=0.5$, $\delta=52$ mm, (*c*) $H/D=0.25$, $\delta=52$ mm, (*d*) $H/D=0.1875$, $\delta=52$ mm, (*e*) $H/D=0.125$, $\delta=52$ mm, and (*f*) $H/D=0.25$, $\delta=26$ mm**

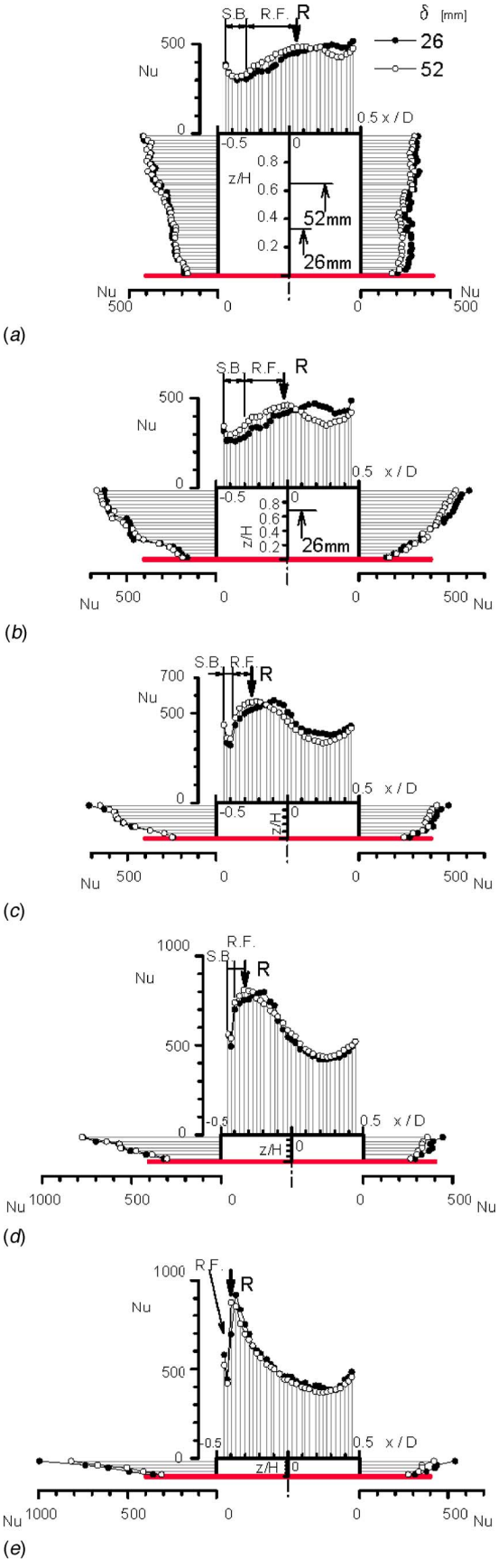


**Fig. 8 Nusselt number on the centerline of the cylindrical protuberance ($D$=80 mm, $U_0$=20 m/s, Re=1.1×10$^5$, $\delta$=52 mm, $y$=0): (*a*) $H/D$=1.0, (*b*) $H/D$=0.5, (*c*) $H/D$=0.25, (*d*) $H/D$=0.1875, and (*e*) $H/D$=0.125**

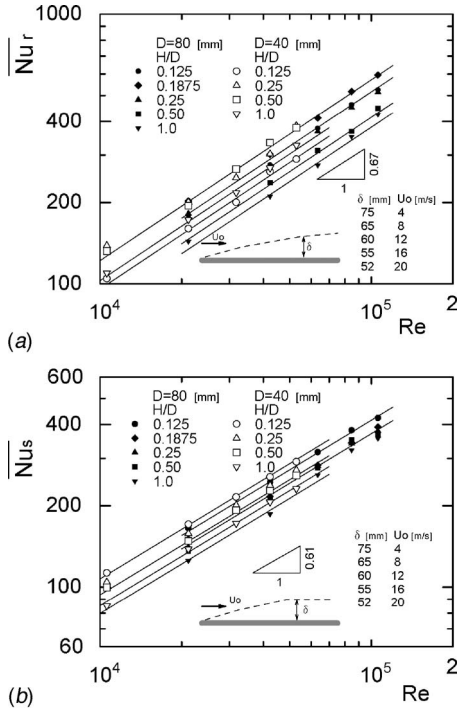


**Fig. 9 The correlation between the average Nusselt number and Re: (*a*) top face and (*b*) side face**

number on the top face and the value of the Nusselt number on the side face in Fig. 7(*e*) are anterior and higher than those in Fig. 7(*f*), respectively.

Figure 8 presents the local Nusselt number distribution along the centerline of the cylindrical protuberance with two different boundary layer thicknesses: 26 and 52 mm. In the figure, the symbols R., R.F., and S.B. denote the reattachment point, the reverse flow region and the separation bubble for $\delta$=52 mm, respectively. Along the top face centerline, the local Nusselt number value reaches a maximum at the reattachment point and its value increases with a decreasing aspect ratio. The minimum Nusselt number value is located in the separation bubble region. The Nusselt number values initially drop and then increase from the reattachment point to the tail edge. Because the thickness of the thermal boundary layer is larger upstream, it vanishes at the tail end. Therefore, the boundary layer thickness affects the position of the maximum and minimum Nusselt number values and the higher the $z/H$ value, the higher Nusselt number along the centerline on the front and rear faces.

**3.3 Average Heat Transfer.** Several dimensionless quantities are now introduced for the discussion of the average Nusselt numbers. The physical quantities that determine the average Nusselt numbers are $Cp$, $D$, $H$, $h$, $U_0$, $u_*$, $\delta$, $\lambda$, $\nu$, and $\rho$. The following dimensionless quantities are obtained by combining these quantities: $u_*/U_0$, $u_*\delta/\nu$, $H/\delta$, $H/D$, Re(=$DU_0/\nu$), Nu(=$hD/\lambda$), and Pr(=$Cp\nu\rho/\lambda$). $Cp$ and Pr are the specific heat and Prandtl number, respectively. The well-known correlation between $u_*/U_0$ and $u_*\delta/\nu$ is

$$\frac{U}{u_*} = 5.85 \log \frac{u_*\delta}{\nu} + 5.56. \tag{5}$$

Furthermore, because $\delta$ depends on $U_0$, a random $\delta$ cannot be set for a given $U_0$. For this reason, $u_*/U_0$ and Re are not independent. In addition, Pr is nearly constant for these experimental conditions. Therefore, the dimensionless quantities can now be reduced to $H/D$, $H/\delta$, Re, and Nu.

Figure 9 presents the average Nusselt numbers for the top and

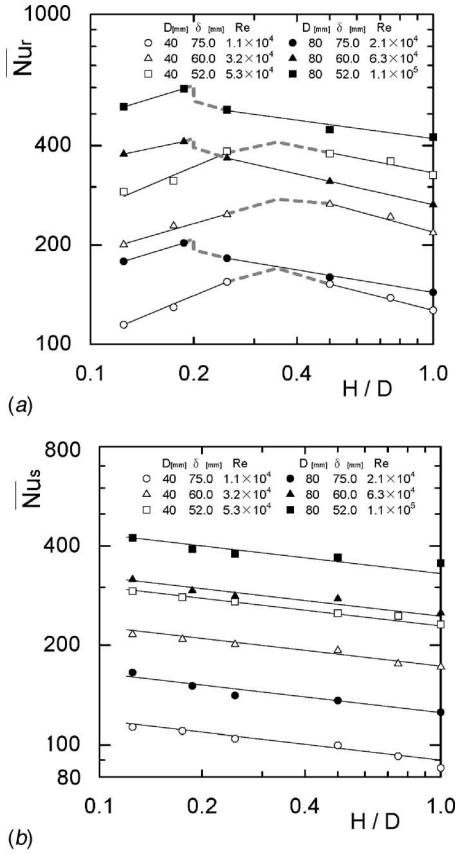


**Fig. 10 The correlation between the average Nusselt number and *H*/*D*: (*a*) top face and (*b*) side face**

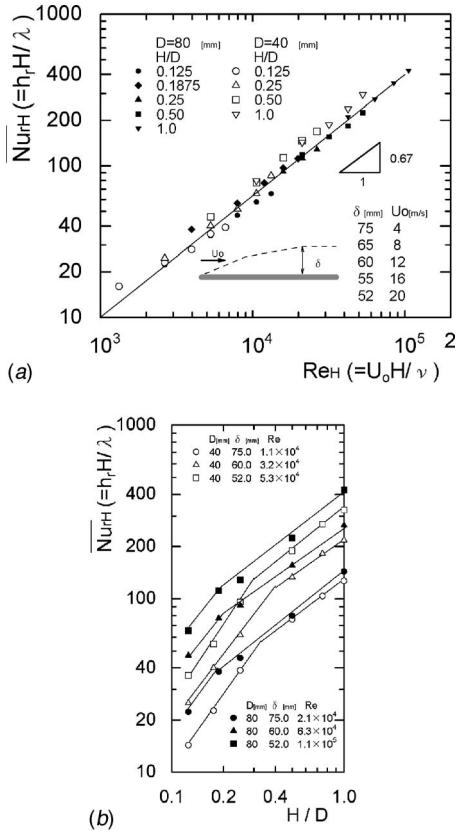


**Fig. 11 $\overline{Nu_{rH}}$ values: (*a*) $Re_H$-$\overline{Nu_{rH}}$ and (*b*) *H*/*D*-$\overline{Nu_{rH}}$**

side faces of the cylindrical protuberance as a function of the Reynolds number. The correlation between the boundary layer thickness $\delta$ and $U_0$ is shown in the figures. Figure 9(*a*) displays the average Nusselt number for the top face $\overline{Nu_r}$. For all cases, the $\overline{Nu_r}$ values increase with a slope of 0.67. $\overline{Nu_r}$ takes on maximum values at $H/D=0.5$ and 0.1875 for the 40 and 80 mm models, respectively. Figure 9(*b*) shows the average Nusselt number for the side face $\overline{Nu_s}$. These $\overline{Nu_s}$ values increase with a slope of 0.61 with respect to the inverse aspect ratio for all cases of the 40 and 80 mm models.

Figure 10 displays the correlation between the average Nusselt numbers on the top and side faces and the aspect ratio $H/D$. Figure 10(*a*) reveals that $\overline{Nu_r}$ assumes a maximum value at a certain aspect ratio. Figure 10(*b*) shows that the $\overline{Nu_s}$ values were found to be inversely proportional to the aspect ratio.

Next, the Reynolds number based on $H$, $Re_H(=U_0H/\nu)$ and the Nusselt number based on $H$, $Nu_H(=hH/\lambda)$ were examined. The results showed that the flow characteristics around the cylindrical protuberance are more strongly influenced by height $H$ than by diameter $D$. Diagrams of $Re_H$-$Nu_{rH}$ and $H/D$-$Nu_{rH}$, which characterize the heat transfer on the top face, are shown in Figs. 11(*a*) and 11(*b*). The slope of the $\overline{Nu_{rH}}$ line is same as that in Fig. 9(*a*) because $Re_H=Re*H/D$ and $\overline{Nu_{rH}}=\overline{Nu_r}*H/D$. The value of $\overline{Nu_{rH}}$ increases with the aspect ratio in Fig. 11(*a*), but $\overline{Nu_r}$ does not increase with the aspect ratio in Fig. 9(*a*). Figure 11(*b*) displays the variation of $\overline{Nu_{rH}}$ with respect to $H/D$. The slopes of $\overline{Nu_{rH}}$ change at certain $H/D$ values and the profiles of $\overline{Nu_{rH}}$ in Fig. 11(*b*) are different from those of $\overline{Nu_r}$ in Fig. 10(*a*) because a change in $H$ is larger than a change in $h_r$. Therefore, Re and $\overline{Nu_r}$ are better suited to characterize the heat transfer around a cylindrical protuberance than $Re_H$ and $\overline{Nu_{rH}}$.

Figure 12 presents the correlation between the average Nusselt number of the top and side faces and $H/\delta$. The Reynolds number exponents 0.67 and 0.61 were obtained from Fig. 9. Figures 12(*a*) and 12(*b*) reveal that $\overline{Nu_r}/Re^{0.67}$ reaches a maximum value at $H/\delta=0.24$ and $\overline{Nu_s}/Re^{0.61}$ increases with decreasing $H/\delta$.

The overall Nusselt number for the cylindrical protuberance is defined as

$$\overline{Nu_m}=\frac{\overline{Nu_r}+4(H/D)\overline{Nu_s}}{1+4(H/D)}. \tag{6}$$

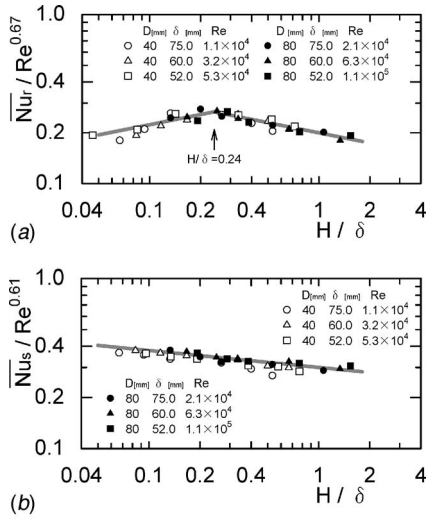


**Fig. 12 The correlation between the average Nusselt number and *H*/$\delta$: (*a*) top face and (*b*) side face**

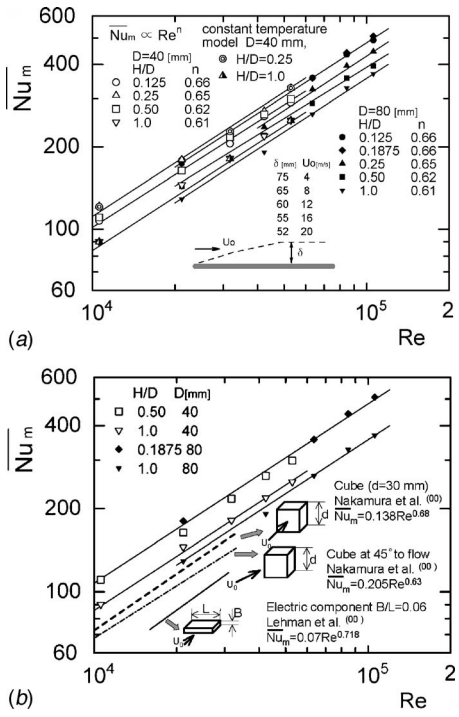


**Fig. 13 Overall Nusselt number: (*a*) variation with *H*/*D* and (*b*) a comparison of the present study with a cube and electrical component**

Figure 13 depicts the correlation between the overall Nusselt number $\overline{\mathrm{Nu}}_m$ and the Reynolds number Re. The exponent of $n$ for the Reynolds number depends on the aspect ratio. Low aspect ratios assume values of $n$ in the vicinity of 0.67, while high aspect ratios assume values for $n$ close to 0.61, as shown in Fig. 13(*a*). The values of $\overline{\mathrm{Nu}}_m$ measured by the constant temperature model agree well with those measured by the constant feat flux model. Figure 13(*b*) provides a comparison between the present study and another geometrical protuberance. The cylindrical protuberance that exhibits optimum $H/D$ conditions has higher $\overline{\mathrm{Nu}}_m$ values than a cube and a flat square electric compartment. The maximum value of $\overline{\mathrm{Nu}}_m$ was found using Fig. 14 to be $H/\delta=0.24$ for aspect ratios in the range of $H/D=0.125$ to 1.0.

The following discussion addresses why $H/\delta$ is the most important factor. Figure 15 is a schematic of the velocity distribution in the boundary layer. Decreasing $H$ and increasing $\delta$ causes the velocity gradient to reach a maximum at $H$, $(du/dz)_{Z=H}$. Hence, the shearing stress $\tau$, $[=\mu(du/dz)]$, and the vorticity $\Gamma$, $[\propto(du/dz)]$, rise. This phenomenon causes the reattachment point on the top face to move forward. When the location of the reattachment point is optimized for increasing heat transfer on the top face, $\overline{\mathrm{Nu}}_r$, $\overline{\mathrm{Nu}}_m$ obtains its maximum value. Therefore, the dimensionless quantity $H/\delta$ is the predominant factor for controlling the heat transfer around a cylindrical protuberance in a turbulent boundary layer.

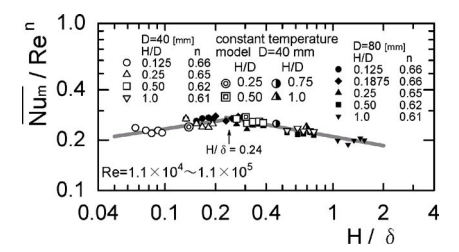


**Fig. 14 The correlation between $\overline{\mathrm{Nu}_m}$/Re and *H*/$\delta$**

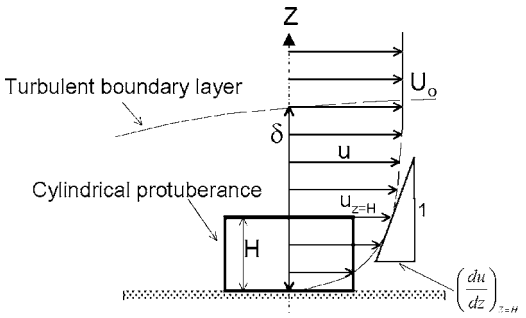


**Fig. 15 Schematic of the velocity distribution in the boundary layer**

## 4 Conclusions

Experimental studies were performed on the local and average heat transfers around a cylindrical protuberance in a turbulent boundary layer. The Reynolds number for these experiments was based on $D$ and ranged from $1.1\times10^4$ to $1.1\times10^5$. The thickness of the turbulent boundary layer at the protuberance, $\delta$, ranged from 26 to 120 mm [12–14].

The experimental results generated the following conclusions. The local Nusselt number on the top face reaches a maximum value at the reattachment point and a minimum value in the separation bubble region. For the side face, the higher $z$, the higher the Nusselt number value. The front-upper area of the side face is the highest Nusselt number region and the downwash and rear-upper areas are other relatively high Nusselt number regions. As a function of the Reynolds number, the average Nusselt number for the top and side faces increase with a slope of 0.67 and 0.61, respectively. The average Nusselt numbers on the top face have a maximum value at $H/\delta=0.24$ within the aspect ratio range of $H/D=0.125$ to 1.0. The average Nusselt number on the side face increases with decreasing $H/\delta$. The overall Nusselt number has a maximum value at $H/\delta=0.24$.

## Nomenclature

$D$ = diameter of the cylindrical protuberance
$d_t$ = diameter of the trip wire
$H$ = height of the cylindrical protuberance
$h$ = local heat transfer
$\overline{h_r}$ = average heat transfer on the top face
$\overline{h_s}$ = average heat transfer on the side face
$\mathrm{Nu}$ = local Nusselt number $=hD/\lambda$
$\overline{\mathrm{Nu}}_r$ = average Nusselt number on the top face $=\overline{h_r}D/\lambda$
$\overline{\mathrm{Nu}}_s$ = average Nusselt number on the side face $=\overline{h_s}D/\lambda$
$\mathrm{Re}$ = Reynolds number $=U_0D/\nu$
$\mathrm{Re}_H$ = Reynolds number $=U_0H/\nu$
$U_0, u$ = free-stream velocity, velocity
$u_*$ = friction velocity $=\sqrt{\tau_0/\rho}=\sqrt{0.0225U_0^2(\nu/U_0\delta)}$
$\Delta u$ = longitudinal velocity fluctuation $=\sqrt{u'^2}$
$X, Y, Z$ = direction
$\delta$ = boundary layer thickness
$\delta_1$ = displacement thickness of boundary layer $=\int_0^\infty(1-u/U_0)dz$
$\delta_2$ = momentum thickness of boundary layer $=\int_0^\infty(1-u/U_0)(u/U_0)dz$

$\lambda, \nu, \rho$ = Thermal conductivity, kinematic viscosity, and density of the fluid
$\tau_0$ = shearing stress at the plane
$\varphi$ = angle

## References


[1] Okamoto, S., and Yagita, M., 1984, "Flow Past Circular Cylinder of Finite Length Placed Normal to Ground Plane in Uniform Shear Flow," Bull. JSME, **27**(229), pp. 1454–1459.

[2] Kawamura, T., Hiwada, M., Hibino, T., Mabuchi, I., and Kumada, X., 1984, "Flow Around a Finite Circular Cylinder on a Flat Plate (Cylinder Height Greater Than Turbulent Boundary Layer Thickness)," Bull. JSME, **27**(232), pp. 2142–2151.

[3] Sakamoto, H., and Arie, M., 1983, "Vortex Shedding From a Rectangular Prism and a Circular Cylinder Placed Vertically in a Turbulent Boundary Layer," J. Fluid Mech., **126**, pp. 147–165.

[4] Park, C. W., and Lee, S. J., 2000, "Free end Effect on the Near Wake Flow Structure Behind a Finite Circular Cylinder," J. Wind. Eng. Ind. Aerodyn., **88**, pp. 231–246.

[5] Okamoto, S., 1991, "Flow Past Circular Cylinder of Finite Length," Trans. Jpn. Soc. Aeronaut. Space Sci., **33-102**, pp. 234–246.

[6] Zdravkovich, M. M., Brand, V. P., Mathew, G., and Weston, A., 1989, "Flow Past Short Circular Cylinders With Two Free Ends," J. Fluid Mech., **203**, pp. 557–575.

[7] Tsutsui, T., Igarash, T., and Nakamura, H., 2000, "Fluid Flow and Heat Transfer Around a Cylindrical Protuberance Mounted on a Flat Plate Boundary Layer," JSME Int. J., Ser. A, **43**(2), pp. 279–287.

[8] Goldstein, R. J., and Karni, J., 1984, "The Effect of a Wall Boundary Layer on Local Mass Transfer From a Cylinder in Cross-Flow," Trans. ASME, Ser. C: J. Heat Transfer **106**, pp. 260–267.

[9] Sparrow, E. M., Stahl, T. J., and Traub, P., 1984, "Heat Transfer Adjacent to the Attached End of a Cylinder in Cross-Flow," Int. J. Heat Mass Transfer, **27-2**, pp. 233–242.

[10] Schlichting, H., 1968, *Boundary Layer Theory*, 6th ed., McGraw-Hill, New York, pp. 534 and 601–602.

[11] Kline, S. J., 1985, "The Purposes of Uncertainty Analysis," ASME Trans. J. Fluids Eng., **107**, pp. 153–160.

[12] Nakamura, H., Igarashi, T., and Tsutsui, T., 2001, "Local Heat Transfer Around a Wall-Mounted Cube in the Turbulent Boundary Layer," Int. J. Heat Mass Transfer, **44**, pp. 3385–3395.

[13] Nakamura, H., Igarashi, T., and Tsutsui, T., 2003, "Local Heat Transfer Around a Wall-Mounted Cube at 45° to Flow in a Turbulent Boundary Layer," Int. J. Heat Fluid Flow, **24**, pp. 807–815.

[14] Lehmann, G. L., and Pembroke, J., 1991, "Forced Convection Air Cooling of Simulated Low Profile Electronic Components: Part 1—Base Case," ASME J. Electron. Packag., **113**, pp. 21–26.

# Functional or Operator Representation of Numerical Heat and Mass Transport Models

**G. Danko**
University of Nevada, Reno,
1664 North Virgina Street, Mailstop 173,
Reno, NV 89557
e-mail: Danko@unr.edu

*A numerical-computational procedure is described to determine a multidimensional functional or an operator for the representation of the computational results of a numerical transport code. The procedure is called numerical transport code functionalization (NTCF). Numerical transport codes represent a family of engineering software to solve, for example, heat conduction problems in solids using ANSYS (a multiphysics software package by ANSYS, Inc.), heat and moisture transport problems in porous media using NUFT (Non-equilibrium, Unsaturated-saturated Flows and Transport—porous-media transport code, developed by John Nitao at the Lawrence Livermore National Laboratory), or laminar or turbulent flow and transport problems using FLUENT (a software package by Fluent, Inc.), a computational fluid dynamic (CFD) model. The NTCF procedure is developed to determine a model for the representation of the code for a variety of time-dependent input functions. Coupled solution of multiphysics problems often require repeated, iterative calculations for the same model domain and with the same code, but with different boundary condition functions. The NTCF technique allows for reducing the number of runs with the original numerical code to the number of runs necessary for NTCF model identification. The NTCF procedure is applied for the solution of coupled heat and moisture transport problems at Yucca Mountain, NV. The NTCF method and the supporting software is a key element of MULTIFLUX (by University of Nevada, Reno), a coupled thermohydrologic-ventilation model and software. Numerical tests as well as applications for Yucca Mountain, NV are presented using both linear and nonlinear NTCF models. The performance of the NTCF method is demonstrated both in accuracy and modeling acceleration.* [DOI: 10.1115/1.2136919]

*Keywords: inverse convolution, system identification, functionalization, input, output, coupled, numerical, transport, heat, moisture, Yucca Mountain*

## Introduction

A general, numerical method is described for phenomenological model identification of boundary-value transport problems. The method is built on the processing of time-dependent boundary value relationships between input and output variables of known analytical or numerical solutions of transport problems. Software codes, available for modeling physical transport problems, can be used to generate numerical outputs for model-building. In transport problems, there exists a causal relationship between input and response variables. Typical examples include the flow of mass, momentum, or energy, generated by boundary-value driving forces.

The purpose of building a phenomenological model between input and response functions is to predict the result of the transport problem in a simple, closed-form, analytical-type expression that is fast to evaluate. The desired form of the model is a linear or nonlinear, multivariable, functional or operator equation or set of equations. Such a model represents a relationship between general, time-variable inputs and outputs, some known and some unknown, considered as boundary values.

A vast literature describes the theory of dynamic system identification and no attempt is made in this paper to provide a review. However, reference to the basic work is in order to recognize the contribution of deFigueiredo, Dwyer, Eykhoff, Kalman, Volterra, Weiner, and Zadek, among many others, in nonlinear system identification [1,2]. Although the tools may be the same, the aim of the work is very different: the main purpose of seeking a numerical transport code functionalization (NTCF) model is to increase computational efficiency for an already given numerical transport model.

The method of identifying the phenomenological model involves a modeling processor that (1) generates a systematic data set, from a numerical transport code (NTC), and (2) identifies a functional or matrix operator equation (or set of equations) from the results. Within its range of applicability, the NTCF model allows one to work directly with matrix equation(s), instead of running the original numerical code, when a boundary variable is changed. Therefore, the NTCF technique may simplify the way a numerical model or software is used, and accelerate the calculations, especially in boundary coupling applications where a large number of iterations is necessary.

The NTCF model is determined numerically, based on a system of solutions of an NTC, by evaluating outputs for a given set of inputs. Figure 1 shows the conceptual logic and data flow charts of the NTCF model identification. The NTCF model is given in an implicit operator equation in Fig. 1, defining a closed-form relationship between general input and output functions. The goal is to find a NTCF model that is much faster to evaluate than the original NTC model. The paper describes the theoretical foundations of the NTCF method, the applicable software functions, analytical and numerical tests, and practical applications.

Contributed by the Heat Transfer Division of ASME for publication in the JOURNAL OF HEAT TRANSFER. Manuscript received December 23, 2004; final manuscript received August 5, 2005. Review conducted by Jay M. Khodadadi. Paper presented at the 2004 ASME Heat Transfer/Fluids Engineering Summer Conference (HTFED2004), July 11, 2004–July 15, 2004, Charlotte, North Carolina, USA.

  

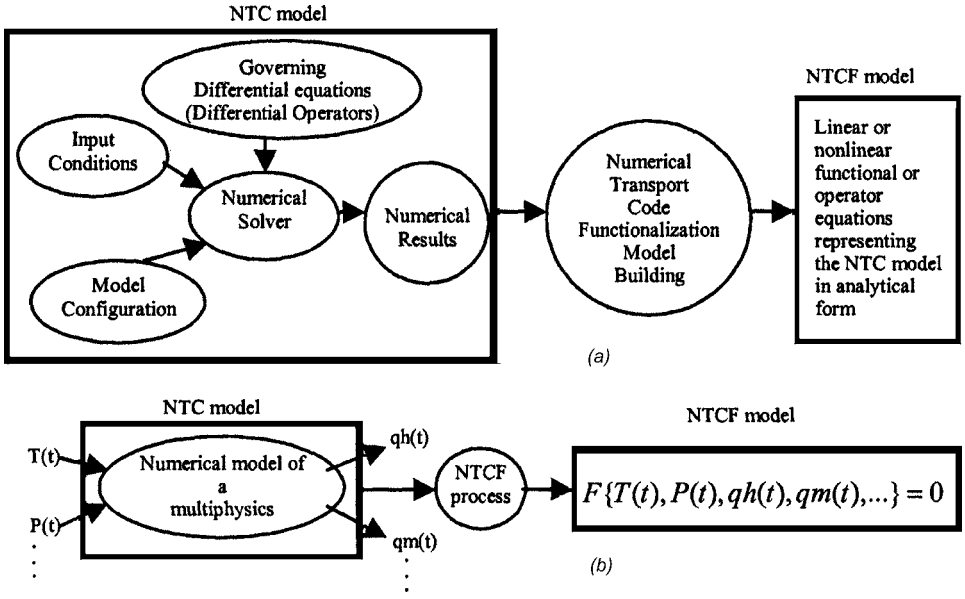


**Fig. 1 (*a*) Logical and (*b*) data flow charts of the NTCF model identification**

## NTCF Model Formulation

**An Intuitive, Linear NTCF Model With Stepwise Boundary Function.** The time-variable relationship between the input (driving force) and output (resulting flux) of a transport model can be expressed in the form of a functional, or a matrix-vector equation. A single-variable, non-steady-state heat transport problem is used as an example to derive the basic matrix-vector equation. According to Duhamel's theorem [3], if $q=A(t)$ is the heat flux density at time $t$ on the surface of a solid in which the initial heat flux is zero while the surface is kept at unit temperature from time zero, then the solution of the problem when the surface is kept at variable temperature $T(t)$ is given by the following functional equation

$$q(t) = \int_{\tau=0}^{t} T(\tau)\frac{\partial}{\partial t}A(t-\tau)d\tau + T(t)A(0) \tag{1}$$

The $A(t)$ function in Eq. (1) is called the indicinal admittance. In order to introduce a boundary variable vector, time divisions $t_1, t_2, \ldots, t_n, \ldots, t_N$ are introduced that eliminate the continuous time-variable. The temporal discretization of $t$ defines an $N$-dimensional space in which $q$ and $T$ vectors of the same dimension can be used and related. In the basic NTCF model, it is assumed that the continuous input variable $T(t)$ is approximated with a stepwise function with $T_i$ constant in each $[t_{i-1}\ t_i]$ interval. Using Eq. (1) for $t=t_i$ the $q_i=q(t_i)$ output component of $q$ can be written for $i=1,\ldots,N$ as follows

$$q(t_1) = T_1 \int_{\tau=0}^{t_1} \frac{\partial}{\partial t_1}A(t_1-\tau)d\tau + T(t_1)A(0)$$

$$\vdots$$

$$q(t_N) = T_1 \int_{\tau=0}^{t_1} \frac{\partial}{\partial t_N}A(t_N-\tau)d\tau + \cdots + T_N \int_{\tau=t_{N-1}}^{t_N} \frac{\partial}{\partial t_N}A(t_N-\tau)d\tau + T(t_N)A(0) \tag{2}$$

The definite integrals in Eq. (2) can be evaluated, first, by substituting a new variable $\lambda=t_i-\tau$, $i=1,\ldots,N$, and, second, by canceling the integration and differentiation in each integral. The results can be written as follows

$$q(t_1) = A(t_1)T_1$$

$$q(t_2) = [A(t_2) - A(t_2-t_1)]T_1 + A(t_2-t_1)T_2$$

$$\vdots$$

$$q(t_N) = [A(t_N) - A(t_N-t_1)]T_1 + [A(t_N-t_1) - A(t_N-t_2)]T_2 + \cdots + A(t_N-t_{N-1})T_N \tag{3}$$

Applying vector-matrix notation in Eq. (3) gives

$$q = [h_{ij}]\cdot T = h\cdot T \tag{4}$$

where

$$h = \begin{bmatrix} A(t_1) & 0 & 0 \\ A(t_2)-A(t_2-t_1) & A(t_2-t_1) & 0 \\ \vdots & & \vdots \\ A(t_N)-A(t_N-t_1) & A(t_N-t_1)-A(t_N-t_2) & \cdots \quad A(t_N-t_{N-1}) \end{bmatrix} \tag{5}$$

The essence of the NTCF technique is that the $h$ matrix of the operator is determined from the numerical transport code being functionalized. The intuitive NTCF modeling method does not require the explicit determination of $A(t)$. Instead, a direct fit to the output data of the NTC is used. The resulting NTCF model will be a quasi-linear fit if the underlying $A$ varies due to nonlinearities. In the simple, one-variable example, $N$ runs are needed with the NTC, each with a different $T$ temperature vector, in order to provide input data for identification of $h$ with a unique solution.

In the intuitive NTCF process, first, a central temperature vector with elements $T_i$, $i=1,\ldots,N$ is selected, and, second, $N$ linearly independent column vectors are formed from $T$ for $N$ runs. This can be accomplished by arranging $T_i$ into a $T$ matrix according to the schematic as follows

$$T = \begin{bmatrix} T_1 & T_1 & T_1 & \cdots & T_1 \\ T_1 & T_2 & T_2 & \cdots & T_2 \\ T_1 & T_2 & T_3 & \cdots & T_3 \\ \vdots & \vdots & \vdots & \ddots & \vdots \\ T_1 & T_2 & T_3 & \cdots & T_N \end{bmatrix} \tag{6}$$

The set of organized, numerical runs with the NTC is comprised of using the $N$ boundary condition histories represented by the $N$ column vectors in the $T$ matrix. The results of the $N$ runs are $N$ response histories $[q_{ij}]$ that can be arranged into a $q$ matrix. Since $q=hT$ is expected according to Eq. (4), $h$ can be expressed as follows

$$h = qT^{-1} \tag{7}$$

Since the input $T$ matrix is specially constructed, the inverse, $T^{-1}$ matrix will be a triple-diagonal matrix, in which the sum of the elements in the first column or in the first row are both 1, whereas the sum in any other row or column is 0. It can be shown by direct calculation that the $h$ matrix in Eq. (7) is identical to the $h$ matrix in Eq. (5) in a linear case. The $h$ matrix will be a lower-triangle matrix, satisfying the expectation that only past and present boundary condition values may affect a present response. Note that each of the $q_{ij}$ heat flux elements is calculated at the end of the corresponding $[t_{i-1}\ t_i]$ time interval.

Another intuitive variation option was made to the basic NTCF procedure to use the average of the $q_{ij}$ response over the $[t_{i-1}\ t_i]$ time period, instead of the value at the end-point time. Good results with the averaging in practical calculations have led to the following question: can stepwise boundary condition variation be used in the NTC in order to represent piecewise-linear or higher-order interpolation in the NTCF model? This question initiated the application of a built-in, piecewise-linear boundary variation in the NTCF model. It will be shown that the $h$ obtained from Eq. (7) based on the averaged $M_i[q_{ij}]$ responses is identical to the solution for a linear system with a piecewise-linear input variation on the boundary, provided that the time division is equidistant. However, if the time division varies, the simple averaging becomes inadequate and a different, variable-interval averaging must be used as discussed later in the paper.

The advantages of the intuitive NTCF model are that it is robust and always yields a linear matrix equation that fits perfectly to all NTC run results, even if the NTC model is strongly nonlinear. The only condition for solvability is that the inverse of the input $T$ matrix must exist. This condition can easily be satisfied since the construction of the $T$ matrix is under the control of the user.

The disadvantage of the intuitive method is that it requires $N$ independent NTC runs, where $N$ increases with the increase in the number of time divisions. The necessary number of time divisions, which is related to the shape of the input boundary function, $T$, will affect the number of NTC runs that would otherwise be dependent only upon model nonlinearity. In this sense, the effect of the nonlinearity of the input function, $T$, and that of the nonlinearity of the NTC model appears to be linked. Such a linkage, however, is not present in an NTCF model that is built using the analytical approach that will be discussed later in the paper. For example, a linear NTCF model will be built using only two NTC runs, irrespective of the number of time divisions, $N$, related to only the size of the task or the shape of the input function $T$.

**An Analytical Approach to NTCF Model Formulation.** The indicinal admittance, $A(t)$, as a unique NTC system response can be used to build an NTCF model. The $A(t)$ function can be determined numerically in a linear case by inverse convolution, decomposing the $q(t_1), q(t_2), \ldots, q(t_n), \ldots, q(t_N)$ responses obtained for a stepwise boundary function. The inverse convolution may be obtained from Eq. (3) for an equidistant time division as follows

$$A(t_1) = q(t_1)/T_1$$

$$A(t_2) = [q(t_2) - A(t_1)(T_2 - T_1)]/T_1$$

$$\vdots \tag{8}$$

Based on Eq. (8), an inverse convolution procedure "iconv" can be realized. A generalization is made regarding the input data: two different inputs, $T_0(t)$ and $T_1(t)$ are used together with corresponding $q_0(t)$ and $q_1(t)$ responses. The procedure is applied to a stepwise input function difference $T_1(t)-T_0(t)$ and NTC output result function difference $q_1(t)-q_0(t)$ sampled at $\tau \in (0, t]$ time instants. The result is the indicinal admittance $A(t)$ as follows

$$A(t) = \text{iconv}[q_1(t) - q_0(t), T_1(t) - T_0(t)] \tag{9}$$

According to Eq. (9), $A$ is determined from the NTC responses to two different input functions. The $T_0(t)$ input can be constant or zero, but it can be any stepwise-linear (stairs) function as well. $A$ is defined as the NTC system response to a differential input. In this regard, $A$ is a generalization of the classic indicinal admittance that is a system response to a single unit step change in the input. The generalization allows for nonlinear applications in which $A$ will be a quasi-linear, interval-averaged response for an input regime defined by $T_0(t)$ and $T_1(t)$. This feature will be used for building higher-order NTCF models with a series of $A_i$ generator functions as discussed later in the paper.

For appropriately selected $T_0(t)$ and $T_1(t)$ functions, and avoiding zero steps and thus divisions by zero in Eq. (8), the inverse convolution procedure will always yield an $A(t)$ function. However, a question may be raised: how can $A$ be determined for a non-equidistant time discretization? The answer is discussed in Appendix A, in which two numerical examples are included to demonstrate the stability of the numerical inverse convolution in strongly nonlinear cases.

**The Basic NTCF Model With Piecewise-Linear Boundary Function.** A complementary form of the convolution integral in Eq. (1) is used to derive the basic equations for the algorithm for a piecewise-linear boundary function. Linear connection between the base points of a boundary function is often desirable over a stepwise approximation. The evaluation of the NTCF matrices for piecewise and higher-order boundary-value variations in the time domain is based on the second form of the Duhamel's integral as follows

$$q(t_n) = \int_0^{t_n} A(t_n - \tau) T'(\tau) d\tau + A(t_n) T(0) \tag{10}$$

Equation (10) may be obtained by partial integration of Eq. (1). Since $T'$ is the slope, $m$, the integral can be directly evaluated in each time interval. After summation and assuming a stationary initial condition $T_0 = T(0) = 0$, the result is

$$q(t_n) = m_1 \int_0^{t_1} A(t_n - \tau) d\tau + m_2 \int_{t_1}^{t_2} A(t_n - \tau) d\tau + \cdots + m_n \int_{t_{n-1}}^{t_n} A(t_n - \tau) d\tau \tag{11}$$

Each integral in Eq. (11) can be expressed with an integral mean value, $M[A]$. The general term, after substituting $\lambda = t_n - \tau$, is

given

$$M[A]_{t_n-t_{i+1}}^{t_n-t_i} = \frac{1}{(t_{i+1}-t_i)} \int_{t_n-t_{i+1}}^{t_n-t_i} A(\lambda)d\lambda \tag{12}$$

According to Eq. (12), the averaging time intervals in the $M[A]$ integral mean values generally do not coincide with the time division intervals, unless the division is equidistant. In a matrix-vector form, a new, modified interval-averaged $h$ matrix is obtained

$$h = \begin{bmatrix} M[A]_0^{t_1} & 0 & 0 \\ M[A]_{t_2-t_1}^{t_2} - M[A]_0^{t_2-t_1} & M[A]_0^{t_2-t_1} & 0 \\ \vdots & & \vdots \\ M[A]_{t_N-t_1}^{t_N} - M[A]_{t_N-t_2}^{t_N-t_1} & M[A]_{t_N-t_2}^{t_N-t_1} - M[A]_{t_N-t_3}^{t_N-t_2} & \cdots \quad M[A]_0^{t_N-t_{N-1}} \end{bmatrix} \tag{13}$$

The $h$ matrix in Eq. (13) is fundamentally different from that in Eq. (5) in that it represents piecewise-linear connections, instead of steps. The first advantage of the result is that the piecewise connection between the $T_1, \ldots, T_N$ boundary values is generally a better approximation than the stepwise variation for a smooth boundary function. This means that a coarser time division and smaller matrix dimension can be used for the same model accuracy. The second advantage is that the NTC input boundary function variation is still stepwise, that is, a discretized input for generating the required output for the application. The convolution integral is often used to generalize a stepwise solution; this technique is built in the NTCF model.

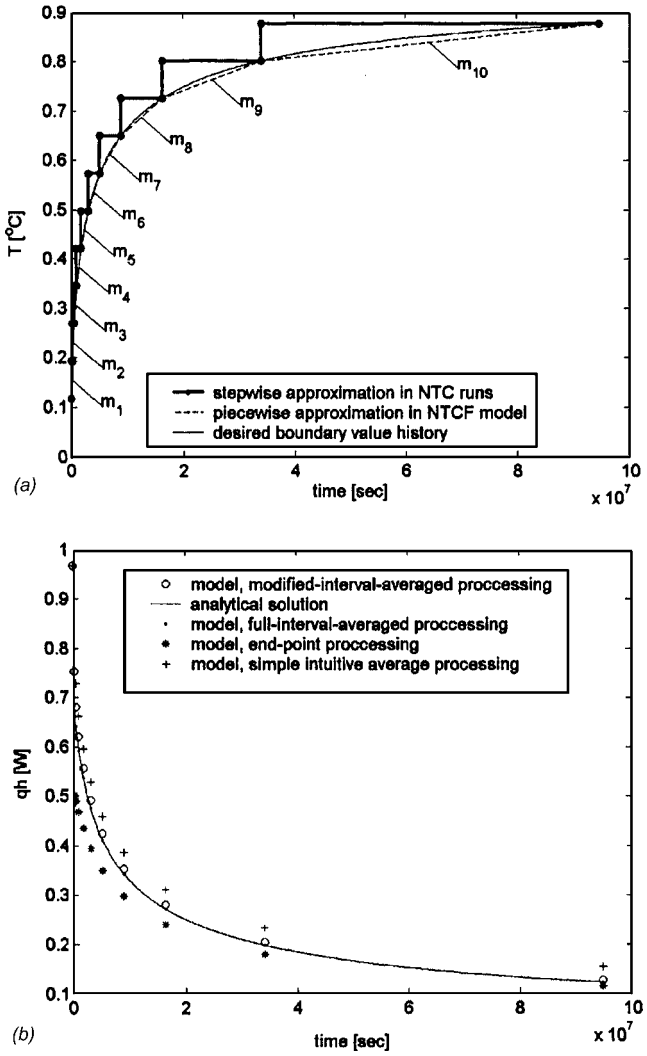


**Fig. 2 (*a*) Stepwise and piecewise input approximations for NTCF algorithm tests. (*b*) Results of three different NTCF post-processing methods.**

In order to evaluate the integral mean values in Eq. (12), the $A(t)$ function has to be numerically determined at fine time subdivisions in each time interval from the NTC run. Since the constant $A(t)$ function is applicable only to a strictly linear case, generalization is needed for nonlinear models. This is accomplished in the basic model using a series of $A_i(t)$ functions and a generalized input variation matrix according to Eqs. (15) and (16), described later in the paper.

Higher-order polynomial connection between base points in the time domain may also be considered. The algorithms may be derived based on quadratic and higher-order boundary function interpolation polynomials as follows

$$T(t) = L_0(T_i, T_{i+1}, \ldots) + L_1(T_i, T_{i+1}, \ldots) \cdot t + L_2(T_i, T_{i+1}, \ldots) \cdot t^2 + \cdots \tag{14}$$

where $L_0, L_1, L_2, \ldots$ are linear functions of $T_i$, $i=1, \ldots, N$. Substituting Eq. (14) into Eq. (10) and performing partial integration, the nonlinear terms will yield interval-dependent constants, and the final result will still be a linear matrix operator in $T$.

In summary, the NTCF method applies a stepwise boundary variation in the NTC runs, and an averaged output evaluation of the responses to represent piecewise-linear, or higher-order polynomial boundary variations in the time domain. The averaging schematics are derived analytically. Numerical integrals are used to approximate the analytical expressions in the NTCF procedure. The results are implemented both in the NTCF runtime organizer to collect responses at fine time subdivisions, and in the post-processor to evaluate the NTCF matrices.

An example is given for comparing stepwise and piecewise approximation results for a simple heat conduction used in the MULTIFLUX and the NTCF tests [4,5]. The input variations and the responses are shown in Figs. 2(*a*) and 2(*b*), respectively. The test example uses an analytical solution, emulating an NTC with a fast-running and precise analytical-based numerical solution for algorithm testing. The model results are shown in Fig. 2(*b*) using three different NTCF postprocessing methods. The modified interval average process according to Eq. (13) is shown to be superior to other representations involving simple averaging and end-point responses.

**Quasi-Linear NTCF Model.** A quasi-linear NTCF model may be determined for nonlinear cases using a generalization of $A_i(t)$ with the application of an $A_1(t), A_2(t), \ldots$ series. First, the stepwise

input variation along the columns in Eq. (6) is modified, by generalization, in order to narrow the range of variation in $T$ around the $T^c=[T_1,\ldots,T_N]^T$ central values. With an appropriate selection of the $f_1,\ldots,f_{N-1}$ functions, the stepwise variations in the columns can be made close to the central values, while keeping the determinant of $T$ nonzero. Narrowing the regime of $T$ will provide a linearized $h$ operator defined around $T^C$. The generalized input matrix is as follows

$$T=\begin{bmatrix} T_1 & T_1 & T_1 & \cdots & T_1 \\ f_1(T_2) & T_2 & T_2 & \cdots & T_2 \\ f_1(T_3) & f_2(T_3) & T_3 & \cdots & T_3 \\ \vdots & \vdots & \vdots & & \vdots \\ f_1(T_N) & f_2(T_N) & f_3(T_N) & \cdots & T_N \end{bmatrix} \tag{15}$$

Second, a set of $q(\tau_i)$ matrices is obtained as a result from the NTC for the $T$ boundary conditions according to the columns in Eq. (15). The $\tau_i$ parameters are varied in the $(0,1]$ interval (excluding zero), where $\tau_i=1$ defines $q$ responses at time-division end-points, while $\tau_i<1$ defines response at time subdivision $i$, a point in each time interval. Third, the $h(\tau_i)$ matrix (an intermediate result) is evaluated for each $i$ time subdivision from Eq. (7), that is, $h(\tau_i)=q(\tau_i)*T^{-1}$. Fourth, the $A_1(\tau_i)$ is determined based on the definition of the indicial admittance, being a response to a unit boundary value change. Multiplying the $h(\tau_i)$ matrix with a unit step vector at $t_1$, the result will be a vector $[A_1(t_1-\tau_i*t_1),A_1(t_2-\tau_i*(t_2-t_1)),\ldots,A_1(t_N-\tau_i*(t_N-t_{N-1}))]^T$, constituting $A_1(\tau_i)$. Fifth, the union of $A_1(\tau_i)$ for $i=1,\ldots,M$ is taken to form a representation of $A_1(t)$ for the entire time regime given at fine time divisions. Finally, the process is repeated with unit step vectors at $t_2,\ldots,t_N$, for obtaining $A_2(t),\ldots,A_N(t)$, the functions needed for the averaging schematic in order to obtain piecewise linear (or higher-order) connection in the time domain. Instead of using Eq. (13), the final $h$ matrix is evaluated as follows for the nonlinear model, processed around the $T^C$ central vector in this generalized case

$$h=\begin{bmatrix} M[A_1]_0^{t_1} & 0 & 0 \\ M[A_1]_{t_2-t_1}^{t_2}-M[A_1]_0^{t_2-t_1} & M[A_2]_0^{t_2-t_1} & 0 \\ \vdots & & \vdots \\ M[A_1]_{t_N-t_1}^{t_N}-M[A_1]_{t_N-t_2}^{t_N-t_1} & M[A_2]_{t_N-t_2}^{t_N-t_1}-M[A_2]_{t_N-t_3}^{t_N-t_2} & \cdots \quad M[A_N]_0^{t_N-t_{N-1}} \end{bmatrix} \tag{16}$$

In summary, the quasi-linear model identification applies the NTC results reported at fine time divisions for the determination of $A_1(t),\ldots,A_N(t)$ generator functions, based on a series of $h(\tau_i)$ matrices, identified in a user-defined domain, e.g., a narrow vicinity of a $T^C$ central boundary variation with time. The $A_i(t)$ generator functions, different in each column in Eq. (16), are used to generate the final $h$ operator for this case.

**Nonlinear NTCF Functional Model Using Volterra Series Solution.** It may be advantageous to pursue an expanded NTCF model fit over a wide range of boundary value variation, applying a Volterra series expression [1], a generalization of the single integral in Eq. (1)

$$q(t)=\int_{\tau=0}^{t} T(\tau)\frac{\partial}{\partial t}A_1(t-\tau)d\tau + \int_{\tau=0}^{t}\int_{\tau=0}^{t} T(\tau_1)T(\tau_2)\frac{\partial^2}{\partial t^2}A_2(t-\tau_1,t-\tau_2)d\tau_1 d\tau_2 + \int_{\tau=0}^{t}\int_{\tau=0}^{t}\int_{\tau=0}^{t}\cdots \tag{17}$$

Modification of Eq. (17) is introduced for NTCF model formulation, namely (a) factorization, (b) diagonalization, and (c) scaling. The fundamental difference between the NTC model-building and the conventional, nonlinear system model identification is that a comprehensive NTCF model is desired to be built on sparse data, that is, a minimum number of NTC runs. Consequently, a successively improving Volterra series with modified, approximate kernels is seen as an advantageous strategy in NTC nonlinear model identification.

(a) *Factorization*. The first modification to Eq. (17) is to approximate the derivative of the second, two-variable $A_2$ kernel with a product of two, one-variable functions, followed by similar simplification in the consecutive terms. For the second kernel as an example, it reads

$$\frac{\partial^2}{\partial t^2}A_2(t-\tau_1,t-\tau_2)=\frac{\partial}{\partial t}A_{2,1}(t-\tau_1)\cdot\frac{\partial}{\partial t}A_{2,2}(t-\tau_2) \tag{18}$$

With this modification, Eq. (17) will not be the same. However, the new functions, $A_{2,1}$ and $A_{2,2}$ will be adjusted to accommodate the change during model fitting.

(b) *Diagonalization*. The second simplification is introduced by equating $A_{2,1}$ with $A_1$. This simplification is considered to be of a weighting choice: for any $A_{2,1}$, an $A_{2,2}$ can be determined. Therefore, the unknown in the second kernel reduces to a one-variable function. Similar simplifications can be made in the consecutive kernels in the higher-order terms, re-using the previous kernels and adding always a new, one-variable function.

After renaming $A_{2,2}$ for $A_2$, the first two terms of the modified Volterra equation read

$$q(t)=\int_{\tau=0}^{t} T(\tau)\frac{\partial}{\partial t}A_1(t-\tau)d\tau + \int_{\tau=0}^{t} T(\tau)\frac{\partial}{\partial t}A_1(t-\tau)d\tau\int_{\tau=0}^{t} T(\tau)\frac{\partial}{\partial t}A_2(t-\tau)d\tau+\cdots \tag{19}$$

The justification for the simplification of the kernel, shown for the second term, is that it is not possible to identify a two-variable $A_2(t,\tau_1,\tau_2)\in R^2$ function from the result of a single $q\in R^1$ output variation. However, a "diagonal" approximation can be used as shown, based on a simplifying restriction regarding the function form.

The $A_1(t,\tau)$ function in the first factor of the second Volterra term is a mere weighting choice. Flexibility in the selection of the

function form for the derivative of $A_1$ allows for other choices than the one described. Modification, e.g., with an additive constant, may be needed for avoiding zero values of the first integral that would result in singularity for the determination of the $A_2$ function from the second integral. For brevity, it is assumed in the further discussions that the integrals do not vanish in the $(0,t]$ interval.

c. *Scaling*. Yet a third modification is needed to make the modified Volterra series successive, which allows for improving the model fit with additional terms, while keeping the previous terms unchanged. For this condition, the $T$ boundary function is measured as a difference from the corresponding input boundary variation that is associated with a particular term. It is assumed that $T_0(t), T_1(t), T_2(t), \ldots$ are used for generating the ${}^N q_0(t)$, ${}^N q_1(t)$, ${}^N q_2(t), \ldots$ NTC outputs at fine $\tau_I$ time divisions. The following scaling is used in the integrals with the first, second, third, etc., kernels

$$I(T - T_0, A_1', t) = \int_{\tau=0}^{t} [T(\tau) - T_0(\tau)] A_1'(t - \tau) d\tau \tag{20}$$

$$I(T - T_1, A_2', t) = \int_{\tau=0}^{t} [T(\tau) - T_1(\tau)] A_2'(t - \tau) d\tau \tag{21}$$

$$I(T - T_0, A_3', t) = \int_{\tau=0}^{t} [T(\tau) - T_3(\tau)] A_3'(t - \tau) d\tau \tag{22}$$

$$\vdots$$

With the notations used in Eqs. (20)–(22), the modified Volterra series is as follows

$$q(t) = q_0(t) + I(T - T_0, A_1', t) + I(T - T_0, A_1', t) \cdot I(T - T_1, A_2', t) + I(T - T_0, A_1', t \cdot I(T - T_1, A_2', t) \cdot I(T - T_2, A_3', t) + \cdots \tag{23}$$

In Eq. (23), the initial $T_0$ may be zero, constant, or a "virgin value" variation, caused by another process. For $T = T_0$, $q = q_0$, that may be nonzero, if the NTC model defines a nonhomogeneous initial and boundary condition problem. As seen in Eq. (23), $T_1$ affects only the second term, $T_2$ only the second and third terms, etc. This property allows for the explicit determination of the $A_1, A_2, \ldots$ successively from a forward progression.

The first term in Eq. (23) is identical to the NTC result for the $T_0$ input, therefore, $q_0(t) = {}^N q_0(t)$. The $A_1(t)$ in the second term of Eq. (23) is identified using the $T_1$ input and the ${}^N q_1(t)$ output. Equations (20) and (23) give

$${}^N q_1(t) - {}^N q_0(t) = \int_{\tau=0}^{t} [T_1(\tau) - T_0(\tau)] A_1'(t - \tau) d\tau \tag{24}$$

The $A_1(t)$ generator function in Eq. (24) can be determined using inverse convolution. Since the $T_1(t) - T_0(t)$ function is stepwise, changing only at $t_1, t_2, \ldots, t_N$ time instants, the integral can be decomposed, and $A_1(\tau)$ be determined at fine $\tau$ subdivisions from the NTC results. Using the notation of Eq. (9)

$$A_1(t) = \text{iconv}[{}^N q_1(t) - {}^N q_0(t), T_1(t) - T_0(t)] \tag{25}$$

The $A_2(t)$ function in the third term of Eq. (23) is identified using the $T_2$ input and the ${}^N q_2(t)$ output. Using Eqs. (21) and (23), the convolution integral with the unknown $A_2(t)$ function can be expressed

$$\frac{{}^N q_2(t) - {}^N q_0(t)}{I(T_2 - T_0, A_1', t)} - 1 = \int_{\tau=0}^{t} [T_2(\tau) - T_1(\tau)] A_2'(t - \tau) d\tau \tag{26}$$

From Eq. (26), $A_2(\tau)$ is determined by inverse convolution

$$A_2(t) = \text{iconv}\left[ \frac{{}^N q_2(t) - {}^N q_0(t)}{I(T_2 - T_0, A_1', t)} - 1, T_2(t) - T_1(t) \right] \tag{27}$$

The procedure for the third and higher Volterra series terms can be repeated. Each time, a new NTC run is needed for input. The general equation for the third term is

$$\frac{{}^N q_3(t) - {}^N q_0(t)}{I(T_3 - T_0, A_1', t) I(T_3 - T_1, A_2', t)} - \frac{1}{I(T_3 - T_1, A_2', t)} - 1 = \int_{\tau=0}^{t} [T_3(\tau) - T_2(\tau)] A_3'(t - \tau) d\tau \tag{28}$$

$A_3(\tau)$ is determined by inverse convolution from the left-hand side of Eq. (28)

$$A_3(t) = \text{iconv}\left[ \frac{{}^N q_3(t) - {}^N q_0(t) - I(T_3 - T_0, A_1', t)}{I(T_3 - T_0, A_1', t) I(T_3 - T_1, A_2', t)} - 1, T_3(t) - T_2(t) \right] \tag{29}$$

In summary, the first four elements of the third-order, modified, approximate Volterra series functional model are completed. The successive procedure may continue by adding new terms.

A few examples are given with first-, second-, and third-order Volterra series NTCF models. The first example is discussed in Appendix B for an analytically constructed, nonlinear model as an emulation of an NTC. This emulated NTC is modeled with first-, second-, and third-order NTCF models and the approximation quality is discussed. The exercises in Appendix B clarify the NTCF model and the relationship between its nonlinearity and the nonlinearity of the input boundary function, two different entities. However, it is not necessary to study Appendix B for following the logic of the rest of the paper.

Other, basic NTCF models are tested elsewhere [4,5]. In addition, the first-order Volterra series solution provides a test for the simplest NTCF model. The NTCF model tests use NUFT as an NTC, calculating temperature-driven, time-dependent heat and moisture fluxes on the surface of a conceptual emplacement tunnel at Yucca Mountain, NV. The setup of the NTC model is identical to the test cases used in Ref. [5] for Yucca Mountain. Based on previous experiences with the problem, nearly linear and moderately nonlinear models are expected, respectively, for the heat and the moisture fluxes.

Figure 3 shows the stepwise input temperature variations, $T_0$, $T_1$, $T_2$, and $T_3$, used for the identification of various NTCF models. Figure 4 depicts two different input temperature variations, $T_a$, and $T_b$, both still stepwise, for NTCF functional model fitness tests. Both $T_a$ and $T_b$ are significantly different in shape from the $T_0$, $T_1$, $T_2$, and $T_3$ inputs to provide for NTCF model validation.

Comparison between the predictions of the three NTCF models and the NTC (NUFT) results for heat is shown in Fig. 5. Figure 5(*a*) proves that all the NTCF models achieve perfect fit for the NTC heat fluxes that are used as input data for model identification. The agreements prove that the identification procedure is correct and the models reproduce the values used for their identification as inputs. This observation indicates that in an iterative application of the NTCF model any NTCF prediction error cancels out upon convergence. That is, at a point of convergence where the input for the NTC model and the NTCF model is the same, the output results from both NTC and NTCF will accurately agree.

Figures 5(*b*) and 5(*c*) show the results of three different NTCF

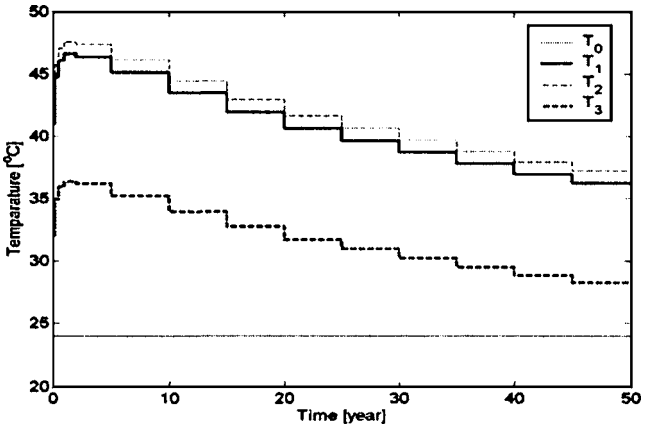


**Fig. 3 Stepwise input temperature variations used for NTCF models identification**

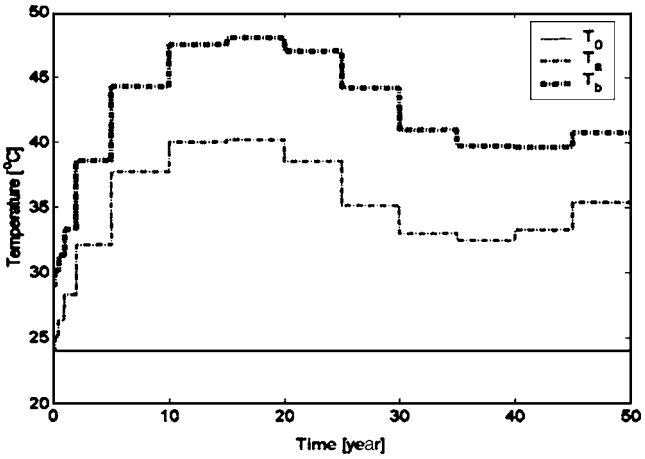


**Fig. 4 Stepwise input temperature variations used for NTCF functional model fitness tests**

models against the direct NTC results for the two different model fitness tests; the results yield nearly perfect agreement for all models. This proves that the problem at hand is nearly, albeit not perfectly, linear, since the method did not show rank deficiency such as when, for example, a second-order parabola is attempted to be fit to three co-linear points.

The three NTCF models and the NTC (NUFT) results for moisture flux are shown in Figs. 6(*a*)–6(*c*). Figure 6(*a*) proves that all the NTCF models achieve perfect fit to the NTC results, verifying the algorithms. Figures 6(*b*) and 6(*c*) show the fitness test results of three different NTCF models against the direct NTC results for the two different model fitness tests; the results show that the NTCF models improve with increasing order; however, the second-order model is nearly as good as the third-order model.

**Nonlinear NTCF Matrix Model Using Volterra Series Solution.** As a last step, the continuous-time, functional NTCF model can be transformed into a discrete-time, matrix model. The

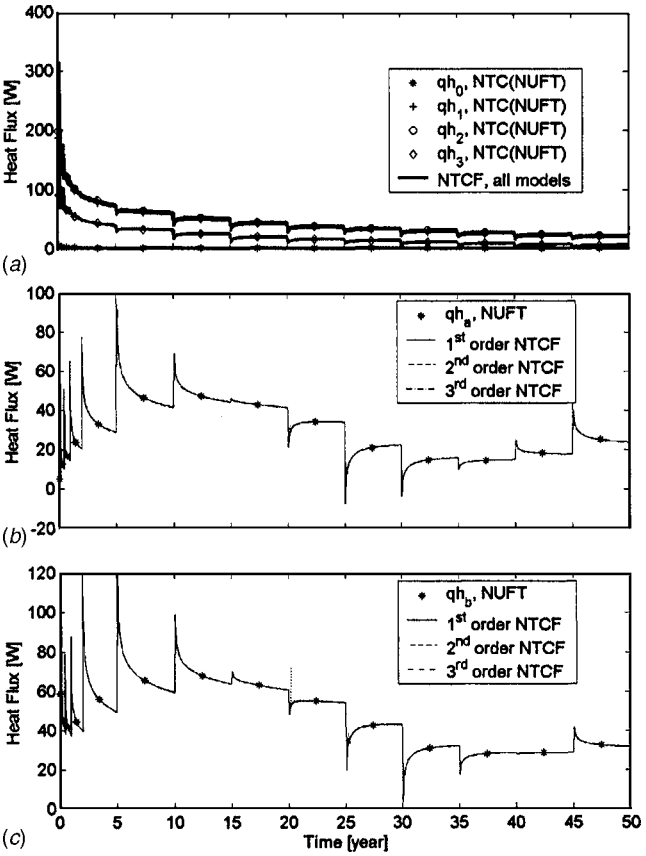


**Fig. 5 Comparison between the first-, second-, and third-order NTCF model results and the NTC (NUFT) results for heat flux; (*a*) back-calculated results used for model identification, (*b*) and (*c*) two NTCF model fitness test results against direct NTC (NUFT) results**

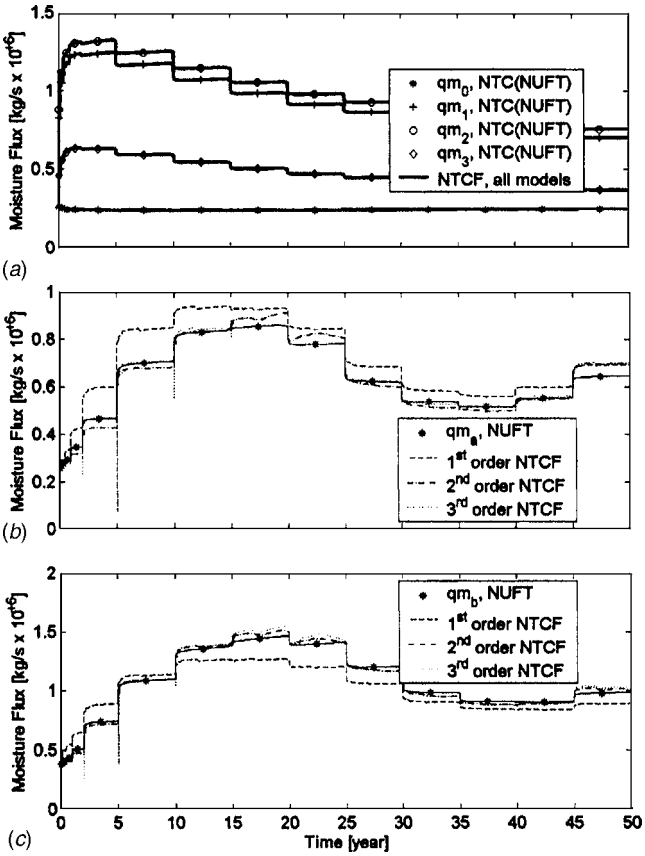


**Fig. 6 Comparison between the first-, second-, and third-order NTCF model results and the NTC (NUFT) results for moisture flux; (*a*) back-calculated results used for model identification, (*b*) and (*c*) two NTCF model fitness test results against direct NTC (NUFT) results**

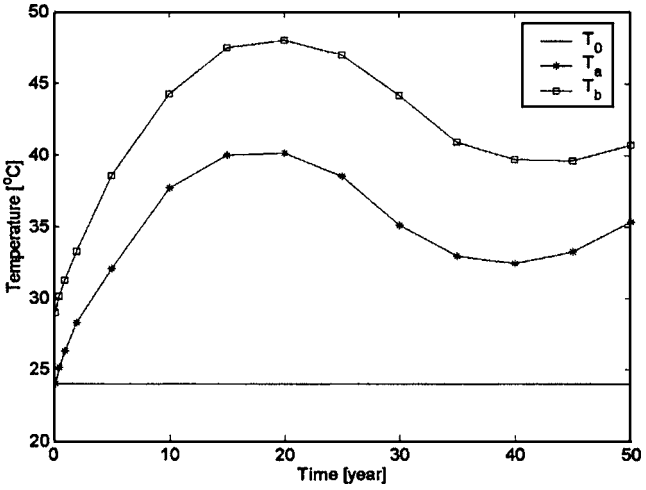


**Fig. 7 Piecewise-linear input temperature variations for $T_a$ and $T_b$**

method described in the foregoing using piecewise-linear or higher-order polynomial connections between base points of the boundary values can be used in the derivation. For piecewise-linear boundary function approximation, Eq. (13) can directly be applied to form $h_1, h_2, h_3, \ldots$ matrices from the $A_1, A_2, A_3, \ldots$ generator functions. With this, the NTCF matrix model from the Volterra functional is as follows

$$q = q_0 + h_1(T - T_0) + [h_1(T - T_0)] * [h_2(T - T_1)] + [h_1(T - T_0)] * [h_2(T - T_1)] * [h_3(T - T_2)] + \cdots \quad (30)$$

The asterisk sign in Eq. (30) denotes an element-by-element multiplication between vectors.

Two examples are given using NTCF matrix operator models based on the previous examples. The input temperature variations are shown in Fig. 7, piecewise-linear for both $T_a$ and $T_b$. The NTCF model results versus the NTC (NUFT) piecewise-linear input boundary function results are shown in Fig. 8 for heat and Fig. 9 for moisture fluxes. The results show excellent agreement between the NTCF models and the NTC results for heat for all models. For moisture flux, a second- or third-order model is seen to be required for efficient modeling with a good predicting power. However, all models provide perfect fit for the input variations used in the model identification, and the trade-off between more frequent refunctionalization versus an increase in the nonlinear NTCF order must be carefully considered and weighted.

**NTCF Model for Multivariate, Multidimensional Problems.** Similar treatment can be used for more than one variable and for domains of more than one layer in the NTC model. A typical example for a two-variable, one-layer quasi-linear model is the transport of heat and moisture in a two-dimensional domain

$$qh = hh(T - T_0) + hm(P - P_0) \quad (31)$$

$$qm = mh(T - T_0) + mm(P - P_0) \quad (32)$$

The heat and the moisture fluxes as time-dependent vectors, $qh$ and $qm$, are functions of both temperature and partial vapor pressure vectors, $T$ and $P$. Four coefficient matrices can be determined using the NTCF procedure, using built-in functions in MULTIFLUX [6]. The model in this simplest, quasi-linear form captures both temperature-driven main effects, and vapor pressure-driven cross effects. Other forms with user-defined equations may also be used.

An example of a multidimensional problem is heat and moisture transport in a three-dimensional domain. Figure 10 shows a four-layer model for which flow interactions between the layers

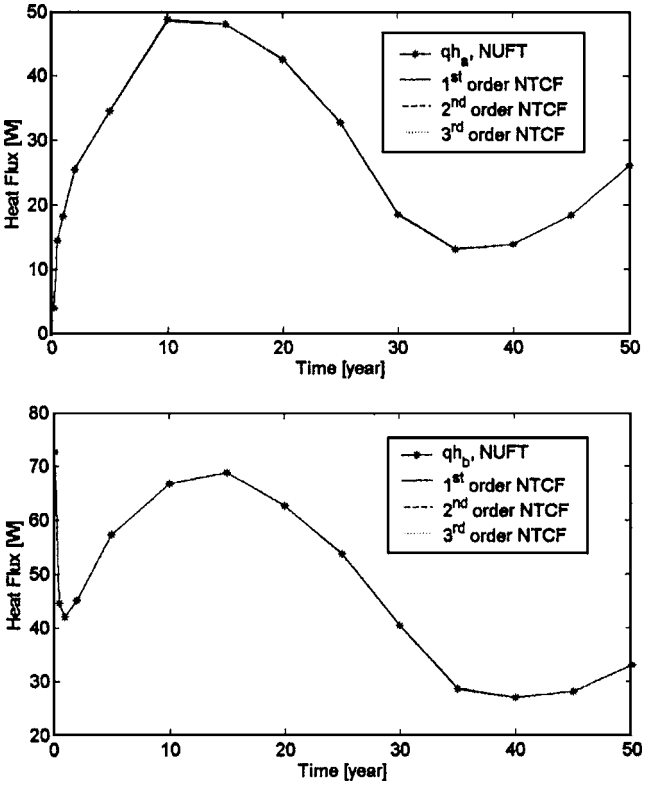


**Fig. 8 All NTCF model results versus the NTC (NUFT) piecewise-linear input boundary function results for heat flux**

are to be included. The $T$ and $P$, time and layer-dependent variables are super-vectors, and the matrix coefficients are super-matrixes. A two-variable, eight-layer NTCF model is used in Ref. [6].

## Applications

**Linearized NTCF Applications.** An independent industry group, Bechtel-SAIC Corp. (BSC), Yucca Mountain Project, NV, has compared the NTCF-based MULTIFLUX results with the results using a conventional ANSYS solution for a ventilation test problem [7]. The comparison of temperatures is shown in Fig. 11. This study proved that the transport processes in the rock were correctly modeled through the application of the NTCF methodology and that correct balancing was achieved between the NTCF and CFD modules responsible for modeling the heat and moisture transport in the airway. Three repetitions of the functionalization, as outside iterations with updated $T^C$ and $P^C$ central boundary values, were needed due to NTC (NUFT) model nonlinearities. A very significant increase in the computational efficiency was achieved using MULTIFLUX, due to the repeated application of the NTCF model, without actually rerunning the NTC (NUFT) model in each iteration step.

Validation tests of the MULTIFLUX code with the NTCF method were made recently [4,5]. One set of tests [4] was made using a quasi-three-dimensional convection-conduction ventilation problem for comparison. The method was to compare solutions to the test problem with the use of MULTIFLUX to the reference, analytical solution. The reference calculation was generated by Professor John Walton, University of Texas, El Paso, using a Carslaw and Jaeger analytical solution [4]. The other solution was made with MULTIFLUX. First, a linearized NTCF model was identified for an arbitrary, small $T^C$ temperature variation within the expected regime using NUFT. Second, a simple CFD model for the air convection was configured within MULTIFLUX, using 500 longitudinal divisions as cells along the air flow.

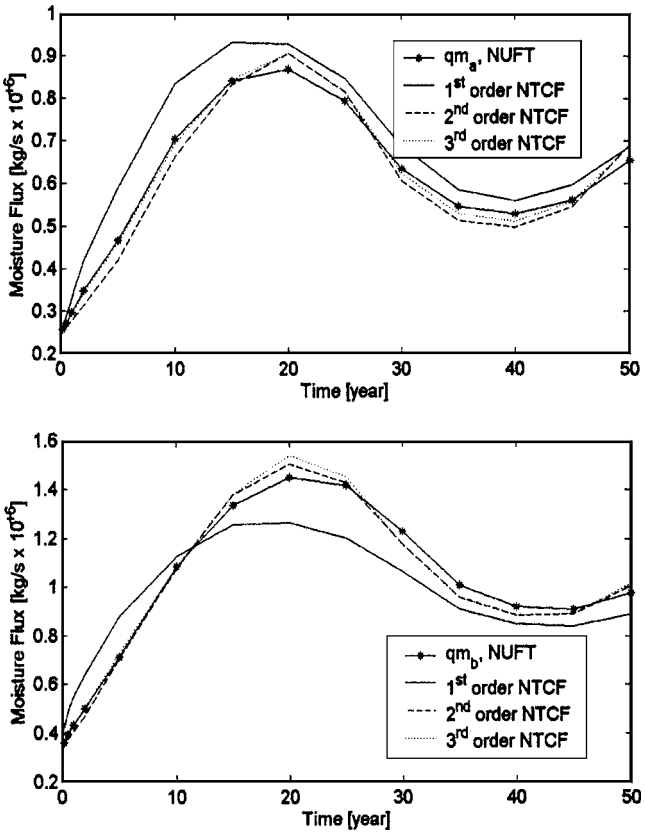


**Fig. 9 All NTCF model results versus the NTC (NUFT) piecewise-linear input boundary function results for moisture flux**

Third, the NTCF wall model and the airflow model were coupled by equating the temperature and heat flux at each division point and time interval. Figure 12 shows the air temperature history comparisons at 1 m, 250 m, and 500 m distances along the airway between the MF and other reference solutions [4]. The test demonstrated that the linearized NTCF model in MF was capable of accurately modeling the time-dependent heat flow. It was proven that refunctionalization was not needed in this low-temperature, nearly linear case. Since only one functionalization was necessary, the MF code produced results faster than the analytical solution, reusing the same matrix model in each cell, although numerical coupling and iterations were needed between the convection in the air channel and the conduction in the wall.

In thermohydrologic-ventilation simulations, the NTCF method may reduce the complete simulation time from several years to a few days or weeks assuming the same computer simulation platform. Estimated reduction in simulation time is reported in Ref. [6], based on comparing runtimes with the NTCF method and a hypothetical case without the NTCF method. It is concluded that without using the NTCF method, but replacing it with direct NTC (NUFT) runs and assuming the same number of balancing iterations, the modeling task would take a minimum of 4.1 years of nonstop computation. The 4.1 year simulation time can be compared to the actual model run time of five weeks, representing 42.6-times faster execution with the NTCF modeling technique.

## Concluding Remarks

As a subset of system identification, a new modeling approach is presented to model an existing NTC model. Simple, linear, or linearized models are described and related to known techniques, with a new approach to represent higher-order interpolation in the boundary-value variations in the NTC model, based on stepwise variation as boundary condition in the NTC model. The NTCF model is presented in a matrix-vector form, the most efficient in computation.

A simplified, successive Volterra series NTCF model is described for nonlinear applications, both in time-continuous functional, as well as in discretized, matrix operator forms. The diagonal approximation and the weighting choice introduced in the formulation seem to have considerable advantages in increasing modeling efficiency. Adding new terms in the Volterra series based on generating new NTC results can compensate for the approximation in the previous, imperfect terms in the series. The accuracy of the NTCF model can be increased by increasing the number of NTC runs used for NTCF model identification.

The simplifications introduced in the modified Volterra series model apply degenerate kernels. The second derivative of the two-dimensional, second-order kernel is approximated by a product of two, one-dimensional functions, the third derivative of the three-dimensional, third-order kernel is approximated by a product of three, one-dimensional functions, etc. This approximation greatly simplifies model identification by reducing the number of NTC runs needed for model-building; however, it may limit the predicting power of the resulting model. Within the context of the NTCF concept, a gradually improving NTCF model with each additional NTC run is seen as a major advantage, even if the model's predictive quality can never be considered perfect. A perfect fit to each NTC run, or nearly perfect fit when the least-square-fit technique is used, assures that the NTCF model results match the holding data, and will converge to the correct solution in iterative calculations.

The NTCF model, as an analytical model form, is scalable; transformations and generalizations by dimensional analysis are applicable.

Numerical examples are presented using heat and moisture fluxes of NTCF model outputs as responses to inputs of first-kind temperature and partial vapor pressure boundary conditions. This input-output selection is used as an example. It is also possible to identify an inverse NTCF model in which second-kind input boundary conditions are applied. For example, boundary heat flux

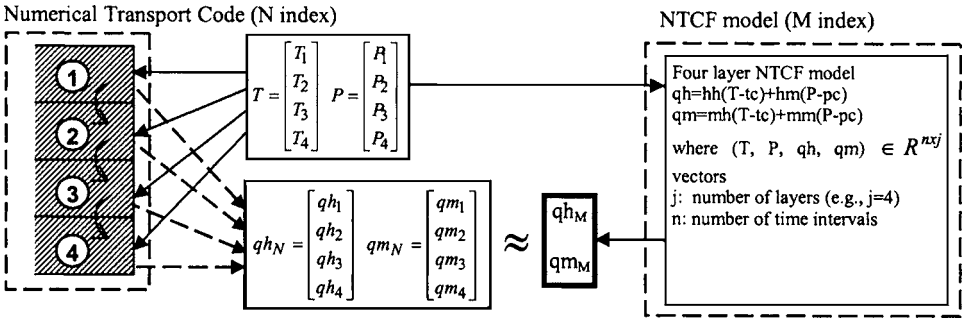


**Fig. 10 Application example of an NTC model (*N* index) and corresponding NTCF model (*M* index) for a four-layer model**

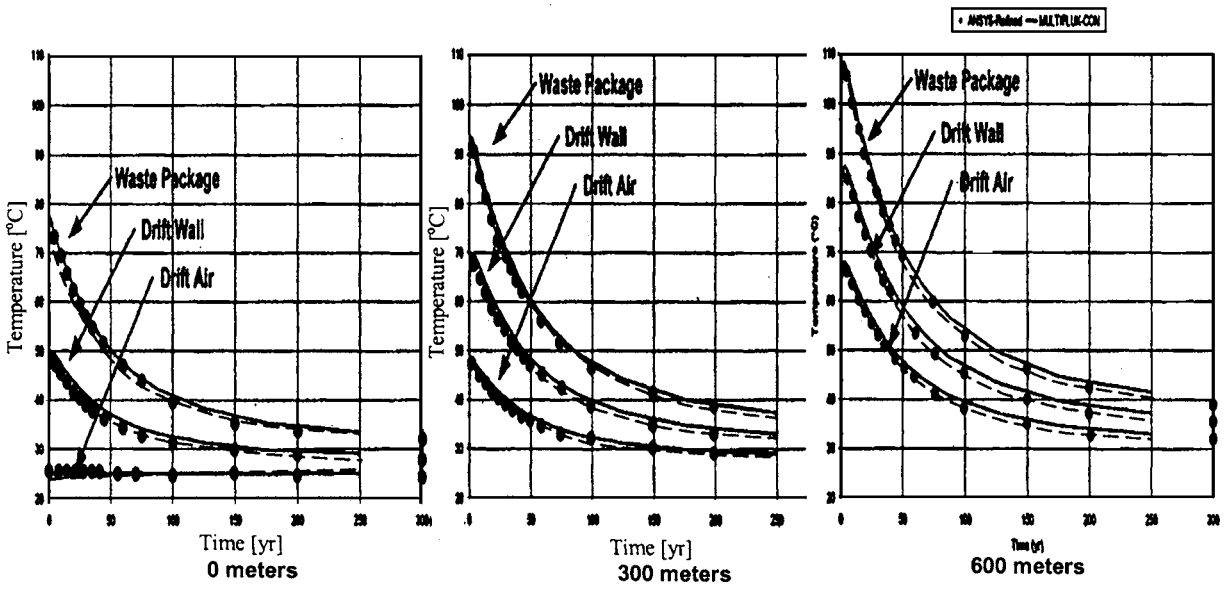


**Fig. 11 Ventilation calculation results of the NTCF-based MULTIFLUX (solid lines) and ANSYS (dots) [7]**

may be an NTCF model input for which surface temperature will become an output. It is interesting to observe that an inverse NTCF model may be derived by directly inverting the NTCF matrix equation. For example, $T=h^{-1}*q$ may directly be obtained from Eq. (4). Such a technique has been used in NTCF model applications in MULTIFLUX [7].

More studies are needed to explore the full potential of the NTCF technique. How does the order in which the boundary input-output functions are used for nonlinear model-building affect the quality of the NTCF model? Should all new NTC runs be used for ever increasing the order of the Volterra-series model, or should a least-square-fit type solution be used with a fixed and low model order? These are some of the questions that require further study.

## Acknowledgment

This work is supported by the Director, Office of Civilian Radioactive Waste Management, Office of Science and Technology and International, of the U.S. Department of Energy. The most able assistance of Mr. D. Bahrami is gratefully acknowledged in preparing the figures and performing the NUFT calculations for the tests. Dr. P. Mousset-Jones is thanked for his editorial assistance in preparation of the final paper.

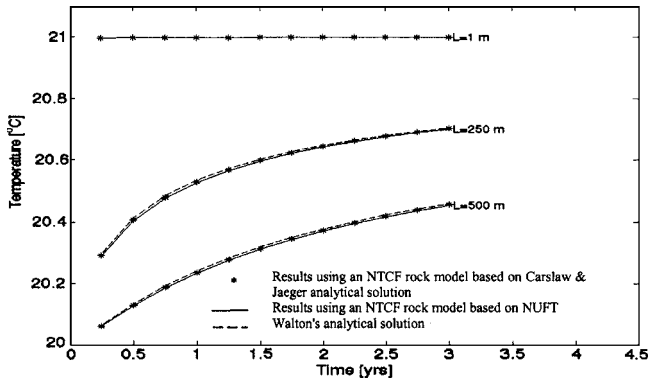


**Fig. 12 Air temperature history comparisons at 1 m, 250 m, and 500 m distance along the airway between a reference analytical solution according to Walton, and MULTIFLUX with NUFT as well as Carslaw and Jaeger rock models [4]**

## Nomenclature

$q$ = heat flux density
$qh$ = heat flux
$qm$ = moisture flux
$t$ = time vector; or continuous time
$t_i$ = $i$th time division
$A(t)$ = indicinal admittance
$C$ = sparse representation of $A$
$T$ = variable temperature
$T_w, T_{wi}$ = coefficient matrices in iconv
$P$ = variable vapor pressure
$h$ = matrix of operator
$L_i$ = linear function
$m$ = slope of the piecewise-linear boundary function
$M$ = integral mean value; also number of time ticks in iconv
$NT$ = number of time subdivisions (ticks) in iconv
$N$ = number of time divisions
$n$ = time division index
$T_c=[T_1,\ldots,T_N]^T$ = central values
$f_1,\ldots,f_{N-1}$ = functions
$\tau$ = time subdivisions; integrating variable
$\tau_C$ = reduced time subdivisions in iconv
$\lambda$ = integrating variable
$I(\,)$ = inverse convolution function
$hh$ = temperature driven NTCF dynamic admittance matrix for heat flow
$mh$ = temperature driven NTCF dynamic admittance matrix for moisture flow
$hm$ = vapor pressure driven NTCF dynamic admittance matrix for heat flow
$mm$ = vapor pressure driven NTCF dynamic admittance matrix for moisture flow
$W$ = weight factors matrix in iconv
$V$ = interpolated weight factors matrix in iconv

### Subscript

$i$ = $i$th time division
$j$ = $j$th time division
0 = initial time

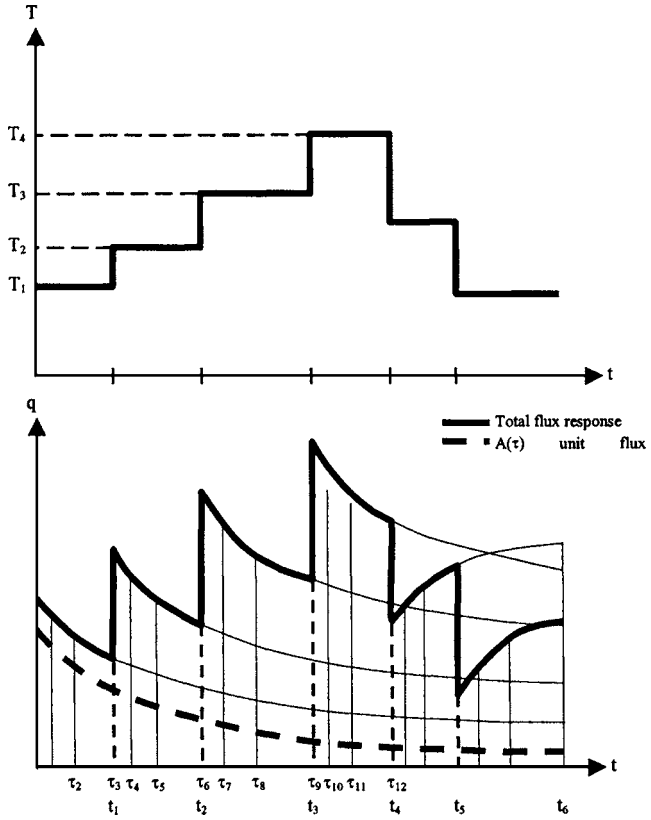


**Fig. 13 Heat flux response to input variable temperature with time ticks**

**Superscript**

$-1$ = inverse of a matrix
$N$ = NTC-generated output results

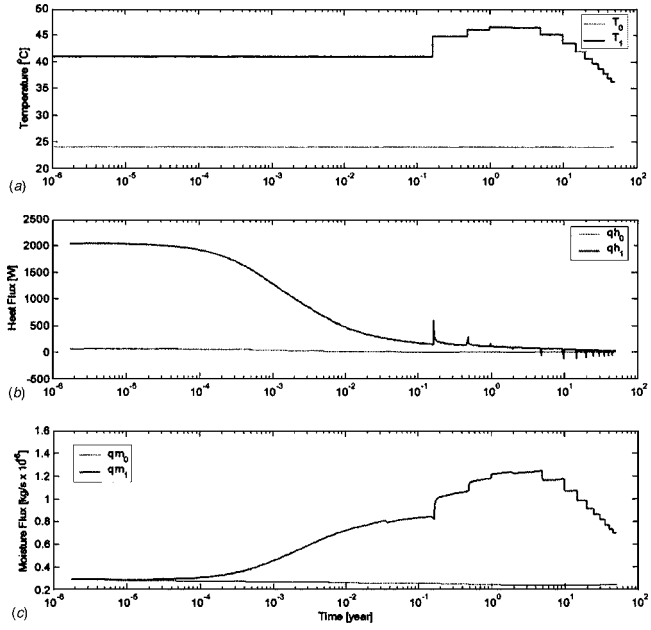


**Fig. 14 Input temperature to NTC (*a*). Output heat flux response from NTC (*b*). Output moisture flux response from NTC (*c*) for low temperature regime. Note the major difference in shape between the heat and the moisture fluxes, the latter being strongly nonlinear.**

$T$ = transpose of a matrix

## Appendix A

The inverse convolution described in Eq. (8) can be used only for equidistant $\tau_1, \tau_2, \ldots, \tau_N$ time divisions. The procedure is generalized for providing a much finer sampling time discretization for $A(\tau)$, where $\tau \in (0, t_N]$, which includes time interval subdivisions called time "ticks." Typically, each $(t_{n-1}, t_n]$ interval is subdivided into 100 subintervals. The relationship between the original time divisions and the time ticks are illustrated in Fig. 13. The procedure is a successive forward progression in which the previous $A(\tau_n)$ values are used for the determination of $A(\tau_m)$ where $\tau_m > \tau_n$. If the $\tau \in (0, t_N]$ temporal discretization is arbitrary, the inverse convolution will involve the interpolation or even the extrapolation of $A(\tau)$ during the progression. This fact makes the procedure prone to numerical instability. Accumulation of error may cause oscillation in $A$ during a procedure of several thousands steps, the typical number of time ticks in a task.

## Improvement and Stabilization

A least-square-fit procedure is developed for stabilization. The basic idea is that a set of $C(\tau)$ is determined with a reduced number of elements relative to $A(\tau)$. $C(\tau)$ will be a sparse representation of $A(\tau)$, that is, $C(\tau_c) = A(\tau_c)$ for $\tau_c$ being a time division for $C$ (called *c_time*) somewhat coarser than the $\tau$ time ticks.

Three steps are needed to derive the foundation equations.

*First*, a matrix-vector equation is expressed between the $q(\tau)$ NTC output and $A(\tau)$ unknown function as two long vectors, based on Eq. (8)

$$q = T_w \cdot A \tag{A1}$$

In Eq. (A1), $T_w$ is a coefficient matrix that is composed of the weighted values of the input function, $T(\tau)$. The definition of $T_w$ is as follows

$$T_w = \sum_{i=1}^{N} T_{wi} \tag{A2}$$

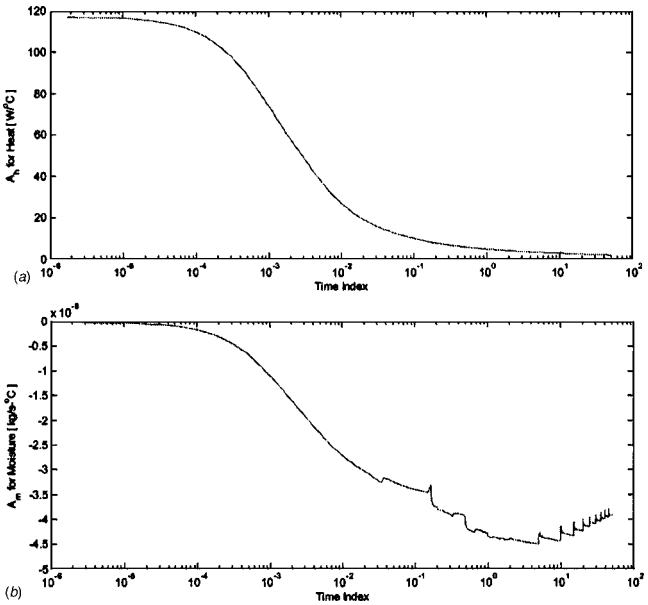


**Fig. 15 Indicinal admittances $A_h$ and $A_m$ for heat flux (*a*); and moisture flux (*b*), obtained by direct inverse convolution for the low temperature regime. Both $A_h$ and $A_m$ are well conditioned.**

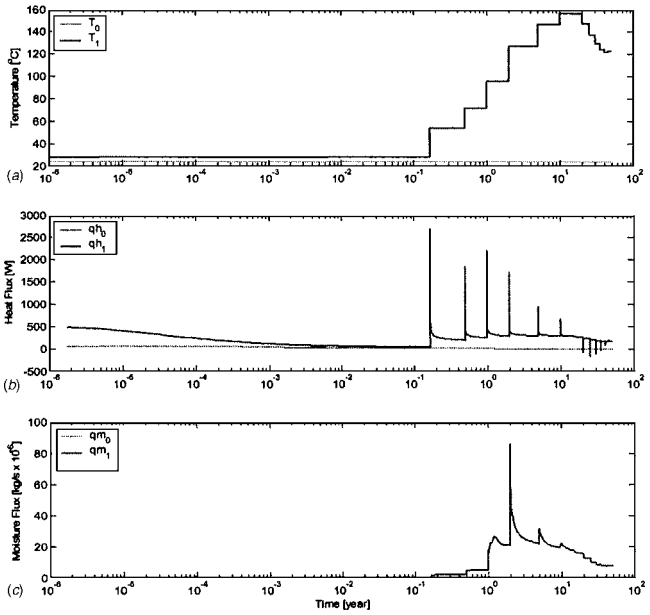


**Fig. 16 Input temperature to NTC (*a*). Output heat flux response from NTC (*b*). Output moisture flux response from NTC (*c*) for high temperature regime.**

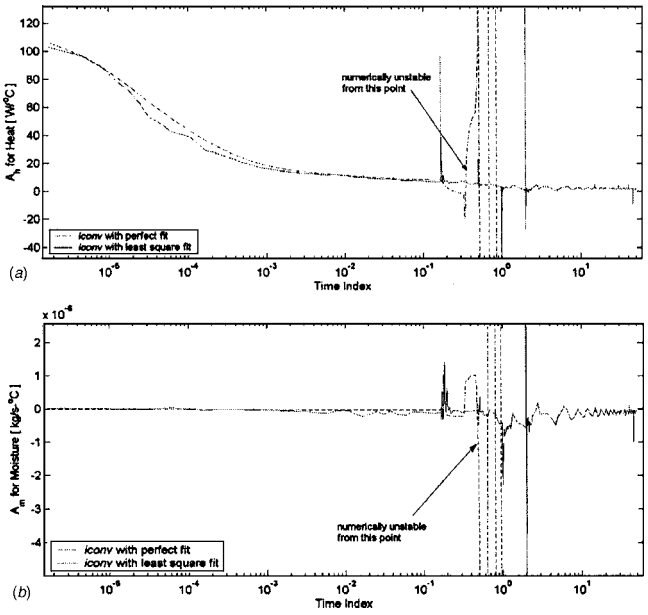


**Fig. 17 Indicinal admittances $A_h$ and $A_m$ for heat flux (*a*); and moisture flux (*b*) fluxes as a function of time obtained by direct as well as least-square-fit inverse convolutions for high temperature regime. The least-square-fit method provides stable results. The direct method becomes numerically unstable from a point marked in the figure; only a few waves are shown, the rest are omitted.**

In Eq. (A2), $T_{wi}$ are $M \times M$ matrices, where $M$ is the total number of ticks. The upper left-hand corner of $T_{w1}$ is an $NT \times NT$ matrix where $NT$ is the number of ticks in each base time interval $(t_{n-1}, t_n]$

$$T_{w1}(i,j) = \begin{bmatrix} T_1 - T_0 & 0 & 0 \\ 0 & T_1 - T_0 & 0 \\ 0 & 0 & \ddots \end{bmatrix} \quad (i,j) \in [1,NT]$$

And the other elements are:

$$T_{w1}(i,j) = 0 \quad \text{for } (i,j) \in [NT,M] \quad \text{where } M = N \times NT \tag{A3}$$

The second $T_{w2}$ matrix involves weight factors. For nonzero elements

$$T_{w2}(i,j) = [(T_2 - T_1)w_{a1}^i \quad (T_2 - T_1)w_{a2}^i \quad (T_2 - T_1)w_{a3}^i \quad \cdots \quad (T_2 - T_1)w_{aM}^i]$$
$$\text{for } i \in [NT+1, 2NT] \text{ and } j \in [1,M] \tag{A4}$$

whereas the other elements are zero:

$$T_{w2}(i,j) = 0 \quad \text{for } i \notin [NT+1, 2NT] \text{ and } j \in [1,M] \tag{A5}$$

The $T_{w3}$ and higher-indexed elements follow the same trend, not written here for brevity.

*Second*, the weight factors $w_{a1}^i, w_{a2}^i, \ldots$ must be defined for each $i$th row in each $T_{wi}$ matrix. These weight factors can be arranged in a matrix form, $W$. In the simplest representation of the exemplary procedure, the weight factors express a linear interpolation of the left and right neighbors. For line $i$ in the $W$ matrix, the nonzero neighbors are

$$W_{i-1} = \frac{t - \tau(i-1)}{\tau(i) - \tau(i-1)} \quad W_i = 1 - W_{i-1}$$

where

$$t = (\tau(i) - t_n) \quad n = \text{int}(i/NT) \tag{A6}$$

*Third*, a matrix-vector relationship is defined between the $A(\tau)$ and $C(\tau_c)$ vectors using another interpolation weight factor matrix, $V$

$$A(\tau) = V \cdot C(\tau) \tag{A7}$$

The $V$ matrix is an $M \times N_c$ matrix where $M$ is the number of ticks and $N_c$ is the number of $\tau_c$ divisions. $V$ in a simplest implementation is a sparse matrix with only two nonzero elements in each $i$th row:

$$V(i,j-1) = \frac{\tau_c(j) - \tau(i)}{\tau_c(j) - \tau_c(j-1)} \quad V(i,j) = 1 - V(i,j-1)$$
$$\text{for } i \in [1,M] \text{ and } \tau_c(j-1) \leqslant \tau_c(i) \leqslant \tau_c(j) \tag{A8}$$

The combination of Eqs. (A1) and (A7) gives

$$q = T_w V C \tag{A9}$$

The result for the determination of the $C(\tau_c)$ reduced-number vector can be made by generating a least-square-fit solution of Eq. (A9). This can be accomplished using a standard technique

$$C = ((T_w V)^T T_w V)^{-1} (T_w V)^T q \tag{A10}$$

*Finally*, the $A(\tau)$ is restored from the $C(\tau_c)$ vector using again linear interpolation according to Eq. (A7)

$$A = V((T_w V)^T T_w V)^{-1} (T_w V)^T q \tag{A11}$$

## Numerical Examples

The NTC is again NUFT, applied to a porous and fractured, partially saturated rock mass. The model domain and the NUFT input parameters are configured for ventilation model calculations for the Yucca Mountain, NV, nuclear waste repository project, described in Refs. [4,5]. Two examples are given for (1) a low input temperature regime and corresponding low nonlinearity, and (2) a high input temperature regime that overlaps the boiling temperature of water. This, in turn, creates strong nonlinearities with latent heat transport as well as convective vapor and moisture flows with advective heat transport superimposed to heat conduc-

tion in the porous rock. It must be pointed out that the temperature-driven moisture flux, also modeled, shows even stronger nonlinearity with temperature.

**Low Temperature Example: Identification of A from direct inverse convolution.** Figure 14 shows the input temperature and the output heat and moisture flux responses from NTC (NUFT). Figure 15 depicts the results from the direct inverse convolution for the heat and moisture models, using the original, 1500 $\tau_i$ time ticks. Both indicinal admittances, $A_h$ and $A_m$ for heat flux and moisture flux are well conditioned.

**High Temperature Example: Identification of A from least-square-fit inverse convolution.** Figure 16 shows the input temperature and the output heat and moisture flux responses from NTC (NUFT). Figure 17 depicts the results from the least-square-fit inverse convolution for the heat and moisture models, using simply every third of the original $\tau_i$ time ticks as the reduced-number time division, *c_time*. Both indicinal admittances, $A_h$ and $A_m$ for heat flux and moisture flux are stable and well-behaving. Figure 17 also shows part of the failed results from the direct inverse convolution. As depicted, from a relatively early point in time, the results for both $A_h$ and $A_m$ start oscillating with increasing amplitude, evidence for error accumulation with time.

## Appendix B

### Strongly Nonlinear NTCF Model Tests

**Purpose.** The purpose of this example is to present the results of a highly nonlinear, hypothetical test case for the NTCF method. A test case is created using an analytical, nonlinear function-function of which the outputs for given inputs can be directly calculated. The analytical outputs will be compared to the calculation results from the numerical NTCF model.

**The Emulated NTC Model as an Analytical Function-Function.** A nonlinear function-function, $q$, is selected as a function of the input function, $T$. This nonlinear function-function generates the output of an emulated NTC model, representing nonlinearity in the physics of the problem

$$q(T) = T\cos\left(\frac{T}{5}\right) \tag{B1}$$

**The Input Boundary Condition Function.** A nonlinear input function, $T$, is selected for the test as a function of time, $t$. This represents the input boundary function for the NTC model

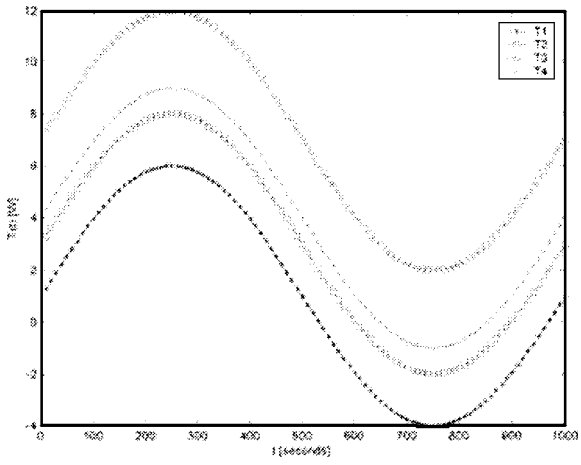

**Fig. 18 Analytical input test functions**

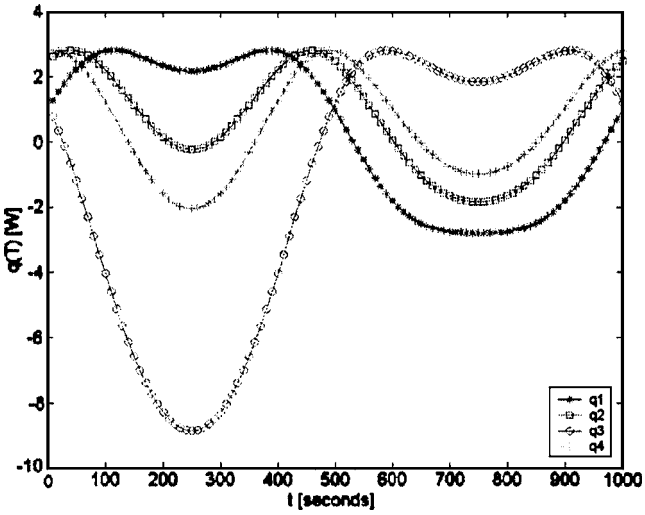


**Fig. 19 Analytical, strongly nonlinear model response functions**

$$T(t) = 5\sin\left(\frac{\pi t}{1000}\right) + c \tag{B2}$$

In Eq. (B2), $c$ will be varied ($c=0$, 2, and 6) to generate three different $T$ input functions $(T_1, T_2, T_3)$ for identifying up to a third-order NTCF model. A $T_4$ input function with $c=3$ will also be used to check how the NTCF model performs in the case of an input function that is not used during model identification.

**Test Execution.** The Volterra series NTCF procedure is used to determine various matrix models up to a third-order for predicting $q$. Three input functions $T_1$, $T_2$, and $T_3$ are used with $c=0$, 2, and 6. The performance of the NTCF model is verified at $T_4$ input function with $c=3$. Figure 18 shows the model identification input functions $T_1$, $T_2$, $T_3$, and the test function $T_4$, while Fig. 19 shows the response functions to the inputs from Eq. (B1).

**Test Results.** Figures 20–22 show that the NTCF model fits the expected output from Eq. (B1) at each input function. This test proves that the NTCF model reproduces the result of the original, nonlinear equation accurately.

The NTCF model-building method is data-based, and it is ob-

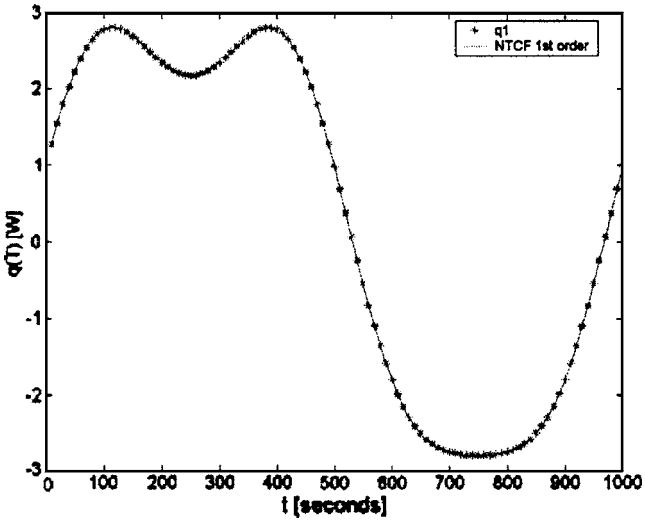


**Fig. 20 Analytical test, first-order model fit at the $T_1$ input function**

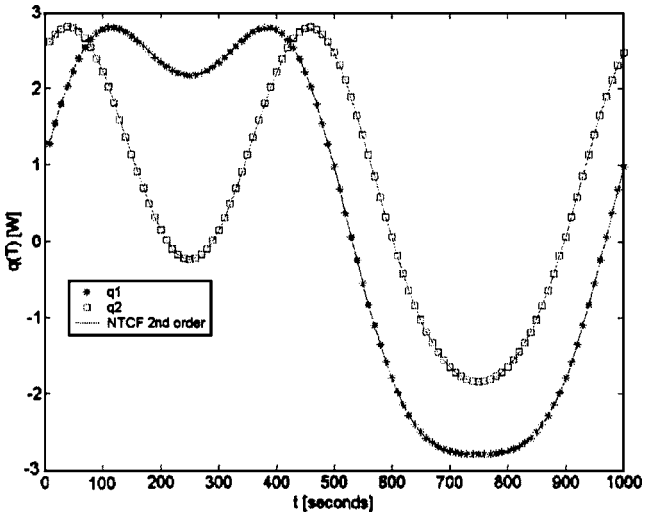


**Fig. 21 Analytical test, second-order model fit at $T_1$ and $T_2$ input functions**

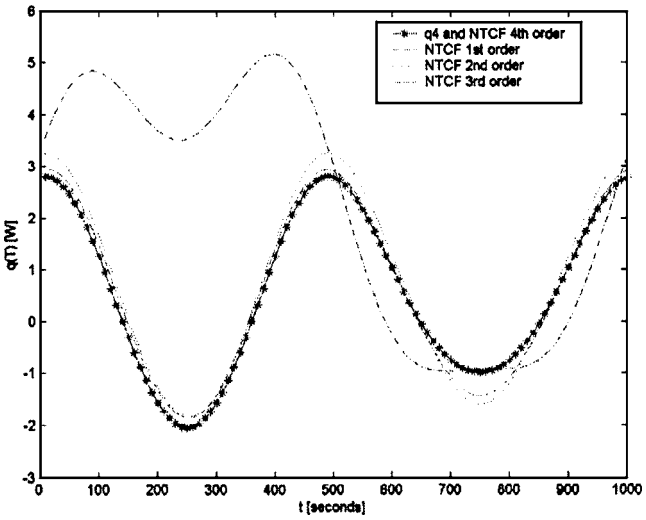


**Fig. 23 Analytical test, model fit comparison at $T_4$ test input function**

viously blind to the fact that in the current test, an analytical equation-model (instead of a numerical one, such as NUFT) is used. The fitting test independently proves that the NTCF method does not copy any error to the final result if it is iterated. Such a case happens when a new input boundary function is obtained from a balancing iteration, and the NTC model is refunctionalized accordingly.

Although the NTCF model stretching error can be eliminated by iteration, it is of practical interest to see how well an NTCF model performs as an "interpolator" or "extrapolator." This case only happens when the input function has not been used in the identification of the NTCF model.

Figure 23 compares the effectiveness of the three different NTCF models at the test input function of $T_4$. The first-order NTCF model used only $T_1$, the second NTCF model used $T_1$ and $T_2$, while the third-order NTCF model applied $T_1$, $T_2$, and $T_3$ simultaneously during model identification. None used $T_4$ as an input in model identification. As shown in Fig. 23, the NTCF model fit in stretching application improves with an increasing order of the model, a rather obvious but satisfying result. While the first-order NTCF model prediction is very poor, the second- and third-order models are closing in on the target. If $T_4$ is added to the inputs for identification of a fourth-order model, a perfect fit will be obtained between the NTC and NTCF models for all curves.

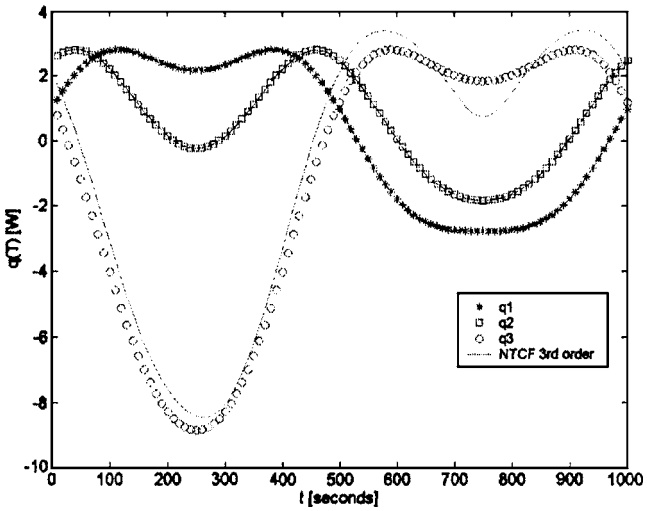


**Fig. 22 Analytical test, third-order model fit at $T_1$, $T_2$, and $T_3$ input functions**

**Conclusions of the Examples.**

i The NTCF model, even a linear, first-order one, can perfectly represent a nonlinear model for a given input.
ii An increase in the order of the NTCF model increases proportionally the number of input functions to which the outputs will be perfectly matched.
iii Between input functions, the quality of the nonlinear NTCF model fit to NTC increases with the increasing order of the NTCF model.

## References


[1] Eykhoff, P., 1974, "*System Identification, Parameter and State Estimation*," John Wiley & Sons, New York.
[2] DeFigueiredo, R. J. P., and Dwyer, T. A. W., III, 1980, "A Best Approximation Framework and Implementation for Simulation of Large-Scale Nonlinear Systems," IEEE Trans. Circuits Syst., **CAS-27**(11).
[3] Carslaw, H. S., and Jaeger, J. C., 1986, Conduction of Heat in Solids, Oxford University Press, 2nd ed., p. 30.
[4] Danko, G., 2003, "Coupled Hydrothermal-Ventilation Studies for Yucca Mountain," Annual Report for 2003, NWRPO-2003-05, Pahrump, Nevada, Nye County Department of Natural Resources.
[5] Danko, G., Bahrami, D., and Lanka, S., 2003, "Technical Support Services for the MULTIFLUX Software," MOL.20031208.0025, Final Report, submitted to BSC, Nevada, Bechtel-SAIC Company.
[6] Danko, G., 2004, "Heat and Moisture Flow Simulation with MULTIFLUX," *Proceedings of ASME, Heat Transfer/Fluid Engineering*, July 11–15, Charlotte, North Carolina.
[7] BSC (Bechtel-SAIC Company), 2002, "Ventilation Model," ANL-EBS-MD-000030 REV. 01D, Las Vegas, Nevada, Bechtel-SAIC Company.

# Analytical Study of Natural Convection in a Cavity With Volumetric Heat Generation

**Mandar V. Joshi**

**U. N. Gaitonde**

**Sushanta K. Mitra**
e-mail: skmitra@me.iitb.ac.in

Department of Mechanical Engineering,
Indian Institute of Technology Bombay,
Mumbai, 400076, India

*An analytical study has been conducted for natural convection in a cavity of different aspect ratios with uniform volumetric heat generation. Two different boundary conditions are investigated for the cavity, viz., all walls are isothermal; two horizontal walls are adiabatic and two vertical walls are isothermal. A stream function vorticity formulation is used where the variables are expanded in terms of Rayleigh number, defined as* $\mathrm{Ra}=g\beta h^5 q'''/\alpha\nu k$. *The governing equations are reduced, to biharmonic equations, and these biharmonic equations are solved using one of the methods, available in the literature. It is observed that the horizontal component of velocity is smaller than the vertical component near the center and the vertical walls of the cavity. The results for velocity profiles are compared with the simulations obtained from Fluent and they are found to be in good agreement.* [DOI: 10.1115/1.2137761]

## Introduction

Natural convection is an important mode of heat transfer and the problem of natural convection arises in many engineering applications. Batchelor's [1] work on natural convection in a differentially heated cavity, is among the first theoretical contribution. In his work, he obtained an asymptotic solution for small Rayleigh numbers, Ra. Cormack, Leal, and Imberger [2] provided the analytical solution for a long cavity ($h/l\rightarrow 0$). They provide a comprehensive summary of the literature available for a differentially heated cavity.

For a fluid layer, with a lower wall adiabatic and upper wall maintained at a constant temperature along with constant volumetric generation in the fluid, Kulacki [3] obtained the critical Rayleigh number, for the transition from the conduction to the convection regime. In this analysis, the critical Rayleigh number is obtained using two methods. The first approach follows the linear theory by Rayleigh, discussed in Drazin and Reid [4], and the second approach is based on the energy method. Fusegi, Hyun, and Kuwara [5] considered a square cavity with differentially heated walls, along with volumetric heat generation, using numerical methods. They have defined two Rayleigh numbers: one based on the temperature difference between the walls, and the other based on heat sources in the cavity. They have studied the effect of these Rayleigh numbers on the flow field. May [6] solved the problem of transient natural convection using the streamfunction vorticity method. He reported that the periodic solution exists for $\mathrm{Ra}>5\times 10^4$. Ciofalo and others [7–9], analyzed low Prandtl number natural convection flows, using the finite volume technique. By successively increasing the Grashoff number, they obtained steady, periodic, and chaotic solutions.

Relatively less literature is available for the study of volumetrically heated cavities using analytical methods. Daniels and Jones [10] considered a long cavity ($h/l\rightarrow 0$), whereas a similar approach was used by Joshi, Gaitonde, and Mitra [11] for a tall cavity ($h/l\rightarrow\infty$). However, to the best of the authors knowledge, no analytical solutions are available in literature for a square cavity with volumetric heat generation. In this work, a methodology has been developed to study the problem of natural convection in a square cavity, using semianalytical methods. As a first step, the method adopted for the tall cavity with volumetric heat generation will be dealt with briefly. The details of this method are provided by Joshi et al. [11]. Subsequently, the square cavity problem will be analyzed, which involves solutions to the biharmonic equation. Two different boundary conditions, viz., all isothermal walls and only horizontal walls adiabatic, are discussed here and the corresponding solutions to the velocity and temperature profiles are obtained here.

## Governing Equations

Figure 1 shows the schematic of a cavity of height $h$, length $l$, and having uniform volumetric heat generation $q'''$. Two different boundary conditions are considered in the present study. In the first problem, the horizontal walls are considered to be adiabatic and the vertical walls are considered isothermal, maintained at temperature $T_0$. In the second problem, all the walls are considered isothermal, maintained at temperature $T_0$. The governing equations for mass, momentum, and energy conservation for the cavity under a steady-state condition with the Boussinesq approximation can be expressed as:

$$\frac{\partial u'}{\partial x'}+\frac{\partial v'}{\partial y'}=0 \tag{1}$$

$$u'\frac{\partial u'}{\partial x'}+v'\frac{\partial u'}{\partial y'}=-\frac{1}{\rho_0}\frac{\partial p}{\partial x'}+\nu\nabla'^2 u' \tag{2}$$

$$u'\frac{\partial v'}{\partial x'}+v'\frac{\partial v'}{\partial y'}=-\frac{1}{\rho_0}\frac{\partial p}{\partial y'}+\nu\nabla'^2 v'+g\beta(T-T_0) \tag{3}$$

$$u'\frac{\partial T}{\partial x'}+v'\frac{\partial T}{\partial y'}=\alpha\nabla^2 T+\frac{q'''}{(\rho_0 c)} \tag{4}$$

where $p=p_0+\rho_0 g y'$, $p_0$ is the static pressure, $\rho_0$ is the density, $\nu$ is the kinematic viscosity, $\alpha$ is thermal diffusivity, $g$ is the gravitational acceleration, $\beta$ is the coefficient of thermal expansion, $T$ is the temperature, and $u'$ and $v'$ are the $x'$ and $y'$ components of velocity, respectively. Equations (2)–(3) can be modified to eliminate pressure using the stream function-vorticity approach, where streamfunction $\psi'$ and vorticity $\omega'$ are defined as $u'=\partial\psi'/\partial y'$, $v'=-\partial\psi'/\partial x'$, and $\omega'=-\nabla'^2\psi'$, $\nabla'^2=\partial^2/\partial x'^2+\partial^2/\partial y'^2$. Hence, Eqs. (2)–(3) can be written in dimensionless form as follows:

Contributed by the Heat Transfer Division of ASME for publication in the JOURNAL OF HEAT TRANSFER. Manuscript received September 27, 2004; final manuscript received April 13, 2005. Review conducted by Jay M. Khodadadi. Paper presented at the 2004 ASME Heat Transfer/Fluids Engineering Summer Conference (HTFED2004), July 11, 2004–July 11, 2004, Charlotte, North Carolina, USA.

  

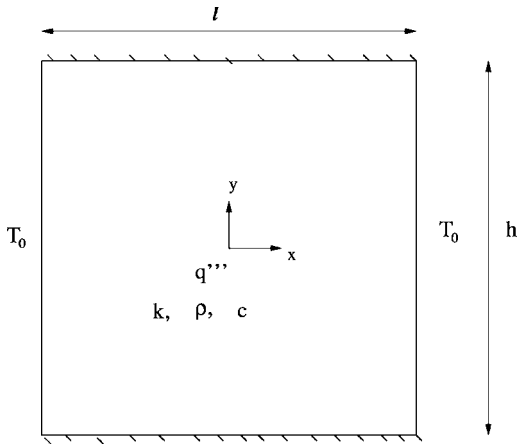


**Fig. 1 Schematic of a cavity with volumetric heat generation**

$$\frac{\mathrm{Ra}}{\mathrm{Pr}}\frac{\partial(\omega,\psi)}{\partial(x,y)} = \nabla^2\omega + \frac{\partial\theta}{\partial x} \tag{5}$$

$$\mathrm{Ra}\,\frac{\partial(\theta,\psi)}{\partial(x,y)} = \nabla^2\theta + 1 \tag{6}$$

where the spatial coordinates are nondimensionalized with the height $h$ of the cavity and, therefore, one can define the following nondimensional quantities:

$$\mathrm{Ra} = \frac{g\beta h^5 q'''}{\alpha\nu k};\quad \theta = \frac{T - T_0}{q'''h^2/k};\quad x = \frac{x'}{h};\quad y = \frac{y'}{h} \tag{7}$$

The velocity boundary conditions can be written as:

$$\psi = 0,\ \frac{\partial\psi}{\partial x} = 0 \quad \text{at } x = \pm\frac{1}{2} \tag{8}$$

$$\psi = 0,\ \frac{\partial\psi}{\partial y} = 0 \quad \text{at } y = \pm\frac{1}{2} \tag{9}$$

The boundary conditions with respect to $\theta$ corresponding to the two types of problems, discussed earlier, can be written as:

$$\theta = 0 \quad \text{at } x = \pm\frac{1}{2} \quad \text{and} \quad \frac{\partial\theta}{\partial y} = 0 \quad \text{at } y = \pm\frac{1}{2} \tag{10}$$

$$\theta = 0 \quad \text{at } x = \pm\frac{1}{2} \quad \text{and} \quad y = \pm\frac{1}{2} \tag{11}$$

In the analysis of a tall cavity, by Joshi et al. [11], it is assumed that for a tall cavity, the flow is predominantly in the vertical direction. Therefore, the streamfunction is assumed to be a function of horizontal coordinate only, i.e., $\psi = \psi(x)$. However, no such assumption is made about the dimensionless temperature $\theta$. It can be shown that under this assumption, the streamfunction equation can be reduced to an ordinary linear differential equation. This ordinary differential equation is solved to give an expression for a stream function, in terms of the horizontal coordinate. This solution of the streamfunction is substituted in the energy equation, to obtain the solution for $\theta$. The expressions for velocity and temperature, can be written as [11]:

$$v_1 = \frac{1}{4m^4} + c_3[e^{-mx_1}\cos mx_1 + e^{-m(1-x_1)}\cos m(1-x_1)] + c_4[e^{-mx_1}\sin mx_1 + e^{-m(1-x_1)}\sin m(1-x_1)] \tag{12}$$

$$\theta_1 = c_4'[e^{-mx_1}\cos mx_1 + e^{-m(1-x_1)}\cos m(1-x_1)] + c_3'[(e^{-mx_1})\sin mx_1 + e^{-m(1-x_1)}\sin m(1-x_1)] + \frac{4m^4}{\mathrm{Ra}}y_1 + \delta \tag{13}$$

where the dimensionless variables are defined as: $x_1 = x'/l$, $y_1 = y'/l$, $v_1 = v'/\mathrm{Ra}_1$, $\theta_1 = (T - T_0)/q'''l^2/k$, $\mathrm{Ra}_1 = g\beta l^5 q'''/\alpha\nu k$, and the constants are defined as:

$$c_3 = \frac{-1}{4m^4}\left(\frac{e^{-m}(m+1)\sin m + e^{-m}\cos m - 1}{e^{-2m} + 2e^{-m}\sin m - 1}\right) \tag{14}$$

$$c_4 = \frac{1}{4m^4}\left(\frac{m - 1 - e^{-m}\sin m + (m+1)e^{-m}\cos m}{e^{-2m} + 2e^{-m}\sin m - 1}\right) \tag{15}$$

$$c_4' = \frac{m - 1 - e^{-m}\sin m + (m+1)e^{-m}\cos m}{2m^2(e - 2m + 2e^{-m}\sin m - 1)} \tag{16}$$

$$c_3' = \frac{(m+1)e^{-m}\sin m + e^{-m}\cos m - 1}{2m^2(e^{-2m} + 2e^{-m}\sin m - 1)} \tag{17}$$

$$\delta = -\frac{[(m+1)e^{-2m} - 2e^{-m}\sin m + 2me^{-m}\cos m + (m-1)]}{[2m^2(e^{-2m} + 2e^{-m}\sin m - 1)]} \tag{18}$$

The value of $m$ is estimated by using the maximum temperature corresponding to a pure conduction in the cavity with volumetric heat generation. The details of the methodology and the results are discussed in [11].

## Solution For a Square Cavity

The quantities, $\psi$, $\omega$, and $\theta$, appearing in Eqs. (5)–(6), can be expanded in terms of power series of Ra as follows:

$$\psi = \psi_0 + \mathrm{Ra}\,\psi_1 + \mathrm{Ra}^2\,\psi_2 + \cdots \tag{19}$$

$$\omega = \omega_0 + \mathrm{Ra}\,\omega_1 + \mathrm{Ra}^2\,\omega_2 + \cdots \tag{20}$$

$$\theta = \theta_0 + \mathrm{Ra}\,\theta_1 + \mathrm{Ra}^2\,\theta_2 + \cdots \tag{21}$$

Substituting this in Eqs. (5)–(6), eliminating $\omega$, and comparing the like powers of Ra, the following expressions are obtained:

**order 0:** (coefficient of constant term)

$$\nabla^2\theta_0 = -1 \tag{22}$$

$$\nabla^4\psi_0 = \frac{\partial\theta_0}{\partial x} \tag{23}$$

**order 1:** (coefficient of Ra)

$$\nabla^2\theta_1 = \frac{\partial(\theta_0,\psi_0)}{\partial(x,y)} \tag{24}$$

$$-\nabla^4\psi_1 = -\frac{\partial\theta_1}{\partial x} + \frac{1}{\mathrm{Pr}}\frac{\partial(-\nabla^2\psi_0,\psi_0)}{\partial(x,y)} \tag{25}$$

**order 2:** (coefficient of $\mathrm{Ra}^2$)

$$\nabla^2\theta_2 = \frac{\partial(\theta_1,\psi_0)}{\partial(x,y)} + \frac{\partial(\theta_0,\psi_1)}{\partial(x,y)} \tag{26}$$

$$-\nabla^4\psi_2 = -\frac{\partial\theta_2}{\partial x} + \frac{1}{\mathrm{Pr}}\left(\frac{\partial(-\nabla^2\psi_0,\psi_1)}{\partial(x,y)} + \frac{\partial(-\nabla^2\psi_1,\psi_0)}{\partial(x,y)}\right) \tag{27}$$

It is observed that at every order, the right-hand sides of the equations are completely known as they contain terms obtained as a solution from the previous order. The left-hand sides are linear terms in terms of an unknown variable. Therefore, at every order a linear equation is obtained. The method of the solution of linear equations, of this form, is discussed in detail in this section.

Considering the solution for the zeroth order, the boundary conditions associated with $\theta$ for the cavity with horizontal walls insulated are given as:

$$\theta_0 = 0 \quad \text{at } x = \pm D \quad \text{and} \quad \frac{\partial \theta_0}{\partial y} = 0 \quad \text{at } y = \pm 1/2 \tag{28}$$

where $D = l/2h$. Equation (22) is same as the conduction equation with a heat generation term, and its solution, subject to the boundary conditions given in Eq. (28), can be written as:

$$\theta_0 = (D^2 - x^2)/2 \tag{29}$$

Substituting Eq. (29) into Eq. (23), the corresponding equation for the streamfunction can be written as:

$$\nabla^4 \psi_0 = -x \tag{30}$$

subject to the boundary conditions:

$$\psi_0 = 0 \quad \text{at } y = \pm \frac{1}{2} \quad \text{and} \quad x = \pm D \tag{31}$$

$$\frac{\partial \psi_0}{\partial x} = 0 \quad \text{at } x = \pm D \quad \text{and} \quad \frac{\partial \psi_0}{\partial y} = 0 \quad \text{at } y = \pm \frac{1}{2} \tag{32}$$

Equation (30) is a nonhomogeneous linear equation and its solution can be written as a sum of a special solution to the above equation and a general solution to the homogeneous biharmonic equation. In this case, a special solution $\psi_{0s}$ is chosen such that it satisfies Eq. (30) and the boundary conditions at $y = \pm 1/2$, which can then be expressed as:

$$\psi_{0s} = \frac{-x\left(y^2 - \frac{1}{4}\right)^2}{24} \tag{33}$$

It can be observed that $\psi_{0s}$ does not satisfy the boundary conditions at $x = \pm D$. Therefore, the corresponding homogeneous solution $\psi_{0h}$ should be chosen such that it satisfies the following conditions:

$$\nabla^4 \psi_{0h} = 0; \quad \psi_{0h} = 0 \quad \text{at } y = \pm \frac{1}{2}; \quad \frac{\partial \psi_{0h}}{\partial y} = 0 \quad \text{at } y = \pm \frac{1}{2} \tag{34}$$

$$\psi_{0h} = \frac{D}{24}\left(\frac{1}{4} - y^2\right)^2 \quad \text{at } x = D; \quad \psi_{0h} = -\frac{D}{24}\left(\frac{1}{4} - y^2\right)^2 \quad \text{at } x = -D \tag{35}$$

$$\frac{\partial \psi_{0h}}{\partial x} = \frac{1}{24}\left(\frac{1}{4} - y^2\right)^2 \quad \text{at } x = D; \qquad \frac{\partial \psi_{0h}}{\partial x} = \frac{1}{24}\left(\frac{1}{4} - y^2\right)^2 \quad \text{at } x = -D \tag{36}$$

After finding, the homogeneous solution $\psi_{0h}$ satisfying the above conditions, the solution for $\psi_0$ can be written as:

$$\psi_0 = \psi_{0s} + \psi_{0h} \tag{37}$$

Assuming that $\psi_{0h}$ is of the form $e^{\lambda x} h(y)$ for some $\lambda$ and some function $h(y)$, Eq. (34) reduces to:

$$\frac{d^4 h}{dy^4} + 2\lambda^2 \frac{d^2 h}{dy^2} + \lambda^4 h = 0 \tag{38}$$

The boundary conditions for $h(y)$ are $h(y) = 0$ and $\partial h/\partial y = 0$ at $y = \pm 1/2$. The even eigenfunctions satisfying the above equation and boundary conditions are given by:

$$\phi_e(y) = \left(y \sin \lambda_e y - \frac{1}{2} \tan \frac{\lambda_e}{2} \cos \lambda_e y\right) \tag{39}$$

where $\lambda_e$ is a complex eigenvalue satisfying

$$\sin \lambda_e = -\lambda_e \tag{40}$$

The odd eigenfunctions are given by:

$$\phi_0(y) = D\left(y \cos \lambda_0 y - \frac{1}{2} \cot \frac{\lambda_0}{2} \sin \lambda_0 y\right) \tag{41}$$

where $\lambda_0$ is a complex eigenvalue satisfying,

$$\sin \lambda_0 = \lambda_0 \tag{42}$$

Both Eqs. (40) and (42) have an infinite number of solutions. Therefore, the general solution for $\phi$ can be written as a sum of solutions corresponding to each eigenvalue. If $\lambda$ is an eigenvalue, then $-\lambda$ and the complex conjugate $\overline{\lambda}$ are also the eigenvalues. Therefore for a real-valued solution of $\psi_{0h}$, the eigenfunctions corresponding to the complex conjugate eigenvalues should be considered together. This expression for $\psi_{0h}$ can be written as:

$$\psi_{0h} = \psi_{ec} + \overline{\psi_{ec}} + \psi_{oc} + \overline{\psi_{oc}} \tag{43}$$

where the eigenfunctions are written in terms of hyperbolic sine and cosine functions as:

$$\psi_{ec} = \sum_1^\infty a_n \sinh(\lambda_{en} x)\phi_{en}(y) + b_n \cosh(\lambda_{en} x)\phi_{en}(y) \tag{44}$$

$$\psi_{oc} = \sum_1^\infty c_n \sinh(\lambda_{on} x)\phi_{on}(y) + d_n \cosh(\lambda_{on} x)\phi_{on}(y) \tag{45}$$

Here $\lambda_{en}$ and $\lambda_{on}$ are $n$th eigenvalues satisfying Eq. (40) and Eq. (42), respectively, and $\phi_{en}$ and $\phi_{on}$ are corresponding eigenfunctions. The coefficients $a_n$, $b_n$, $c_n$ and $d_n$ should be chosen such that they satisfy the boundary conditions at $x = \pm D$. The boundary conditions given by Eq. (36) are even functions of $y$. Therefore, it is sufficient to consider only even eigenfunctions given by Eq. (39). Also, the boundary conditions of $\psi$ at $x = D$ are exactly negative of the boundary conditions at $x = -D$. This indicates that it is sufficient to consider only $\sinh \lambda_{en} x$ components from Eq.(43) in the expansion of $\psi$. Therefore, a general expression of $\psi$ given by Eq. (43) can be simplified as:

$$\psi_{0h} = \sum_{n=1}^\infty h_n \sinh(\lambda_{en} x)\phi_{en}(y) + \overline{h_n} \sinh(\overline{\lambda_{en}} x)\overline{\phi_{en}(y)} = \sum_{n=1}^\infty 2 \,\text{Real}[h_n \sinh(\lambda_{en} x)\phi_{en}(y)] \tag{46}$$

where the constants $h_n$ are obtained by using the method described by Shankar [12].

As outlined by Shankar [12], the infinite series of $\psi_{0h}$ is truncated to first $N$ terms and $n$ equidistant points are chosen between $0 \leqslant y < 0.5$ such that for a given set of coefficients $h_n$, the error made in satisfying the boundary conditions at $x = D$ is calculated for each of these $n$ points.

$$\psi_0 = \psi_{0s} + \psi_{0h} = \frac{-x\left(y^2 - \frac{1}{4}\right)^2}{24} + 2 \,\text{Real}\left(\sum_{n=1}^N h_n \sinh(\lambda_{en} x)\phi_{en}(y)\right) \tag{47}$$

Equation (47) can then be substituted on the right-hand side of Eq. (24) to obtain an equation for $\theta_1$ as:

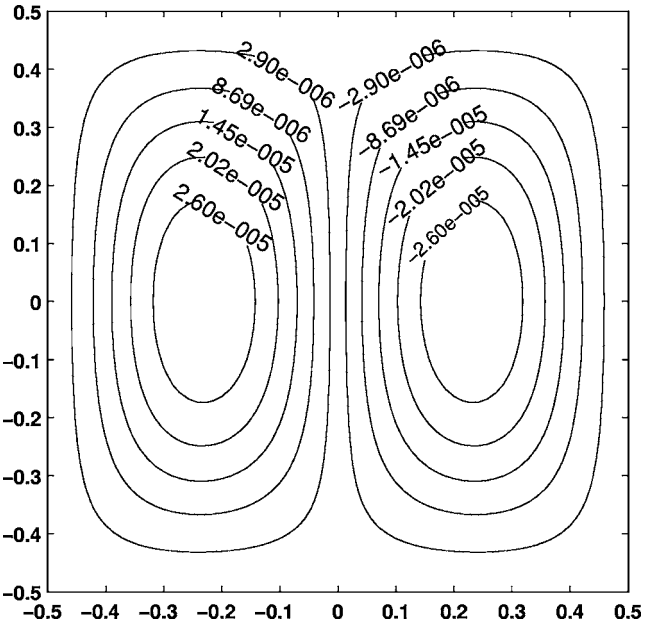


**Fig. 2 Streamlines for square cavity with isothermal walls**

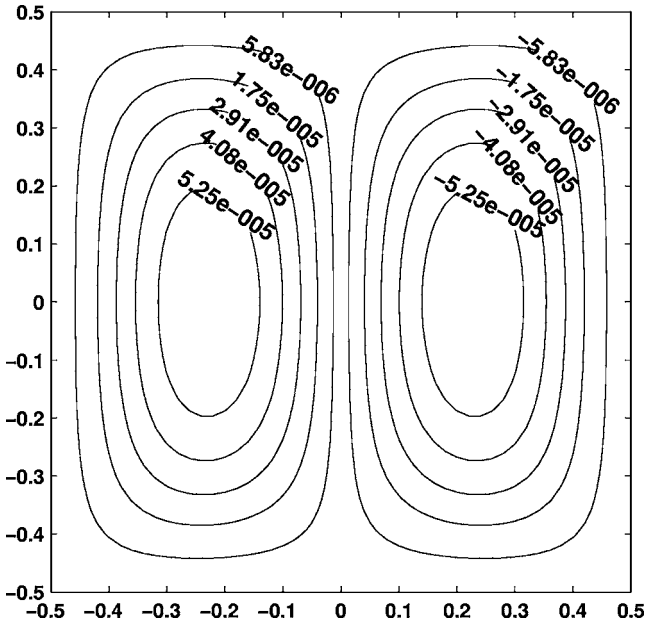


**Fig. 3 Streamlines for square cavity with horizontal walls adiabatic**

$$\nabla^2\theta_1 = \frac{1}{6}x^2y\left(y^2-\frac{1}{4}\right) - 2\,\text{Real}\left(x\sum_1^N h_n \sinh(\lambda_{en}x)\phi'_{en}(y)\right) \tag{48}$$

which resembles a standard Poisson equation whose solution can be obtained by using the Fourier series expansion method. Hence, one can obtain the following expressions:

$$\theta_1 = \theta_{11s} + \theta_{11h} + \theta_{12} \tag{49}$$

$$\theta_{11s} = (y^5/120 - y^3/144 + y/384)x^2 + (-y^7/2520 + y^5/1440 - y^3/1152 + 11y/23\,040) \tag{50}$$

$$\theta_{11h} = \sum_{k=1}^{\infty} f_k \sin(2k-1)\pi y \cosh(2k-1)\pi x \tag{51}$$

$$\theta_{12} = \sum_{m=1}^{\infty}\sum_{n=1}^{\infty} A_{mn}\cos\frac{(2m-1)\pi x}{2D}\sin(2n-1)\pi y \tag{52}$$

$$f_k = \frac{4\displaystyle\int_0^{1/2}\theta_{11h}(D,y)\sin(2k-1)\pi y}{\cosh(2k-1)\pi D} \tag{53}$$

$$A_{mn} = \int_0^{1/2}\int_0^{D} 8\frac{Su(x,y)\cos\dfrac{(2m-1)\pi x}{2D}\sin(2n-1)\pi y}{D\left[\left(\dfrac{(2m-1)\pi}{2D}\right)^2 + (2n-1\pi)^2\right]} \tag{54}$$

$$Su(x,y) = -2\,\text{Real}\left(x\sum_1^{\infty} h_n \sinh\lambda_{en}x\phi'_{en}(y)\right) \tag{55}$$

where $\phi'_{en}(y)$ is $d\phi_{en}(y)/dy$. The integrals of $f_k$ and $A_{mn}$ are evaluated numerically. Thus, combining all these, an expression for $\theta$ can be written as:

$$\theta = \theta_0 + \text{Ra}\,\theta_1 \tag{56}$$

It can be pointed out that similar expressions can be obtained for a cavity with all walls isothermal. The governing equations and the nondimensionalization is the same as that used earlier. The analysis remains the same until Eq. (27). However, the boundary conditions for $\theta_0$ are as follows:

$$\theta_0 = 0 \quad \text{at } x = \pm D \quad \text{and} \quad y = \pm 1/2 \tag{57}$$

and hence the corresponding solution for $\theta_0$ can be written as:

$$\theta_0 = \frac{\left(\dfrac{1}{4}-y^2\right)}{2} + \sum_{k=1}^{\infty} B_k \cos(2k-1)\pi y \cosh(2k-1)\pi x \tag{58}$$

$$B_k = \frac{(-4)^k}{\cosh[(2k-1)\pi D][(2k-1)\pi]^3} \tag{59}$$

Therefore, substituting the expression for $\theta_0$ in Eq. (23), the following equation for $\psi$ is obtained:

$$\nabla^4\psi_0 = \sum_{k=1}^{\infty}(2k-1)\pi B_k \cos(2k-1)\pi y \sinh(2k-1)\pi x \tag{60}$$

The solution to above equation can be obtained as a summation of a special solution and general solution, as done for the earlier case.

$$\psi_0 = \psi_{0s} + \psi_{0h} \tag{61}$$

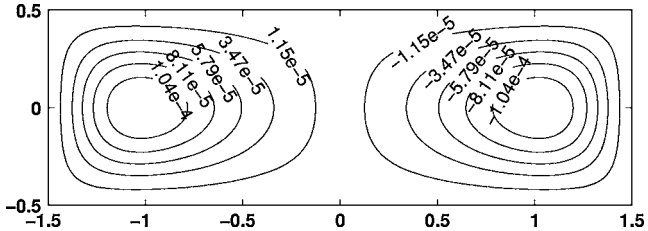


**Fig. 4 Streamlines for cavity of aspect ratio 3 with isothermal walls**

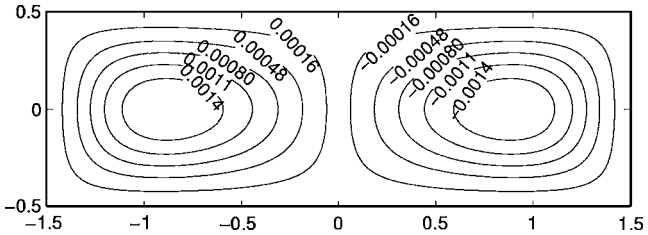


**Fig. 5 Streamlines for cavity of aspect ratio 3 with horizontal walls adiabatic**

$$\psi_{0s} = \sum_{k=1}^{\infty} C_k \left( \frac{1}{4} - y^2 \right) \cos(2k-1)\pi y \sinh(2k-1)\pi x \qquad (62)$$

$$C_k = \frac{(-1)^k}{2(2k-1)^4 \pi^4 \cosh(2k-1)\pi D} \qquad (63)$$

$$\psi_{0h} = 2\,\mathrm{Real}\left( \sum_{n=1}^{N} h_n \sinh \lambda_{en} x \phi_{en}(y) \right) \qquad (64)$$

The constants $h_n$ are evaluated using Shankar's [12] method. The evaluation for $\theta_1$ becomes mathematically complex, for the case of isothermal walls and hence $\theta_1$ could not be evaluated for this case.

## Results and Discussion

In the present study, the coefficients $h_n$ were calculated by solving the system of linear equations using MATLAB. The calculations were done for 40 and 80 eigenfunctions, respectively. However, no significant difference was observed in both the calculations. This indicates that 40 eigenfunctions are sufficient to approximate the infinite series. Calculations of the streamfunction were carried out for the cavity for two different boundary conditions, viz., all walls isothermal and horizontal walls adiabatic and vertical walls isothermal.

Figures 2 and 3 show the streamlines for a square cavity with all walls isothermal and with horizontal walls insulated, respectively. For both these cases, the streamfunction plots appear qualitatively similar, but the actual values of the stream function are different in both cases. Such differences are more pronounced for the cavity with aspect ratio 3, as shown in Figs. 4 and 5. It can be observed in both cases that the streamfunction values for all walls isothermal are approximately half the corresponding values for the case of horizontal walls adiabatic.

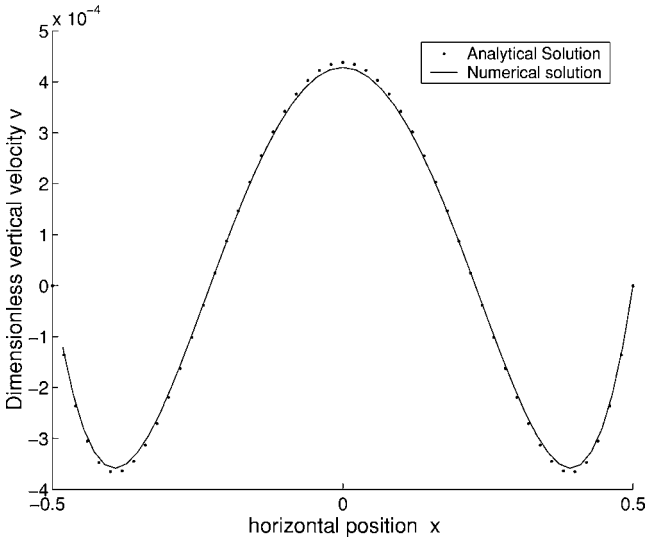


**Fig. 7 Vertical velocity profiles along the horizontal centerline for cavity with horizontal walls adiabatic**

Figure 6 shows the plot of the vertical component of velocity $v$ along the horizontal centerline. The results are compared with numerical simulations carried out using commercial software, FLUENT. In all the FLUENT simulations carried out, a $40 \times 40$ grid was used. Only small differences were found when the simulations were repeated on an $80 \times 80$ grid. A Prandtl number of 0.7 was used in all the simulations. Full Navier–Stokes equations were solved, using the SIMPLE method for pressure–velocity coupling and second-order upwind method for momentum discretizations.

It is found that for Ra=4900, the centerline vertical velocity is zero at dimensionless distance $x=0.22$. Figure 7 shows the plot of vertical velocity along the horizontal centerline, for a square cavity with horizontal walls adiabatic. In this case also, the velocity profile is qualitatively similar, but the magnitude of velocity is approximately twice that compared to the isothermal case, as shown in Fig. 6.

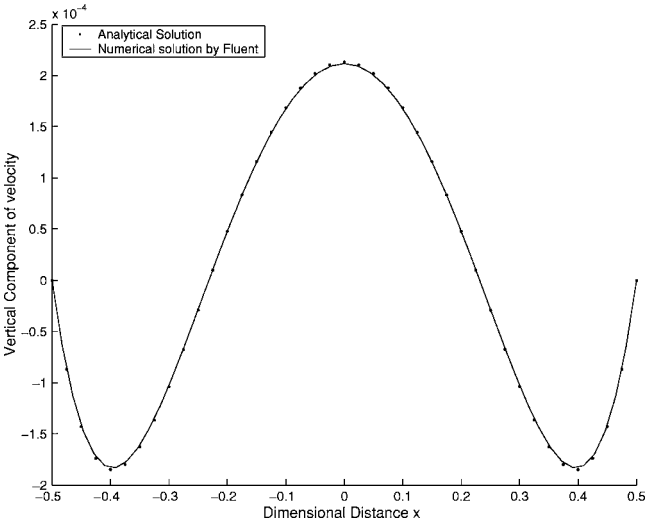


**Fig. 6 Vertical velocity profile along the horizontal centerline for cavity with isothermal walls**

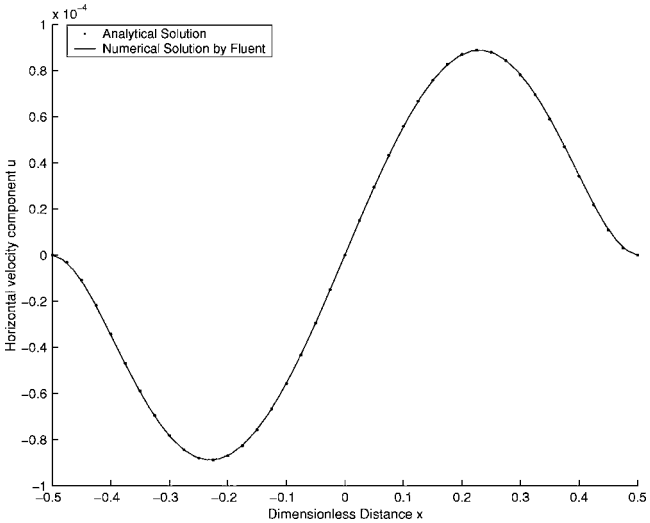


**Fig. 8 Horizontal velocity profile along $y=0.25$ for cavity with isothermal walls**

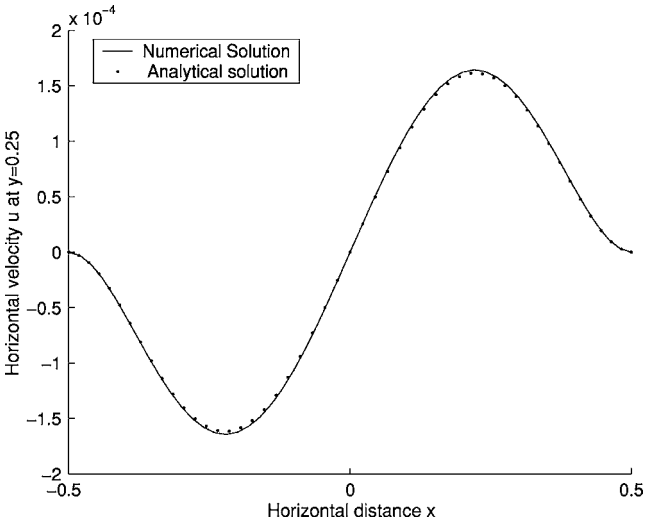


**Fig. 9 Horizontal velocity profile along $y=0.25$ for a cavity with horizontal walls adiabatic**

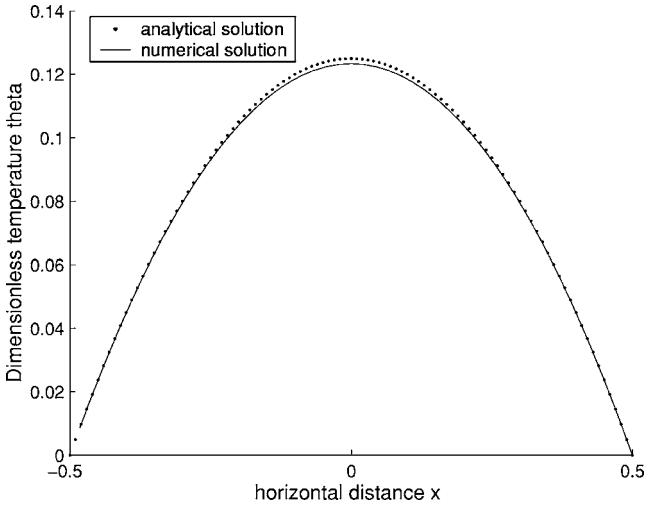


**Fig. 11 Variation of dimensionless temperature $\theta$ along horizontal centerline**

Figures 8 and 9 show the variation of horizontal velocity along the line $y=0.25$ for two different boundary conditions. The location $y=0.25$ is in the upper half of the cavity. It is observed that the velocity is negative for negative $x$ and positive for positive $x$.

Figure 10 shows the isotherms for the a square cavity with horizontal walls adiabatic at $\mathrm{Ra}=1000$, and the corresponding variation of temperature along the horizontal centerline is shown in Fig. 11. It is observed that the temperature is maximum at the center of the cavity and it decreases near the walls.

It is to be noted that in the earlier study [11], the analysis allowed only the vertical component of velocity to be evaluated for the cavity. In the present approach, it is possible to obtain both the velocity components within the cavity for any aspect ratio also. In addition to this, as mentioned earlier, in principle it is possible to obtain the solution at higher orders of Ra. The most difficult task is to find the particular solution to the biharmonic solution at every order. As the order of the solution increases, the series expansions becomes more and more complex. Therefore, in the present study, the solutions are restricted to the smaller orders only. It is reported in the literature [6] that periodic solutions are obtained for $\mathrm{Ra}=5\times10^4$. Such transient phenomena cannot be observed using the steady-state approach discussed here. Therefore, the maximum Rayleigh number considered here is 4900 which is approximately 1/10th this value. In spite of these limitations, the agreement of the results with the simulations suggests that smaller-order solutions are able to capture the essential flow characteristics for the square cavity with internal heat generation.

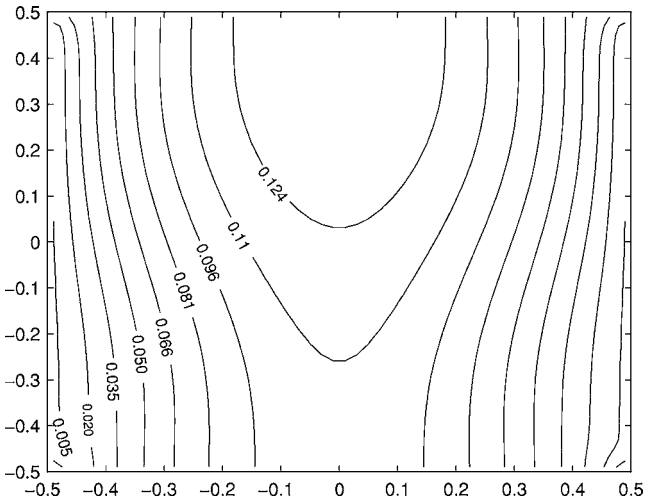


**Fig. 10 Isotherms for a square cavity with horizontal walls adiabatic**

## Conclusions

An analytical approach is formulated for studying natural convection in a cavity of arbitrary aspect ratio with uniform internal heat generation. The governing equations are written in terms of streamfunction and vorticity formulation and the variables are expanded in terms of the Rayleigh number. The solution to this problem with the appropriate boundary conditions involves solving for a biharmonic equation. It is observed that the velocity profiles are in good agreement with the numerical simulations obtained from Fluent. It is also found that a lower-order solution is adequate to capture the natural convection in the cavity.

## Nomenclature

$c$ = specific heat capacity
$g$ = acceleration due to gravity
$h$ = height of the cavity
$k$ = thermal conductivity
$l$ = length of the cavity
$p$ = pressure
Pr = Prandtl number
$q'''$ = heat generation per unit volume
Ra = Raleigh number
$T$ = temperature
$T_0$ = temperature at the boundaries
$u$ = dimensionless velocity in the $x$ direction
$v$ = dimensionless velocity in the $y$ direction
$x$ = dimensionless horizontal coordinate
$y$ = dimensionless vertical coordinate
$\theta$ = dimensionless temperature
$\psi$ = dimensionless stream function
$\omega$ = dimensionless vorticity

$\frac{\partial(f,g)}{\partial(x,y)}$ = Jacobian defined as $\left(\frac{\partial f}{\partial x}\frac{\partial g}{\partial y}-\frac{\partial f}{\partial y}\frac{\partial g}{\partial x}\right)$

## References


[1] Batchelor, G. K., 1953, "Heat Transfer by Free Convection Across a Closed Cavity Between Vertical Boundaries at Different Temperatures," Q. Appl. Math., **12**, pp. 209–233.

[2] Cormack, D. E., Leal, L. G., and Imberger, J., 1974, "Natural Convection in a Shallow Cavity With Differentially Heated End Walls. Part I. Asymptotic Theory," J. Fluid Mech., **65**, pp. 209–229.

[3] Kulacki, F. A., and Goldstein, R. J., 1975, "Hydrodynamic Instability in Fluid Layers With Uniform Volumetric Energy Sources," Appl. Sci. Res., **31**, pp. 81–109.

[4] Drazin, P. G., and Reid, W. H., 1981, *Hydrodynamic Stability*, Cambridge University Press, London.

[5] Fusegi, T., Hyun, J. M., and Kuwara, K., 1992, "Natural Convection in a Differentially Heated Cavity With Internal Heat Generation," Numer. Heat Transfer, Part A, Part A, **21**, pp. 215–229.

[6] May, H. O., 1991, "A Numerical Study on Natural Convection in an Inclined Square Enclosure Containing Internal Heat Resources," Int. J. Heat Mass Transfer, **34**, pp. 919–928.

[7] Di Piazza, I., and Ciofalo, M., 2000, "Low-Prandtl Number Natural Convection in Volumetrically Heated Rectangular Enclosures I, AR=4," Int. J. Heat Mass Transfer, **43**, pp. 3027–3051.

[8] Arcidiacono, S., Di Piazza, I., and Ciofalo, M., 2001, "Low-Prandtl Number Natural Convection in Volumetrically Heated Rectangular Enclosures II Square Cavity, AR=1," Int. J. Heat Mass Transfer, **44**, pp. 537–550.

[9] Arcidiacono, S., and Ciofalo, M., 2001, "Low-Prandtl Number Natural Convection in Volumetricaly Heated Rectangular Enclosures III. Shallow Cavity, AR=0.25," Int. J. Heat Mass Transfer, **44**, pp. 3053–3065.

[10] Daniels, P. G., and Jones, O. K., 1998, "Convection in a Shallow Rectangular Cavity Due to Internal Heat Generation," Int. J. Heat Mass Transfer, **41**, pp. 3979–3987.

[11] Joshi, M. V., Gaitonde, U. N., and Mitra, S. K., 2004, "Analytical Study of Natural Convection in a Cavity With Volumetric Heat Generation," in *Proceedings of ASME Heat Transfer/Fluids Engineering Summer Conference*, HT-FED2004-56302.

[12] Shankar, P. N., 1993, "The Eddy Structure in Stokes Flow in a Cavity," J. Fluid Mech., **250**, pp. 371–383.

**Piotr Filar**
Interdisciplinary Graduate School of Engineering Sciences,
Kyushu University,
Kasuga Koen 6-1,
816-8580 Fukuoka, Japan

**Elzbieta Fornalik**[1]
Interdisciplinary Graduate School of Engineering Sciences,
Kyushu University,
Kasuga Koen 6-1,
816-8580 Fukuoka, Japan and
Department of Theoretical Metallurgy and Metallurgical Engineering,
AGH University of Science and Technology,
30 Mickiewicz Avenue,
30-059 Krakow, Poland

**Toshio Tagawa**

**Hiroyuki Ozoe**

Interdisciplinary Graduate School of Engineering Sciences,
Kyushu University,
Kasuga Koen 6-1,
816-8580 Fukuoka, Japan

**Janusz S. Szmyd**
Department of Theoretical Metallurgy and Metallurgical Engineering,
AGH University of Science and Technology,
30 Mickiewicz Avenue,
30-059 Krakow, Poland

# Numerical and Experimental Analyses of Magnetic Convection of Paramagnetic Fluid in a Cylinder

*The magnetic convection of paramagnetic fluid in a cylindrical enclosure is studied experimentally and numerically. The upper side wall of the cylinder is cooled and the lower side wall heated, an unstable configuration. The whole system is placed coaxially in a bore of a superconducting magnet in the position of the minimum radial component of magnetic buoyancy force at the middle cross section of the enclosure. The stable configuration — when the whole system is placed inversely and the horizontal axial case are also considered. As a paramagnetic fluid an aqueous solution of glycerol with the gadolinium nitrate hexahydrate is used. The isotherms in the middle-height cross section are visualized by thermochromic liquid crystal slurry. For the unstable configuration the magnetic buoyancy force acts to assist the gravitational buoyancy force to give multiple spoke patterns at the mid cross section. The stable configuration gives an almost stagnant state without the magnetic field. Application of the magnetic field induces the convective flow similar to the unstable configuration. For the horizontal configuration a large roll convective flow (without the magnetic field) is changed under the magnetic field to the spoke pattern. The numerical results correspond to the experimental results.*
[DOI: 10.1115/1.2142334]

*Keywords: magnetic buoyancy force, gravitational buoyancy force, convection, thermosyphon, visualization, numerical simulation*

## 1 Introduction

The convection of fluid has been known to be affected by the magnetic field depending on its electroconductivity. The liquid metal has a large value of the electroconductivity and the Lorentz force acts under a magnetic field. Some of the early works are discussed in the book of Chandrasekhar [1]. There are a plenty of applications of the Lorentz force for industry [2,3]. On the other hand, the nonelectroconducting fluid such as air, water, etc., has been considered to be insensitive to the magnetic field for many years. However, probably with an invention of oxide materials which have almost no electric resistance at high temperature [4], super-conducting magnets become commercially available to allow various experiments under very strong magnetic fields [5–8]. The theoretical modeling and numerical analyses for these phenomena have been reported progressively [9–11]. These new phenomena have been known to be caused by the magnetic (or magnetization or magnetizing) force [12]. This magnetic force $\mathbf{f}_{\mathrm{mag}}$ is proportional to the volumetric magnetic susceptibility of materials $\chi_m$ ($=\rho\chi$ where $\rho$ is the density and $\chi$ is the mass magnetic susceptibility), the gradient of the square of the magnetic induction $\nabla\mathbf{b}^2$, and inversely proportional to the magnetic permeability $\mu_m$, i.e., $\mathbf{f}_{\mathrm{mag}}=\chi_m\nabla\mathbf{b}^2/(2\mu_m)$. This force acts for the nonuniform magnetic fields and becomes large for materials with large absolute value of volumetric magnetic susceptibility. These nonelectroconducting materials are classified either paramagnetic ($\chi_m>0$) or diamagnetic ($\chi_m<0$) materials. Paramagnetic materials are attracted toward the stronger magnetic field and the diamagnetic ones are repelled. Furthermore, the mass magnetic susceptibility of paramagnetic materials $\chi$ has been known to be inversely proportional to its absolute temperature according to the Curie's law [12]. This temperature dependence of magnetic susceptibility was modeled by Tagawa et al. [11] in the momentum equation just like a Boussinesq approximation and has been employed to analyze various convections caused by a magnetic field [9–11]. This magnetic force is caused by a large electric current in a superconducting magnet whose cylindrical geometrical size is typically about 0.50 m in diameter and 0.60 m long in vertical height. This magnet can be oriented in any direction and can be employed to control various transport phenomena even in the field of constant gravitational acceleration field on Earth. The motivation of the present study is to see three extreme cases of orientation of the magnetic field on the convection of fluid in a cylindrical enclosure parallel, inversely parallel, or lateral with the gravitational acceleration. The convection of fluid can be studied in various configurations but in the present work, the thermosyphonlike system is adopted for the possible application for the fluid mixing with and/or without a gravitational acceleration.

[1]Corresponding author; e-mail: elaf@agh.edu.pl
Contributed by the Heat Transfer Division of ASME for publication in the JOURNAL OF HEAT TRANSFER. Manuscript received February 9, 2005; final manuscript received July 26, 2005. Review conducted by John H. Lienhard V.

  

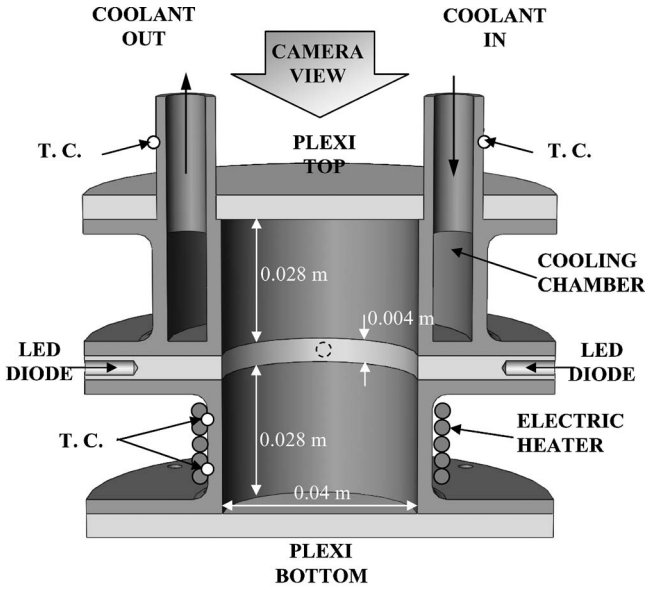


**Fig. 1 Schematical view of the experimental apparatus**

The single phase closed thermosyphon was studied experimentally and theoretically by Japikse et al. [13] in 1971. They found the appearance of an angular pattern in the enclosure midheight, resulted from the crossing streams of warm and cold fluid. Bayley and Lock [14], Lock and Liu [15], and Lock and Kirchner [16] studied the various effects of geometrical configurations, inclination angles, and fluid properties on the convection mode and the heat transfer rate in the closed thermosyphon. Ishihara et al. [17,18] provided the experimental and numerical investigations of the thermosyphon system both in the cylindrical and rectangular geometries. They reported the angular patterns observed in the horizontal sections of the system whose number depended on the fluid properties, and the geometrical and thermal conditions.

Although the study on the magnetic convection is progressing very dynamically, the effect of magnetic field on the convection of a paramagnetic liquid in the thermosyphonlike configuration has not been studied so far. In the present paper the experimental visualization of the flow modes of a paramagnetic fluid under the magnetic field in the thermosyphon configuration are compared with the numerical results.

## 2 Experimental System

The experimental investigation is carried out for the thermosyphonlike enclosure presented in Fig. 1. Its inner diameter is 0.04 m and height 0.06 m. The enclosure consists of the cooled and heated copper parts separated by the 0.004 m thick Plexiglas adiabatic zone. The cooled part is a thermostating jacket filled with the water from a constant-temperature bath. A wire heater coated by rubber is used to heat the lower part of the enclosure. It is winded on the outer surface of the copper cylinder and connected to a dc power supply. The temperatures of the cooled and heated walls are measured by the T-type thermocouples. Two thermocouples are placed on the inlet and outlet of the coolant and the other two are located on the surface of the heated part. They are marked as the white circles named T.C. in Fig. 1.

The 50% volume aqueous solution of glycerol is selected as a working fluid but this mixture is diamagnetic. Therefore the crystals of $Gd(NO_3)_3 \cdot 6H_2O$ are dissolved in the working fluid increasing its magnetic susceptibility. The 0.5 mol/kg concentration of gadolinium nitrate hexahydrate is prepared as a working fluid. The viscosity, density, and magnetic susceptibility of this fluid are measured but the other physical properties are estimated for 50% aqueous solution of glycerol from [19]. The properties are summarized in Table 1.

**Table 1 The properties of 0.5 mol/kg solution of gadolinium nitrate in the glycerol aqua solution (vol. 50%) at $\theta_{ref}=298$ K and $p_{ref}=1013$ hPa and the dimensions of the enclosure**

| Property | Value | Unit |
|---|---|---|
| $h$ | 0.06 | m |
| $r_0$ | 0.02 | m |
| $c_p$ | $3.283\times10^{3}$ | J/(kg K) |
| $\alpha$ | $1.1415\times10^{-7}$ | $m^2/s$ |
| $\beta$ | $0.445\times10^{-3}$ | $K^{-1}$ |
| $\eta$ | $(6.145\pm0.064)\times10^{-3}$ | Pa·s |
| $\mu_m$ | $4\pi\times10^{-7}$ | H/m |
| $\nu$ | $(4.80\pm0.05)\times10^{-6}$ | $m^2/s$ |
| $\rho$ | $1281\pm1$ | $kg/m^3$ |
| $\chi_0$ | $17.839\times10^{-5}$ | |
| Pr | 42.1 | |

The relative magnitude between the magnetic force versus the gravitational force for the paramagnetic fluid as represented by the last two terms of Eq. (3) shown later can be computed for the present system as follows:

$$\begin{aligned}\mathbf{f}_{mag}/\mathbf{f}_{grav} &= [1+(\beta\theta_0)^{-1}][\rho\chi\nabla\mathbf{b}^2/(2\mu_m)]/(\rho g)\\ &= [1+(0.445\times10^{-3}\times298)^{-1}](13.926\times10^{-8}\\ &\quad\times140)/(2\times4\pi\times10^{-7}\times9.81)\\ &= 6.75 \quad \text{for } \nabla\mathbf{b}^2 = 140\ \mathrm{T}^2/\mathrm{m}.\end{aligned}$$

This magnitude of $\nabla\mathbf{b}^2=140\ \mathrm{T}^2/\mathrm{m}$ is available for the superconducting magnet with maximum strength of 5 T or less and the magnetic force is much greater than the gravitational force for the present experiment.

The temperature field of the fluid in the middle-height cross section (in the adiabatic zone) is visualized by using the thermochromic liquid crystal slurry. It has a color range from 291 K to 294.7 K. The liquid crystals are illuminated by the four light-emitting diodes (LED) placed at the perimeter of the adiabatic zone. The color images of the isotherms are taken by a digital camera. The detailed correspondence between the color and temperature with this liquid crystal was reported by Ozoe et al. [20] for the model system of Czochralski melt motion and not repeated herein in detail.

In the experiment three configurations of the enclosure (unstable, stable, and horizontal) are considered. They are presented in Fig. 2: in Fig. 2(*a*) the unstable (heated from the lower side wall and cooled from the upper one); in Fig. 2(*b*) the stable (heated from the upper side wall and cooled from the lower one); and in Fig. 2(*c*) the horizontal configurations of the system. In every case the enclosure is placed in a bore of the superconducting magnet at the same level. The middle-height cross section is placed at 0.07 m from the level of solenoid center. That level represents the minimum radial component of the magnetic buoyancy force.

The visualization is done for various Rayleigh numbers and various magnetic field strengths (0 T, 1 T, and 2 T). The visualized and computed cases are listed in Table 2.

## 3 Experimental Results

Figure 3 shows the experimental results of temperature field visualization. Figure 3(*a*) presents the photograph of isotherms in the cylinder cross section at the middle height for the unstable configuration of the system (Fig. 2(*a*)), at $\mathrm{Ra}=1.69\times10^{5}$ and the magnetic field of 0 T. This configuration is called unstable due to the convection induced even without a magnetic field. Five red and five blue alternating angular spokes can be seen. The red color

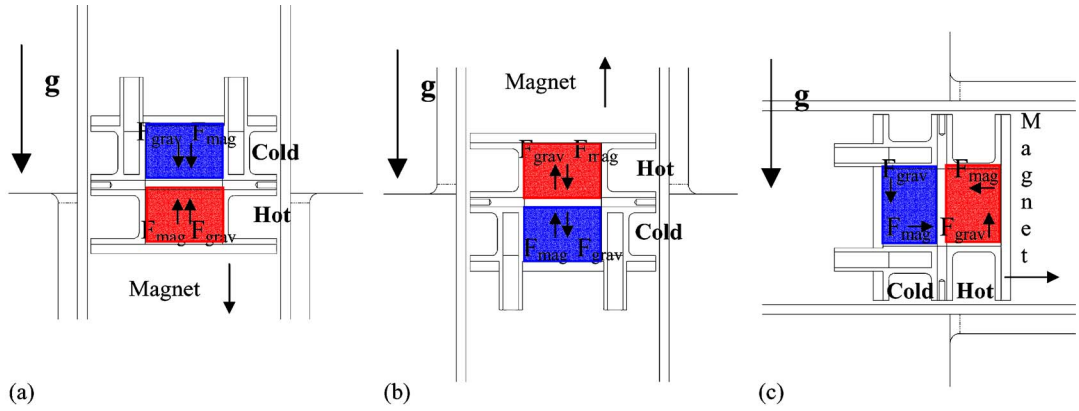


**Fig. 2 The configurations of modeled system; (*a*) unstable, (*b*) stable, and (*c*) horizontal**

indicates the cold fluid and the blue one represents the hot fluid. This condition of $Ra=1.69\times10^5$ corresponds to a temperature difference of 2.65 K. However this small temperature difference makes about 1% difference in the mass magnetic susceptibility since it is proportional to the inverse of its absolute temperature. On the other hand, the density change for liquid with the equation of state $\rho=\rho_0/(1+\beta(\theta-\theta_0))$ gives only 0.1% difference for the gravity force.

Figure 3(*b*) presents the results at $Ra=1.67\times10^5$ and 1 T of the magnetic induction for the unstable configuration of the system. The applied magnetic field intensifies the convection and the hot wall temperature decreases slightly under the uniform heat flux with the constant temperature at the cooling wall. This slight decrease in the hot wall temperature decreases the Rayleigh number slightly. The six red and six blue angular spokes can be seen.

Figure 3(*c*) shows a photograph of the isotherms at the middle-height cross section for the stable configuration (Fig. 2(*b*)) at $Ra=2.57\times10^5$ and without a magnetic field. The enclosure heated from the upper and cooled from the lower parts of the side walls represents the gravitationally stable configuration and the almost conduction state is expected. The experimental visualization shows the uniform color of the cross section, which suggests that the fluid in the whole illuminated section has almost the same temperature. When the maximum magnetic induction achieves the level of 2 T, strong convection occurs as presented in Fig. 3(*d*). It shows the photograph of isotherms at the cylinder middle height for the stable configuration, at $Ra=1.89\times10^5$ and 2 T of the magnetic induction. Seven spokes of red and blue colors can be observed. The spoke pattern is characteristic for the unstable configuration and it means that even in the stable configuration the convective motion can be observed when the magnetic field is strong enough.

Figure 3(*e*) shows the photograph of isotherms at the cylinder middle height for the horizontal configuration of the system (Fig. 2(*c*)), at $Ra=1.70\times10^5$ and 0 T of the magnetic induction. Without a magnetic field the cold fluid flow (indicated by the red color) is present in the bottom part of the visualized cross section, while the hot fluid indicated by the blue color appears in the top part of that plane. It suggests one global convective roll. Figure 3(*f*) shows the photograph of the temperature field for the horizontal configuration at $Ra=1.51\times10^5$ and 2 T of the magnetic induction. Two spokes of the red color near the left-hand-side and right-hand-side antipodes of the cross section can be visible. The hot spokes indicated by the blue color are not observed, probably because of the low color resolution of the liquid crystals in the upper area of the temperature range. The appearance of the spoke patterns similar to the patterns presented in Figs. 3(*a*), 3(*b*), and 3(*d*) suggests that the axial horizontal driving force due to magnetic field appears in the horizontal system.

**Table 2 Computed and experimental cases**

| Configuration | Rayleigh number, Ra | Magnetic ind., b (T) |
|---|---|---|
| Unstable | $1.69\times10^5$ | 0 |
| Unstable | $1.67\times10^5$ | 1 |
| Stable | $2.57\times10^5$ | 0 |
| Stable | $1.89\times10^5$ | 2 |
| Horizontal | $1.70\times10^5$ | 0 |
| Horizontal | $1.51\times10^5$ | 2 |

## 4 Computational System

**4.1 Modeled System.** The system in Fig. 4(*a*) corresponds to the real system investigated experimentally, although several assumptions are made for simplification. The system consists of a cylindrical enclosure with an aspect ratio $AR=(h/r_0)=3$, filled with paramagnetic liquid. The upper 7/15 part of the cylinder side wall is isothermally cooled and the lower 7/15 one is isothermally heated. The central 1/15 part of the cylinder side wall and the top/bottom end plates are assumed to be thermally adiabatic. The hot wall of the experimental enclosure is heated with an uniform heat flux, but in the numerical analysis this condition is replaced by isothermal heating to maintain the same Rayleigh number. The cylindrical side wall is made of copper as described later and this assures an almost isothermal condition.

The properties of the working fluid correspond to the properties of the fluid employed in the experimental analysis. The fluid properties together with the dimensions of the enclosure are listed in Table 1.

Figures 4(*b*) and 4(*c*) show the vectors of magnetic induction $\mathbf{b}$ and $\nabla\mathbf{b}^2$ to show the distribution of these vectors for 5 T at the solenoid center.

**4.2 Mathematical Model and Numerical Implementation.** The mathematical model for the magnetic buoyancy force for paramagnetic fluid was developed by Tagawa et al. [11] following the work by Bai et al. [12]. The fluid is assumed to be Newtonian, incompressible, and the Boussinesq approximation is employed.

The governing equations consist of the continuity Eq. (1), the energy Eq. (2), the coupled momentum Eq. (3), and the Biot Savart's Eq. (4). They could be written as follows in dimensionless form:

$$\nabla\cdot\mathbf{V}=0 \tag{1}$$

$$\frac{DT}{D\tau}=\nabla^2T \tag{2}$$

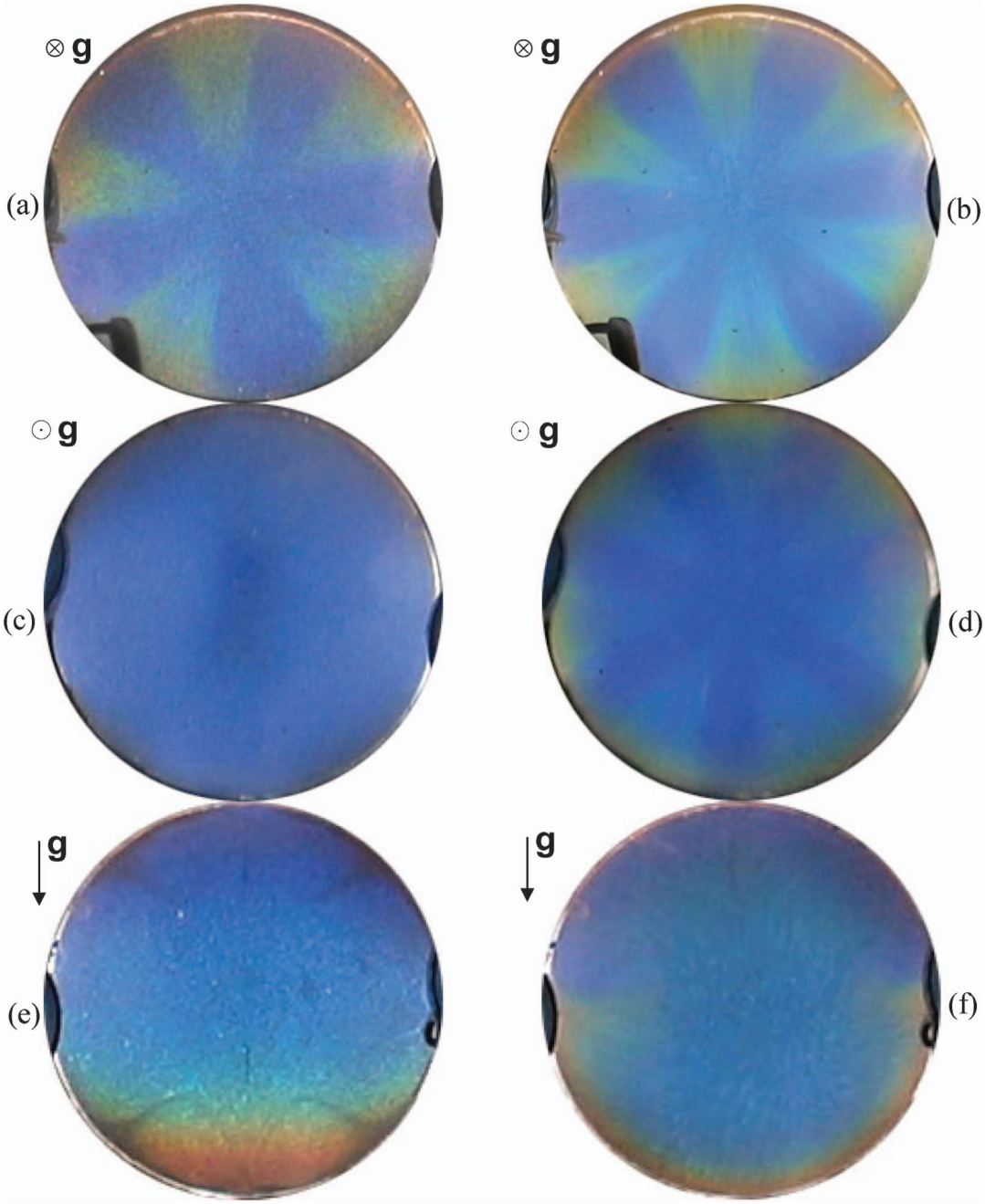


**Fig. 3 Photographs of the isotherms at the midheight of the cylinder: (*a*) at Ra=1.69×10$^5$ and *b*=0 T, unstable configuration, (*b*) at Ra=1.67×10$^5$ and *b*=1 T, unstable configuration, (*c*) at Ra=2.57×10$^5$ and *b*=0 T, stable configuration, (*d*) at Ra=1.89×10$^5$ and *b*=2 T, stable configuration, (*e*) at Ra=1.70×10$^5$ and *b*=0 T, horizontal configuration, and (*f*) at Ra=1.51×10$^5$ and *b*=2 T, horizontal configuration**

$$\frac{D\mathbf{V}}{D\tau} = -\nabla P + \mathrm{Pr}\nabla^2\mathbf{V} + \mathrm{RaPr}T\left[-\frac{[1+1/(\beta\theta_0)]}{2}\gamma\nabla\mathbf{B}^2 + (\mathbf{e}_z)\right] \tag{3}$$

$$\mathbf{B} = \frac{1}{4\pi}\oint_{\mathrm{coil}}\frac{d\mathbf{S}\times\mathbf{R}}{\mathbf{R}^3} \tag{4}$$

with the following dimensionless variables:

$$P = p/p_0, \quad \mathbf{R} = \mathbf{r}/r_0, \quad \mathbf{S} = \mathbf{s}/r_0, \quad T = (\theta-\theta_0)/(\theta_{\mathrm{hot}}-\theta_{\mathrm{cold}}),$$
$$\mathbf{V} = \mathbf{v}/u_0, \quad \tau = t/t_0, \quad b_0 = \mu_m i/r_0, \quad p_0 = \rho_0\alpha^2/r_0^2,$$
$$t_0 = r_0^2/\alpha, \quad u_0 = \alpha/r_0, \quad \theta_0 = (\theta_{\mathrm{hot}}+\theta_{\mathrm{cold}})/2.$$

The characteristic nondimensional variables are defined as follows:

$$\mathrm{Pr} = \nu/\alpha \quad \text{the Prandtl number}$$

$$\mathrm{Ra} = g\beta(\theta_{\mathrm{hot}}-\theta_{\mathrm{cold}})r_0^3/(\alpha\nu) \quad \text{the Rayleigh number}$$

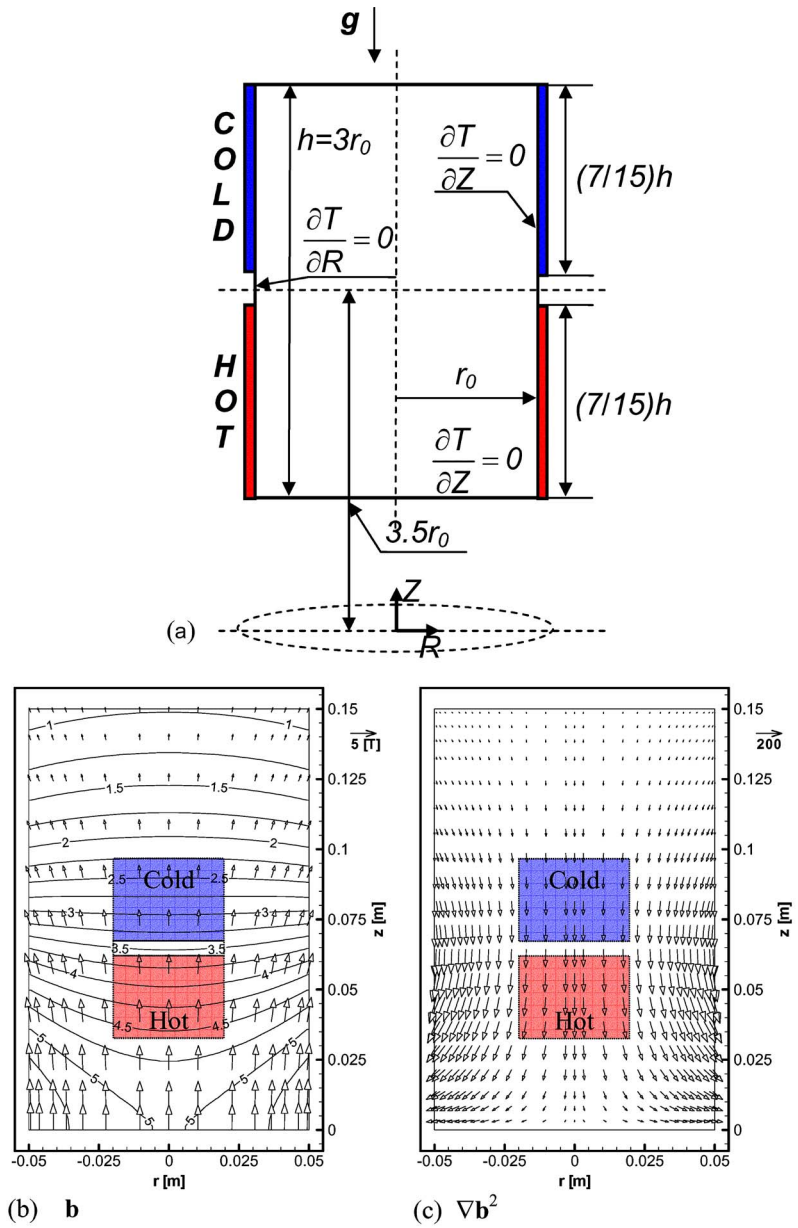


**Fig. 4** (*a*) **Modeled system in the unstable configuration,** (*b*) **distribution of magnetic induction b,** (*c*) **distribution of gradient of square magnetic induction** $\nabla \mathbf{b}^2$

$\gamma = \chi b_0^2/(\mu_m g r_0)$ the gamma parameter

The problem is solved over the staggered grid system $16 \times 37 \times 45$ in the radial, in the angular and in the axial directions, respectively. The numerical error in the similar system [10] was computed as 4% or less for much coarse grids of $21 \times 21 \times 11$ and the error is expected to be much less for the present system. The initial and boundary conditions are as follows: At $\tau = 0$, $\mathbf{V} = \mathbf{0}$, $T = 0$, At $0 \leqslant R \leqslant 1.0$ and $Z = 0$, $Z = 3.0$ (the adiabatic bottom and top end plates)

$$\mathbf{V} = \mathbf{0}, \quad \partial T/\partial Z = 0,$$

At $R = 1$ and $0 \leqslant Z \leqslant 1.4$ (cylinder wall—the heating zone)

$$\mathbf{V} = \mathbf{0}, \quad T = +0.5,$$

At $R = 1$ and $1.4 < Z < 1.6$ (cylinder wall—the adiabatic zone)

$$\mathbf{V} = \mathbf{0}, \quad \partial T/\partial R = 0,$$

At $R = 1$ and $1.6 \leqslant Z \leqslant 3$ (cylinder wall—the cooling zone)

$$\mathbf{V} = \mathbf{0}, \quad T = -0.5.$$

The mathematical problem of a computational singularity at the radial center is circumvented by the technique of Ozoe and Toh [21]. The computations are carried out with the three-dimensional Highly Simplified Marker and Cell (HSMAC) [22] algorithm with the third-order upwind scheme applied for the inertial terms.

Numerical computations are carried out for the same conditions as the experiment. The dimensionless parameters are computed from the experimental conditions and the properties of the fluid. As for the unstable configuration of the system, convection is

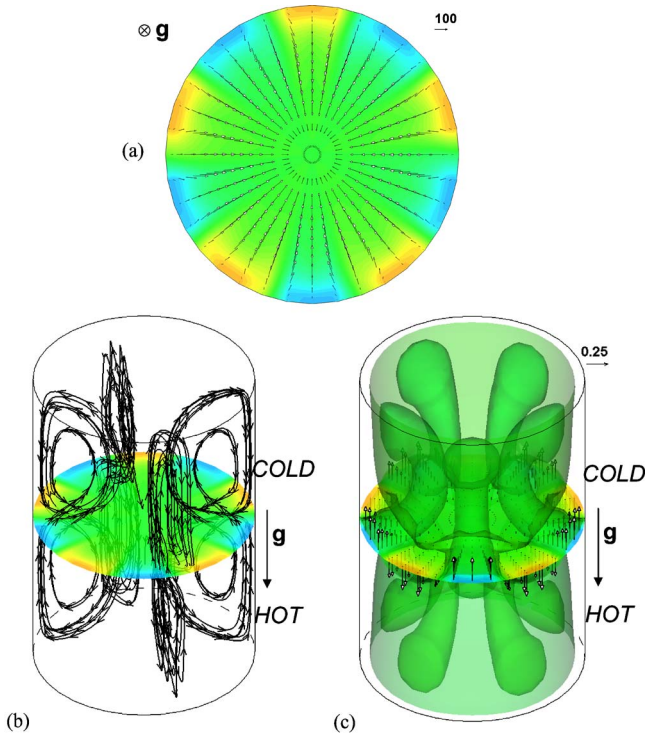


**Fig. 5 The results for the unstable system at Ra=1.69×10^5 and *b*=0 T: (*a*) computed isothermal contours with velocity vectors; (*b*) computed isotherms at cylinder midheight and three-dimensional demonstration of long time streak lines; and (*c*) isothermal contours at *T*=±0.05 and the gravitational buoyancy force vectors**

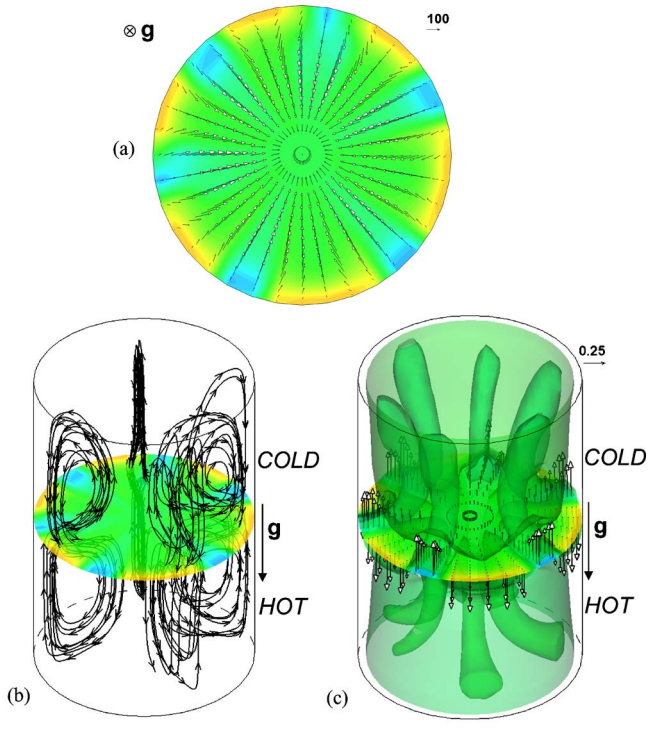


**Fig. 6 The results for the unstable system at Ra=1.67×10^5 and *b*=1 T: (*a*) computed isothermal contours with velocity vectors; (*b*) computed isotherms at cylinder midheight and three-dimensional demonstration of long time streak lines; and (*c*) isothermal contours at *T*=0.01 and *T*=0.08 and the total force vectors**

calculated under the magnetic induction 0 and 1 T, for the stable and horizontal configurations, computations for 0 and 2 T are carried out.

## 5 Comparison of Computational Results With Experiments

**5.1 Unstable Configuration of the System.** As shown in Fig. 2(*a*), the enclosure is heated from the lower side wall and cooled from the upper side wall and the convection occurs even without a magnetic field. Figure 5 shows the calculated results at Ra $=1.69\times10^5$ and the magnetic field of 0 T. Figure 5(*a*) shows the calculated isotherms and velocity vectors at the cylinder middle height. Five spokes of light gray color (representing the cold fluid) and five dark gray (representing the hot fluid) placed alternatively along the perimeter of the cross section can be counted. They correspond to the five blue and five red spokes presented in Fig. 3(*a*). Figure 5(*b*) shows calculated isotherms at the middle-height cross section with the three-dimensional demonstration of long time streak lines starting from four different angular positions. The fluid moves upward near the lower heated side wall, then proceeds toward the enclosure center at the middle height and near the center ascends toward the top of the cylinder. Finally fluid descends along the upper cooled side wall. This trajectory is typical for the thermosyphon systems and was reported by Japikse et al. [13] and Ishihara et al. [17,18]. Figure 5(*c*) shows the fingerlike isothermal contours of $T=-0.05$ and $T=0.05$ and the gravitational buoyancy force vectors $\mathbf{F}_{\text{grav}}$ drawn at the cylinder middle height. The isothermal contours correspond to the five spoke patterns obtained at the middle-height level of the enclosure.

Figure 6 presents the computed results at Ra $=1.67\times10^5$ and 1 T of the magnetic induction. In Fig. 6(*a*) the six spokes of light gray (dilute color spokes of cold fluid) and dark gray (dark color spokes of hot fluid) can be counted in the computed result similarly to the six red and blue spokes observed in Fig. 3(*b*). Figure 6(*b*) shows calculated isotherms at the cylinder middle height with the three-dimensional demonstration of long time streak lines starting from four different angular positions. Figure 6(*c*) shows the isothermal contours of $T=0.01$ and $T=0.08$ and the total force vectors $\mathbf{F}_{\text{mag}}+\mathbf{F}_{\text{grav}}$ drawn at the cylinder middle height. The magnetic field does not change the general flow structure, but the number of spokes increases from five to six. The finger-shape isothermal contours become distorted slightly. The magnetic susceptibility of paramagnetic fluid is proportional to the inverse of its absolute temperature by Curie's law as reflected in Eq. (3). The cold fluid is relatively attracted to the magnet and the hot fluid is repelled. The cold fluid at the cylinder middle height, indicated by the red color falls down due to its higher density and simultaneously it is attracted downward by the magnetic buoyancy force. The hot fluid of low density flows upward driven by the gravitational buoyancy force and repelled upward by the magnetic buoyancy force. The difference in the total force vectors shown in Figs. 5 and 6 is due to the magnetic buoyancy force. For 0 T and 1 T of the magnetic induction, computed numbers of spokes agree with that of the experiment to support present theoretical approach.

**5.2 Stable Configuration of the System.** The stable configuration of the system is shown in Fig. 2(*b*). This configuration is a reversed configuration of the previous system. The enclosure is heated from the upper side wall and cooled from the lower part. Under such a configuration, the fluid is almost stagnant in the gravitational field and the convection becomes very weak. Figure 7 presents the computed results at Ra $=2.57\times10^5$ and without a magnetic field. Figure 7(*a*) shows the calculated isotherms and velocity profiles at the cylinder middle height. It shows only one color, suggesting the isothermal field, which is similar to the tem-

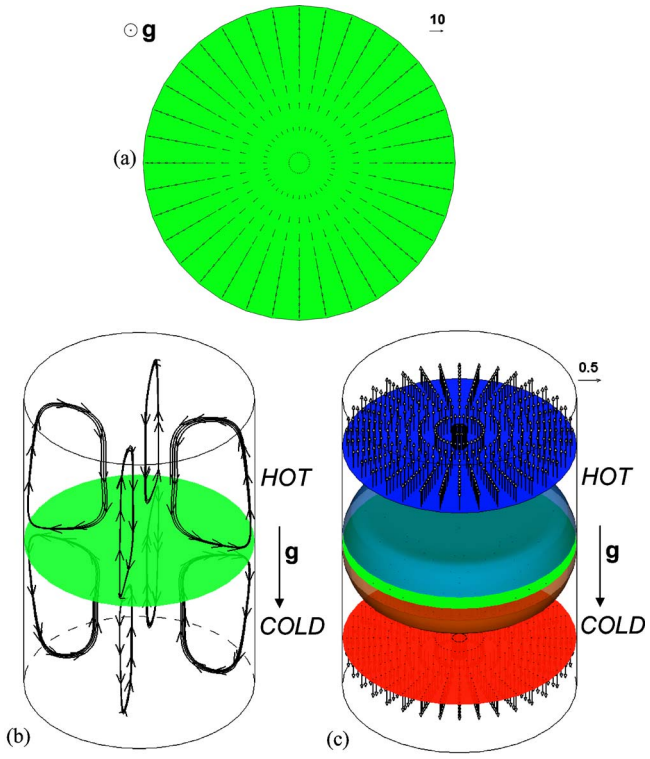


**Fig. 7 The isotherms for the stable system at Ra=2.57×10$^5$ and *b*=0 T: (*a*) computed isothermal contours with velocity vectors; (*b*) computed isotherms at cylinder midheight and three-dimensional demonstration of long time streak lines; and (*c*) isothermal contours at *T*=±0.4 and gravitational buoyancy force vectors**

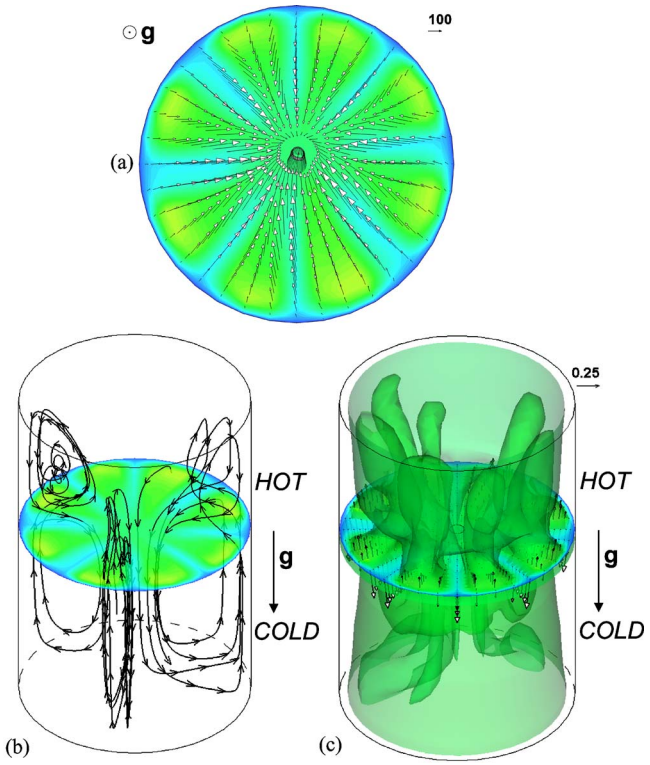


**Fig. 8 The results for the stable system at Ra=1.89×10$^5$ and *b*=2 T: (*a*) computed isothermal contours with velocity vectors at *Z*=1.68; (*b*) computed isotherms at *Z*=1.68 and three-dimensional demonstration of long time streak lines; and (*c*) isothermal contours at *T*=0.04 and *T*=0.1 and total force vectors**

perature field presented in Fig. 3(*c*). Figure 7(*b*) shows calculated isotherms at the cylinder middle height with three-dimensional demonstration of long time streak lines. This shows two separate axially symmetric natural convection cells in the lower and upper parts of the enclosure. There is no flow crossing the middle-height plane. Figure 7(*c*) shows the isothermal contours of $T=-0.4$ and $T=0.4$ and the gravitational buoyancy force vectors $\mathbf{F}_{\text{grav}}$ at $Z=0.5$, 1.5, and 2.5. The strongly temperature stratified situation can be observed with the vectors of gravitational buoyancy force drawn in three horizontal levels at $Z=0.5$, $Z=1.5$, and $Z=2.5$, respectively. Since the temperature at the middle-height plane $Z=1.5$ is $T\approx 0$, almost no buoyant force appears. The cold fluid marked with the red color fills the lower part of the enclosure due to its higher density, and the hot fluid indicated by the blue color remains in the upper part of the enclosure.

Figure 8 presents the calculated results at $\text{Ra}=1.89\times10^5$ and 2 T of the magnetic induction. Figure 8(*a*) shows the calculated isotherms and velocity profiles at $Z=1.68$. The calculation for the stable configuration under 2 T of the magnetic induction shows eight angular spokes, while the experimental result in Fig. 3(*d*) shows seven spokes. For the present case, the spokes are shown at the level slightly above the cylinder middle height $Z=1.68$, so that spokes appear clearly. This plane corresponds to the height 0.0036 m above the middle-height visualization cross section in the experimental enclosure. In the experiment, the LEDs for the flow illumination are located at the middle height of the enclosure. At this level spokes could be also visible in the experiment due to the diffusion of an illuminating light. The magnetic induction of 2 T overcomes the temperature stratification and induces the convection in the originally stagnant system. Figure 8(*b*) presents calculated isotherms at the cylinder middle-height level and the three-dimensional demonstration of long time streak lines starting from three different angular positions, while in Fig. 8(*c*) the isothermal contours of $T=0.04$, $T=0.1$, and the total force vectors $\mathbf{F}_{\text{mag}}+\mathbf{F}_{\text{grav}}$ at $Z=1.5$ (the cylinder middle-height cross section). The magnetic induction of 2 T overcomes the gravitational buoyancy force and induces the convection in the system. The long time streak lines are similar to those of the unstable system without a magnetic field presented in Fig. 5(*b*). The fluid moves along the trajectories driven by the magnetic buoyancy force. The calculated isothermal contours are typical for the natural convection inside the thermosyphon heated from the lower part of the side wall and cooled from the upper one.

**5.3 Horizontal Configuration of the System.** The horizontal configuration of the system is shown in Fig. 2(*c*). Figure 9 presents the computed results at $\text{Ra}=1.70\times10^5$ and 0 T of the magnetic induction. Figure 9(*a*) shows the calculated isotherms, velocity profiles in the cylinder middle-height cross section. The light gray color in the bottom part of the visualized cross section represents the cold fluid, while the dark gray color in the top part represents the hot fluid. This flow structure is similar to the one presented in Fig. 3(*e*). It suggests that the global convection cell appears for the horizontal system under the nonmagnetic field. Figure 9(*b*) shows the perspective view of the present system. Figure 9(*c*) shows the isothermal contours of $T=-0.1$, $T=0$, $T=0.1$, and the gravitational buoyancy force vectors $\mathbf{F}_{\text{grav}}$, drawn at $Z=0.5$, 1.0, 1.5, 2.0, and 2.5. The long time streak lines shown in Fig. 9(*b*) and the isothermal contours presented in Fig. 9(*c*) confirm the single roll convection mode inside the enclosure, with the fluid partially heated and partially cooled along the side wall.

Figure 10 shows the calculated isotherms in the cylinder middle-height cross section for the horizontal configuration of the system, at $\text{Ra}=1.51\times10^5$ and 2 T of the magnetic induction. The

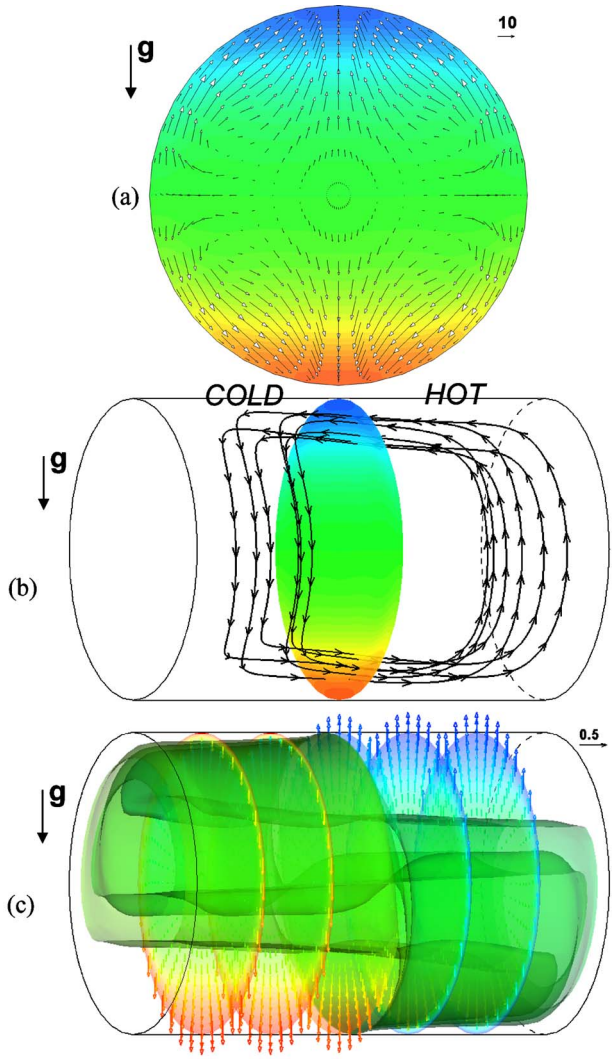


**Fig. 9 The isotherms for the horizontal system at Ra=1.70 $\times 10^5$ and $b=0$ T: (*a*) computed isothermal contours with velocity vectors at the midheight; (*b*) computed isotherms at the cylinder midheight and three-dimensional demonstration of long time streak lines; and (*c*) isothermal contours and the gravitational buoyancy force vectors. Isothermal contours are at $T=0$ and $T=\pm 0.1$**

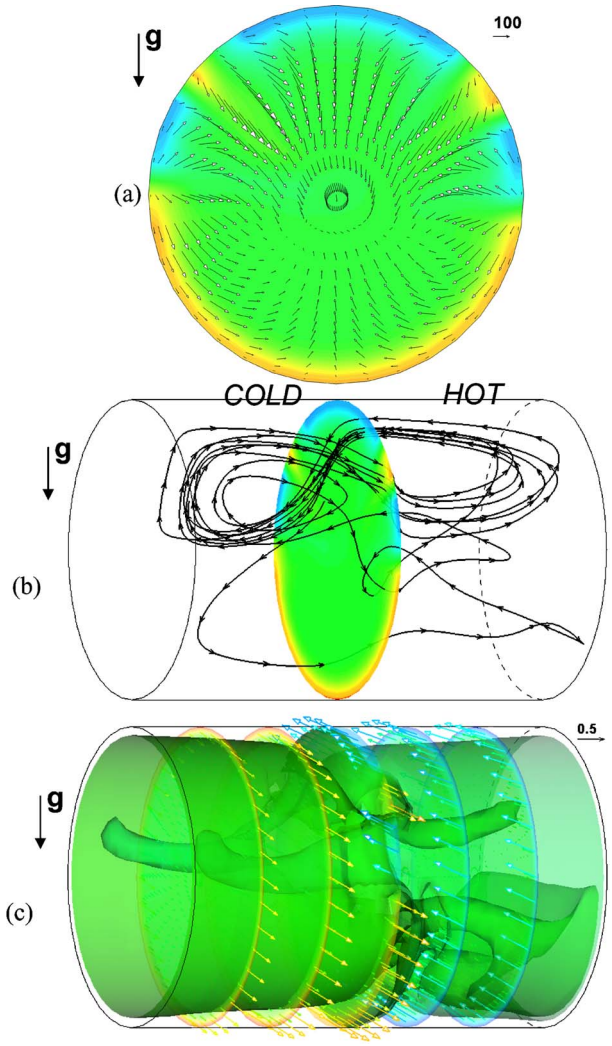


**Fig. 10 The isotherms for the horizontal system at Ra=1.51 $\times 10^5$ and $b=2$ T: (*a*) computed isothermal contours with velocity vectors at the midheight; (*b*) computed isotherms at cylinder midheight and three-dimensional demonstration of long time streak lines; and (*c*) isothermal contours and total force vectors. Isothermal contours are at $T=-0.04$ and $T=0.08$**

numerical calculation gives two hot and two cold spokes (Fig. 10(*a*)). The magnitude of the velocity reference vector presented in Fig. 10(*a*) is ten times larger than that in Fig. 9(*a*), for the nonmagnetic case. Figure 10(*b*) shows calculated isotherms in the middle-height cross section with the three-dimensional demonstration of long time streak lines. Figure 10(*c*) shows the isothermal contours of $T=-0.04$, $T=0.08$, and the total force vectors $\mathbf{F}_{\mathrm{mag}}+\mathbf{F}_{\mathrm{grav}}$ drawn at $Z=0.5$, 1.0, 1.5, 2.0, and 2.5. It is apparent from Figs. 10(*b*) and 10(*c*) that the magnetic induction of 2 T intensifies extensively the fluid flow in the horizontal configuration of the system and the angular spokes appear. The long time streak lines have "eightlike," double loop shapes. Such structures are characteristic for the unstable system described before.

## 6 Conclusions

The 50% volume glycerol aqueous solution of 0.5 mol/kg of gadolinium nitrate hexahydrate (paramagnetic) is studied for the convection mode in a thermosyphonlike cylinder under the gravitational and magnetic fields with the thermochromic liquid crystal slurry for a temperature visualization. When the upper side wall of a cylinder is at a lower temperature, the spoke pattern is observed at a midheight. The number of spokes increases with the magnetic induction generated by the coil located below the cylinder. When a whole system is placed upside down, the fluid becomes the temperature stratified in the gravitational field but presents a spoke pattern at 2 T. When the cylinder axis is placed horizontally, the bulk convection cell appears in the gravitational field but changes to a spoke pattern under 2 T. Three-dimensional numerical computations are simultaneously carried out and give a good agreement with the experimental observation.


## Acknowledgment

A part of this work was supported by European Commission (Project Dev-CPPS, FP6-No. 002968).


## Nomenclature

$AR$ = $(h/r_0)$ dimensionless aspect ratio of the cylinder $(-)$

$\mathbf{B}$ = $(\mathbf{b}/b_0)$ dimensionless magnetic induction $(-)$

$\nabla \mathbf{B}^2$ = dimensionless gradient of the square magnetic induction (−)
$\mathbf{b}$ = $(b_r, b_z)$ magnetic induction (T=(V s)/m$^2$)
$b_0$ = $(\mu_m i / r_0)$ reference magnetic induction (T)
$\nabla \mathbf{b}^2$ = gradient of the square magnetic induction (T$^2$/m)
$C_{gad}$ = molar concentration of gadolinium nitrate (mol/kg)
$d$ = diameter of cylinder (m)
$\vec{\mathbf{e}}_z$ = unit vector in the vertical direction (−)
$\mathbf{f}_{grav}$ = $\rho g$ (N/m$^3$)
$\mathbf{f}_{mag}$ = $(1+(\beta\theta_0)^{-1})\chi_m \nabla \mathbf{b}^2/(2\ \mu_m)$ (N/m$^3$)
$\mathbf{F}_{grav}$ = $\mathbf{f}_{grav}/\mathbf{f}_{grav}$ (−)
$\mathbf{F}_{mag}$ = $\mathbf{f}_{mag}/\mathbf{f}_{grav}$ (−)
$g$ = gravitational acceleration (m/s$^2$)
$h$ = height of cylinder (m)
$i$ = electric current (A)
$P$ = $(p/p_0)$ dimensionless pressure (−)
Pr = $(\nu/\alpha)$ Prandtl number (−)
$p$ = pressure (Pa)
$p_0$ = $(\rho_0 \alpha^2 / r_0^2)$ reference pressure (Pa)
$p_{ref}$ = pressure equal to 101, 300 (Pa)
$R$ = $(r/r_0)$ dimensionless radial coordinate (−)
Ra = $(g\beta(\theta_{hot}-\theta_{cold})r_0^3/(\alpha\nu))$ Rayleigh number (−)
$r$ = radial coordinate (m)
$r_0$ = inner radius of the cylinder (m)
$\mathbf{S}$ = $(\mathbf{s}/r_0)$ dimensionless periphery line of the coil vector (−)
$\mathbf{s}$ = periphery line of the coil vector (m)
$T$ = $((\theta-\theta_0)/(\theta_{hot}-\theta_{cold}))$ dimensionless temperature (−)
$t$ = time (s)
$t_0$ = $(r_0^2/\alpha)$ reference time (s)
$\mathbf{V}$ = $(\mathbf{v}/u_0)$ dimensionless velocity vector (−)
$\mathbf{v}$ = $(u,v,w)$ velocity vector (m/s)
$u_0$ = $(\alpha/r_0)$ reference velocity (m/s)
$Z$ = $(z/r_0)$ dimensionless axial coordinate (−)
$z$ = axial coordinate (m)

### Greek Letters

$\alpha$ = thermal diffusivity (m$^2$/s)
$\beta$ = thermal expansion coefficient (1/K)
$\gamma$ = $(\chi b_0^2/(\mu_m g r_0))$ dimensionless gamma parameter (−)
$\theta$ = temperature (K)
$\theta_0$ = $(\theta_{hot}+\theta_{cold})/2$ reference temperature (K)
$\theta_{ref}$ = temperature equal to 298 (K)
$\theta_{cold}$ = temperature of cooled part of enclosure (K)
$\theta_{hot}$ = temperature of heated part of enclosure (K)
$\mu$ = viscosity (Pa s)
$\mu_m$ = magnetic permeability in vacuum (H/m)
$\nu$ = kinematic viscosity (m$^2$/s)
$\rho$ = density (kg/m$^3$)
$\rho_0$ = reference density (kg/m$^3$)
$\chi_m$ = $(\rho\chi)$ volumetric magnetic susceptibility (−)
$\chi$ = mass magnetic susceptibility (m$^3$/kg)

## References


[1] Chandrasekhar, S., 1961, *Hydrodynamic and Hydromagnetic Stability*, Dover Publications, Inc., New York.
[2] Ozoe, H., 2000, "Effect of a Magnetic Field in Czochralski Silicon Crystal Growth," *Modelling of Transport Phenomena in Crystal Growth*, WIT Press, Southampton, pp. 201–237.
[3] Ezaki, K., Kaneda, M., Tagawa, T., and Ozoe, H., 2003, "Numerical Computation for the Melt Convection of the Model System of Continuous Steel Casting With Various Magnetic Fields," ISIJ Int., **43**, pp. 907–914.
[4] Bednorz, J. G., and Muller, K. A., 1986, "Possible High $T_C$ Superconductivity in the Ba–La–Cu–O System," Z. Phys. B: Condens. Matter, **64**, pp. 189–193.
[5] Braithwaite, D., Beaugnon, E., and Tournier, R., 1991, "Magnetically Controlled Convection in a Paramagnetic Fluid," Nature (London), **354**, pp. 134–136.
[6] Wakayama, N. I., 1993, "Magnetic Promotion of Combustion in Diffusion Flames," Combust. Flame, **93**, pp. 207–214.
[7] Ikezoe, Y., Hirota, N., Nakagawa, J., and Kitazawa, K., 1998, "Making Water Levitate," Nature (London), **393**, pp. 749–750.
[8] Wakayama, M., and Wakayama, N. I., 2000, "Magnetic Acceleration of Inhaled and Exhaled Flows in Breathing," Jpn. J. Appl. Phys., Part 1, **39**, pp. 262–264.
[9] Kaneda, M., Tagawa, T., and Ozoe, H., 2002, "Convection Induced by a Cusp-Shaped Magnetic Field for Air in a Cube Heated From Above and Cooled From Below," ASME J. Heat Transfer, **124**, pp. 17–25.
[10] Maki, S., Tagawa, T., and Ozoe, H., 2002, "Enhanced Convection or Quasi-Conduction States Measured in a Superconducting Magnet for Air in a Vertical Cylindrical Enclosure Heated From Below and Cooled From Above in a Gravity Field," ASME J. Heat Transfer, **124**(4), pp. 667–673.
[11] Tagawa, T., Shigemitsu, R., and Ozoe, H., 2002, "Magnetizing Force Modeled and Numerically Solved for Natural Convection of Air in a Cubic Enclosure: Effect of the Direction of the Magnetic Field," Int. J. Heat Mass Transfer, **45**, pp. 267–277.
[12] Bai, B., Yabe, A., and Wakayama, N. I., 1991, "Quantitative Analysis of Air Convection Caused by Magnetic-Fluid Coupling," AIAA J., **37**(12), pp. 1538–1543.
[13] Japikse, D., Jallouk, P. A., and Winter, E. R. F., 1971, "Single-Phase Transport Processes in the Closed Thermosyphon," Int. J. Heat Mass Transfer, **14**, pp. 869–887.
[14] Bayley, F. J., and Lock, G. S. H., 1965, "Heat Transfer Characteristics of the Closed Thermosyphon," ASME J. Heat Transfer, **87**, pp. 30–40.
[15] Lock, G. S. H., and Liu, Y., 1989, "The Effect of Geometry on the Performance of the Closed Tube Thermosyphon at Low Rayleigh numbers," Int. J. Heat Mass Transfer, **32**(6), pp. 1175–1182.
[16] Lock, G. S. H., and Kirchner, J. D., 1992, "Some Characteristics of the Inclined, Closed Tube Thermosyphon Under Low Rayleigh Number Conditions," Int. J. Heat Mass Transfer, **35**(1), pp. 165–173.
[17] Ishihara, I., Fukui, T., and Matsumoto, R., 2002, "Natural Convection in a Vertical Rectangular Enclosure With Symmetrically Localized Heating and Cooling Zones," Int. J. Heat Fluid Flow, **23**, pp. 366–372.
[18] Ishihara, I., Imanishi, R., Fujiwara, M., and Matsumoto, R., 2002, "Natural Convection in a Single-Phase Closed Thermosyphon," Proc. 10th Int. Symposium on Flow Visualization, Kyoto, Japan, FO332.
[19] VDI-Wärmeatlas, VDI-Verlag, 1997.
[20] Ozoe, H., Toh, K., and Inoue, T., 1991, "Transition Mechanism of Flow Modes in Czochralski Convection," J. Cryst. Growth, **110**, pp. 472–489.
[21] Ozoe, H., and Toh, K., 1998, "A Technique to Circumvent a Singularity at a Radial Center With Application for a Three-Dimensional Cylindrical System," Numer. Heat Transfer, Part B, **33**(3), pp. 355–365.
[22] Hirt, C. W., Nichols, B. D., and Romero, N. C., 1975, "A Numerical Solution Algorithm for Transient Fluid Flows," Technical Report No. LA-5852, Los Alamos Scientific Laboratory.

Journal of Heat Transfer

Technical Briefs

# Measured Film Cooling Effectiveness of Three Multihole Patterns

**Yuzhen Lin**

**Bo Song**[1]

**Bin Li**[2]

**Gaoen Liu**

National Key Laboratory on Aero-Engines,
Institute of Thermal Power Engineering,
Beijing University of Aeronautics and Astronautics,
Beijing, 100083, P.R. China

*As an advanced cooling scheme to meet increasingly stringent combustor cooling requirements, multihole film cooling has received considerable attention. Experimental data of this cooling scheme are limited in the open literature in terms of different hole patterns and blowing ratios. The heat-mass transfer analogy method was employed to measure adiabatic film cooling effectiveness of three multihole patterns. Three hole patterns differed in streamwise row spacing* ($S$)*, spanwise hole pitch* ($P$)*, and hole inclination angle* ($\alpha$)*, with the first pattern* $S/P=2$ *and* $\alpha=30°$*, the second* $S/P=1$ *and* $\alpha=30°$*, and the third* $S/P=2$ *and* $\alpha=150°$*. Measurements were performed at different blow ratios* ($M=1-4$)*. Streamwise coolant injection offers high cooling protection for downstream rows. Reverse coolant injection provides superior cooling protection for initial rows. The effect of blowing ratio on cooling effectiveness is small for streamwise injection but significant for reversion injection.* [DOI: 10.1115/1.2137762]

*Keywords: adiabatic film cooling effectiveness, multihole pattern, blowing ratio, heat-mass transfer analogy*

## Introduction

Modern gas turbines are required to operate at increased temperatures to achieve higher performance and lower fuel consumption. This trend results in the reduction of cooling air used for protecting combustor liner walls. The film cooling scheme for combustors has developed from convection/film cooling, multilayer-wall internal cooling to multihole film cooling (Mellor [1]). The configuration of multihole film cooling is illustrated in Fig. 1: a large number of holes are drilled on the combustor liner wall, normal or inclined to the wall surface, arranged in a specific pattern. This cooling scheme functions through three processes. First, when the coolant flows through the annular passage, heat is absorbed by the coolant from the hot wall by convection. Second, the coolant passes through the small holes, leading to the so-called internal heat convection to further cool the wall. Third, when the coolant is discharged from the holes, it forms a cooling film. The second process accounts for the higher level of overall cooling effectiveness of this cooling scheme than a conventional slot film cooling scheme [1]. The second cooling process contributes to the same degree provided the same hole diameter and inclination angle as well as the same number of holes per unit area (hole opening density). Therefore, the potential to further enhance cooling lies in the third process as different hole patterns could lead to different adiabatic film cooling effectiveness ($\eta$).

Previous studies of $\eta$ for the inclined multihole film cooling are summarized in Table 1. Mayle et al. [2] and Sasaki et al. [3] studied the local and spanwise averaged $\eta$ within and after the hole patterns. As these studies were intended for application to turbine blades, the blowing ratio used was lower than combustor needs. Martiny et al. [4] investigated the flow and cooling characteristics of a multihole wall with relatively high blowing ratios, but the published data were limited to only averaged $\eta$ for initial rows. Andrews et al. [5] measured the temperature in the film boundary layer and the adiabatic wall temperature. They found the reverse-injection provided good film protection for the front part of the wall. But this work did not determine the spatial distribution of $\eta$. It is noticed that the hole opening density varied among those studies. Previous research also dealt with multihole cooling with the holes normal to the wall surfaces (Metzger et al. [6], Andrews et al. [7–12], and Harrington et al. [13]). All the abovementioned research used the heat transfer method, i.e., with the heated main flow and coolant injection while keeping the wall adiabatic. The heat-mass transfer analogy method, without the worry of obtaining the adiabatic condition and the associated heat loss error, turns out to be an attractive alternative. Pedersen [14] used this method in a study of $\eta$ downstream of one row of holes.

The current work employed the heat-mass transfer analogy method to measure adiabatic film cooling effectiveness of three different multihole patterns. The combinations of multihole pattern and blowing ratio differed from previous research. As such, the current work adds data to the literature on multihole film cooling.

## Experimental Method

The experiments were performed in the low speed wind tunnel of the Institute of Thermal Power Engineering of Beijing University of Aeronautics and Astronautics. Figure 2 shows the schematic of the experimental setup and Fig. 3 shows a zoom-in view of the test section. The main flow passage was $120\times150$ mm$^2$ in cross section, representing the combustor passage. The main flow had a uniform velocity and temperature. The coolant plenum simulated the outer annulus passage with $21\times120$ mm$^2$ in cross

[1]Currently with Gardner Denver, Inc.
[2]Currently with China Gas Turbine Institute.

Contributed by the Heat Transfer Division of ASME for publication in the JOURNAL OF HEAT TRANSFER. Manuscript received May 16, 2004; final manuscript received August 3, 2005. Review conducted by Phillip M. Ligrani.

  

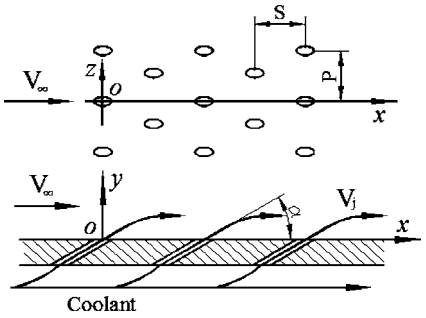


**Fig. 1 Configuration of multihole film cooling**

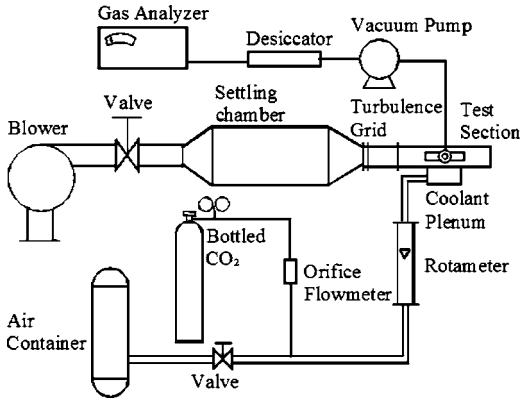


**Fig. 2 Schematic of the experimental setup**

section. The multihole test plate, which simulated the combustor liner and isolated the coolant plenum and main flow passage, was flush-mounted on the main flow side. Supplied by a blower, the main flow entered the test section after passing through a settling chamber. A turbulence grid was placed 280 mm upstream of the test section. According to Ballal and Lefebvre [15], the turbulence grid was designed to generate a turbulence intensity of 12.2%. The coolant was a mixture of air and $CO_2$ with a specified $CO_2$ concentration.

The heat-mass transfer analogy method was employed in the experiments. The energy and mass equations are analogous at the turbulent flow conditions [16]. When the boundary conditions are analogous, i.e., using the impermeable wall for the mass transfer to represent the adiabatic wall for the heat transfer, the solutions of the heat transfer can be deduced from the mass transfer. Another requirement for the heat-mass transfer analogy method is that the turbulent Lewis Number ($Le_t$) be unity. More detailed description of the heat-mass transfer analogy method to measure $\eta$ was given by Lin [17]. The adiabatic film cooling effectiveness ($\eta$) was finally determined by the ratio of mass fractions

$$\eta = \frac{c_\infty - c_w}{c_\infty - c_j} \tag{1}$$

where $c_j$ and $c_\infty$ were determined at the beginning of the experiment. $c_w$ at different locations of the wall surface was measured with the sampling system. As shown in Fig. 3, the sampling probe was traversed on the wall surface in an accuracy of 0.2 mm, served by the traverse assembly. The sampling probe was made of stainless steel tubing ($\Phi 1.0 \times 0.2$ mm). The probe head was specially trimmed to have a sharp leading edge (thickness of 0.03 mm) such that the probe head could be placed closer to the wall surface, with the center of the sampling hole 0.33 mm from the wall surface. In the experiments, the probe was always oriented with the head facing the coolant jets. The sample gas on the surface was absorbed by a vacuum pump, passing through the sampling probe and a desiccator, finally sent to an infrared $CO_2$ analyzer, with which the sample concentration was determined. The velocity of the absorbed sample gas at the probe head was controlled to 10–20% of the main flow velocity to diminish the disturbance to the flow. The flow rate of the absorbed sample gas was less than 3% of the injection flow rate from one hole.

Test conditions of the experiments are listed in Table 2. The experiments were conducted at the ambient pressure and temperature. The variation of the blowing ratio was primarily achieved by using different ratios of the coolant injection velocity to the main flow velocity. It should be noted that Table 2 shows the range of $V_\infty$, $T_\infty$, and $T_j$ varying from tunnel entry to entry. For a specific entry, those parameters were invariant and the temperature difference between the main and injection flow was within 1°C. The experimental uncertainty of the film cooling effectiveness primarily depended on the precision of the infrared $CO_2$ analyzer, with other uncertainty sources of secondary importance. By applying the error propagation algorithm, the typical uncertainty for $\eta$ was estimated to be ±3% with a confidence level of 95% [Lin, 17].

Three multihole test plates were designed for the experiments. They were made of brass, all in staggered patterns. The geometries are compared in Table 3. As the plates have the same hole diameter and hole opening density, the parametric effect of $S/P$ and $\alpha$ on $\eta$ can be assessed, respectively.

## Results

**Preliminary Measurements.** Preliminary measurements were performed to verify the surface-traverse sampling method. Conventional slot film cooling was checked. The slot used in the test was 2 mm in height and had a lip with a thickness of 1.5 mm. The test was conducted at two mainstream velocities of 12 and 20 m/s and the ambient condition. The measured $\eta$ was compared to the

**Table 1 Previous studies on the inclined multihole film cooling**

| Authors | Mayle et al. [2] | Sasaki et al. [3] | Martiny et al. [4] | Andrews et al. [5] |
|---|---|---|---|---|
| Hole Array | Staggered | Staggered | Staggered | Staggered |
| Hole Pitch Ratio (P/d) | 8, 10, 14 | 3 | 4.5 | 11 |
| Row Spacing Ratio (S/d) | 6.9, 8.7, 12.1 | 5, 10 | 7.6 | 11 |
| Inclination Angle (α) | 30 deg | 45 deg | 17 deg | 30 deg<br>150 deg |
| Blowing Ratio (M) | 0.25~2.0 | 0.15~0.5 | 0.5~4.0 | 1-14 |
| $T_{aw}$ Measurement | Radiometer | Infrared camera | Thermography | Thermocouple |

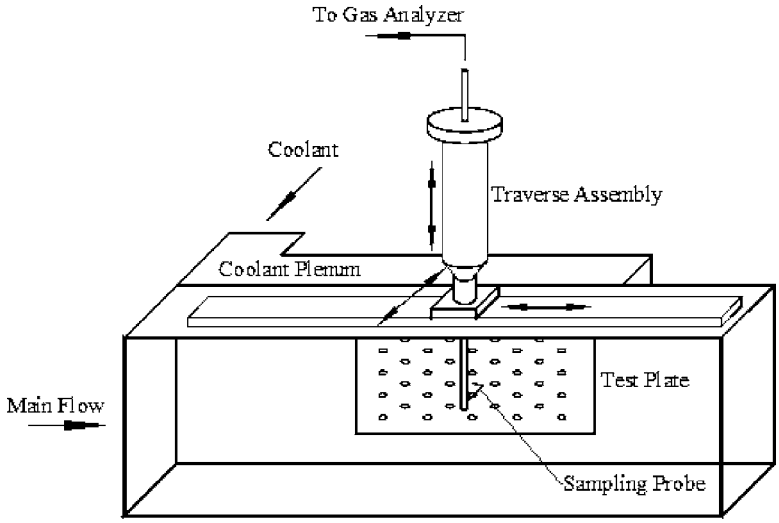


**Fig. 3 Test section**

correlations established by previous research [18,19], as shown in Fig. 4. It is seen that the current measured results lie between the two correlations.

Measurements of a single hole and a single row of holes were performed to document the basic cooling characteristic, by which multirow holes formed a full-coverage film. The single hole geometry was $\alpha=30°$ and $d=1.5$ mm. The single row of holes had the same hole geometry plus $P/d=4$. Figure 5 shows the experimental results. $\eta$ of the single hole along the line $z/d=0.00P/d$ decreased rapidly from 0.4 at $x/d=2$ to 0.1 at $x/d=5$, then continued to decrease mildly through $x/d=38$. $\eta$ of the single row along the line $z/d=0.00P/d$ nearly overlapped the single-hole results from $x/d=2$ to $x/d=12$, then slowly increased to 0.12 and kept this value toward more downstream. $\eta$ of the single row along the lines $z/d=0.25P/d$ and $z/d=0.50P/d$ gradually increased from zero at $x/d=0$ to 0.12 at $x/d=28$, from where $\eta$ of the single row kept the same value along the three $z/d$ lines. These results indicate that the single hole failed to form an effective film but the single row could do so although the cooling effectiveness was very low. The results exhibit the spanwise cooling "even-out" of a single row, a necessary function to form an effective film. Measured $\eta$ by Pedersen et al. [14] was imposed on Fig. 5 for reference. Lower $M$ and $P/d$ in their research (thus less jet penetration and the coolant jets closer to each other) explained the higher $\eta$ in their work at the initial region $x/d=5-20$. More downstream, measured $\eta$ from both experiments reached nearly the same level.

**Local $\eta$ Distribution.** Figure 6 shows $\eta$ distribution of SP2-30 at $M=2.01$ and 3.84. This pattern had the same pitch ($P$) as the

**Table 2 Test conditions**

| Parameter | Value |
|---|---|
| Main Flow Velocity $V_\infty$ (m/s) | 15~22 |
| Main Flow Temperature $T_\infty$ (℃) | 0~30 |
| Injection Flow Velocity $V_j$ (m/s) | 15~68 |
| Injection Flow Temperature $T_j$ (℃) | 0~30 |
| Blowing Ratio M | 1~4 |
| Density Ratio $\rho_j/\rho_\infty$ | 1.03~1.08 |
| $CO_2$ Concentration of Injection $C_j$ | 6% |
| $CO_2$ Concentration of Mail Flow $C_\infty$ | 0.05% |

**Table 3 Test plate geometries**

| Test Plate | d(mm) | P/d | S/d | α(deg) | t/d |
|---|---|---|---|---|---|
| SP2-30 | 1.5 | 4 | 8 | 30 | 4 |
| SP2-150 | 1.5 | 4 | 8 | 150 | 4 |
| SP1-30 | 1.5 | 5.67 | 5.67 | 30 | 4 |

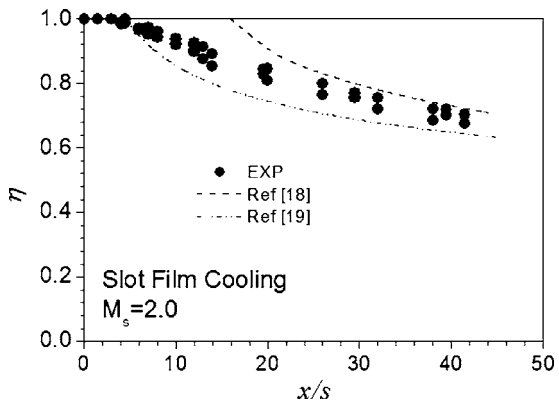


**Fig. 4 Comparison of the measured and correlated $\eta$ of slot film cooling**

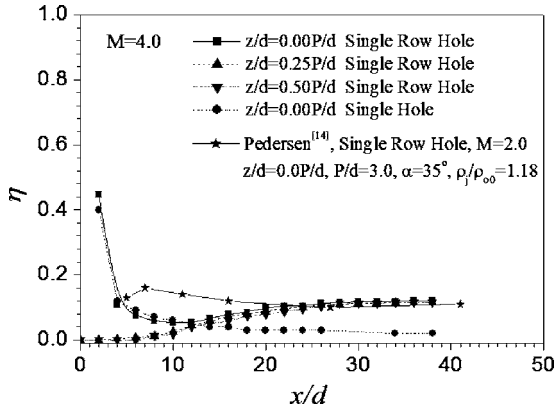


**Fig. 5 Measured $\eta$ of the single hole and the single row**

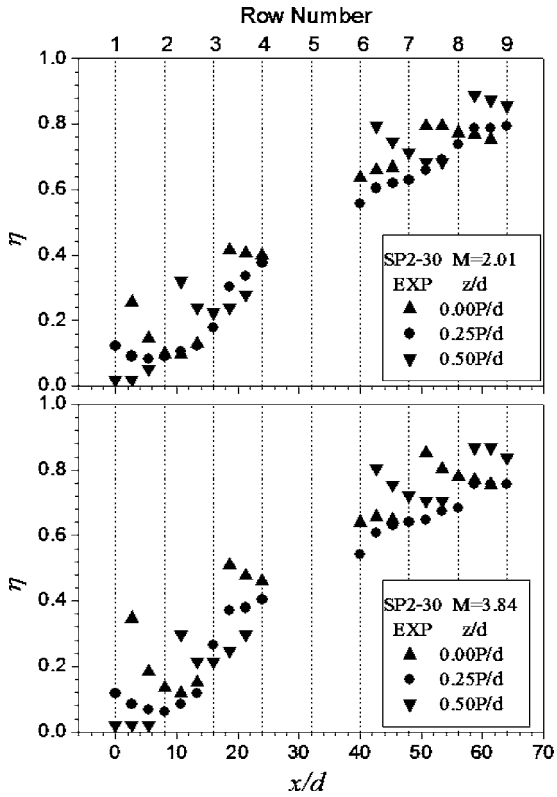


**Fig. 6 Local $\eta$ of Pattern SP2-30**

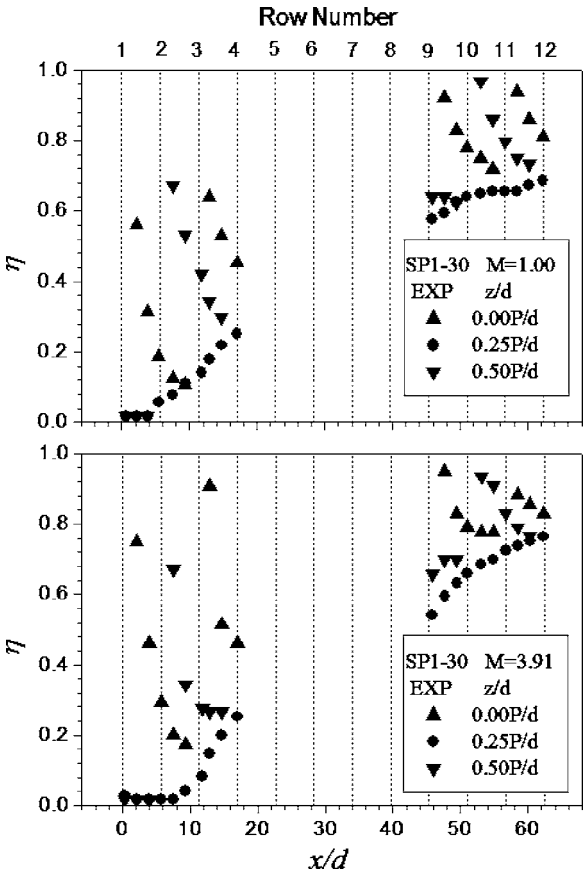


**Fig. 8 Local $\eta$ of Pattern SP1-30**

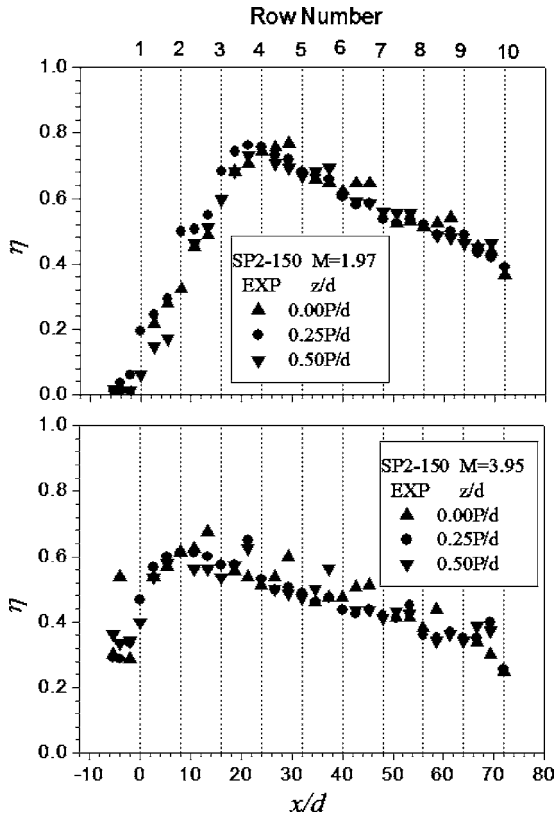


**Fig. 7 Local $\eta$ of Pattern SP2-150**

single row discussed above. It is seen that $\eta$ was low at the initial rows, called the initial region. Downstream of the initial region was the transitional region, which was characterized by a rapid increase of $\eta$. The transitional region included three to six rows. After that was the developed region, where $\eta$ was high up to 0.8 and the spanwise cooling uniformity was better than upstream. Apparently, for a streamwise injection multihole pattern, the developed region is the most desired in application. Figure 6 shows streamwise cooling decay after each row and overall cooling accumulation with the contributions row by row. This is another function necessary for the multihole cooling scheme to form an effective film besides the spanwise cooling "even-out" mentioned above. Comparing results of the two blowing ratios shows that the blowing ratio exerted small influence on $\eta$.

SP2-150 had the same hole array as SP2-30 except for the inclination angle changed to 150°, leading to the reverse coolant injection. Figure 7 shows the measured local $\eta$ of this pattern at two blowing ratios, which were totally different from SP2-30 in that cooling rapidly reached to the maximum at the initial rows and then decreased gradually downstream. Unlike SP2-30, blowing ratio had a large influence on $\eta$ for the reverse injection. Higher blowing ratio had lower $\eta$ with the maximum cooling occurring more upstream. Another difference of the reverse injection from the streamwise injection was that there was no significant $\eta$ distinction along three $z/d$ lines, indicating that the reverse injection had better spanwise cooling uniformity than the streamwise injection.

Figure 8 shows local $\eta$ for SP1-30 at $M=1.00$ and 3.91. The cooling characteristic of this pattern is similar to SP2-30 except for a little poorer spanwise cooling uniformity due to the enlarged pitch ($P$). Similar to SP2-30, the effect of blowing ratio on $\eta$ was small of this pattern.

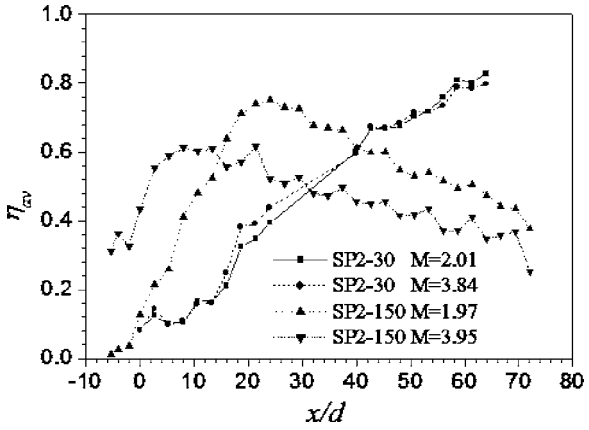


**Fig. 9 Averaged $\eta$ of SP2-30 and SP2-150**

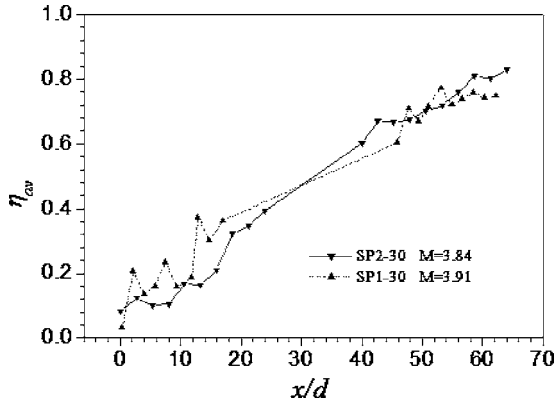


**Fig. 10 Averaged $\eta$ of SP1-30 and SP2-30**

**Spanwise Averaged $\eta$.** In addition to local $\eta$, spanwise averaged adiabatic film cooling effectiveness ($\eta_{av}$) was assessed. $\eta_{av}$ is defined as

$$\eta_{av} = \sum_{i=1}^{n} \eta(x/d)_i/n \tag{2}$$

where $\eta_{av}$ is the arithmetically averaged value of local $\eta$ at the same $x/d$ position. The index "$i$" stands for different spanwise stations ($z/d=0$, $z/d=0.25P/d$, and $z/d=0.5P/d$). The symbol "$n$" stands for the total number of the spanwise stations at the same $x/d$ position.

Figure 9 compared $\eta_{av}$ of SP2-30 and SP2-150 at two similar blowing ratios ($M\approx 2$ and 4). In addition to the local $\eta$ results shown above, the averaged $\eta$ gives a direct view of the effect of the injection angle on the cooling variation with $x$ positions. The streamwise injection resulted in high cooling effectiveness in the downstream region while the reverse injection had high cooling effectiveness at the initial rows. If these two configurations were combined in applications, i.e., using the reverse injection at the initial rows and using the streamwise injection in the downstream region, an optimal $\eta$ distribution could be obtained. Figure 9 also suggests that the effect of blowing ratio was little for the streamwise injection but considerable for the reverse injection.

Figure 10 compared $\eta_{av}$ of SP2-30 and SP1-30 at one similar blowing ratio ($M\approx 4$). It is seen that SP2-30 had lower cooling effectiveness at initial rows but increased more rapidly toward downstream than SP1-30. As such, the two patterns tended to the same high level of cooling effectiveness in the developed region.

## Conclusions

Adiabatic film cooling effectiveness ($\eta$) of three inclined multihole patterns was measured using the heat-mass transfer analogy method. The hole arrangements and blowing ratio were chosen to be representative of combustor application. Investigations of the measured local $\eta$ in each hole pattern and the spanwise averaged $\eta$ lead to the following conclusions. (1) The conventional streamwise injection has high cooling effectiveness at downstream locations while the reverse injection excels in protecting upstream regions. (2) The ratio of row spacing to spanwise pitch has a small effect on overall cooling effectiveness; a smaller pitch is better for spanwise cooling uniformity and should be favored for a pattern with more rows of holes available. (3) Blowing ratio has a small influence on cooling effectiveness for the streamwise injection but considerable influence for the reverse injection. (4) For combustor wall cooling, a combined use of different hole patterns is of promise for an optimal cooling scheme design.

## Nomenclature

- $C$ = mass fraction
- $d$ = hole diameter
- Le = Lewis number (Le=Sc/Pr)
- $M$ = blowing ratio ($M=\rho_j V_j/\rho_\infty V_\infty$)
- $P$ = hole-to-hole pitch in a row
- Pr = Prandtl number
- $S$ = row-to-row spacing
- $s$ = slot height in slot film cooling
- Sc = Schmidt number
- $t$ = thickness of the test plate slot lip thickness in slot film cooling
- $T$ = temperature
- $V$ = velocity
- $x$ = coordinate in the streamwise direction
- $y$ = coordinate perpendicular to the wall surface
- $z$ = coordinate in the spanwise direction
- $\alpha$ = inclination angle
- $\eta$ = adiabatic film cooling effectiveness $\eta=(T_\infty-T_{aw})/(T_\infty-T_j)$

### Subscripts

- av = spanwise average
- aw = adiabatic wall
- $j$ = coolant injection
- $s$ = slot
- $t$ = turbulent
- $w$ = wall
- $\infty$ = mainstream

## References


[1] Mellor, A. M., 1991, *Design of Modern Turbine Combustor*, Academic, New York.

[2] Mayle, R. E., and Camarata, F. J., 1975, "Mutihole Cooling Film Effectiveness and Heat Transfer," ASME J. Heat Transfer, **97**(2), pp. 534–538.

[3] Sasaki, M., Takahara, K., Kumagai, T., and Hanano, M., 1979, "Film Cooling Effectiveness for Injection From Multirow Holes," ASME J. Eng. Power, **101**(1), pp. 101–108.

[4] Martiny, M., Schulz, A., and Wittig, S., 1995, "Full-Coverage Film Cooling Investigations: Adiabatic Wall Temperatures and Flow Visualization," ASME Paper No. 95-WA/HT-4.

[5] Andrews, G. E., Khalifa, I. M., Asere, A. A., and Bazdidi-Tehrani, F., 1995, "Full Coverage Effusion Film Cooling with Inclined Holes," ASME Paper No. 95-GT-274.

[6] Metzger, D. E., Takeuchi, D. I., and Kuenstler, P. A., 1973, "Effectiveness and Heat Transfer with Full Coverage Film Cooling," ASME Paper No. 73-GT-18.

[7] Andrews, G. E., Gupta, M. L., and Mkpadi, M. C., 1985, "Full Coverage Discrete Hole Wall Cooling: Cooling Effectiveness," Int. J. Turbo Jet Engines, **2**, pp. 199–212.

[8] Andrews, G. E., Asere, A. A., Gupta, M. L., and Mkpadi, M. C., 1985, "Full Coverage Discrete Hole Wall Cooling: The Influence of Hole Size," Int. J. Turbo Jet Engines, **2**, pp. 213–225.

[9] Andrews, G. E., Alikhanizadeh, M., Asere, A. A., Hussain, C. I., Khoskbar Azari, M. S., and Mkpadi, M. C., 1986, "Small Diameter Film Cooling Holes:

Wall Convective Heat Transfer," ASME J. Turbomach., **108**, pp. 283–289.
[10] Andrews, G. E., and Bazdidi Tehrani, F., 1989, "Small Diameter Film Cooling Holes: The Influence of The Number of Holes," ASME Paper No. 89-GT-7.
[11] Andrews, G. E., Asere, A. A., Gupta, M. L., Mkpadi, M. C., and Tirmahi, A., 1990, "Full Coverage Discrete Hole Wall Cooling: The Influence of The Number of Holes and Pressure Loss," ASME Paper No. 90-GT-61.
[12] Andrews, G. E., Bazdidi-Tehrani, F., Hussain, C. I., and Pearson, J. P., 1991, "Small Diameter Film Cooling Holes: The Influence of The Hole Length," ASME Paper No. 91-GT-344.
[13] Harrington, M. K., McWaters, M. A., Bogard, D. G., Lemmon, C. A., and Thole, K. A., 2001, "Full-Coverage Film Cooling With Short Normal Injection Holes," ASME Paper No. 2001-GT-0130.
[14] Pedersen, D. R., Eckert, E. R. G., and Goldstein, R. J., 1977, "Film Cooling With Large Density Difference Between The Main Stream and Secondary Fluid Measured By The Heat-Mass Transfer Analogy," ASME J. Heat Transfer, **99**(2), pp. 620–627.
[15] Ballal, D. R., and Lefebvre, A. H., 1980, "Weak Extinction Limitis of Turbulent Heterogeneous Fuel/Air Mixtures," ASME J. Eng. Power, **102**(2), pp. 416–421.
[16] Eckert, E. R. G., and Drake Jr., M. R., 1987, *Analysis of Heat and Mass Transfer*, Hemisphere, New York.
[17] Lin, Y., 1997, "Study of the Inclined Multihole Film Cooling Scheme for Application to Aeroengine Combustors," Ph.D. dissertation, Beijing University of Aeronautics and Astronautics.
[18] Ballal, D. R., and Lefebvre, A. H., 1973, "Film-Cooling Effectiveness in the Near Slot Region," ASME J. Heat Transfer, **95**, pp. 256–266.
[19] Ballal, D. R., and Lefebvre, A. H., 1972, "A Proposed Method for Calculating Film-Cooled Wall Temperatures in Gas Turbine Combustion Chambers," ASME Paper No. 72-WA/HT-24.

# Thermal Analysis of Inclined Micro Heat Pipes

**D. Sugumar**
Faculty of Manufacturing Engineering,
National Technical University College of Malaysia,
Locked Bag 1200,
Ayer Keroh, 75450 Malaysia
e-mail: sugumar@kutkm.edu.my

**Kek-Kiong Tio**
Faculty of Engineering & Technology,
Multimedia University,
Bukit Beruang,
75450 Malacca, Malaysia
e-mail: kktio@mmu.edu.my

*The effect of gravity is investigated for the case of inclined-triangular- and trapezoidal-shaped micro heat pipes (MHPs). The study is limited to the case of positive inclination, whereby the condenser section is elevated from the horizontal position. The results show that the axial distribution of the liquid phase is changed qualitatively. While the liquid distribution still increases monotonically starting from the evaporator end, it reaches its maximum value not at the condenser end but at a certain point in the condenser section, beyond which the liquid distribution decreases monotonically. This maximum point, where potentially flooding will first take place, results from the balance between the effects of gravity and the heat load on the MHPs. As the liquid distribution assumes its greatest value at the maximum point, a throat-like formation appears there. This formation is detrimental to the performance of MHPs, because it hinders, and at worst may block, the axial flow of the vapor phase. The results also show that the maximum point occurs further away from the condenser end for a triangular-shaped MHP compared to a trapezoidal-shaped MHP.* [DOI: 10.1115/1.2137763]

*Keywords: micro heat pipes, porous medium, heat transfer*

## Introduction

Since their initial conceptualization by Cotter [1], micro heat pipes have attracted numerous analytical studies [2–7]. In the existing literature, most studies deal primarily with horizontal micro heat pipes and relatively few are focused on inclined micro heat pipes in a systematic way. It is, therefore, the purpose of this paper to analyze some of the most important aspects of inclined micro heat pipes, with a view on more comprehensive studies in the future. The model used in this paper is the one-dimensional porous medium model originally developed by Tio et al. [2]. This model is selected for its simplicity and accuracy, which is established by Tio et al. [2], in their comparison of experimental results and those predicted by the model. Figure 1 is the schematic diagram of an inclined micro heat pipe showing its three sections (evaporator, adiabatic, and condenser sections) as well as the liquid and vapor flows. Figure 2 depicts the two cross-sectional shapes which we shall deal with.

Contributed by the Heat Transfer Division of ASME for publication in the JOURNAL OF HEAT TRANSFER. Manuscript received July 28, 2004; final manuscript received August 9, 2005. Review conducted by Raj M. Manglik

## Analysis

Following Tio et al. [2], we assume that the flow channel of a micro heat pipe is sufficiently small that we can regard it as a pore of a porous medium. Using Darcy's equations for a one-dimensional two-phase flow and Laplace's capillary equation, we can then derive an ordinary differential equation governing the liquid volume fraction $s$ in a micro heat pipe of polygonal cross section [2]:

$$\frac{ds}{d\hat{x}} = \frac{s^{3/2}}{\omega}\left[\mathrm{Ca}\left(\frac{1}{s^3} + \frac{\gamma}{(1-s)^3}\right)\hat{m} - \mathrm{Ga}\,.\,\sin\theta\right] \tag{1}$$

where $\gamma$ is the vapor-liquid ratio of their kinematic viscosities, $\theta$ is the angle of inclination of the micro heat pipe (see Fig. 1), and

$$\hat{x} = \frac{x}{L} \tag{2}$$

is the dimensionless axial coordinate originating from the evaporator end, $L$ being the length of the micro heat pipe. The capillary number Ca, gravity number Ga, and the geometrical constant $\omega$ are given by

$$\mathrm{Ca} = \left(\frac{Q}{\rho_l h_{fg} A}\right) \Bigg/ \left(\frac{\sigma K (L_e/L)}{2\mu_l L (A)^{1/2}}\right) \tag{3}$$

$$\mathrm{Ga} = \frac{2gL(\rho_l - \rho_v)(A/N)^{1/2}}{\sigma} \tag{4}$$

$$\omega = N^{1/2}\left[\frac{\cos\vartheta\cos(\phi+\vartheta)}{\sin\phi} + (\phi+\vartheta) - \frac{\pi}{2}\right]^{1/2} \tag{5}$$

where $Q$ is the rate of heat transport, $\rho$ denotes density, $\sigma$ is the surface tension, $h_{fg}$ is the latent heat of evaporation, $\mu$ denotes dynamic viscosity, $g$ is the gravitational acceleration, $A$ is the cross-sectional area of the micro heat pipe, and $N$ is the number of corners of the cross section. The constant $K$ in Eq. (3) is given by

$$K = \frac{2}{C_K} D_h^2 \tag{6}$$

where $C_K$ are constant values [8] for various shapes of cross section and $D_h$ is the hydraulic diameter of the micro heat pipe's cross section. The values of $C_K$ are reproduced and tabulated in Table 1. Finally, the angular quantities $\phi$ and $\vartheta$ in Eq. (5) are the half angle of a corner of the micro heat pipe's cross section and the contact angle of the liquid phase. In our study, we only deal with the special case of zero contact angle; thus, $\vartheta = 0$ in all our calculations. The quantity $\hat{m}$, which appears in Eq. (1), is defined as

$$\hat{m} = \dot{m} \Bigg/ \left(\frac{Q\,.\,L}{h_{fg} L_e}\right) \tag{7}$$

where $\dot{m}$ is the mass flow rate of the liquid and vapor phases through a cross section of the micro heat pipe. In our study, we assume that the heat entering and leaving the heat pipe is uniformly distributed over the length of the evaporator and condenser, respectively. Under this assumption, we can write

$$\hat{m} = \begin{cases} \hat{x} & \hat{x} \leqslant \dfrac{L_e}{L}, \\ \dfrac{L_e}{L} & \dfrac{L_e}{L} \leqslant \hat{x} \leqslant 1 - \dfrac{L_c}{L}, \\ \dfrac{L_e}{L_c}(1-\hat{x}) & 1 - \dfrac{L_c}{L} \leqslant \hat{x} \leqslant 1, \end{cases} \tag{8}$$

where $L_e$ and $L_c$ are the lengths of the evaporator and condenser, respectively.

  

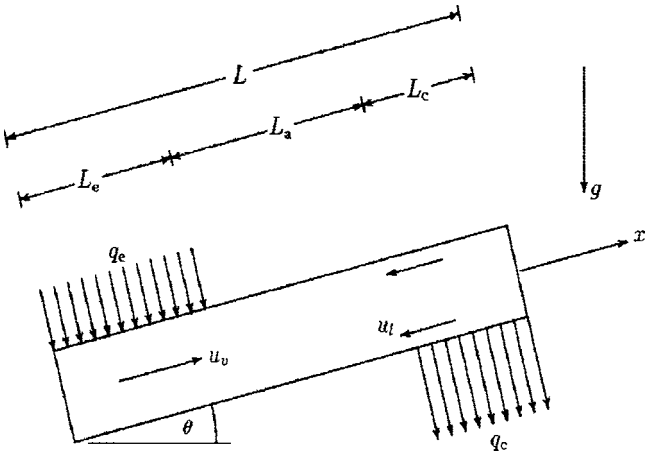


**Fig. 1 A schematic diagram of an inclined micro heat pipe, $\theta$ being the angle of inclination**

We note that Eq. (1) is valid for a micro heat pipe of polygonal cross section only. For a micro heat pipe of cross-sectional shape of a cusped diamond, we can, following the same steps leading to Eq. (1), derive

$$\frac{d\alpha}{d\hat{x}} = \frac{(1-\cos\alpha)^2}{4(1-\pi/4)^{1/2}\sin\alpha}\left[\mathrm{Ca}\left(\frac{1}{s^3}+\frac{\gamma}{(1-s)^3}\right)\hat{m} - Ga\sin\theta\right] \tag{9}$$

where $\alpha$, the angle as defined in Fig. 2($b$), is related to the liquid volume fraction $s$ through

$$s = \frac{\mathrm{Ca}}{4(1-\pi/4)}\left[\tan\alpha - \left(\frac{\pi}{2}-\alpha\right)(\sec\alpha-1)^2 - \alpha\right] \tag{10}$$

We note that Eqs. (9) and (10) are valid only for the special case of $\vartheta=0$.

As mentioned earlier, we shall only deal with micro heat pipes having a cross-sectional shape of a triangle or a cusped diamond. Accordingly, we set $N=3$ and $\phi=30°$ in Eqs. (4) and (5) for a triangle and $N=4$ for a cusped diamond. Then, our main task is to integrate Eq. (1) or (9) subject to the appropriate "initial" condition. For this, we use the fourth-order Runge-Kutta scheme. Having obtained $s(\hat{x})$, we then proceed to determine the charge level, $M$, of the micro heat pipe. In dimensionless form, it is given by

$$\hat{M} = \frac{M}{AL\rho_l} = \left(\frac{\rho_v}{\rho_l}\right) + \left[1-\left(\frac{\rho_v}{\rho_l}\right)\right]\int_0^1 s(\hat{x})d\hat{x} \tag{11}$$

## Discussion

The micro heat pipes selected for our study all have the same cross-sectional area and the same evaporator, adiabatic, and condenser lengths listed in Table 2. As pointed out by Tio et al. [2], the performance of a horizontal micro heat pipe is limited by the onset of dryout at the evaporator end or the onset of flooding at the condenser end, depending on its charge level. If the micro heat pipe is filled exactly up to the optimal level, its performance is limited by the simultaneous onsets of dryout at the evaporator end and flooding at the condenser end. Moreover, the heat transport rate associated with the simultaneous onsets of dryout and flooding is the maximum of all allowable ones without the occurrence of dryout or flooding. We call this maximum heat transport rate the heat transport capacity of the micro heat pipe [2]. We also note that the heat transport capacity and the required optimal charge level are both functions of the operating temperature of the micro heat pipe. For an inclined micro heat pipe, its heat transport capacity is also limited by the simultaneous onsets of dryout and flooding; however, as we shall see shortly, the onset of flooding takes place not at the condenser end but at some distance from it. For easy reference, the liquid volume fractions associated with the onsets of dryout and flooding are tabulated in Table 1. Note that, for safety reasons, the volume fraction for the onset dryout is set to be 0.01, instead of the physical value of 0.

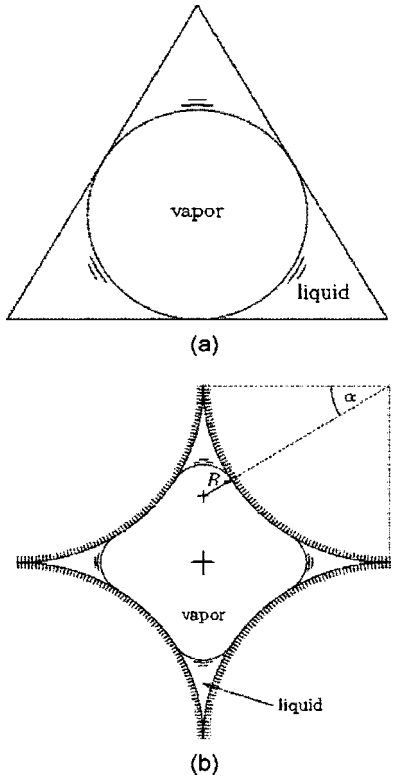


**Fig. 2 Geometry of different cross-sectional shapes of micro heat pipes. (*a*) Equilateral triangle and (*b*) cusped diamond.**

For an inclined micro heat pipe, gravity can enhance or inhibit its performance, depending on its orientation. The orientation of the micro heat pipe in this paper is limited to that depicted in Fig. 1. In the following discussion, the influence of gravity is investigated for an inclined micro heat pipe designed for horizontal orientation. The liquid saturation profile inside a horizontally orientated equilateral-triangle- and cusped diamond-shaped micro heat pipe always shows an increase from a minimum point at the evaporator end ($x=0$) to a maximum point at the condenser end ($\hat{x}=1.0$). If a horizontal micro heat pipe with a constant heat load $Q$ is inclined from its horizontal orientation, the liquid saturation inside the micro heat pipe is redistributed in the axial direction, as depicted in Figs. 3 and 4 for an equilateral-triangle and cusped-diamond micro heat pipe, respectively. For both types of micro

**Table 1 The values of $C_K$, $s_{cl}$, $s_{fl}$, $\alpha_{cl}$, and $\alpha_{fl}$**

| | $C_K$ | $s_{cl}$ | $s_{fl}$ | $\alpha_{cl}$ | $\alpha_{fl}$ |
|---|---|---|---|---|---|
| Triangle | 53.30 | 0.010 | 0.395 | - | - |
| Cusped Diamond | 26.42 | 0.010 | 0.372 | 0.200 | 0.785 |

**Table 2 Axial dimensions of investigated micro heat pipes**

| | |
|---|---|
| $L$ | 0.05 m |
| $L_a$ | 0.0246 m |
| $L_e$ | 0.0127 m |
| $L_c$ | 0.0127 m |

heat pipes, the liquid saturation gradually increases in the evaporator section but decreases near the condenser end when the angle of inclination is increased. Interestingly, the maximum point (or the point where, potentially, flooding first takes place) in the condenser section does not occur at the condenser end ($\hat{x}=1.0$). Rather, it occurs further away from the condenser end ($\hat{x}<1.0$), when the angle of inclination is increased. The explanation for the formation of this maximum point away from the condenser end is due to the balance between the gravitational effect, which tends to move all the liquid from the condenser toward the evaporator section, and the heat load which tends to move the liquid upward toward the condenser section. This balance then results in $ds/d\hat{x}=0$, which corresponds to the maximum point.

This maximum point in the condenser section forms a throat-like formation that can narrow down the passage of the vapor flow. This type of observation constitutes a serious concern since the formation of the "throat" might become closed and form a "liquid bridge" blocking the flow of vapor toward the remaining section of the micro heat pipe, which is detrimental to its performance. However, for this particular case, the thickness of the "throat" decreases when the angle of inclination is increased, as seen in Figs. 3 and 4. Thus, while the maximum point moves toward the adiabatic section as the angle of inclination is increased, the potential adverse effects of the throat are mitigated by the decrease in its thickness.

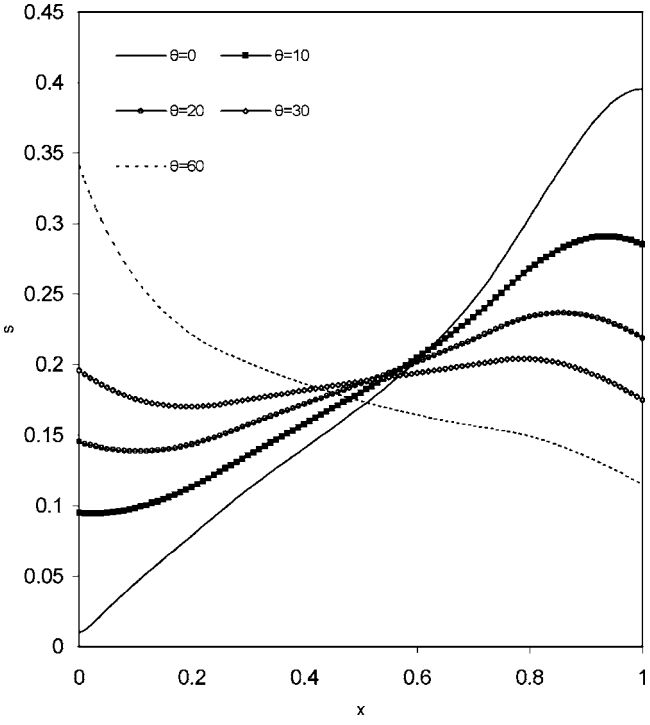


**Fig. 3 Profiles of liquid volume fraction for different angles of inclination for an equilateral-triangle-shaped micro heat pipe (Ca=0.0274; $\hat{M}$=0.187; working fluid=water; operating temperature=60 °C)**

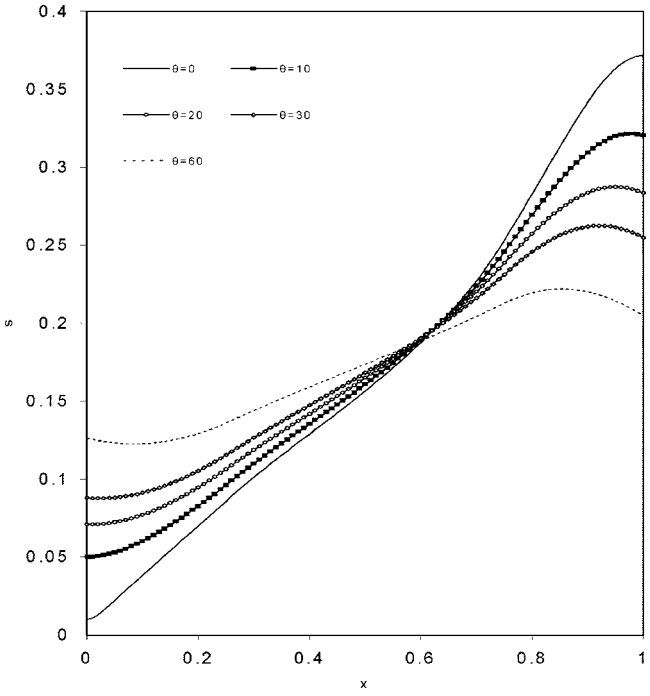


**Fig. 4 Profiles of liquid volume fraction for different angles of inclination for a cusped-diamond-shaped micro heat pipe (Ca=0.1204; $\hat{M}$=0.172; working fluid=water; operating temperature=60 °C)**

Figure 5 illustrates the maximum allowable heat transport rate for an inclined equilateral-triangle- and cusped-diamond-shaped micro heat pipe designed for horizontal orientation. It is observed that for a constant operating temperature of 60 °C with water as the working fluid, the allowable heat transport rate of the micro heat pipes increases with an increase in angle of inclination. The increase in maximum allowable heat transport rate for the two types of cross-sectional shape can be explained by examining the effects of capillary and gravitational forces. The heat transport capacity of a horizontal micro heat pipe is provided mainly by its working fluids ability to circulate effectively, under the constraint of other factors, such as the micro heat pipe's geometry. For a positively inclined micro heat pipe, the additional driving agent of the gravitational force enhances the circulation rate of the working fluid, which in turn, results in an increase in the allowable heat transport rate.

From Fig. 5, it can be seen that the maximum allowable heat transport rate (which is limited by dryout at the evaporator end) of a cusped-diamond-shaped micro heat pipe outperforms an equilateral-triangle-shaped micro heat pipe when it is positively inclined. However, the relative increase in heat transport rate when the angle of inclination is increased from 0° to 60° is starkly different for an equilateral-triangle- and cusped-diamond-shaped micro heat pipe. The differences in the rate of increase can be explained by examining the relative importance of gravity, for the case of an equilateral triangle and cusped diamond. If we examine Fig. 5, it is apparent that the relative importance of gravity is more prominent in an equilateral-triangle micro heat pipe than a cusped-diamond-shaped micro heat pipe, based on the increase in its allowable heat transport rate when the angle of inclination is increased from 0° to 60°. For a cusped-diamond-shaped micro heat pipe, due to the relatively less prominent effect of gravity, the circulation rate of the working fluid is minimally enhanced by

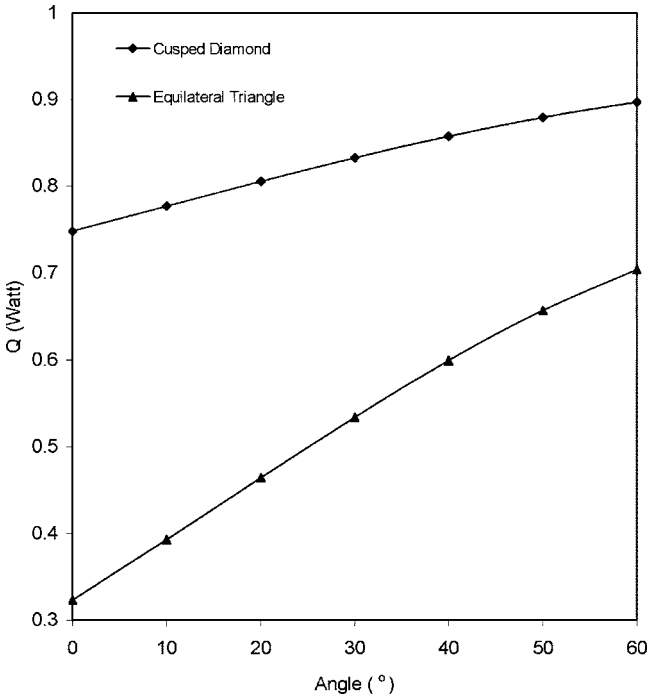


**Fig. 5 Maximum allowable heat transport rate of different types of micro heat pipe designed for a horizontal orientation as a function of the angle of inclination (working fluid=water; operating temperature=60 °C)**

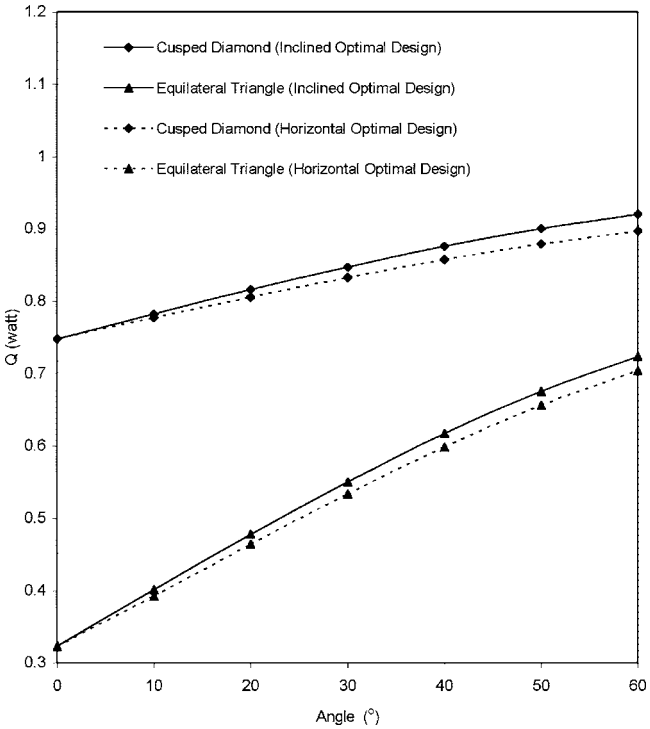


**Fig. 7 Heat transport capacity for different types of cross-sectional-shaped micro heat pipe as a function of the angle of inclination (working fluid=water; operating temperature =60 °C)**

gravity when the micro heat pipe is inclined. On the other hand, for an equilateral-triangle-shaped micro heat pipe, due to the relatively more prominent effect of gravity, the circulation rate of the working fluid is strongly enhanced by gravity when it is inclined. Hence, the relatively higher liquid circulation rate increases the maximum allowable heat transport rate of an equilateral-triangle-shaped micro heat pipe compared to a cusped-diamond-shaped micro heat pipe.

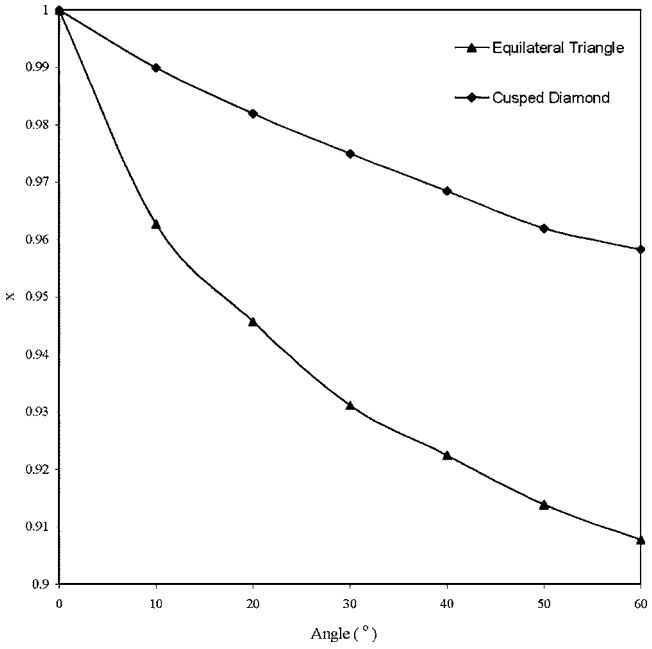


**Fig. 6 Location in the axial direction of the onset of flooding for different cross-sectional-shaped micro heat pipes as a function of its angle of inclination (working fluid=water; operating temperature=60 °C)**

It is interesting to observe that when the angle of inclination is increased, the position of the maximum point or flooding limit shifts further away from the condenser end ($\hat{x}_0 < 1.0$). This is due to the increased effects of gravity, which tends to move the liquid phase toward the evaporator section. As explained earlier, when the angle of inclination is increased, the gravitational effect becomes more prominent, whereby the balance between the gravity and the heat load ($ds/d\hat{x}=0$) is achieved progressively away from the condenser end. The stronger the effect of gravity, the further away from the condenser end the balance is reached. By comparing the relative distance from the condenser end where the flooding limit occurs, as illustrated in Fig. 6, we can conclude that the effect of gravity is relatively less prominent in a cusped-diamond-shaped micro heat pipe than in one of the equilateral-triangle shape. As explained earlier, the effect of gravity tends to cause the liquid film inside an inclined micro heat pipe to become progressively thicker away from the condenser end. The stronger the effect of gravity, the further the liquid is drawn or accumulated away from the condenser end, to form a throat against the vapor flow in the condenser section [6]. Obviously, the most likely location where this may occur is $\hat{x}_0$ where the liquid saturation is maximum. Figure 6 illustrates the position of $\hat{x}_0$ as a function of angle of inclination.

Figure 7 illustrates the heat transport capacity of an inclined equilateral-triangle- and cusped-diamond-shaped micro heat pipes. The micro heat pipes are optimally charged with water and the operating temperature is 60 °C. The associated charge level is plotted in Fig. 8. The dashed curve in Fig. 7 depicts the maximum allowable heat transport rate of an inclined micro heat pipe designed for horizontal orientation. The comparison of the maximum allowable heat transport rate of the two operating conditions,

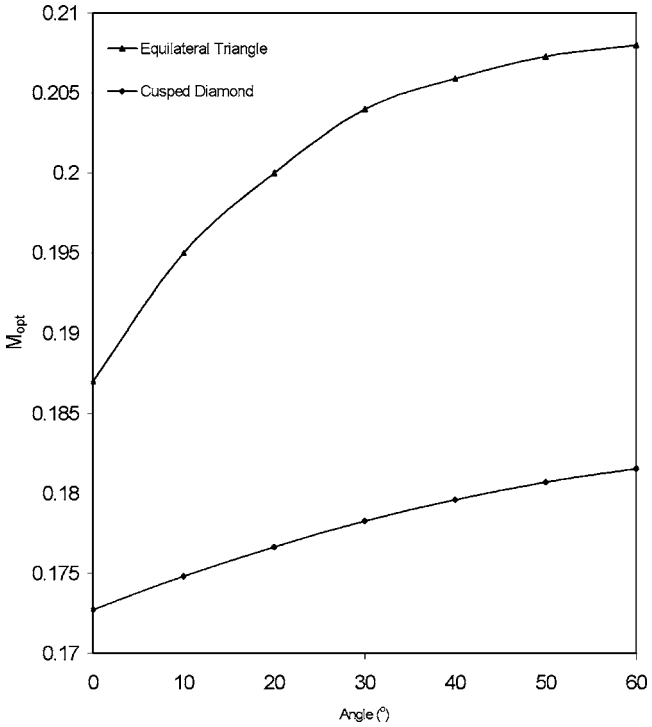


**Fig. 8 Optimal charge level for different types of cross-sectional-shaped micro heat pipe as a function of the angle of inclination (working fluid=water; operating temperature =60 °C)**

i.e., optimally charged for an inclined and horizontal orientation, shows that the difference in maximum allowable heat transport rate is not large.

From Fig. 7, we can clearly see that the heat transport capacity increases when the angle of inclination is increased for both types of micro heat pipe. However, if we examine Fig. 6, we see that the axial position where flooding first takes place $\hat{x}_0$, moves further away from the condenser end when the angle of inclination is increased. As mentioned in the earlier paragraph, $\hat{x}_0$ should be as close to $\hat{x}=1.0$, to avoid the possibility of a liquid bridge blocking the vapor flow passage inside the condenser section. By comparing Figs. 6 and 7, we can conclude that for a fixed angle of inclination, a cusped-diamond-shaped micro heat pipe is superior in performance than an equilateral-triangle micro heat pipe based on its heat transport capacity and the position where flooding first takes place.

## Concluding Remarks

From the results obtained, it is shown that the effect of gravity cannot be neglected for an inclined micro heat pipe. The effect of gravity is shown to be more prominent for an equilateral-triangle-shaped micro heat pipe than a cusped-diamond shape. The liquid fraction distribution along the axial direction inside the micro heat pipe is significantly distorted for an inclined micro heat pipe, with the occurrence of a maximum point away from the condenser end. From the results obtained, the allowable heat transport rate of a micro heat pipe designed for horizontal orientation increases when it is positively inclined.

## Nomenclature

$A$ = cross-sectional area
Ca = capillary number
$D_h$ = hydraulic diameter
$h_{fg}$ = latent heat of evaporation
$K$ = permeability
$L$ = length of micro heat pipe
$L_a$ = length of adiabatic section
$L_e$ = length of evaporator section
$L_c$ = length of condenser section
$\dot{m}$ = mass flow rate
$\hat{m}$ = as defined in Eq. (8)
$M$ = mass of working fluid
$\hat{M}$ = charge level
$N$ = number of corners
$q_c$ = rate of heat flow across a unit length of condenser
$q_e$ = rate of heat flow across a unit length of evaporator
$Q$ = rate of heat transport
$s$ = volume fraction occupied by liquid phase
$T$ = temperature
$w$ = side of triangle (0.001 m)
$x$ = distance from evaporator end
$\hat{x}$ = dimensionless x
$\gamma$ = viscosity ratio
$\vartheta$ = contact angle
$\mu$ = dynamic viscosity
$\nu$ = kinematic viscosity
$\rho$ = mass density
$\sigma$ = surface tension
$\phi$ = half angle of a corner
$\alpha$ = as defined in Fig. 2(*b*)
$\theta$ = angle of inclination

### Subscript

cl = of capillary limit
fl = of onset of flooding
$l$ = of liquid
$\nu$ = of vapor

## References

[1] Cotter, T. P., 1984, "Principles and Prospects of Micro Heat Pipes," *Proceedings of the 5th International Heat Pipe Conference*, Tsukuba, Japan, pp. 328–335.
[2] Tio, K. -K., Liu, C. Y., and Toh, K. C., 2000, "Thermal Analysis of Micro Heat Pipe Using a Porous Medium Model," Heat Mass Transfer, **36**, pp. 21–28.
[3] Longtin, J. P., Badran, B., and Gerner, F. M., 1994, "A One Dimensional Model of Micro Heat Pipe During Steady State-State Operation," J. Heat Transfer, **116**, pp. 709–715.
[4] Babin, B. R., Peterson, G. P., and Wu, D., 1990, "Steady-State Modeling & Testing of a Micro Heat Pipe," J. Heat Transfer, **112**, pp. 595–601.
[5] Khrustalev, D., and Faghri, A., 1994, "Thermal Analysis of a Micro Heat Pipe," J. Heat Transfer, **116**, pp. 189–198.
[6] Wang, C. Y., Groll, M., Rosler, S., and Tu, C. J., 1994, "Porous Medium Model for Two-Phase Flow in Mini Channels with Applications to Micro Heat Pipes," Heat Recovery Syst. CHP, **14**, pp. 377–389.
[7] Sugumar, D., and Tio, K. -K., 2003, "Heat Transport Limitation of a Triangular Micro Heat Pipe," *ASME 1st International Conference on Microchannels and Minichannels*, pp. 739–746.
[8] Shah, R. K., and London, A. L., 1978, *Laminar Flow Forced Convection in Ducts*, Academic, New York.

# Maximizing Heat Transfer Through Joint Fin Systems

**A.-R. A. Khaled**[1]
Thermal Engineering and Desalination Technology Department,
King AbdulAziz University,
P.O. Box 80204,
Jeddah 21589, Saudi Arabia

*Heat transfer through joint fins is modeled and analyzed analytically in this work. The terminology "joint fin systems" is used to refer to extending surfaces that are exposed to two different convective media from its both ends. It is found that heat transfer through joint fins is maximized at certain critical lengths of each portion (the receiver fin portion which faces the hot side and the sender fin portion that faces the cold side of the convective media). The critical length of each portion of joint fins is increased as the convection coefficient of the other fin portion increases. At a certain value of the thermal conductivity of the sender fin portion, the critical length for the receiver fin portion may be reduced while heat transfer is maximized. This value depends on the convection coefficient for both fin portions. Thermal performance of joint fins is increased as both thermal conductivity of the sender fin portion or its convection coefficient increases. This work shows that the design of machine components such as bolts, screws, and others can be improved to achieve favorable heat transfer characteristics in addition to its main functions such as rigid fixation properties.* [DOI: 10.1115/1.2137764]

*Keywords: joint fins, heat transfer, enhancements, maximum, extended surfaces*

## 1 Introduction

Heat transfer through extending surfaces was studied extensively in the literature [1,2]. In this work, it is proposed to utilize joints like bolts, screws, and similar existing mechanical components to transfer heat in addition to their main fixation function. These mechanical components form extending surfaces which can participate in heat transfer especially if the two ends of these components are exposed to different convective media. The terminology "joint fins" is used to refer to these components. Heat transfer through joint fins is analyzed analytically in this work in order to explore their thermal behavior so that improvements in joint designs can be achieved.

## 2 Problem Formulation

Consider a thin wall separating two convective media from both its left and right sides. The convection coefficient and the freestream temperature on the left side are $h_1$ and $T_{\infty 1}$, respectively, while they are $h_2$ and $T_{\infty 2}$ on the right side. It is assumed that $T_{\infty 1} > T_{\infty 2}$. The convective media with temperature $T_{\infty 1}$ is referred to as the "source" while the other one is referred to as the "sink." Utilizing Newton's law for cooling, it can be shown that the wall temperature is equal to

$$T_S = \left[\left(\frac{h_1}{h_2}\right)T_{\infty 1} + T_{\infty 2}\right] \Big/ \left[\left(\frac{h_1}{h_2}\right) + 1\right] \tag{1}$$

If a very long fin having a uniform cross-sectional area penetrates through a wall linking thermally both the source and the sink. The terminology "joint fin" is used in this work to refer for such kinds of fin systems. It is assumed that the conduction heat transfer at the fin tips on the source and the sink sides is negligible and that the convection coefficient for the fin in the source side is $h_{f1}$ while it is $h_{f2}$ on the sink side as illustrated in Fig. 1. The heat transfer through the joint fin is equal to

$$q_f = \frac{\sqrt{h_{f1}k_1PA_C}}{1 + \sqrt{\dfrac{h_{f1}k_1}{h_{f2}k_2}}}(T_{\infty 1} - T_{\infty 2}) \tag{2}$$

where $k_1$ and $k_2$ are the thermal conductivity for the fin on the source and the sink sides, respectively. $P$ is the perimeter of the fin cross section and $A_C$ is the cross-sectional area of the fin. The portion of the fin on the source side is referred to in this work as the "receiver fin portion" while the other portion is referred to as the "sender fin portion." The temperature at the intersection between the receiver and sender portions of the fin $T_b$ is equal to the following

$$T_b = \frac{\sqrt{\dfrac{h_{f1}k_1}{h_{f2}k_2}}T_{\infty 1} + T_{\infty 2}}{\sqrt{\dfrac{h_{f1}k_1}{h_{f2}k_2}} + 1} \tag{3}$$

The fin effectiveness can be calculated from

$$\varepsilon_f = \frac{q_f}{q_{\text{no fin}}} = \left[\left(\frac{h_1 + h_2}{h_1h_2}\right)\sqrt{\frac{h_{f1}k_1P}{A_C}}\right] \Big/ \left[1 + \sqrt{\frac{h_{f1}k_1}{h_{f2}k_2}}\right] \tag{4}$$

The fin effectiveness is greater than one when

$$\sqrt{\frac{h_{f1}k_1}{h_{f2}k_2}} < \left(\frac{h_1 + h_2}{h_1h_2}\right)\sqrt{\frac{h_{f1}k_1P}{A_C}} - 1 \tag{5}$$

Define $\gamma$ and $\beta$ as ratios of the heat transfer represented by Eq. (2) to fin heat transfer in the absence of the sender and receiver fin portions, respectively, with fin base temperature equal to $T_s$ (Eq. (1)). It can be shown that $\gamma$ and $\beta$ are equal to

$$\gamma = \left[\frac{h_1}{h_2} + 1\right] \Big/ \left[1 + \sqrt{\frac{h_{f1}k_1}{h_{f2}k_2}}\right] \tag{6}$$

$$\beta = \left[\frac{h_2}{h_1} + 1\right] \Big/ \left[1 + \sqrt{\frac{h_{f2}k_2}{h_{f1}k_1}}\right] \tag{7}$$

They are greater than unity when

$$\gamma > 1 \Rightarrow \frac{h_{f1}k_1}{h_{f2}k_2} < \left(\frac{h_1}{h_2}\right)^2 \tag{8}$$

$$\beta > 1 \Rightarrow \frac{h_{f1}k_1}{h_{f2}k_2} > \left(\frac{h_1}{h_2}\right)^2 \tag{9}$$

Now, consider that this fin has a finite length $L$ and insulated from both its ends. The fin heat transfer can be calculated from either the receiver or the sender fin portions. It is equal to the following in dimensionless form

[1]Corresponding author. Tel: +966 2 6402000 Ext. 68185; Fax: +966 2 6952182; e-mail: akhaled@kaau.edu.sa

Contributed by the Heat Transfer Division of ASME for publication in the JOURNAL OF HEAT TRANSFER. Manuscript received April 29, 2005; final manuscript received September 14, 2005. Review conducted by Yogendra Joshi.

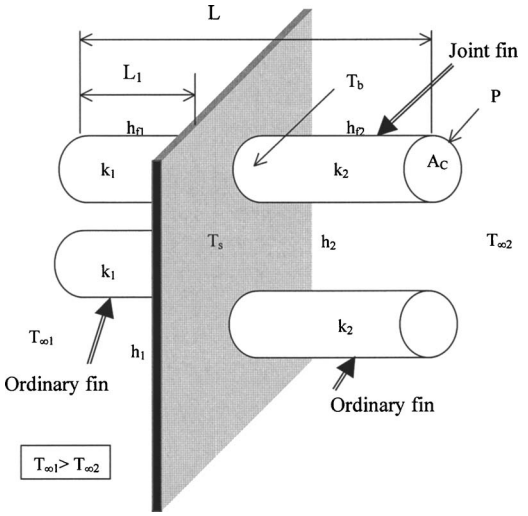


**Fig. 1 Schematic diagram for a joint fin and ordinary extended surfaces**

$$\Theta = \frac{q_f}{\sqrt{h_{f1}k_1PA_C}(T_{\infty_1} - T_{\infty 2})} = \frac{\tanh[m_1L(L_1/L)]}{1 + \dfrac{\tanh[m_1L(L_1/L)]}{\tanh\left[m_1L\sqrt{\left(\dfrac{h_{f2}}{h_{f1}}\right)\left(\dfrac{k_1}{k_2}\right)}(1-(L_1/L))\right]}\sqrt{\left(\dfrac{h_{f1}}{h_{f2}}\right)\left(\dfrac{k_1}{k_2}\right)}} \tag{10}$$

where $m_1$ and $m_2$ (the receiver and sender fin portion indices) are equal to

$$m_1 = \sqrt{\frac{h_{f1}P}{k_1A_C}} \quad m_2 = \sqrt{\frac{h_{f2}P}{k_2A_C}} \tag{11}$$

The fin base temperature is

$$T_b = \frac{\dfrac{\tanh[m_1L_1]}{\tanh[m_2(L-L_1)]}\sqrt{\dfrac{h_{f1}k_1}{h_{f2}k_2}}T_{\infty 1} + T_{\infty 2}}{1 + \dfrac{\tanh[m_1L_1]}{\tanh[m_2(L-L_1)]}\sqrt{\dfrac{h_{f1}k_1}{h_{f2}k_2}}} \tag{12}$$

It can be shown that the rate of fin heat transfer through the fin can be maximized for the value of $L_1/L$ that satisfies

$$\left(\frac{dq_f}{dL_1}\right)\bigg|_{L=L_1^*} = 0 \Rightarrow \frac{\sinh(m_1L(L_1^*/L))}{\sinh(m_2L(1-(L_1^*/L)))} = \frac{m_1}{m_2}\sqrt{\frac{h_{f2}}{h_{f1}}} = \sqrt{\frac{k_2}{k_1}} \tag{13}$$

Substituting Eq. (13) in Eq. (10) will result in the following:

$$\Theta_{\max} = \frac{\tanh[m_1L(L_1^*/L)]}{1 + \dfrac{\cosh\left[m_1L\sqrt{\left(\dfrac{h_{f2}}{h_{f1}}\right)\left(\dfrac{k_1}{k_2}\right)}(1-(L_1^*/L))\right]}{\cosh[m_1L(L_1^*/L)]}\sqrt{\dfrac{h_{f1}}{h_{f2}}}} \tag{14}$$

Of special interest is the case when $m_1L_1^* \gg 2.3$ and $m_2/m_1 > 1.0$. The solution to Eq. (13) is

$$\frac{L_1^*}{L} \cong \frac{\dfrac{m_2}{m_1} + \dfrac{1}{2m_1L}\ln\left(\dfrac{k_2}{k_1}\right)}{\dfrac{m_2}{m_1} + 1} = \frac{\sqrt{\dfrac{k_1}{k_2}}\sqrt{\dfrac{h_{f2}}{h_{f2}}} + \dfrac{1}{2m_1L}\ln\left(\dfrac{k_2}{k_1}\right)}{\sqrt{\dfrac{k_1}{k_2}}\sqrt{\dfrac{h_{f2}}{h_{f1}}} + 1} \tag{15}$$

As such, the fin transfers the maximum heat, which is equal to

$$(q_f)_{\max} \cong \frac{\sqrt{h_{f1}k_1PA_C}(T_{\infty_1} - T_{\infty 2})}{1 + \sqrt{\dfrac{h_{f1}k_1}{h_{f2}k_2}}} \tag{16}$$

Another interesting special case is when $m_1 = m_2 = m$. This case corresponds to a fin that has $h_{f1}k_2 = h_{f2}k_1$. The value of $L_1$ that maximizes the rate of heat transfer through the fin $(L_1^*)$ can be obtained from Eq. (13). It is equal to

$$\frac{L_1^*}{L} = \frac{1}{2mL}\ln\left[\left(\operatorname{csch}(mL)\sqrt{\frac{k_1}{k_2}} + \coth(mL) + 1\right) \Big/ \left(\operatorname{csch}(mL)\sqrt{\frac{k_1}{k_2}} + \coth(mL) - 1\right)\right] \tag{17}$$

The heat transfer for this case is equal to

$$\Theta_{\max} = \frac{\tanh[mL(L_1^*/L)]}{1 + \dfrac{\cosh[mL(1-(L_1^*/L))]}{\cosh[mL(L_1^*/L)]}\sqrt{\dfrac{k_1}{k_2}}} \tag{18}$$

Equation (15) predicts that as $h_{f2}$ increases, $L_1^*$ increases where $L_1^*$ approaches $L$ as $h_{f2}$ approaches infinity. For this case, maximum heat transfer approaches the following value

$$\lim_{h_{f2}\to\infty}(q_f) = h_{f1}PL(T_{\infty_1} - T_{\infty 2}) \tag{19}$$

Define $\lambda$ as the thermal performance factor for the joint fin. This factor represents the ratio fin heat transfer per unit volume to the maximum fin heat transfer represented by Eq. (19) per unit volume. As such, the performance factor for the joint fin with insulated tips is equal to

$$\lambda = \frac{\tanh[m_1L(L_1/L)]}{m_1L\left(1 + \dfrac{\tanh[m_1L(L_1/L)]}{\tanh[m_2L(1-(L_1/L))]}\sqrt{\dfrac{h_{f1}}{h_{f2}}}\sqrt{\dfrac{k_1}{k_2}}\right)} \tag{20}$$

The maximum thermal performance factor

$$\lambda_{\max} = \frac{\tanh[m_1L(L_1^*/L)]/(m_1L)}{1 + \dfrac{\cosh[m_2L(1-L_1^*/L)]}{\cosh[m_1L(L_1^*/L)]}\sqrt{\dfrac{h_{f1}}{h_{f2}}}} \tag{21}$$

The performance factor for joint fins having $L_1$ satisfying Eq. (15) is equal to

$$\lambda_{\max} \cong \frac{1}{\left(1 + \sqrt{\left(\dfrac{h_{f1}}{h_{f2}}\right)\left(\dfrac{k_1}{k_2}\right)}\right)m_1L} \tag{22}$$

while it is equal to the following when $m_1 = m_2$

$$\lambda_{\max} = \frac{\tanh[mL(L_1^*/L)]/mL}{1 + \dfrac{\cosh[mL(1-(L_1/L))]}{\cosh[mL(L_1^*/L)]}\sqrt{\dfrac{k_1}{k_2}}} \tag{23}$$

Equation (23) suggests that the performance factor of the proposed fin increases as $m_1L$ decreases or as $h_{f2}$ or $k_2$ increase.

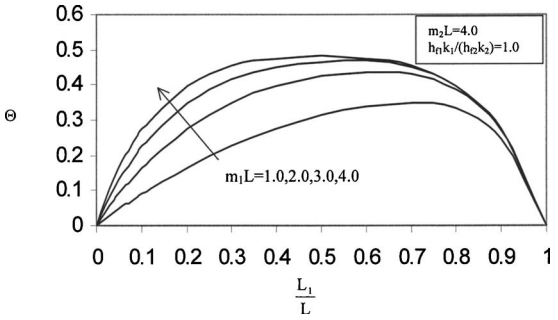


**Fig. 2 Variation of the dimensionless heat transfer with the relative length $L_1/L$ and $m_1L$**

## 3 Discussion of the Results

Increasing both the thermal conductivity and the convection coefficient of the sender fin portion increases both the fin effectiveness $\varepsilon_f$ and the first heat transfer ratio $\gamma$ while it reduces the second heat transfer ratio $\beta$ as seen from Eqs. (4), (6), and (7), respectively. When the controlling parameter $h_{f1}k_1/h_{f2}k_2$ is less than $(h_1/h_2)^2$, the joint fin transfers heat more than the receiver fin portion alone. Joint fin transfers more heat than the receiver fin portion alone when the sender fin portion is made from a material with a large thermal conductivity or when the convection coefficient between that portion and the sink is very large. On the other hand, the previous condition results in increasing heat transfer from the sender fin portion alone over that for the joint fin. Joint fins will transfer the same heat as compared to the receiver fin portion alone and the sender fin portion alone when $h_{f1}=h_{f2}=h_1=h_2$ and $k_1=k_2$.

Figure 2 shows the effects of the length of the receiver fin portion on the fin heat transfer for a joint fin with a finite length. It is noticed that heat transfer increases as the receiver fin portion index increases and it is maximized for certain lengths of the receiver fin portion. That critical length decreases as the receiver fin portion index increases while it increases as the sender fin portion index increases and it increases as the ratio $k_2/k_1$ increases. It can be shown from Fig. 2 that heat transfer is maximized at $L_1/L\sim0.8$ when $k_2/k_1=0.5$ and $h_{f1}=h_{f2}$. This is almost corresponds to a joint with the sender portion made from copper while the receiver portion is made from aluminum. This example shows that a 25% increase in heat transfer can be obtained by setting $L_1/L\sim0.8$ compared to when $L_1/L$ is set to be 0.5.

Figure 3 shows that the critical length of the receiver fin portion increases as $h_{f2}$ increases. That length can be minimized at a certain value of the sender fin portion thermal conductivity. The joint fin performance factor increases as both the thermal conductivity and the convection coefficient of the sender fin portion increases Eq. (20). That thermal performance factor decreases as the joint fin index parameter increases when it is the same for both portions as shown in Eq. (23).

## 4 Conclusions

Fin effectiveness was found to increase as both the thermal conductivity and the convection coefficient of the sender fin portion increase. Also, It was found that heat transfer through finite joint fins is maximized for certain lengths of the receiver fin portion depending on the thermal conductivities of both joint fin portions as well as on convection coefficients for both joint fin portions. That length was found to increase as the convection coefficient of the sender fin portion increases. Moreover, the length of the receiver fin portion can be further minimized while heat transfer through the joint fin is maximized at a certain value of the thermal conductivity of the sender fin portion. Eventually, thermal performance of joint fins was found to increase as both thermal conductivity of the sender fin portion and its convection coefficient increase. Finally, joint connections like bolts, needles, pins, and others can be redesigned in order to have favorable heat transfer characteristics in addition to their main function as to provide good fixation features.

## Nomenclature

$h_1$ = convection coefficient on the source side
$h_2$ = convection coefficient on the sink side
$h_{f1}$ = convection coefficient for the receiver fin portion
$h_{f2}$ = convection coefficient for the sender fin portion
$k_1$ = thermal conductivity of the receiver fin portion
$k_2$ = thermal conductivity of the sender fin portion
$L$ = fin length
$L_1$ = length of the receiver fin portion
$L_1^*$ = critical length of the receiver fin portion
$m_1$ = fin index of the receiver fin portion
$m_2$ = fin index of the sender fin portion
$q_f$ = heat transfer through the joint fin

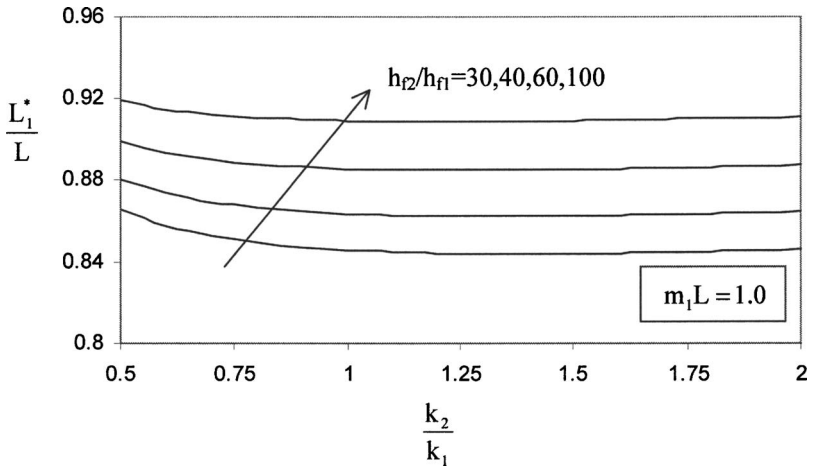


**Fig. 3 Variation of the relative critical length $L_1^*/L$ with $h_{f2}/h_{f1}$ and $k_2/k_1$ (Eq. (15))**

$T_b$ = base temperature
$T_{\infty 1}$ = freestream temperature of the source
$T_{\infty 2}$ = freestream temperature of the sink

**Greek symbols**

$\Theta$ = dimensionless heat transfer
$\beta$ = first in heat transfer ratio
$\varepsilon_f$ = joint fin effectivness
$\gamma$ = second heat transfer ratio
$\lambda$ = fin performance parameter

## References


[1] Lienhard, J. H., IV, and Lienhard, J. H., V, 2004, *A Heat Transfer Textbook*, Phlogiston, Cambridge, MA.
[2] Gardner, K. A., 1945, "Efficiency of Extended Surfaces," Trans. ASME, **67**, 621–631.

# Heat Conduction in Multiply Adjoined Anisotropic Media with Embedded Point Heat Sources

**Y. C. Shiah**[1]

**Po-Wen Hwang**

**Ruey-Bin Yang**

Department of Aeronautical Engineering,
Feng Chia University,
100 Wenhwa Road, Seatwen 407,
Taichung, Taiwan, R.O.C.

*In this article the direct domain-mapping technique is applied in the boundary element method (BEM) to investigate the heat conduction in composites consisting of multiple anisotropic media with embedded point heat sources. By use of a linear coordinate transformation, the physical domain is mapped to an auxiliary plane for 2D or space for 3D, where the heat conduction is considered isotropic. However, the interfaces of adjoined materials with dissimilar properties will overlap or separate in the mapped plane or space. For the use of the subregioning technique in BEM to solve such problems, the thermal equilibrium condition for interfaces is developed to account for boundary distortions. In the mapped plane or space, not only the locations but also the strength of heat sources are transformed accordingly. After the problem is solved in the mapped plane or space, the obtained numerical solution is thereafter interpolated and transformed back to the one in the physical domain.*
[DOI: 10.1115/1.2137765]

*Keywords: direct domain-mapping, boundary element method, anisotropic heat conduction, non-homogeneous anisotropic media, point heat sources*

## Introduction

Materials with anisotropic properties have been extensively used in numerous applications since the early 1960s. For various purposes, composites are often constructed by combining two or more anisotropic materials such that the physically or chemically different phases will make possible the high performance. In achieving this high performance, the interaction between component materials in the interface is of utmost importance. As can be commonly observed in industry nowadays, many practical heat conduction problems in engineering may involve internal heat sources present in anisotropic media due to internal chemical reactions or electrical heating. To date, investigations on the multidimensional heat conduction problems in multiply adjoined media with internal heat sources still, indeed, remain extremely scarce in the open literature due to the complexities arising from the anisotropic heat fluxes across interfaces of dissimilar materials. In recent decades, many analytical works have been presented to deal with relevant anisotropic heat conduction problems. There are too many to include them all herein, and, thus, only a few are mentioned as examples. Tauchert and Akoz [1] used complex conjugate quantities to solve the thermal field in a two-dimensional anisotropic slab. Mulholland and Gupta [2] investigated a three-dimensional anisotropic body by using coordinate transformations to principal axes. Chang [3] solved the heat conduction problem in a three-dimensional configuration by conventional Fourier transformation. By a transformation of anisotropic problems to orthotropic ones, Poon [4] first investigated the anisotropic temperature field in layered composites. Thereafter, Poon [5] treated the anisotropic heat conduction problem by further extending the transformation such that the mapped domain is governed by isotropic heat conduction. However, such treatment to analytically solve anisotropic heat conduction problems with finite domains has not been so generally successful due to the complexities arising from distorted boundaries and their associated boundary conditions after transformation. Although some analytical solutions have been obtained for a few specific problems, recourse to numerical methods is generally necessary for practical engineering problems.

In contrast with the domain solution technique, namely, the finite element method and the finite difference method, the boundary element method (BEM) has been recognized as an efficient numerical tool for engineering analyses due to its distinctive feature that only the boundary needs to be modeled. In their efforts to transform the extra volume integral appearing in the associated anisotropic thermoelasticity boundary integral equation [6,7], Shiah and Tan [8] applied such linear coordinate transformation in the BEM to numerically treat the anisotropic thermal field problem. As a result of such transformation, the mapped domain is then considered "isotropic," albeit distorted in the auxiliary plane. In conjunction with the BEM's multiple reciprocity method, Shiah and Lin [9] also applied the domain-mapping scheme to numerically solve the anisotropic field problem involving arbitrary volume heat sources present in the domain. By further extending the transformation for three-dimensional (3D) cases, Shiah and Tan [10] adopted the scheme to solve 3D anisotropic heat conduction problems by the BEM. For the related works, Yan et al. [11] studied two-layered isotropic bodies with homogeneous form, where the Green function solution is adopted to incorporate the effects of internal heat source. Hsien and Ma [12] used a linear coordinate transformation to solve the heat conduction problem for a thin-layer medium with anisotropic properties. Also, Ma and Chang [13] applied the similar methodology to analyze anisotropic multi-layered media.

As the foundation to further treat the associated thermoelasticity problem by the BEM, the present work is to solve, by the domain mapping technique, the temperature field in nonhomogeneous anisotropic media subjected to internal point heat sources. As mentioned earlier, the process is essential to enable the exact volume integral transformation for the associated thermoelasticity problem [6] treated in a sequentially coupled manner.

Despite its obvious significance in engineering, the associated thermoelasticity problem in the BEM still remains unexplored. This is mainly due to the complexities arising from anisotropic thermoelasticity as well as the complicated interfacial conditions between conjoint anisotropic materials. In the direct domain-mapping scheme, the interfaces of dissimilar materials shall overlap or separate in the mapped plane for 2D or in space for 3D. In this article the thermal equilibrium conditions for interfaces between conjoint anisotropic materials, which are required for applying the BEM's sub-regioning technique, are presented for both 2D and 3D cases. Traditionally, regular interface conditions will require the same coordinates of interfaces for isotropic materials. However, the newly derived interface conditions have taken into account the overlapping or separation of interfaces. This technique is first introduced and implemented for both 2D and 3D cases. In the mapped plane or space, not only the locations but also the strength of the concentrated heat sources are transformed accordingly for each component material. The proposed scheme has been implemented into computer codes by slightly modifying a

[1]Associate Professor, Tel: 886-4-2451-7250 ext. 3956, Fax: 886-4-2451-0862, e-mail: ycshiah@fcu.edu.tw

Contributed by the Heat Transfer Division of ASME for publication in the JOURNAL OF HEAT TRANSFER. Manuscript received June 6, 2004; final manuscript received January 6, 2005. Review conducted by Gang Chen.

  

readily available BEM program for solving the standard Laplace equation. At the end, a numerical example is provided to demonstrate the validity as well as the applicability of the developed program codes.

## Direct Domain-Mapping

For the heat conduction problem involving anisotropic media with the presence of internal point heat sources, following the tensor notation with repeated indices implying summation over them, the governing partial differential equation for each component sub-domain may be expressed as

$$K_{ij}T_{,ij} = -\sum_{m=1}^{n} S_m \delta_m \quad (i = 1,2,3 \text{ and } j = 1,2,3) \tag{1}$$

where the notation of a comma is used to stand for spatial differentiation; $T$ represents temperature change, and $K_{ij}$ are conductivity coefficients. In Eq. (1), the terms on summation are for a discrete distribution of concentrated heat sources with strength magnitude $S_m$ at point $m$ and $\delta_m$ stands for the Dirac delta function at the point. From thermodynamic principals and Onsagar's reciprocity relation, we get the following characteristics for general three-dimensional cases

$$\begin{gathered} K_{11} > 0 \quad K_{22} > 0 \quad K_{33} > 0 \quad K_{12} = K_{21} \quad K_{13} = K_{31} \quad K_{23} = K_{32} \\ K_{11}K_{22} - K_{12}^2 > 0 \quad K_{11}K_{33} - K_{13}^2 > 0 \quad K_{22}K_{33} - K_{23}^2 > 0 \end{gathered} \tag{2}$$

The analysis can be significantly simplified in the case of orthotropy, where the cross-derivative terms are absent. As a result, a commonly adopted approach to treat the fully anisotropic problem is, first, to determine the principal axes ($\zeta_1$, $\zeta_2$, and $\zeta_3$) by rotating the original Cartesian axes such that the cross-derivative terms will disappear before any further numerical treatments. In other words, under the rotated coordinate system, the governing equation becomes

$$K_1^* \frac{\partial^2 T}{\partial \zeta_1^2} + K_2^* \frac{\partial^2 T}{\partial \zeta_2^2} + K_3^* \frac{\partial^2 T}{\partial \zeta_2^2} = -\sum_{m=1}^{n} \hat{S}_m \hat{\delta}_m \tag{3}$$

where $K_i^*$ represents the conductivity coefficients in the direction of the principal axes, and the caret notation for the heat source terms is used to denote corresponding heat sources under the rotated axes. Such an approach has been used in the finite element method [14,15], the finite difference method [16], and also the BEM [17,18]. The procedure to reduce Eq. (3) into the canonical form of the standard Poisson's equation by scaling the principal coordinates has also been discussed in, e.g., Barnerjee and Butterfield [18]. In this scheme, the analysis is carried out in the rotated, scaled coordinate system of the principal axes. However, reports of this procedure being applied to practical problems in general anisotropy remain very scarce in the BEM literature. Another attractive approach to numerically treat the anisotropic problem, proposed by Shiah and Tan [8,10], is to employ a coordinate transformation such that $T$ in the transformed domain is governed by the standard Poisson's equation. For two-dimensional cases, the linear transformation between both coordinate systems may be generally expressed as

$$[\hat{x}_1 \ \hat{x}_2]^T = [F(K_{ij})][x_1 \ x_2]^T \quad [x_1 \ x_2]^T = [F^{-1}(K_{ij})][\hat{x}_1 \ \hat{x}_2]^T \tag{4}$$

where $[F(K_{ij})]$ (or $[F^{-1}(K_{ij})]$), the transformation (or the inverse transformation) matrix in terms of the invariant coefficients, has its component element $[F_{mn}(K_{ij})]$ (or $[F_{mn}^{-1}(K_{ij})]$). The linear transformation allows the analysis to be carried out using any standard BEM codes for the potential theory, albeit on a distorted domain in the mapped plane. With this transformation, any physical quantity like the temperature variation must remain unchanged at corresponding points on the physical and mapped plane. The value of its normal gradient across the boundary can be obtained via

$$\begin{aligned} \frac{dT}{dn} &= (T_{,\underline{1}}F_{11} + T_{,\underline{2}}F_{21})n_1 + (T_{,\underline{1}}F_{12} + T_{,\underline{2}}F_{22})n_2 \\ \frac{dT}{d\hat{n}} &= (T_{,1}F_{11}^{-1} + T_{,2}F_{21}^{-1})\hat{n}_1 + (T_{,1}F_{12}^{-1} + T_{,2}F_{22}^{-1})\hat{n}_2 \end{aligned} \tag{5}$$

where $n_i$ and $\hat{n}_i$ denote components of the unit outward normal vector on the domain boundary defined in the physical and mapped domain, respectively; the underline is used to refer to the mapped plane defined by the $\hat{x}_i$ coordinate system. As is presented in detail by Shiah and Tan [8], the mapping takes the following form

$$\mathbf{F} = \begin{pmatrix} \sqrt{\Delta}/K_{11} & 0 \\ -K_{12}/K_{11} & 1 \end{pmatrix} \quad \mathbf{F}^{-1} = \begin{pmatrix} K_{11}/\sqrt{\Delta} & 0 \\ K_{12}/\sqrt{\Delta} & 1 \end{pmatrix} \quad \Delta = K_{11}K_{22} - K_{12}^2 \tag{6}$$

For three-dimensional cases [10], the transformation is given by

$$\begin{aligned} \mathbf{F} &= \begin{pmatrix} \sqrt{\Delta}/K_{11} & 0 & 0 \\ -K_{12}/K_{11} & 1 & 0 \\ \alpha_1 & \alpha_2 & \alpha_3 \end{pmatrix} \\ \mathbf{F}^{-1} &= \begin{pmatrix} K_{11}/\sqrt{\Delta} & 0 & 0 \\ K_{12}/\sqrt{\Delta} & 1 & 0 \\ (-K_{12}\alpha_2 - K_{11}\alpha_1)/\alpha_3\sqrt{\Delta} & -\alpha_2/\alpha_3 & 1/\alpha_3 \end{pmatrix} \end{aligned} \tag{7}$$

where $\alpha_i$ are given by

$$\begin{aligned} \alpha_1 &= (K_{12}K_{13} - K_{23}K_{11})/\sqrt{\omega} \\ \alpha_2 &= (K_{12}K_{23} - K_{13}K_{22})/\sqrt{\omega} \end{aligned} \tag{8}$$

$$\alpha_3 = \Delta/\sqrt{\omega} \quad \omega = K_{11}K_{33}\Delta - K_{11}K_{22}K_{13}^2 + 2K_{11}K_{12}K_{13}K_{23} - K_{23}^2K_{11}^2$$

From thermodynamic considerations, it can be proved that the transformation parameter $\omega$ appearing in the above-noted transformation is always positive [10]. Through the above-described transformation, the anisotropic field involving internal point heat source is now governed by

$$T_{,\underline{ii}} = -\sum_{m=1}^{n} S'_m \delta'_m \tag{9}$$

where the equivalent source strength $S'_m$ for both 2D and 3D cases is given by

$$S'_m = S_m K_{11}/\Delta \tag{10}$$

Up to this point, the steps to reduce the anisotropic problem to one of "isotropy" have been presented. The primary goal, however, is to numerically solve the anisotropic field problem by the BEM. The implementation of this domain mapping technique in BEM will now be discussed.

## BEM Treatment of Domain Mapping

As is well established in the BEM literature, the temperature change $T$ and its normal gradient $q = dT/dn$ along the boundary of a solution domain, where $n$ is the unit outward normal vector, are related by the following boundary integral equation

$$\begin{aligned} c(P)T(P) = &\int_S q(Q)U(P,Q)d\hat{S}(Q) - \int_S T(Q)V(P,Q)d\hat{S}(Q) \\ &- \sum_{m=1}^{n} S'_m U(P,M_n) \end{aligned} \tag{11}$$

where $P$ and $Q$ are the source and field points on the boundary, respectively; $M_n$ is the $n$th internal heat-source point. In Eq. (11),

the value of $c(P)$ depends on the geometry at $P$, and $U(P,Q)$ and $V(P,Q)$ represent the fundamental solutions for the temperature and its normal gradient, respectively. The fundamental solutions are given by

$$U(P,Q) = \begin{cases} \dfrac{1}{2\pi}\ln\left(\dfrac{1}{r}\right) & \text{for 2D} \\ \dfrac{1}{4\pi r} & \text{for 3D} \end{cases}$$

$$V(P,Q) = \begin{cases} \dfrac{-1}{2\pi r} r_{,i} n_i & \text{for 2D} \\ \dfrac{-1}{4\pi r^2} r_{,i} n_i & \text{for 3D} \end{cases} \tag{12}$$

Also in Eq. (11), $\hat{S}$ is used to denote the distorted boundary defined in the mapped plane or space. As the usual process in the BEM analysis for solving Eq. (11) for a single domain, the solution domain is discretized into an assemblage of elements, each of which is defined by a finite number of nodes. Writing Eq. (11) for each of these distinct nodes with appropriate shape functions for the interpolation of the solution variables will result in a set of simultaneous equations for the unknown temperature or normal temperature gradient at the nodes. However, the collocation process for solving this boundary integral equation needs to be carried out on the distorted boundary. This therefore calls for immediate transformation of the input Neumann conditions [10] according to

$$\frac{dT}{d\hat{n}} = \left(\frac{\partial T}{\partial x_1}\frac{K_{11}}{\sqrt{\Delta}} + \frac{\partial T}{\partial x_2}\frac{K_{12}}{\sqrt{\Delta}} - \frac{\partial T}{\partial x_3}\frac{(K_{12}\alpha_2 + K_{11}\alpha_1)}{\sqrt{\Delta}\alpha_3}\right)\hat{n}_1 + \left(\frac{\partial T}{\partial x_2} - \frac{\partial T}{\partial x_3}\frac{\alpha_2}{\alpha_3}\right)\hat{n}_2 + \left(\frac{\partial T}{\partial x_3}\frac{1}{\alpha_3}\right)\hat{n}_3 \tag{13}$$

By omitting the temperature gradient in the direction of the $x_3$ axis, Eq. (13) also holds for 2D cases. With properly posed boundary conditions, a set of simultaneous equations for the unknown temperatures or normal temperature gradients at nodal points resulting from the collocation process may now be solved using the standard matrix method. The solved potential gradients, however, need to be further processed to obtain corresponding values for the actual physical domain. The reader may refer to Refs. [8,10] for details regarding the processes and only the key steps are described as follows

$$\frac{dT}{dn} = \hat{\boldsymbol{\varphi}}_i^T \mathbf{F}\frac{\mathbf{F}^T\hat{\mathbf{n}}^T}{|\mathbf{F}^T\hat{\mathbf{n}}|} \tag{14}$$

where $\hat{\mathbf{n}}$ is the outward normal vector on the boundary of the mapped domain, expressed in terms of its components $\hat{n}_i$ in the $\hat{x}_i$ direction; $\hat{\boldsymbol{\varphi}}_i$, the temperature gradient along the mapped boundary, is defined by

$$\hat{\boldsymbol{\varphi}}_i = \left(\frac{\partial T}{\partial \hat{x}_1}\ \frac{\partial T}{\partial \hat{x}_2}\ \frac{\partial T}{\partial \hat{x}_3}\right) \tag{15}$$

Again, the temperature gradient in the third direction may be omitted to account for 2D cases.

To numerically calculate the normal temperature gradient at boundary nodes via Eq. (14), $\hat{\boldsymbol{\varphi}}_i^T$ needs to be first computed by

$$\frac{\partial T}{\partial \hat{x}_1} = \frac{\partial T}{\partial \hat{n}}\cdot\hat{n}_1 + \frac{\partial T/\partial\hat{\xi}(\hat{\eta}_2\hat{n}_3 - \hat{\eta}_3\hat{n}_2) + \partial T/\partial\hat{\eta}(\hat{\xi}_3\hat{n}_2 - \hat{\xi}_2\hat{n}_3)}{\sqrt{(\hat{\xi}_2\hat{\eta}_3 - \hat{\xi}_3\hat{\eta}_2)^2 + (\hat{\xi}_3\hat{\eta}_1 - \hat{\xi}_1\hat{\eta}_3)^2 + (\hat{\xi}_1\hat{\eta}_2 - \hat{\xi}_2\hat{\eta}_1)^2}}$$

$$\frac{\partial T}{\partial \hat{x}_2} = \frac{\partial T}{\partial \hat{n}}\cdot\hat{n}_2 + \frac{\partial T/\partial\hat{\xi}(\hat{\eta}_3\hat{n}_1 - \hat{\eta}_1\hat{n}_3) + \partial T/\partial\hat{\eta}(\hat{\xi}_1\hat{n}_3 - \hat{\xi}_3\hat{n}_1)}{\sqrt{(\hat{\xi}_2\hat{\eta}_3 - \hat{\xi}_3\hat{\eta}_2)^2 + (\hat{\xi}_3\hat{\eta}_1 - \hat{\xi}_1\hat{\eta}_3)^2 + (\hat{\xi}_1\hat{\eta}_2 - \hat{\xi}_2\hat{\eta}_1)^2}} \tag{16}$$

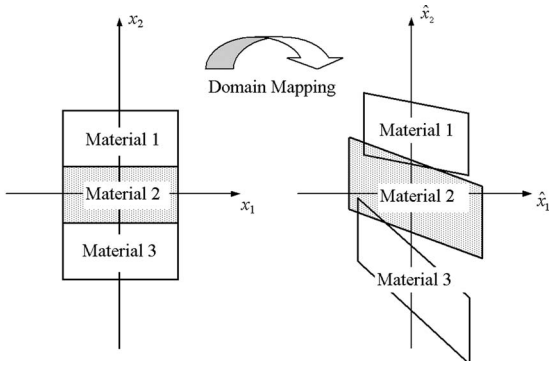


**Fig. 1 Direct domain mapping of a composite consisting of multiple anisotropic materials**

$$\frac{\partial T}{\partial \hat{x}_3} = \frac{\partial T}{\partial \hat{n}}\cdot\hat{n}_3 + \frac{\partial T/\partial\hat{\xi}(\hat{\eta}_1\hat{n}_2 - \hat{\eta}_2\hat{n}_1) + \partial T/\partial\hat{\eta}(\hat{\xi}_2\hat{n}_1 - \hat{\xi}_1\hat{n}_2)}{\sqrt{(\hat{\xi}_2\hat{\eta}_3 - \hat{\xi}_3\hat{\eta}_2)^2 + (\hat{\xi}_3\hat{\eta}_1 - \hat{\xi}_1\hat{\eta}_3)^2 + (\hat{\xi}_1\hat{\eta}_2 - \hat{\xi}_2\hat{\eta}_1)^2}}$$

where $\hat{\xi}_i$ and $\hat{\eta}_i$ stand for components of the unit vector of the local coordinate axes $\hat{\xi}$ and $\hat{\eta}$, respectively, which are mutually orthogonal and both tangent to the boundary surface. For 2D cases, the above equation also holds if $\hat{\eta}_i$ and the temperature gradients $\partial T/\partial\hat{x}_3$ and $\partial T/\partial\hat{\eta}$ are omitted. In Eq. (16), the temperature gradient $\partial T/\partial\hat{n}$ is directly obtained from the solution of the boundary integral equation for the distorted domain, while the other two temperature gradients $\partial T/\partial\hat{\xi}$ and $\partial T/\partial\hat{\eta}$ can be computed using the standard numerical interpolation scheme involving shape functions. The same applies for the computation of $\hat{\xi}_i$ and $\hat{\eta}_i$ in this equation. Therefore, the normal temperature gradient for the physical domain can be readily computed using Eqs. (14) and (16).

Obviously, it can be seen that the algorithm developed for solving the 2D or 3D anisotropic temperature field is relatively simple when compared with the other schemes reported in the open literature. The only necessary modifications of an available BEM computer program that is developed for isotropic problems are the preprocessing of the coordinate transformation using Eq. (7) and the inputted temperature gradients using Eq. (13). After the boundary integral equation, Eq. (11), is solved for unknowns, one may directly obtain the temperature field and also its normal gradients via the postprocessing of the calculated temperature gradients by Eq. (14). This approach may be applied to solve the thermal field in non-homogeneous media that consist of multiple anisotropic materials with different properties as well. The discussion in the following will then focus on how to apply this algorithm to this problem.

## Interface Conditions Between Dissimilar Anisotropic Materials

In the DDM to solve the anisotropic thermal field, the boundary of the physical domain will be distorted in the mapped plane (or space), where the solution domain is considered "isotropic." To apply the conventional sub-regioning technique in the BEM to solve the thermal field in a domain that consists of multiple isotropic media, one needs to supply appropriate thermal compatibility and equilibrium condition along interfaces of conjoint materials. This sub-regioning technique is well established in the open BEM literature and, thus, no further elaboration on this process is made herein. As mentioned earlier, due to the boundary distortion in the mapped plane (or space) for anisotropic materials, the interfaces of conjoint materials with different properties will thus overlap or separate as schematically illustrated in Fig. 1 for a typical 2D case. As a result of the interface overlapping or sepa-

ration, the direct use of the conventional thermal equilibrium condition to solve the associated thermal field in the mapped plane or space, albeit considered "isotropic," will not be valid anymore.

To apply the conventional sub-regioning technique to solve the boundary integral equation, each pair of points along the interface shall require two interface conditions—the compatibility and the equilibrium condition. For a general non-cracked interface between isotropic materials, the compatibility condition is described by

$$T^{(1)} = T^{(2)} \tag{17}$$

where the superscripts (1) and (2) are used to denote material 1 and 2, respectively. Since temperature is a scalar that does not depend on its defined coordinate system, this relation still holds for anisotropic materials, even though the distorted interfaces may overlap/separate in the mapped plane or space. However, due to the distortion of boundaries that results in misalignment of the unit outward normal vectors along the interfaces of adjacent materials, denoted by $\hat{n}^{(1)}$ and $\hat{n}^{(2)}$, the thermal equilibrium of normal heat fluxes needs to be reformulated accordingly. For this purpose, consider first the heat fluxes out of the interfaces between adjacent materials 1 and 2 in the physical plane, denoted by $Q_i^{(1)}$ and $Q_i^{(2)}$, respectively. The thermal equilibrium between adjacent materials states that the sum of the normal heat fluxes across their interfaces shall vanish, i.e.

$$Q_i^{(1)} n_i^{(1)} + Q_i^{(2)} n_i^{(2)} = 0 \tag{18}$$

which, for anisotropic materials, is further written as

$$\sum_{m=1}^{2} K_{ij}^{(m)} T_{,j}^{(m)} n_i^{(m)} = 0 \tag{19}$$

By use of Eq. (7) and the chain rule to make differentiations accordingly, Eq. (19) can be expanded to yield

$$\begin{aligned}\sum_{m=1}^{2} \{&[T_{,\underline{1}}^{(m)} \sqrt{\Delta^{(m)}} + T_{,\underline{3}}^{(m)} (K_{11}^{(m)} \alpha^{(m)} + K_{12}^{(m)} \beta^{(m)} + K_{13}^{(m)} \gamma^{(m)})] n_1^{(m)} \\ &+ [T_{,\underline{1}}^{(m)} K_{12}^{(m)} \sqrt{\Delta^{(m)}} / K_{11}^{(m)} + T_{,\underline{2}}^{(m)} \Delta^{(m)} / K_{11}^{(m)} + T_{,\underline{3}}^{(m)} (K_{12}^{(m)} \alpha_1^{(m)} \\ &+ K_{22}^{(m)} \alpha_2^{(m)} + K_{32}^{(m)} \alpha_3^{(m)})] n_2^{(m)} + [T_{,\underline{1}}^{(m)} K_{13}^{(m)} \sqrt{\Delta^{(m)}} / K_{11}^{(m)} \\ &+ T_{,\underline{2}}^{(m)} \Delta^{(m)} / K_{11}^{(m)} + T_{,\underline{3}}^{(m)} (K_{13}^{(m)} \alpha_1^{(m)} + K_{23}^{(m)} \alpha_2^{(m)} + K_{33}^{(m)} \alpha_3^{(m)})] n_3^{(m)}\} \\ &= 0\end{aligned} \tag{20}$$

which can be abbreviated into a simple tensor form

$$\sum_{m=1}^{2} (T_{,\underline{1}}^{(m)} \sqrt{\Delta^{(m)}} K_{1i}^{(m)} + T_{,\underline{2}}^{(m)} \Delta^{(m)} (\delta_{2i} + \delta_{3i}) + T_{,\underline{3}}^{(m)} K_{11}^{(m)} K_{ij}^{(m)} \alpha_j^{(m)}) n_i^{(m)} = 0 \tag{21}$$

From the coordinate transformation defined previously, the unit base vectors for the mapped and the original space system, denoted, respectively, by $\hat{e}_1$ and $e_1$, are related by

$$\hat{e}_1 \propto (\sqrt{\Delta}/K_{11}) e_1 \quad \hat{e}_2 \propto (-K_{12}/K_{11}) e_1 + e_2$$
$$\hat{e}_3 \propto (\alpha_1 e_1 + \alpha_2 e_2 + \alpha_3 e_3) \tag{22}$$

where the symbol "$\propto$" is to denote the mapping between both of the coordinate systems. We may now derive the expression for outward normal vector on the distorted boundary surface as follows

$$\begin{aligned}\hat{n} = \hat{n}_1 \hat{e}_1 + \hat{n}_2 \hat{e}_2 + \hat{n}_3 \hat{e}_3 &\propto \hat{n}_1 (\sqrt{\Delta}/K_{11}) e_1 + \hat{n}_2 [(-K_{12}/K_{11}) e_1 + e_2] \\ &+ \hat{n}_3 (\alpha_1 e_1 + \alpha_2 e_2 + \alpha_3 e_3) \propto (\hat{n}_1 \sqrt{\Delta}/K_{11} - \hat{n}_2 K_{12}/K_{11} + \hat{n}_3 \alpha_1) e_1 \\ &+ (\hat{n}_2 + \hat{n}_3 \alpha_2) e_2 + (\hat{n}_3 \alpha_3) e_3 \propto n_1 e_1 + n_2 e_2 + n_3 e_3\end{aligned} \tag{23}$$

Therefore, the unit outward normal vectors along the boundary surface for both of the coordinate systems are related by

$$\begin{aligned} n_1 &= (\hat{n}_1 \sqrt{\Delta}/K_{11} - \hat{n}_2 K_{12}/K_{11} + \hat{n}_3 \alpha_1)/\Omega \\ n_2 &= (\hat{n}_2 + \hat{n}_3 \alpha_2)/\Omega \\ n_3 &= \hat{n}_3 \alpha_3/\Omega \end{aligned} \tag{24}$$

where $\Omega$ is defined by

$$\Omega = \sqrt{(\hat{n}_1 \sqrt{\Delta}/K_{11} - \hat{n}_2 K_{12}/K_{11} + \hat{n}_3 \alpha_1)^2 + (\hat{n}_2 + \hat{n}_3 \alpha_2)^2 + (\hat{n}_3 \alpha_3)^2} \tag{25}$$

By substituting Eq. (24) into Eq. (21) followed by tedious algebraic processes, one may eventually obtain a simple yet very useful condition

$$\sum_{m=1}^{2} \frac{\Delta^{(m)}}{\Omega^{(m)} K_{11}^{(m)}} \cdot \frac{dT^{(m)}}{d\hat{n}^{(m)}} = 0 \tag{26}$$

which considers the balance of normal heat fluxes across the interfaces of two adjacent anisotropic materials. It should be noted that Eq. (26) still holds for 2D cases if $\Omega$ is given by omitting the third component of the unit outward normal vector, $\hat{n}_3$. Thus, Eq. (26) is considered the general thermal-equilibrium form between bonded interfaces of two adjacent anisotropic materials for both 2D and 3D cases.

For a non-homogeneous composite that consists of several dissimilar materials bonded together, it is necessary to divide the domain into several subregions, treating each of them in turn. It would evidently be difficult, if not impossible, to derive an integral equation which is valid over all the external boundaries of the different material regions without due consideration for the interfaces between them. For such problems, the boundary integral equation can be written for each material subregion in turn; the appropriate compatibility and equilibrium conditions, described, respectively, by Eq. (17) and Eq. (26), are then enforced at the interface boundaries in the mapped plane or space. After the boundary integral equation (11) is solved for all unknowns along boundaries, the obtained temperature field for the mapped domain still stays unvaried for corresponding nodes, while the temperature gradients for the physical domain boundaries can be computed via the process as discussed previously. To demonstrate the veracity as well as the applicability of the proposed scheme, three numerical examples are presented next.

## Numerical Examples

Requiring only relatively minor modifications, the proposed scheme has been implemented into existing BEM program codes, originally designed for the isotropic potential theory. Three numerical examples are investigated that involve anisotropic heat conduction in multiply joined media with discrete distributions of point heat sources in subregions. In the first two examples, a material combination of two commonly used crystals in the semiconductor industry, quartz for material 1 and a single crystal alumina $Al_2O_3$ for material 2, is arbitrarily chosen to demonstrate the scheme's generality in handling full anisotropy. With the addition of a third material, bismuth, to the material combination chosen in examples I and II, the third example is to show the applicability of the proposed scheme to generally complicated interfaces of more than two combined materials. With asterisks denoting values in the directions of principal axes, the conductivity coefficients of these materials, categorized as the trigonal system, are listed as follows [19]:

| Materials | $K_{11}^* = K_{33}^*$ | $K_{22}^*$ (W/m °C) |
|---|---|---|
| Quartz | 6.5 | 11.3 |
| $Al_2O_3$ | 25.2 | 23.1 |
| Bismuth | 9.24 | 6.65 |

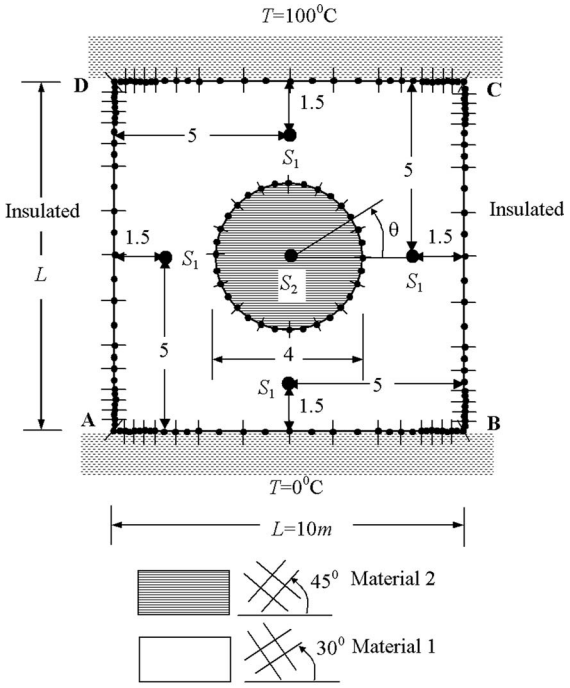


**Fig. 2 A square block embedded with a core column and its BEM meshes for Problem 1**

For modeling the domain boundaries in the three problems, quadratic isoparametric elements are employed for the boundary element analysis. For the sole purpose of verifications, the three example problems are also solved using ANSYS, commercial computer software based upon the finite element method.

**Example I.** As schematically depicted in Fig. 2, the first problem considered is a 10 m × 10 m square block (material 1) in which a core column (material 2) with a diameter 4 m is embedded. Suppose temperature distribution is independent of the third direction in the $x_3$ axis such that we may treat this problem as a 2D case. As the thermal boundary conditions for this problem, sides *AB* and *CD* are prescribed with temperature changes 0 °C and 100 °C, respectively, while the other two surfaces are thermally insulated. As shown in Fig. 2, suppose there is a discrete distribution of five heat sources with different strength $S_1 = 1000\ (\mathrm{W/m^3})$ and $S_2 = 2000\ (\mathrm{W/m^3})$ in material 1 and 2, respectively. To illustrate the capability of the proposed scheme in handling full anisotropy, materials' principal axes are arbitrarily chosen to be oriented 30° and 45° counterclockwise for material 1 and 2, respectively. Also shown in the same figure is the BEM mesh modeling of the boundary that employs 96 quadratic isoparametric elements with a total of 192 nodes. By enforcing the interface conditions given by Eq. (17) and Eq. (26) at interface nodes, we may then apply the sub-regioning technique followed by the postprocess described previously to convert the solution to the one for the physical domain. To simulate the point heat sources in ANSYS, the meshes need to be clustered in their vicinity. The FEM modeling in ANSYS employs 46800 PLANE-55 with a total of 47,041 nodes for the analysis. The computed temperatures along the insulated surfaces, normalized by $\Delta T = 100\,^\circ\mathrm{C}$, are plotted in Fig. 3. Also, the normalized temperature gradients, $dT/dn \cdot L/\Delta T$, from the solutions of BEM and FEM are plotted in Fig. 4. Figure 5 shows the variation of the normalized temperature, $T/\Delta T$, around the circumference of the core column from the both approaches. As can be obviously seen from the comparisons shown in Figs. 3–5, excellent agreement between both solutions indeed verifies the veracity of the promposed BEM scheme. The minor discrepancies observed for the both solutions

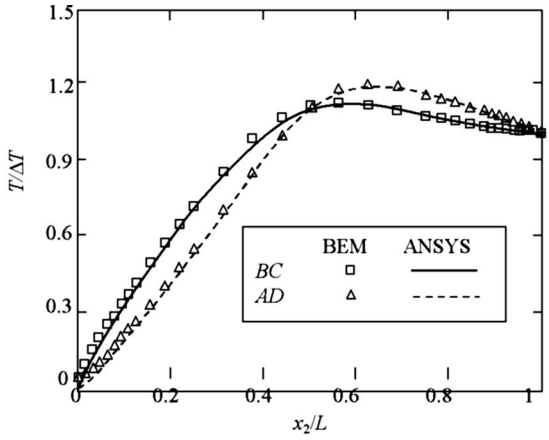


**Fig. 3 Variation of normalized temperature, $T/\Delta T$, along *BC* and *AD***

are, in fact, mainly due to the FEM modeling of the concentrated heat sources that require fine meshes in the vincinity of the heat source points.

**Example II.** To show the validity of the proposed scheme for 3D cases, the second problem we treat is to consider a long composite bar made by bonding together two rectangular bars made of quartz and a single crystal $Al_2O_3$ as shown in Fig. 6. The two ends are prescribed Dirichlet conditions with $T_1 = 0\,^\circ\mathrm{C}$ and $T_2$

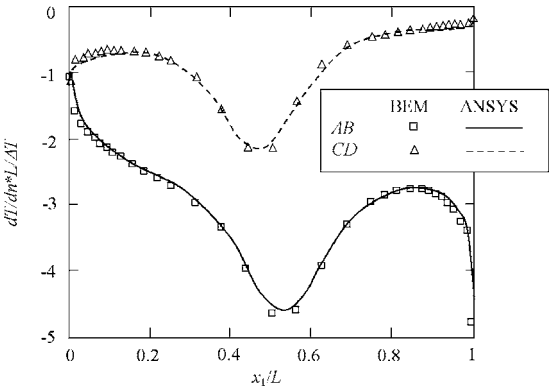


**Fig. 4 Variation of normalized temperature gradients, $dT/dn \cdot L/\Delta T$, along *AB* and *CD***

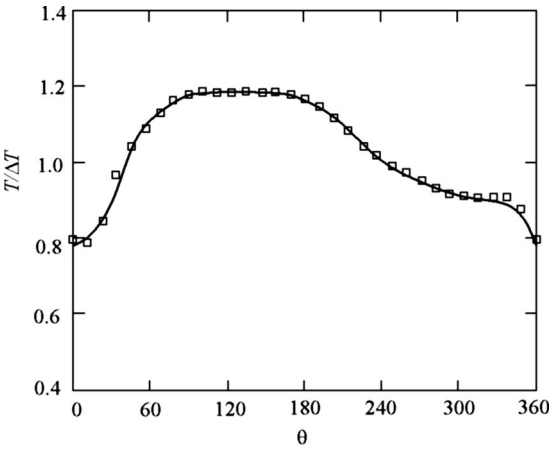


**Fig. 5 Variation of normalized temperature, $T/\Delta T$, along the circumference of the core material**

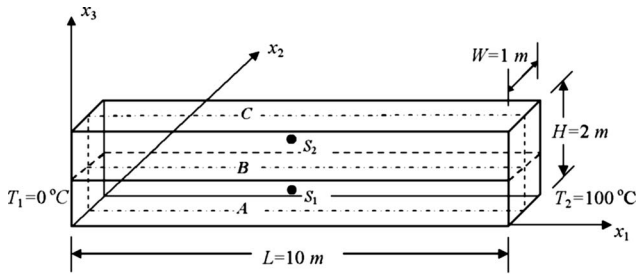


**Fig. 6 A composite bar with concentrated heat sources**

$=100\,^\circ$C for the left and the right surface, respectively, while the remaining sides are thermally insulated. To demonstrate the generality of the proposed scheme for full anisotropy, the principal axes for both materials are arbitrarily oriented in a direction by rotating the first, second, and third axes with respect to the corresponding global Cartesian coordinate by 30°, 45°, and 60°, respectively. Suppose there exist two concentrated heat sources, each of which is located at the midpoint of material 1 and 2 with strength $S_1=1000$ (W/m$^3$) and $S_2=2000$ (W/m$^3$), respectively. Figure 7 shows the mesh discretization for the boundary surfaces, where 88 rectangular elements with a total of 496 boundary nodes are applied. To simulate the concentrated heat sources with convergent accuracy, the FEM modeling of the domain employs 16,0000 SOLID-70 elements with a total of 173,061 nodes. Since it is hard to present the whole 3D solutions with comparison of results in the limited space of this paper, only the variation of the normalized temperatures, $T/\Delta T$ ($\Delta T=100\,^\circ$C), along the midline of interface planes is plotted in Fig. 8. As can be seen from the figure, the temperature keeps rising up to the point near the source and then starts to decline to the boundary value at the right end. Once again, the 3D solution from the present BEM approach agrees with the FEM analysis done in ANSYS.

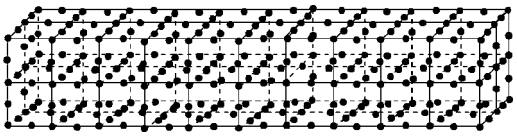

**Fig. 7 Boundary meshes used for the BEM analysis for Example II**

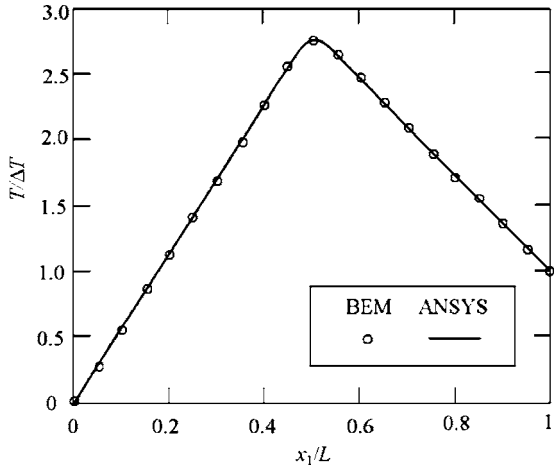


**Fig. 8 Variation of normalized temperature, $T/\Delta T$, along the midline of interfaces for Example II**

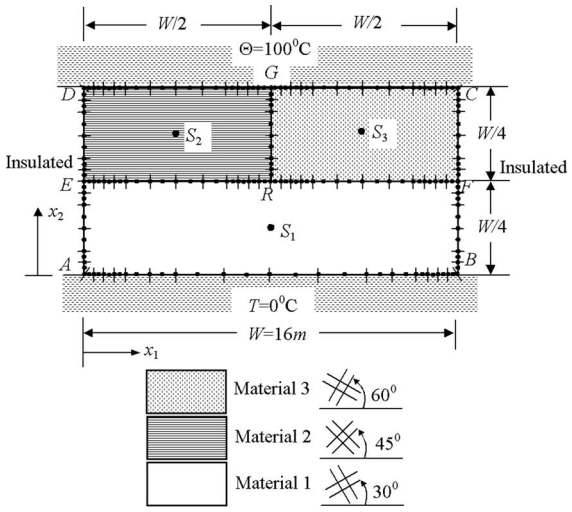


**Fig. 9 A rectangular composite subjected to internal concentrated heat sources—Example III**

**Example III.** To show the applicability of the proposed BEM scheme for a somewhat more complicated case, the last example problem considers a composite structure consisting of three different anisotropic materials with intersecting interfaces as shown in Fig. 9. The materials' principal axes are arbitrarily chosen to be oriented with 30°, 45°, and 60° measured counterclockwise from the $x_1$ axis for material 1, 2, and 3, respectively. Also, the temperature is assumed to have a two-dimensional distribution as in Example I. Sides *AB* and *CD* are prescribed with the temperature changes 0 °C and 100 °C, respectively, while the top and bottom surfaces are thermally insulated. Suppose there exist three concentrated heat sources with strength $S_1=1000$ (W/m$^3$), $S_2=2000$ (W/m$^3$), and $S_3=3000$ (W/m$^3$) located at the midpoint of material 1, 2, and 3, respectively. Also shown in Fig. 9 is the BEM mesh discretization that only 124 quadratic isoparametric elements with a total of 261 nodes are applied to model the whole boundaries. To enforce the compatibility and equilibrium conditions at interface nodes between any two adjacent materials, not only all corners but also point *R* for material 1 require double-node modeling. For the FEM modeling in ANSYS, 51,200 PLANE-77 elements with a total of 155,200 nodes are applied. Figure 10 shows the comparison of the results for the variation of the normalized temperatures, $T/\Delta T$ ($\Delta T=100\,^\circ$C), along surfaces

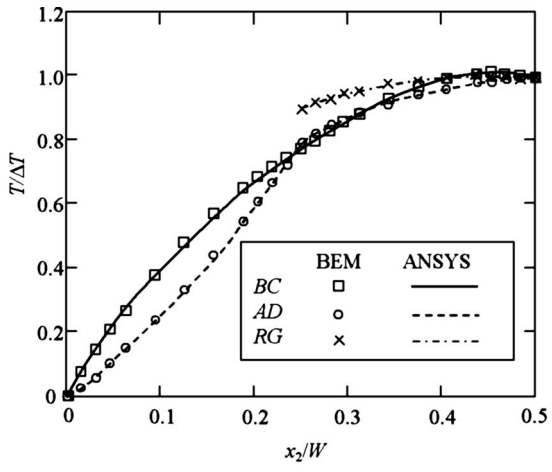


**Fig. 10 Variation of the normalized temperatures, $T/\Delta T$, along surfaces *BC*, *AD*, and *RG***

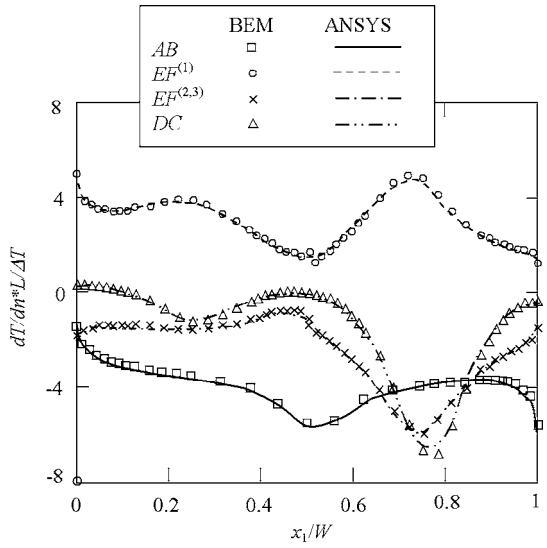


**Fig. 11 Variation of the normalized temperature gradients, $dT/dn \cdot L/\Delta T$, along surfaces *AB*, *EF*, and *DC***

*BC*, *AD*, and *RG*. In a similar manner, the computed temperature gradients along surfaces AB, *EF*, and *DC* are normalized as before and plotted in Fig. 11 for comparison of both results obtained by the BEM and the FEM. It is perhaps worth noting that the normal temperature gradients, $dT/dn$, on the upper interface $EF^{(2)}/EF^{(3)}$ and the lower interface $EF^{(1)}$ are different due to dissimilarity of material properties. As is expected, fluctuations of the temperature gradients appear near those spots that are susceptible to the concentrated heat sources. Also, the variation of normalized temperatures along the interface *EF* is plotted in Fig. 12 for both results obtained by the BEM and the FEM. Once again, excellent agreement between both solutions is observed.

## Conclusion

In this paper, the DDM technique is applied effectively in BEM as an alternative numerical tool to study the 2D and 3D anisotropic heat conduction in a multiply joined medium that are embedded with concentrated heat sources. This is achieved by mapping the physical domain into another coordinate plane or space where the temperature field is governed by the standard Poisson's equation. Therefore, the fully anisotropic field problem can be solved using standard BEM codes for "isotropic" problems governed by Poisson's equation, with relatively minor modifications to deal with preprocessing of the input data and postprocessing of the spatial gradients of the temperature. By such transformation, the strength of concentrated heat sources is converted with a transformation factor. Due to the boundary distortions of adjacent components, the mapping shall result in overlapping/separation of interfaces, which requires formulating appropriate compatibility and equilibrium equations. In this paper, the appropriate compatibility and equilibrium equations for both 2D and 3D cases are derived that account for thermal balance between interfaces. With the obvious ease of applying the proposed DDM technique, three numerical examples are provided to illustrate the ease and accuracy of this proposed scheme.

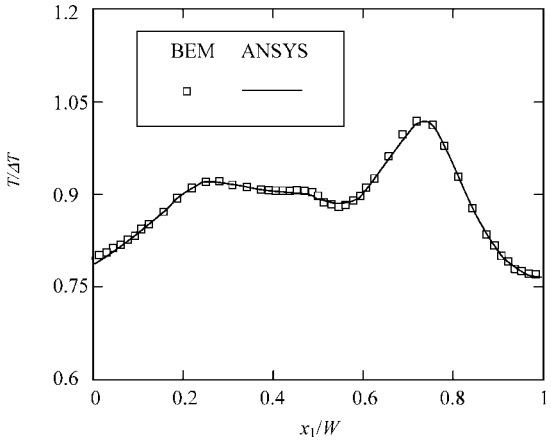


**Fig. 12 Variation of the normalized temperatures, $T/\Delta T$, along interface *EF***

## Acknowledgment

The authors gratefully acknowledge financial support by the National Science Council of Taiwan, Republic of China (Grant Nos. NSC-92-2212-E-035-012 and NSC-93-2212-E-035-006).

## Nomenclature

- $\mathbf{F}$ = matrix of coordinate transformation
- $K_{ij}$ = conductivity coefficients
- $M_n$ = $n$th internal heat-source point
- $P$ = source points
- $Q$ = field points
- $S_m$ = heat source strength at point $m$
- $\hat{S}$ = distorted boundary in the mapped plane or space
- $T$ = temperature change
- $U$ = fundamental solution for temperature
- $V$ = fundamental solution for normal temperature gradient
- $n_i$ = components of the unit outward normal vector on the physical domain boundary
- $\hat{n}_i$ = components of the unit outward normal vector on the mapped domain boundary
- $x_i$ = Cartesian coordinates for the physical domain
- $\hat{x}_i$ = new Cartesian coordinates for the mapped domain
- $\hat{\varphi}_i$ = temperature gradients along the mapped boundary
- $\hat{\xi}, \hat{\eta}$ = local coordinate axes tangent to the mapped boundary surface in space
- $\delta_m$ = Dirac delta function at point $m$

## References

[1] Tauchert, T. R., and Akoz, A. Y., 1975, "Stationary Temperature and Stress Fields in an Elastic Anisotropic Slab," J. Appl. Mech., **42**, pp. 647–650.
[2] Mulholland, G. P., and Gupta, B. P., 1977, "Heat Transfer in a Three-Dimensional Anisotropic Solid of Arbitrary Shape," J. Heat Transfer, **99**, pp. 135–137.
[3] Chang, Y. P., 1977, "Analytical Solution for Heat Conduction in Anisotropic Media in Infinite Semi-Infinite, and Two-Place-Bounded Regions," Int. J. Heat Mass Transfer, **20**, pp. 1019–1028.
[4] Poon, K. C., 1979, "Transformation of Heat Conduction Problems in Layered Composites from Anisotropic to Orthotropic," Lett. Heat Mass Transfer, **6**, pp. 503–511.
[5] Poon, K. C., Tsao, R. C. H., and Chang, Y. P., 1979, "Solution of Anisotropic Problems of First Class by Coordinate Transformation," J. Heat Transfer, **101**, pp. 340–345.
[6] Shiah, Y. C., and Tan, C. L., 1998, "Exact Boundary Integral Transformation of the Thermoelastic Domain Integral in BEM for General 2D Anisotropic Elasticity," Comput. Mech., **23**, pp. 87–96.
[7] Shiah, Y. C., and Tan, C. L., 1998, "Calculation of Interior Point Stresses in 2-D Boundary Element Analysis of Anisotropic Bodies with Body Forces," J. Strain Anal. Eng. Des., **34**, pp. 117–128.
[8] Shiah, Y. C., and Tan, C. L., 1998, "BEM Treatment of Two-dimensional Anisotropic Field Problems by Direct Domain Mapping," Eng. Anal. Boundary Elem., **20**, pp. 347–351.
[9] Shiah, Y. C., and Lin, C. Y., 2002, "Anisotropic Heat Conduction Involving Internal Arbitrary Volume Heat Generation Rate," Int. Commun. Heat Mass Transfer, **29**(8), pp. 1079–1088.

[10] Shiah, Y. C., and Tan, C. L., 2004, "BEM Treatment of Three Dimensional Anisotropic Field Problems by Direct Domain Mapping," Eng. Anal. Boundary Elem., **28**(1), pp. 43–52.
[11] Yan, L., Sheikh, A. H., and Beck, J. V., 1993, "Thermal Characteristics of Two-Layered Bodies with Embedded Thin-Film Heat Source," J. Electron. Packag., **115**, pp. 276–283.
[12] Hsieh, M. H., and Ma, C. C., 2002, "Analytical Investigations for Heat Conduction Problems in Anisotropic Thin-Layer Media with Embedded Heat Sources," Int. J. Heat Mass Transfer, **45**, pp. 4117–4132.
[13] Ma, C.-C., and Chang, S.-W., 2004, "Analytical Exact Solutions of Heat Conduction Problems for Anisotropic Multi-Layered Media," Int. J. Heat Mass Transfer, **47**, pp. 1643–1655.
[14] Segerlind, L. J., 1984, *Applied Finite Element Analysis*, Wiley, New York.
[15] Zienkiewicz, O. C., 1977, *The Finite Element Method*, McGraw-Hill, Maidenhead.
[16] Li, W. H., 1983, *Fluid Mechanics in Water Resources Engineering*, Allyn and Bacon, Toronto, ISBN 0205078958.
[17] Bruce, E., and Lejeune, A., 1989, "An Effective Solution of the Numerical Problems at Multi-domain Points for Anisotropic Laplace Problems," Advances in Boundary Elements Vol. 2, edited by C. A. Brebbia and J. J. Connor, *Proc. 11th Int. Conf. Boundary Element Methods*, Cambridge, MA, Springer, Berlin.
[18] Banerjee, P. K., and Butterfield, R., 1981, *Boundary Element Methods in Engineering Science*, McGraw-Hill, Maidenhead, ISBN 0070841209.
[19] Nye, J. F., 1960, *Physical Properties of Crystals, Their Representation by Tensors and Matrices*, Clarendon, Oxford.